Nanostructures and their physicochemical modification as tool to control cell function

Dissertation

zur Erlangung des

Doktorgrades der Ingenieurwissenschaften (Dr.-Ing.)

des

Zentrums für Ingenieurwissenschaften

der Martin-Luther-Universität

Halle-Wittenberg,

vorgelegt

von Herrn Dipl.-Ing. Marcus S. Niepel

geboren am 18. November 1980 in Reichenbach/ V.

Gutachter: Prof. Dr. rer. nat. habil. Thomas Groth

Prof. Dr.-Ing. habil. Dr. h.c. Joachim Ulrich

Prof. Dr. rer. nat. habil. Regine Willumeit

Tag der öffentlichen Verteidigung: 16.07.2014

Meiner Familie

INDEX

Abbreviations

(PH)$_4$	terminal heparin layer		ERK	extracellular signal regulated kinase
(PH)$_4$P	terminal poly (ethylene imine) layer		EUV	extreme ultraviolet
2D	two-dimensional		FA	focal adhesion
3D	three-dimensional		FAK	focal adhesion kinase
a.u.	arbitrary units		FBR	foreign body reaction
AC	alternating current		FBS	fetal bovine serum
AAS	antibiotic-antimycotic-solution		FIB	focused ion beam
AFM	atomic force microscopy		FITC	fluorescein isothiocyanate
ANOVA	analysis of variance		FN	fibronectin
Au	gold		FNG	fibrinogen
BCMN	block-copolymer micelle nanolithography		Fyn	tyrosine-specific phospho-transferase
BODIPY	fluorescent F-actin stain		GAG	glycosaminoglycan
BSA	bovine serum albumin		GB	grain boundaries
CCM	colloid crystal mask		GEL	gelatin
CHCA	α-cyano-4-hydroxycinnamic acid		GTPase	guanosine triphosphate hydrolase
ChS	chondroitin sulfate		H, HEP	heparin
CLSM	confocal laser scanning microscope		HDF	human dermal fibroblasts
COL	collagen		HMDS	hexamethyldisilazane
CS	cellulose		i.e.	*id est* = that means
CSL	cover slips		IgG	immunoglobulin G
CY2	polyclonal goat anti-mouse Cy2 conjugated secondary antibody		IHP	inner Helmholtz plane
			ILK	integrin-linked kinase
DABCO	1,4-diazabicyclo-(2,2,2)-octane		IPTS	3-isocyanatopropyl triethoxysilane
DC	direct current		IU	international units
DLVO	Derjaguin, Landau, Verwey, Overbeek		LAM	laminin
DMEM	Dulbecco's modified Eagle's medium		LB	Langmuir-Blodgett
			LIL	laser interference lithography
DMF	*N,N* - dimethyl formamide		MALDI	matrix-assisted laser desorption/ionization
DMSO	dimethyl sulfoxide		µCP	microcontact printing
DNA	deoxyribonucleic acid		MAPK	mitogen activated protein kinase
EBPVD	electron beam physical vapor deposition		MEK	methyl ethyl ketone
ECM	extracellular matrix		MES	2-(*N*-morpholino) ethane sulfonic acid
EDC	1-ethyl-3-(3-dimethylaminopropyl) carbodiimide		M$_n$	number average molar mass
EDTA	ethylenediaminetetraacetic acid		mPEG	methoxy-poly (ethylene glycol)
e.g.	*exempli gratia* = for example			

IV

mPEGA	α-methoxy-ω-amino poly (ethylene glycol)
MS	mass spectrometry
MUDA	11-mercaptoundecanoic acid
M_w	weight average molar mass
Nd:YAG	neodymium-doped yttrium aluminum garnet
NHS	*N*-hydroxysuccinimide
NIL	nanoimprint lithography
NMR	nuclear magnetic resonance
NSL	nanosphere lithography
OEG	2-[methoxy (polyethyleneoxy) propyl] trimethoxysilane
OHP	outer Helmholtz plane
P, PEI	poly (ethylene imine)
PAA	poly (acrylic acid)
PAH	poly (allylamine hydrochloride)
PBS	phosphate buffered saline
PCSA	polarizer compensator sample analyzer
PDMS	poly (dimethyl siloxane)
PEL	polyelectrolyte
PEM	polyelectrolyte multilayers
PFA	paraformaldehyde
pH	pH value
PLL	poly (L-lysine)
PS-NP	polystyrene nanoparticles
PS/P2VP	poly (styrene)-block-poly (2-vinylpyridine)
PSS	poly (styrene sulfonate)
PSU	polysulfone
PZC	point of zero charge
RCA	Radio Corporation of America
RhoA	Ras homolog gene family, member A
RI	refractive index
ROCK	Rho associated coiled-coil protein kinase
ROI	regions of interest
RT	room temperature
SAM	self-assembled monolayer
SBL	scanning beam lithography
SD	standard deviation

SDS	sodium dodecyl sulfate
SEM	scanning electron microscope
SFIL	step and flash imprint lithography
SH2	Src homology 2
Si	silicon
SPL	scanning probe lithography
Src	proto-oncogene encoding a tyrosine kinase
STM	scanning tunneling microscopy
TCPS	tissue culture polystyrene
TE	tissue engineering
TEA	triethylamine
TMS	tetramethylsilane
TOF	time of flight
TO-PRO 3	nucleic acid stain
Urea	mPEG-urea
UV	ultraviolet
VN	vitronectin
WCA	water contact angle
ZEN	Zeiss efficient navigation
ZP	zeta potential

Symbols

®	registered Trademark	V	volume
A	cross section area	Y	molarity of heparin for calculation of labeling
a_i	nanoparticle dimension (i = ML - monolayer, i = DL - double layer)	β (Beta)	optical path length
c	concentration	γ_{lv}	surface tension between liquid-vapor phases
d	film thickness	γ_{sl}	surface tension between solid-liquid phases
D	PS-NP diameter		
Da	Dalton	γ_{sv}	surface tension between solid-vapor phases
d_i	nanoparticle distance (i = ML - monolayer, i = DL - double layer)	δ_i (delta)	phase difference (i = i - incident light, i = 2 - reflected light)
dI	streaming current difference	Δ (Delta)	phase shift angle
dp	pressure difference	$\Delta\theta$ (Delta Theta)	contact angle hysteresis
dU	streaming potential difference	ε (Epsilon)	permittivity in vacuum
f	frequency	ε_o (Epsilon zero)	relative dielectric constant
I	ionic strength	ζ (Zeta)	zeta potential
k	cantilever spring constant	η (Eta)	dynamic viscosity
L	length of the streaming channel	θ_i (Theta)	water contact angle (i = a - advancing, i = r - receding)
n	refractive index	κ (Kappa)	specific conductivity of the channel
pI	isoelectric point	λ (Lambda)	wavelength
pK_a	acid dissociation constant	ρ (Rho)	density
r	reflectivity	τ^0 (Tau)	water adhesion tension
R	resistance	ϕ_i (Phi)	angle of light beam (i = 1 - incident light, i = 2 - refraction light)
R_a	roughness average		
RMS	root mean square	$\Psi(x)$ (Psi x)	potential at position x
R^p, R^s	reflection coefficient (p - parallel, s - perpendicular)	Ψ_d (Psi d)	potential at distance d of slipping plane
$\tan\Psi$	ratio of reflection coefficient		

Abstract

The modification of biomaterial surfaces at the nanoscale offers great potential for precise control of biological events such as protein adsorption as well as cell adhesion, proliferation, and differentiation. Self-assembled monolayers (SAM) are used here to control protein adsorption and, subsequently, cell adhesion on planar surfaces. Commercially available PEG-containing silanes are compared with silanes that are synthesized during the PhD work and it is shown that the chain length of these silane-based SAM is crucial for the efficacy of protein repellence. The results obtained on planar surfaces are transferred to nanostructured materials. These nanostructures are generated using the so-called nanosphere lithography (NSL) which enables for the design of regular ordered gold nanostructures of tetrahedral shape on planar model substrates. The size and distance of the obtained nanostructures is controlled by using colloids with various diameters for colloidal mask formation. The combination of NSL with SAM creates a highly selective, nanostructured system whose wettability is dependent on the type of terminating molecule. Further, it is shown that single proteins selectively adsorb on top of the nanostructures, which are modified with a terminating carboxyl group, and not on the passivated interstices bearing a terminal methyl group, but intramolecular PEG units. In addition, adhesion and growth of human dermal fibroblasts (HDF) is highly affected by size and distance of the nanostructures with decreasing trend of cell size with increasing nanostructure dimension. Further, it is shown that the cell's fibronectin (FN) matrix synthesis is influenced, too. Interestingly, the FN fibrils are linked to the hexagonal close-packed patterns. Already heterogenic by topography and chemical modification, the system presented here is additionally altered introducing viscoelastic properties. The layer-by-layer (LbL) technique, based on electrostatic interaction of oppositely charged molecules, is used here for the first time in combination with the NSL and multilayers of heparin (HEP) and poly (ethylene imine) (PEI) are assembled on top of the nanostructures. Moreover, among various parameters that can be controlled, the pH value is used in this study as tool to modify multilayer composition and properties. Thereby, the adjustment to acidic or alkaline values for the HEP solution at later stages of multilayer assembly apparently influences surface characteristics. The strong hydrophobicity of pristine nanostructures is drastically changed to highly hydrophilic surfaces. Further, the introduction of the macromolecules results in differences in surface charge and topography in dependence on the terminating molecule. Finally, such unique system noticeably affects adhesion and proliferation of HDF in an opposite manner if compared to the unmodified nanostructured biomaterials, meaning that cell size is slightly increasing with increasing nanostructure dimension. Owing to its high degree of heterogeneity as well as the manifold options for regulation, the presented system offers great potential to guide stem cell differentiation in the future or can find application in *in situ* transfection of cells due to the high affinity of PEI to DNA constructs.

Zusammenfassung

Die Modifikation von Biomaterialoberflächen im Nanometerbereich hat ein großes Potenzial zur präzisen Steuerung biologischer Prozesse wie Proteinadsorption sowie Adhäsion, Wachstum und Differenzierung von Zellen. Selbstorganisierende Monoschichten (*engl. self-assembled monolayers* (SAM)) werden hier verwendet, um die Adsorption von Proteinen und anschließend die Adhäsion von Zellen auf ebenen Oberflächen zu regulieren. Dabei werden kommerziell erhältliche und mit PEG-Einheiten versehene Silane mit solchen verglichen, welche während der Entstehung dieser Arbeit synthetisiert wurden, und es wird gezeigt, dass die Kettenlänge der SAM entscheidend für die Wirksamkeit der Proteinabweisung ist. Die Ergebnisse von planaren Oberflächen werden anschließend auf nanostrukturierte Materialien übertragen. Diese Strukturen werden mit der sogenannten Nanosphären-Lithographie (NSL) generiert, welche es erlaubt, regelmäßig angeordnete, tetraedrische Goldstrukturen auf ebenen Modellsubstraten zu erzeugen. Größe und Abstand der Nanostrukturen können dabei relativ einfach über den Durchmesser der verwendeten Kolloide zur Maskenbildung gesteuert werden. Die Kombination der NSL mit SAM erzeugt dabei ein hoch selektives, nanostrukturiertes System dessen Benetzbarkeit von der Art der terminalen Moleküle abhängt. Des Weiteren wird gezeigt, dass einzelne Proteine selektiv auf den Strukturen, welche durch Modifizierung eine terminale Karboxylgruppe enthalten, und nicht auf den passivierten Strukturzwischenräumen adsorbieren, welche zwar terminal eine Methylgruppe, aber im Molekül PEG-Einheiten aufweisen. Darüber hinaus werden Adhäsion und Wachstum von humanen dermalen Fibroblasten (HDF) deutlich von Größe und Abstand der Nanostrukturen beeinflusst, wobei ein Trend von abnehmender Zellgröße mit zunehmender Strukturgröße feststellbar ist. Zusätzlich wird gezeigt, dass auch die Synthese der zellulären Fibronektinmatrix beeinflusst wird, denn interessanterweise sind die Fibronektinfibrillen mit den hexagonal gepackten Strukturen verknüpft. Obwohl bereits heterogen durch die Kombination von Topographie mit Oberflächenchemie eröffnet die Erzeugung viskoelastischer Parameter auf den Strukturen zusätzliche Kontrollmöglichkeiten. Die Layer-by-Layer (LbL) Methode, welche auf der elektrostatischen Wechselwirkung entgegengesetzt geladener Moleküle basiert, wird dabei zum ersten Mal in Kombination mit der NSL verwendet und Multischichten von Heparin (HEP) und Polyethylenimin (PEI) werden auf den Goldstrukturen erzeugt. Von den verschiedenen Parametern, die kontrolliert werden können, um Multischichtzusammensetzung und Eigenschaften zu modifizieren, wird in dieser Arbeit die Änderung des pH-Wertes der Polyelektrolytlösungen zur Steuerung der Multischichteigenschaften verwendet. Hierbei führt die Einstellung von sauren oder alkalischen pH-Werten der HEP-Lösung zu einem fortgeschrittenen Zeitpunkt der Multischichtbildung zu spezifischen Oberflächeneigenschaften. Die ausgeprägte Hydrophobie der unbehandelten Nanostrukturen wird dabei in eine außerordentliche Hydrophilie umgewandelt. Des Weiteren

2

führt die Adsorption der Makromoleküle zu Änderungen der Oberflächenladung sowie in der Oberflächenstruktur, natürlich in Abhängigkeit vom terminalen Molekül. Ferner fördert dieses einzigartige System Adhäsion und Wachstum von HDF in entgegengesetzter Art und Weise als die nativen, nanostrukturierten Biomaterialien. Dies soll heißen, dass die Größe adhärenter Zellen mit zunehmender Strukturgröße ebenfalls zunimmt. Aufgrund der hohen Heterogenität sowie der vielfältigen Möglichkeiten zur Regulierung der Oberflächeneigenschaften bietet das vorgestellte System ein großes Potenzial, die Stammzelldifferenzierung in Zukunft positiv zu beeinflussen. Darüber hinaus kann es durch die hohe Affinität von PEI zu DNA-Konstrukten Anwendung bei der *in situ* Transfektion von Zellen finden.

1   Nanostructured biomaterial surfaces

1.1   General Introduction

The definition of biomedical materials or biomaterials is primarily depending on the research focus and type of application [1]. The profound amount of nowadays applications makes the definition even more difficult. Typically, biomaterials are materials which are intended to interact with biological systems for the purpose of diagnosis and treatment or which are implanted into a host system for the replacement of tissues, organs or body functions; either permanently or temporarily [1]. Biomaterials research is an interdisciplinary field that ranges from classical biomaterials to materials used in tissue engineering (TE) or regenerative medicine [1], where degradation and biomimetics play an important role. Moreover, countless applications for various purposes are imaginable, desirable or put already into practice ranging from small biosensors to large implants or artificial organs. Permanent bone implants, for example, are matched with their effect on osseointegration, the rate of implant stabilization and the mechanical strength as opposed to autologous bone. A central role in fulfilling the desired prerequisites plays a biomaterial's biocompatibility. Already in 1987, D.F. Williams argued, "biocompatibility is the ability of a material to perform with an appropriate host response in a specific application." [1]. However, that definition is not carved into stone and is subject to changes at all times since the biocompatibility might vary in dependence on the type of application. Nevertheless, it is a base for future definitions. Examples for such host responses include the absence of blood clotting or bacterial colonization and straightforward healing, whereas specific applications include examples such as sutures, membranes for hemodialysis, urinary catheters, artificial hip-joints, etc. [1]. The interaction between the host system and the material itself can range from short- (minutes to hours) to long-term (days to month) intervals, whereas the host response typically starts immediately upon contact with the material. As a result, individual materials are classified regarding their property into biotolerant, bioinert or bioactive [2]. Thereby, bioactive materials promote tissue regeneration positively leading to consolidation of the implant at the interface of the material to the host tissue. Thus, biocompatibility cannot be removed from its context of definition and a number of *in vitro* and *in vivo* experiments are necessary to evaluate biomaterial properties in terms of biodegradability, toxicity, immune response, etc. [3]. In addition to biocompatibility, other biomaterial characteristics such as physical (e.g. rigidity, elasticity, or durability) and chemical (e.g. stability, inertness, or reactivity) properties are important for biomedical applications. At this time, surface functionalization with bioactive molecules is investigated intensively to introduce a biofunctionality in materials generally used in TE and other biomedical applications [4, 5]. Additionally, the continuous development of biomaterials permanently improves the host response in dependence on the desired application; for example adding features affecting their

biodegradability, bioactivity, etc. or to avoid undesirable side effects such as foreign body reaction (FBR) or stress shielding. In conclusion, the precise control of biomaterials bulk and surface properties is crucial to their medical as well as economic success in implantology, TE, and regenerative medicine. Thus, important parameters of material characteristics affecting interaction with proteins and cells are discussed in the following sections.

1.1.1 Biomaterials and their properties

As mentioned earlier, biomaterial properties (i.e. bulk and surface properties) are crucial and, of course, have to meet certain requirements in dependence on the biomaterial's type of clinical application. These properties can be separated into physical (topography, geometry, mechanics, etc.) and chemical (type and amount of functional groups, etc.) characteristics [1]. Thus, surface properties affect, either alone or in combination with other properties, a material's surface energy [6, 7], surface potential [8, 9], or surface roughness among others [10, 11]. It is a challenging task for researchers to design materials matching mechanical/ viscoelastic properties, defined by the bulk, with unique surface properties. The latter ones are of upmost importance since surfaces form an interface between the material and the host tissue, which is a critical element [12] influencing subsequent events such as protein adsorption, adhesion, proliferation, and differentiation of cells *in vitro* and *in vivo* [1]. A material's surface chemistry is defined by type and presence of atoms and bonds that can be prone to more or less simple modifications in dependence on the environment, which, in turn, can be permanent or transient in state. However, the type of modification clearly depends on the material class. Metals as well as ceramics/ glasses, once oxidized, are a source for metal or non-metal ions. Polymers offer a great variability in modification. Their composition can be controlled to manipulate the presence and amount of functional side groups such as amino, carbonyl, carboxyl, hydroxyl, methyl, sulfate or sulfonate groups. Further, their structure is defined by the composition of the main chain, consisting of carbon, nitrogen, or oxygen atoms, etc. Nevertheless, the functional side groups can be chemically modified resulting in changes of their interfacial properties [6, 7, 13].

The wetting properties of a biomaterial are an important parameter for biomedical applications since they determine the adsorption of proteins and, subsequently, adhesion of cells. Non-polar regions on material surfaces result in a hydrophobic character, where water does not adsorb to a high extent nor is it absorbed. Further, water at hydrophobic surfaces is less dense and possesses higher interfacial energy [14]. It equilibrates its chemical potential with water in the bulk phase away from the surface by an increase in partial volume. In contrast, hydrophilic materials are characterized by polar regions leading to a tight binding of high-dense water. If a material is in contact with an aqueous environment, a thermodynamic driving force

results in the reduction of the interfacial energy at the solid-liquid interface [15], which is important for biological events. Upon water contact, polar regions of hydrophilic materials dissociate, which results in electrostatic attraction of molecules from the aqueous phase. However, since biological media are typically buffered with salt ions, the electrostatic attraction can be screened and decays with the *Debye-Hückel*-length, as described by the DLVO theory [16]. Hence, not only the simple presence of dissociable groups on a material's surface, but also the amount and distribution across that surface affect material properties. In addition, water can result in swelling of material interfaces affecting mechanical properties and that phenomenon is used, for example, in hydrogels, which bind or even absorb water to a high extent [17, 18]. The interfacial free energy important for the degree of biological response is also influenced by phase segregation during or after processing [19-21]. Hence, surface enrichment can occur in metal alloys as well as in polymers, which also influences the interfacial energy of the material, resulting in variations in the water structure close to the surface and, thus, influencing subsequent events such as protein adsorption [22]. Finally, physical interfacial material properties such as structure, roughness, or porosity affect the interaction with aqueous media resulting in roughness-dependent wettability [23].

1.1.2   Interactions of biomaterials with their environment

In dependence on the material properties, a complex cascade of events starts at the interface upon contact with a biological environment. There, most biomaterials are interacting with an aqueous milieu, where water as major component dissolves salts and macromolecules. Water forms transient 3D clusters that vary in size, are stabilized by hydrogen bonds, and are based on Lewis-acid-base association. Owing to its amphoteric, strong (di) polar character and small molecule size it initially interacts with a material surface before other molecules are able to do so [24]. The cluster structure of water is distorted upon contact with biomaterial surfaces and, thereby, the orientation of the water molecules is dependent on the materials chemistry. High-dense water can be found on hydrophilic surfaces within the immobile hydrodynamic layer close to the surface, resulting in a strong barrier for the adsorption of macromolecules. In contrast, water in contact with hydrophobic surfaces is less dense due to an increased order within the water network. Hence, the barrier effect is reduced due to a lowered entropy within the water clusters close to the material surface and, thus, protein adsorption might be increased in comparison to hydrophilic surfaces [14]. As a result, material-protein or material-cell interactions are not solely influenced by the material surface properties, but also by the presence of primarily surface bound water. Upon contact with a biological environment, protein adsorption and cell adhesion follow a distinct hierarchy on material surfaces. As long as proteins from the surrounding body fluids are available cells will never attach to a substrate's

surface directly under physiological conditions [25], which is also valid for many *in vitro* conditions, where typically heat-inactivated sera are used as medium supplements. As a result, before cells make contact with biomaterial surfaces, proteins are transferred to the substrate via diffusion or convection [26] and the adsorption starts immediately [27]. Due to higher adsorption kinetics, smaller proteins initially adsorb in dependence on the concentration in solution and the diffusion coefficient [28], whereas at later stages larger proteins replace the smaller ones due to a higher affinity because of generally larger numbers of binding sites [27]. This so-called 'Vroman' effect is dependent on the material surface properties and is not valid on highly hydrophobic surfaces. Attractive interaction forces between proteins and surfaces can be both long- and short-ranged [27] and are dependent on the physicochemical properties of the material, such as surface energy, surface potential, presence of functional groups, etc. [8, 10, 29]. Long-range forces include *Coulomb* i.e. electrostatic interactions that can be either attractive or repulsive due to the presence of charged functional groups within the protein structure. In contrast, attractive short-range forces include *van der Waals* interactions, hydrogen bonding, acid-base, or hydrophobic interactions, whereas hydration forces or steric repulsions represent repulsive short-range interactions. Here, the chain length of surface bound molecules influences the repulsion strength. Long-chain molecules compress during protein contact which results in entropy loss and absence of protein adsorption [30]. In contrast, short-chain molecules have less freedom for conformational changes and tight water binding is the mechanism behind protein repellency [30]. The primary structure of proteins is defined by their amino acid sequence, whereas secondary, tertiary, and quaternary structure determine a proteins dimensionality. However, due to the different properties of amino acids proteins can possess hydrophilic and/ or hydrophobic structural parts as well as positive and/ or negative charged domains, rendering them amphiphilic and amphoteric. Hence, their net charge at physiological conditions can be positive or negative in dependence on their isoelectric point (pI) and it is determined by the pH value and ionic strength of the ambient phase. The knowledge of the pI can be used to tailor optimal requirements for protein-surface-interaction. Here, an opposite net charge of protein and material surface supports the adsorption [27, 31]. Additionally, even the net charge of a protein is positive it may carry negatively charged residues and vice versa [26]. The heterogeneity of proteins leads to surface enrichment of domains on the outer regions that are able to interact with the surface [22]. Further, amino acids are located primarily in the outer regions of the proteins in polar solvents due to their hydrophilicity [27], which can be beneficial for adsorption to polar and hydrophilic surfaces [22]. Time-based conformational changes are caused by non-polar or highly charged surfaces due to structural rearrangements by hydrophobic or electrostatic interactions to minimize the *Gibbs* free energy [27, 32]. These conformational changes can lead to undesired physiological effects such as activation of blood clotting, inflammation, or delay of implant

healing [33-35]. Thermodynamically, the entropy-driven rearrangement of water at surfaces leads to protein adsorption and the increase in entropy is larger on hydrophobic surfaces [14]. In addition, protein adsorption can be blocked due to large hydration forces or steric hindrance [27]. The tight, immobile water layer on highly hydrophilic surfaces with polar moieties hampers protein adsorption to a high extent [36]. Further, the presence of hydrophilic, mobile macromolecules with a high surface coverage such as poly (ethylene glycol) (PEG), which creates a repulsive barrier, can have a similar effect due to a change in entropy and, thus, the *Gibbs* free energy [37, 38]. Hence, blocking of protein adsorption on highly hydrophilic surfaces makes them unfavorable for colonization of implants or scaffolds with tissue cells, but desirable for blood-contacting applications [39]. Additionally, the concentration of proteins in solution can influence their orientation, which can affect their packing density on the surface, too. Consequential, their activity and functionality can be changed or even lost, which is also the case upon conformational changes on highly hydrophobic surfaces [9, 27].

1.1.3   Cells and biomaterial surfaces

Cellular reactions, such as adhesion, migration, proliferation, differentiation and survival are important for biomedical applications since they are highly dependent on the bulk and especially the surface characteristics of the biomaterial. Cells in tissues such as connective tissue, muscle tissue, nerve tissue, or epithelia are adhesion-dependent cells, i.e. their survival and growth are not only influenced by cell-material, but also by cell-cell interactions. Except in epithelia, cells are typically embedded in a 3D network, called the extracellular matrix (ECM), consisting of fibrillar structures, the proteoglycans made of glycosaminoglycans (GAG), and soluble factors, the glycoproteins [40]. Adhesion of cells to this network is regulated by cell surface receptors that link the cell to proteins such as collagen (COL), fibronectin (FN), laminin (LAM), and others [41], which, in turn, induce signal transduction processes within the cells that regulate cell survival, motility, growth, and differentiation [42]. Cell adhesion to biomaterial surfaces can occur on a physical as well as on a biological base [43]. However, the initial main driving forces for cell adhesion are based on the same principles as previously described for protein adsorption, i.e. cells are transported to the material interface (e.g., by gravitational forces, convection, *Brownian* motion, or active movement) and short- and long-range interaction forces influence the strength of cell-material-interactions [16]. Here, terminal functional groups on material surfaces can influence the interaction and it was found *in vitro* that carboxyl or amino groups promote, while methyl or hydroxyl groups as well as macromolecules such as PEG hamper cell adhesion and proliferation [6, 10, 44]. Besides, the wettability of surfaces is affected by the presence of functional groups and it was proven that moderately wettable surfaces with water contact angles (WCA) between ~40° and ~70°

support cell adhesion to a higher extent then highly hydrophilic or hydrophobic surfaces [10, 14, 45]. Further, cellular membranes consist of glycosylated proteins, proteoglycans, phospholipids, glycolipids, as well as polysaccharides. Due to their negative net charge, mainly attributed to the sialic acids present in the glycoproteins [46], positively charged interfaces attract cells to a higher degree than negatively charged surfaces, where electrostatic repulsion dominates [43]. Nevertheless, the electrostatic interaction forces are influenced by the ionic strength of the ambience and might be shielded upon increase in salt concentration, resulting in reduced repulsive *Coulomb* forces [47]. Besides charge and wettability, viscoelastic properties play a crucial role in contact-mediated cell adhesion and growth. Typically, tissue cells sense the physical properties of the ECM and transform mechanical forces and deformations in chemical signals, which leads to arrangement of cellular and extracellular structures [48]. The elasticity of the environment is probed by anchoring and pulling of the cells which leads to changes in the internal cell architecture such as cytoskeletal rearrangement, focal adhesion (FA) dynamics and other processes by actin-myosin-driven contractility [48]. Since cells from different tissues are exposed to different external forces such as compression (bone cells), shear flow (blood cells), or stretching (muscle cells), they also respond in a different manner to biomaterial elasticity [49]. Hence, cells from soft connective tissues or epithelia respond with improved adhesion on softer surfaces in comparison to bone-derived cells such as osteoblasts, which positively respond to stiffer substrates [50-53]. Finally, among physical surface features, roughness and topography play also an important role in mediating cell adhesion, proliferation, or even differentiation and it was found that rough surfaces promote adhesion to a higher extent [54, 55]. However, such a general rule cannot be defined for surface topographies varying in geometry since cells of different origin do react in a different manner on surfaces with the same feature dimensions [56]. Nevertheless, it is possible to outline certain thresholds for various surface topographies to predict cellular response to some extent [56-58]. The mechanisms behind cellular response to certain material surface characteristics are quite complex and the biological processes of contact-mediated adhesion and growth are briefly explained here, which is also reviewed in more detail elsewhere [42, 48, 59]

Cell adhesion on a biological base is driven by binding of cell surface receptors to extracellular ligands [41, 60]. The so-called integrins play a crucial role in mediating signals from outside of the cell to its inner part (Figure 1.1). They are responsible for cytoskeletal rearrangement, formation of focal complexes and activation of downstream signaling pathways important for cell proliferation, differentiation, and gene expression [41, 61]. These transmembrane proteins consist of α and β subunits and 24 combinations with unique binding specificities and signaling properties are known [41, 42]. Integrin clustering occurs upon binding to ECM ligands that leads to conformational changes in the transmembrane proteins.
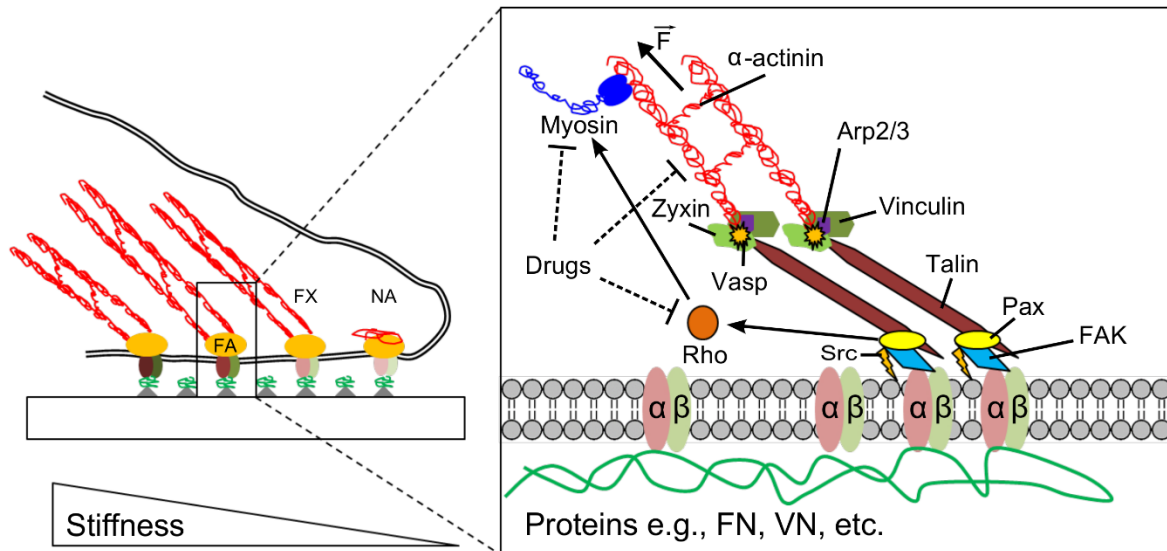
Figure 1.1 - Mechanotransduction at focal adhesions (FA). <u>Left:</u> nascent adhesions (NA) are formed upon integrin clustering which mature to focal complexes (FX) and more stable focal adhesions (FA). This process is controlled by actin-myosin II contractility and dependent on the substrate stiffness, surface topography, or other external forces (e.g., optical or magnetic tweezers). <u>Right:</u> simplified model of FA structure. α/β: alpha and beta subunit of integrins; protein assemblies (Src - proto-oncogene encoding a tyrosine kinase, FAK - focal adhesion kinase, Pax - paxillin, Vasp - vasodilator stimulating phosphoprotein, Arp2/3 - actin-related protein 2 and 3); F: force delivered by actin-myosin II contractility. Integrin clustering can induce RhoA signaling that increases myosin contractility and, thus, results in unfolding of proteins. The application of pharmacological drugs can influence myosin contractility and actin polymerization (adapted from [62]).

Typically, integrins bind to a small peptide sequence present in extracellular proteins. The so-called RGD-sequence, a combination of arginine-glycine-aspartic acid, can be found in ECM proteins such as FN, vitronectin (VN), osteopontin, bone sialoprotein, etc. and the mechanisms behind are well understood [63]. Hence, the cytoplasmic domains of *α* and *β* subunits are exposed to enable binding of focal complex proteins such as focal adhesion kinase (FAK), integrin-linked kinase (ILK), or Src. However, FAK, the non-receptor tyrosine kinase, is not directly activated by integrins, but may be recruited either directly or via cytoskeletal proteins to setup connections with the cytoplasmic tail of the *β* subunits [64, 65]. Due to its ability to foster cell adhesion and spreading processes, FAK is a crucial regulator in integrin mediated signaling [66]. Once activated, FAK results in extracellular signal regulated kinase (ERK)/ mitogen activated protein kinase (MAPK) activation, where ERK as member of the MAPK family is responsible for gene transcription up-regulation necessary for cell cycling and replication [67, 68]. Important for cell proliferation and differentiation, the ERK/ MAPK pathway regulates osteogenic differentiation of stem cells positively [69]. FAK autophosphorylates upon activation (Tyr[397]) and creates a binding site for the Src homology 2

(SH2) domain of Src and Fyn. In dependence on the receptor occupancy integrin clustering occurs, resulting in recruitment of intracellular proteins such as paxillin, talin, α-actinin, and vinculin in focal complexes (Figure 1.1) [63, 70]. Src can also phosphorylate FAK at Tyr^{925} which creates a binding site for Ras guanosine 59-triphosphate exchange factor (mSOS) and growth factor receptor-bound protein 2 (Grb2) [42]. This results in FAK-linking to signaling pathways influencing cytoskeletal arrangement and activates the MAPK pathway. The different phosphorylation pathways are triggered by various integrins, which activate MAPK and ras-raf pathway, the Jun kinase pathway, and the Ras homolog gene family, member A (RhoA)/ Rho associated coiled-coil protein kinase (ROCK) pathway [63]. Hence, lamellipodia as well as filopodia formation are affected leading to cell motility. Thereby, the density of extracellular signals and their mobility decisively influences the extent of actin stress fiber formation in focal complexes. The small GTPase protein RhoA and its effector ROCK are also enabled by activated FAK [71, 72]. Both are responsible for stress fiber formation in regulating the actin cytoskeleton and focal adhesions (FA). The switching from low to highly spread cells is associated with the generation of mechanical tension, which is based on RhoA-dependent actin-myosin II contractility (Figure 1.1) [73]. RhoA promotes precisely this tension generation by phosphorylation of its effector ROCK, which indirectly increases the phosphorylation of the myosin light chain [74]. Hence, mechanical and topographical surface characteristics can control adhesion, proliferation, or even differentiation of cells. In particular, cell shape, intracellular tension and RhoA expression play an important role [75]. Thereby, FA produce mechanical tension by connecting the cell skeleton with the ECM and by assembly and phosphorylation of mechano-sensitive kinases. Thus, it is crucial to control precisely biomaterial surface properties at the nanoscale and various surface modification techniques are reviewed in the following section.

1.2   Fabrication of nanostructures

Many of today's materials used for biomedical applications possess excellent intrinsic physical and chemical properties. However, since these materials typically interact with the biological environment through their surface, it is reasonably to focus on the modification of the outermost areas of materials at the micro- or even nanoscale. Hence, surface modification techniques aim to change and control the interfacial energy that could cause undesired side effects of materials for intended clinical use due to uncontrolled adsorption of proteins. Further, in dependence on the biomedical application, cell adhesion and growth can be supported or inhibited by biomaterial surface modification. Methods used for that purpose are manifold and are primarily based on chemical or physical modification. Surface self-assembly [18], vapor deposition [76], and surface coating or entrapment [77, 78] are physical methods based on

electrostatic interaction, *van der Waals* forces, hydrogen bonding, or hydrophobic interactions. Chemical techniques, in turn, bind molecules to or generate functional groups on material surfaces [79, 80]. Further, surface grafting is an important technique to modify biomaterial surfaces and functional compounds can be either 'grafted from' or 'grafted to' the materials [81]. Since the interaction of intracellular structures with extracellular domains typically occurs at the nanoscale in biomedical applications, it seems reasonable not only to modify a material's chemistry, but also its topography in similar orders of magnitude. Hence, cellular events such as adhesion, proliferation, migration, survival, or differentiation can be controlled [82, 83]. The field of nanotechnology dramatically gained increasing interest during the past two decades. It all started with a talk given by Richard P. Feynman more than 50 years ago [84]. In his famous lecture "There's plenty of room at the bottom" he explored apparently simple and elegant possibilities of working at the atomic scale and the results would be intriguing. Many applications were expected and are already applied in fields such as electronics, solar cells, and biosensors. Moreover, nanofabrication already found its way to biomedicine and TE. As a result, the demand for well-characterized nanomaterials, that can be used for example as diagnostic tools, drug delivery systems, implant materials, and especially for TE applications, is steadily increasing [85]. Methods for design and production of materials with nanoscale-controlled surface properties such as chemistry, topography, or micromechanics are widespread and the ability to control nanofeature dimensions has drastically improved during the past couple of years. However, the overview given here focusses only on methods generating nanostructures on material surfaces, since the techniques used during the PhD work belong to that sector. The two well-known major routes for nanofabrication, the so-called 'top-down' and 'bottom-up' methodologies, are described in detail in the following sections and are further summarized in excellent reviews [56, 86, 87]. Additionally, major nanofabrication techniques are listed in Table 1.1.

1.2.1 *Top-down* nanofabrication

Top-down approaches use various techniques to machine nanofeatures into a surface of bulk materials. Lithography or precision engineering are basically used in semiconductor industry and these techniques were improved to a high extent during the last three decades. Miniaturization is important not only for technical devices, but also for biomedical applications, which increases the input in basic research for improving the resolution of miniaturized components. Nanostructures can be obtained by adding or removing material to/ from surfaces and using lithography methods it can be done either in parallel (e.g., optical lithography) or sequential (e.g., focused ion beam (FIB) lithography) fashion. A highly advanced photolithographic technique applies a patterned chrome coating with linear dimensions on a

quartz plate where collimated light is projected. The resulting image on a photoresist at the focal plane is almost four times smaller than the original patterns. However, this technique is capable of patterning a relatively large area on planar surfaces (~8 cm²) within just a few seconds, which is basically interesting for the semiconductor industry. Using high energy light with a short wavelength (e.g., UV light) can result in either positive or negative patterns, since the typically organic photoresist becomes either more soluble or cross-links and becomes more stable against proper solvents [88-90]. New optics and shorter wavelengths are necessary to increase storage and processing capability of central processing units (CPU) [87]. Sequential, but slow methods such as scanning beam lithography (SBL) are capable of generating features with high resolution (<50 nm) and are primarily used to design high-resolution photomasks for pattern transfer [87]. Time and costs required to fabricate the photomasks can be a significant disadvantage of conventional photolithography. However, laser interference lithography (LIL) is capable to design simple patterns without using a photomask [91, 92]. Here, multiple laser beams are used to design patterns in photoresists by interference. Expensive projection optics is not required and upon use of various mirrors, regular spaced arrays of lines or dots are created. The choice of laser wavelength can result in high-resolution patterns using LIL [93-95]. Sequential techniques are slower and more expensive due to point-by-point writing than parallel techniques, where patterns are created simultaneously using photomasks. The technical challenges increase using shorter wavelengths and alternatives such as electron beam lithography (EBL) overcome these limitations. EBL is capable to design patterns with <10 nm resolution at ideal conditions [96]. The high-priced conventional techniques are commercially available. However, due to their high costs (purchase, installation, and maintenance) they are restricted to semiconductor fabrication. Further, biomedical applications require also the fabrication of nanofeatures on non-planar surfaces, which these tools are usually not capable.

Other lithographic and patterning techniques were developed over the years to overcome the limitations of conventional lithographic techniques. In 1988, Whitesides and colleagues introduced the soft lithography at Harvard [97]. In principle, an elastomeric stamp made of poly (dimethyl siloxane) (PDMS) is used as mask, stamp, or mold to pattern design and replication and methods such as microcontact printing (μCP), replica molding, or microtransfermolding were developed [87]. The main advantage over conventional techniques is that soft lithography has not to be performed in a clean room, which is important for electrical storage and processing devices to avoid failure. Hence, soft lithography is open to many research institutions since it can be applied at standard lab conditions and incorporated dust particles would not lead to failure of the complete generated patterned device. In replica molding, a master, typically created with conventional techniques, is pressed into PDMS for pattern transfer resulting in a patterned replica upon solidification of the liquid polymer [98, 99].

The advantage of soft molds is their possible use with non-planar, rigid, or soft material surfaces, while hard molds typically require planar, rigid surfaces. However, even though curved or planar surfaces can be patterned, nanostructures necessary for complex nanoelectronics cannot be designed since deformations of the soft PDMS lead to errors and misalignment of patterns that would lead to failure of electronic chips since different materials contribute to integrated circuits by layer stacking. That drawback can be overcome in part using rigid stamps, which are used for relief printing and injection molding by transferring the patterns into a monomer or polymer substrate. However, the resolution of molding or embossing is limited since the applicability to design nanostructures with the mold is highly influenced by the processing time, the release of the mold from the polymer, the alignment with features on the substrate as well as the maintenance of the mold. Further, materials should be processable to obtain the features of the mold with high fidelity. Additionally, swellings of the master by the used monomers as well as distortions in the transferred patterns are limiting factors. Finally, it is important if the molded material fills the mold completely, if the material tends to entrap gas bubbles, how the kinetics are, if there is a residual scum layer after molding, and how mold, polymer, and substrate are matching as a system in total.

An additional technique which uses rigid masters for replica molding is the so-called step and flash imprint lithography (SFIL) [100-102]. Here, a pattern is etched into a quartz plate by photolithography leading to a master with low relief. A photocurable liquid with a low viscosity is used and the mold is pressed into this solution, which contains a low molecular weight monomer and a photoinitiator. The monomer polymerizes upon exposure to UV light through the quartz mask while in contact with the mold and creates an inverse replica of the substrate [100-102]. A similar approach is used by the so-called nanoimprint lithography (NIL). However, the polymer used for molding is heated to its glass transition or even close to its melting temperature to simplify the embossing process and the patterns are transferred by pressure [103, 104]. NIL is also called 'hot embossing' and it is capable of printing patterns to large wafers in a single step [105, 106]. Many different materials can be used for NIL and the resolution goes down to features as small as 5 nm with high aspect ratios [107]. In summary, patterns can be printed in parallel over large areas using molding or embossing. Even functional structures applied for microelectronics and optics, both inorganic- and organic-based, can be embossed [101, 108, 109]. However, the high-resolution masters are typically fabricated by conventional lithography, which increases the costs of nanofabrication. Nevertheless, due to large number of repetitions of the replication process the whole technique becomes less expensive. Still, surface fouling as well as the thickness of the residual layer limits the number of replications. Overall, the resolution of patterns to be embossed has increased during recent years and the number of materials, replicas as well as transferred surface area has increased, too.

Another useful tool in soft lithography is the μCP, where material is transferred to a substrate by printing using a PDMS stamp [110-112]. μCP is often used to transfer thiols to appropriate substrates by placing the PDMS stamp into the thiol solution and the pattern is defined by the regions of the stamp in contact with the substrate, where covalent binding occurs [112, 113]. Advantageous for the technique are the soft, flexible PDMS stamp as well as the conformal contact at the atomic level, which enables for printing over large areas (>50 cm²) [114] as well as on arched surfaces [115, 116]. In summary, μCP enables for the control of surface characteristics in well-defined regions at the nanometer-scale. Possible applications of the transferred inks include reversible or permanent electrical contacts, patterns for use in biotechnology, or etch resists. Nevertheless, feature distortions during printing as well as surface diffusion of printed molecules limit the resolution [87].

Table 1.1 - Overview on selected nanofabrication methods (adapted from [56])

Fabrication method	Feature size [nm]	Advantages	Disadvantages
EBL	• ≥3 - 5 for single feature [96] • ≥30 - 40 for arrays of features [96]	• Precise geometries • No mask needed • Computer-controlled	• Expensive • Time consuming • Small surface coverage
Colloidal lithography	• ≥20 [117]	• Easier to pattern larger areas than with EBL [118]	• Specific feature geometries not possible
Photolithography	• ≥0.5 [119]	• Precise geometries and patterns	• Expensive equipment • Large feature size
Chemical etching	• Dependent on etchant used and time [120] • ≥1	• Simple, fast • No special equipment needed • Inexpensive • Control over pore size and distribution	• Specific feature geometries not possible • Insufficient strength of materials
Polymer demixing	• Vertical: ≥13 [121]	• Simple, fast and inexpensive	• Only pits, islands can be created [122]
Phase separation	• Pore sizes ≥1 [123]	• Porous scaffolds • No special equipment needed • Controlled porosity	• No organized pattern possible
Self-assembly	• Tailored by molecule design	• Self-assembly into higher-order structures	• Requires molecules that will self-assemble [124]

An additional top-down approach with potential nanofabrication is the scanning probe lithography (SPL) [125]. Here, features can be written in parallel or serial fashion from macroscopic to atomic scale in dependence on the sharpness of the pen. In SPL, species present on a substrate's surface undergo changes upon contact with the pen, which are

induced by mechanical, electrical, magnetic, or chemical interactions. The dip-pen nanolithography (DPN) is one approach to deposit nanoparticles or molecules selectively on substrate surfaces [126, 127]. Material inked to an AFM tip is transferred to a surface in serial writing with the scanning probe and can create features with lateral resolutions as small as 50 nm [128]. The manipulations of atoms or particles by SPL are more allocated to bottom-up approaches. However, before SPL techniques can be used for large area patterning, considerable improvements have to be made such as simultaneous pattern writing using multiple probes in parallel [129, 130], which allows higher sample throughput.

1.2.2 *Bottom-up* nanofabrication

In contrast to the top-down approaches, larger, more complex structures are formed in the bottom-up approaches by self-assembly of smaller and simpler building blocks such as atoms, molecules, nanoparticles, etc. Bottom-up approaches are simpler than methods using the top-down approach and they are capable of forming complex 3D structures cost-effective in large quantities at the sub-10 nm scale. Per definition, self-assembly is the spontaneous organization of two or more components into larger aggregates using covalent and/ or non-covalent bonds under absence of external forces or spatial constraints [131]. Bottom-up approaches can be subdivided into non-templated or templated self-assembly. While the former one is simpler and cost-effective, provided the process parameters are controlled precisely, the latter one often requires a preceding modification step using top-down approaches. The spontaneous assembly of components into a desired structure is one of the most appealing aspects of non-templated self-assembly. Its simplicity and potential efficiency to achieve an ordered structure only by mixing of components makes it attractive to many research institutions. Methods belonging to this approach include self-assembled monolayers (SAM) [10, 132] or self-assembled nanostructures from block copolymers [133, 134]. These structures themselves can function as templates for metallic or semiconducting nanostructures [135]. Further, the layer-by-layer (LbL) technique, which will be later discussed in more detail, can also be used to design nanostructures in *z*-direction as well as in lateral direction [136-138]. However, in basic research of cellular events such as ligand-induced integrin clustering processes, gold nanoparticle arrays have been a promising tool [139] since a binding site for the cells transmembrane receptors, the integrins, is represented only by one single, biofunctionalized gold nanoparticle [140]. The so-called block-copolymer micelle nanolithography (BCMN) can be used to alter the particle spacing which leads to a variation in ligand-ligand spacing as well as variations in molecule density on the substrate [141, 142]. The substrates are placed into a solution containing poly (styrene)-block-poly (2-vinylpyridine) (PS/P2VP) micelles which are loaded with auric acid. After adsorption and hexagonal

arrangement of the micelles to a monolayer (ML), a treatment with hydrogen plasma simultaneously reduces the auric acid to gold nanoparticles, which are deposited onto the substrate, while removing the polymer shell. Hence, nanoparticle distance and, thus, the space in between the ligands can be easily controlled by micelle self-assembly as well as the polymer´s molecular weight [142]. Another versatile, fast, and inexpensive bottom-up approach to generate nanostructures is the polymer demixing technique [143, 144]. Thermodynamics lead to demixing of polymer mixtures that result in nanostructured substrates and patterns of different surface energy [145]. It was found that polymers are only miscible at low polymer concentrations in dependence on their interaction with each other and with the solvent [146]. The solvent evaporates during spin coating and the polymers start to demix at a critical concentration. Further, the initial polymer concentration and the coating speed define the lateral design of the generated nanostructures [143]. In addition, the ambient humidity influences the nanostructure distribution since high values can lead to perforated polymer films [147] due to polymer-water-interactions [148], where the water condensates on cooled polymer solutions [149, 150]. As a result, this phenomenon can be used to design honeycomb structures at humid conditions [151]. Functional nanostructures using self-assembly also include self-assembled magnetic nanoparticles [152] which can store large amounts of information. Nevertheless, to enhance the magnetic properties the particles are typically annealed that could result into coalescence [153].
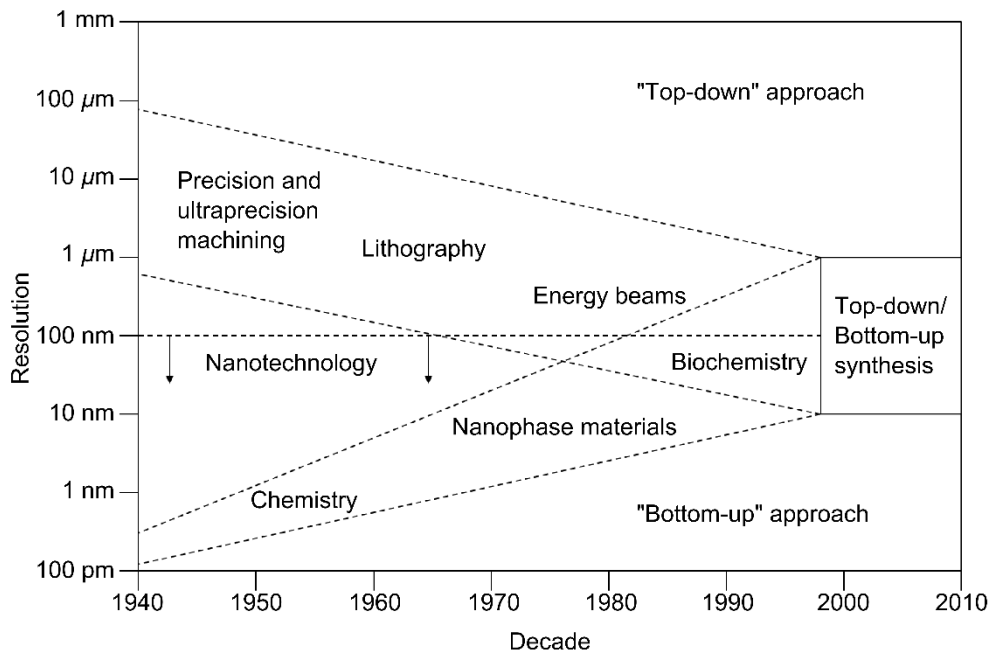

Figure 1.2 - Junction of "Top-down" and "Bottom-up" approaches for possible hybrid techniques in the future. (adapted from [154])

Since non-templated self-assembly is prone to producing defects and the size of areas with perfect periodicity is limited to micrometer-sized areas in lateral dimension, it is not widely

used for nanofabrication [87]. As a result, <u>templated self-assembly</u> might be an option. Here, patterned elements are introduced into the self-assembled nanostructures, which could also lead to an increase of order within the self-assembled structures. Surface topography, electric [155] and magnetic fields [156], or shear forces [157] can be used for directing the self-assembly. Top-down strategies are typically used to design patterns for templated self-assembly that later on direct the bottom-up assembly of molecules, macromolecules, or colloids. Hence, micrometer-sized or larger domains of defect-free patterns can be achieved using templating from molecules, from particles, or using external forces [87].

1.2.3 A closer look

Since the presented work aimed to design chemically modified nanostructures to control cellular processes, the two main approaches used are described in more detail. Nanostructured surfaces were obtained on planar surfaces using the so-called nanosphere lithography (NSL), while these nanostructures were modified at later stages using the Layer-by-Layer (LbL) technique. Hence, pros and cons as well as challenges of both methods are briefly discussed here.

1.2.3.1 Nanosphere lithography (NSL)

Owing to its potential to design regular and homogeneous arrays of nanostructures of different size in a relative low-cost way the NSL is a promising tool in nanofabrication. NSL combines advantages of both top-down and bottom-up approaches and is divided into two fabrication steps. First, a homogeneous mask is designed on a flat substrate surface, which has been chemically treated to enhance its hydrophilicity, using a suspension of monodisperse spherical colloids, typically polystyrene nanoparticles (PS-NP). Hence, a hexagonal close-packed (*hcp*) mono- (ML) or double layer (DL) is formed upon drying, which is also called colloidal crystal mask (CCM) [158]. Subsequently, a patterned surface is achieved by deposition of typically noble metals such as gold through the gaps of the arranged beads. After removing the mask by sonication in adequate solvents or by simple stripping, surfaces with ordered nanostructures are obtained, which can be further modified by annealing to achieve sample crystallization or induce a change in the crystallographic phase.

The self-organization of the colloids into *hcp* masks belongs to the characteristics of bottom-up approaches, while the structured layers obtained after metal vapor deposition similar to conventional lithography can be assigned to the top-down approach. Hence, the NSL is often called a hybrid technique bridging both approaches. Also known as colloidal lithography [159, 160] or natural lithography [161], the NSL was first reported by Fischer and Zingsheim in 1981 [162]. Even though their intention was not the formation of lithographic

colloidal masks, they formed an ordered monolayer of colloids on a glass substrate by solvent evaporation obtaining small-area particle monolayers and introducing the term 'naturally' assembled PS-NP. The lithographic approach was described by Deckman and Dunsmuir [161] one year later, who expanded the application of nanospheres to more than just a simple deposit material. They developed the spin coating process to obtain particle arrays, which also led to point defects or dislocations in the micrometer scale [163]. Due to the primarily self-organization of particles to *hcp* masks on a macroscopic substrate rather than by photolithography, the term 'natural lithography' was introduced.

Hulteen and van Duyne [164] renamed the approach in the mid of the 1990s to the nowadays commonly known NSL. They also focused their work on DL formation leading to smaller dot-like structures that correspond to the reduced interstices in a close-packed structure. The metallic patterns obtained by NSL have unique plasmon resonance properties as investigated by van Duyne *et al.* [165, 166], who focused on biosensor development based on surface enhanced Raman spectroscopy. In addition, the stability as well as the mechanisms of mask formation have been extensively studied by various groups both experimentally and theoretically and the NSL gained in interest during recent years owing to its ability to form nanostructures in all three dimensions [159, 167-169].

It is crucial for large-area fabrication of nanostructures to obtain almost defect-free *hcp* masks and many groups have been working on different strategies in recent years to improve its quality using different strategies. Focusing on 2D PS-NP masks, the major methods will be briefly described here. One method to obtain particle lattices is based on <u>self-assembly during solvent evaporation</u>. Here, the solvent evaporates from a droplet of diluted colloid suspension after deposition on a substrate surface. A meniscus is formed between the particles during solvent evaporation inducing attractive capillary forces that lead particle self-assembly. This self-assembly process is basically driven by convective transport of the particles together with the capillary forces [170], while the rate of solvent evaporation determines order/ disorder as well as quality of the particulate arrays [171]. Further, temperature as well as humidity control might lead to particle ML even on tilted substrates [172]. Hence, a precise control of the process parameters is crucial to avoid mixed multilayer structures and many other experiments were performed successfully [173, 174]. Another approach to obtain PS-NP mask is based in <u>dip coating</u> which was developed by Nagayama *et al.* and is based on their work on solvent evaporation [175, 176]. Here, it is crucial to monitor not only the evaporation rate, but also to precisely control the drawing speed to obtain large-area arrays. Since particle layers are formed on both sides of the substrate, which increases the amount of the particle suspension, Nagao *et al.* combined evaporation and dip coating [177]. Here, a particle suspension droplet is placed on a substrate surface that is toppled vertically. Upon drying of the suspension, a lattice is obtained still having many defects. However, particle multilayers can be obtained

repeating the process. A widely used method to obtain PS-NP masks is based on spin coating of particle suspensions, which can accelerate solvent evaporation [161, 164]. Here, quality and thickness of the resulting masks are affected to a high extent by speed, PS-NP size, wettability of the substrate, etc. Spin coating protocols described in the literature vary and are sometimes indefinite [178-180]. Thus, there is a need for precise experimental protocols to obtain large-area, well-ordered masks for nanostructure development. The potential for mass production and scale-up is high for the spin coating approach due to the rapid implementation and compatibility with wafer-scale processes. It was found that large-area of *hcp* masks are preferentially formed at high rotation speed leading to defect-free areas up to 200 μm^2 using PS-NP of 500 nm in diameter [181] and are in accordance with other studies [182, 183]. Theoretically, in partially immersed particles on a horizontal surface, interparticle capillary forces arise [171]. Increased capillary forces develop due to increased liquid surface deformation upon thinning of the liquid. Thereafter, more particles move to the nucleus due to convection that compensates the evaporated solvent in the already ordered masks. As a result, particles from thicker parts are dragged to thinner regions. New particles keep in touch with the domains due to hydrodynamics (pressuring) and capillary forces (capturing). When the liquid layer thickness is as small as the particle diameter, the assembly to ordered arrays continues [170]. Hence, the thickness of the evaporating film defines the order process to a high extent and it was shown that this is inversely proportional to the speed [182]. In addition, it was found that a rapid evaporation leads to more uniformly arranged ML and colloidal crystals [183, 184] and that the acceleration in the initial stages of the spin coating is crucial for high percentage of *hcp* masks [181]. A very recent paper by Chen *et al.* provided many details for efficient and controllable fabrication of large-area, uniform ML or multilayer formation, contributing to the knowledge of ML formation in dependence on speed and acceleration [185]. An additional method to design PS-NP lattices in based on self-assembly at the interface of two media. Here, one approach is the Langmuir-Blodgett (LB) coating, which is based on the preparation and transfer of particle ML from an air-liquid interface onto a solid substrate, withdrawing it in a controlled manner from the trough. Surfactants [186] or modified particles with enhanced hydrophobicity [187] are used to form *hcp* lattices on the liquid surface and additionally compressing it with a barrier to ensure a constant pressure during substrate removal, leading to macroscopic nanopatterned area. A second approach using the air-liquid interface is based on controlled evaporation, where the initial step is similar to that of the LB technique. In contrast to that technique, the floating ML is not compressed with a barrier simplifying the method. Moreover, the substrate is kept immersed during evaporation [188, 189]. Here, *hcp* areas larger than 150 μm^2 were obtained tilting the substrate slightly using PS-NP of 200 nm in diameter [190]. Besides the air-liquid interface, self-assembly can also occur at the liquid-liquid interface of two non-miscible liquids [191]. Nanospheres trapped at the

interface form a ML that can be deposited on a substrate by evaporation of one phase or by a removal procedure. However, this technique requires a careful handling for optimal ML assembly. One more technique for lattice formation is based on electrophoretic deposition using two electrodes to confine the particle suspension. The particles move and assembly at the electrode interface upon application of an electric field. Limited to conducting substrates such as indium tin oxide (ITO) glass, 2D [192] and 3D [193] particle systems have been studied using either direct current (DC) [194-196] or alternating current (AC) [197, 198]. The advantage of AC is the possible use of particles of any type independent of the media permitting high field strengths without electrolysis of water [197]. The last method to use particle self-assembly uses pre-patterned substrates. This template-assisted assembly is employed to form more complex structures, which are difficult to achieve with traditional self-assembly processes. The substrates used for self-assembly are pre-patterned either chemically or physically and require a preceding modification step that increases time and costs. Conventional lithographic techniques such as optical lithography [199] or EBL are used to physically modify a substrates surface and the packing of the colloids can be controlled changing the patterned geometry as well as the ratio particle size to pattern size [200, 201]. In contrast, nanoparticles might selectively adsorb on chemically patterned surfaces [202, 203]. Here, evaporation, spin coating, or electrophoretic deposition can be used in dependence on the nature of the interaction.

1.2.3.2   Layer-by-Layer (LbL) technique

The well-known principle of the LbL technique was first described by Iler in his pioneering work in the mid of the 1960s. He defined a thin film fabrication based on alternating adsorption of oppositely charged species [204]. Decher and co-workers adapted the principle of alternate adsorption of polyelectrolytes (PEL) from aqueous solutions onto charged surfaces and established the nowadays widely used LbL method [205]. Due to the basic principle of self-assembly and self-organization of PEL in an aqueous environment the method can be applied to materials of virtually any type of shape, provided the surface is charged [206, 207]. Basically, PEL multilayer (PEM) formation, based on electrostatic interaction and ion pairing, can lead to material coatings with unique properties [208-211]. Besides electrostatic forces, other forces such as hydrogen bonding, charge transfer, covalent binding, specific or hydrophobic interactions might contribute to PEM assembly and stability since the intrinsic net charge of PEL depends on the conditions of the surrounding aqueous environment [212]. Schlenoff and co-workers modified the idea of electrostatic interaction and formed a concept based on intrinsic (i.e. PEL of opposite charge) versus extrinsic (i.e. counter ions) interplay [213, 214]. A further main driving force in PEM formation is the increase in entropy due to the release of counter ions since the enthalpic part of the *Gibbs* free energy is a non-factor in such processes [215, 216]. PEL used for PEM formation are polymers with more than one ionic group, as the

term '*poly*electrolytes' implies. These groups are dissociable and the adsorption behavior is defined by the environmental conditions. PEL are typically distinguished into polyacids, polybases or polyampholytes according to their charge. Polyacids are dissociated into polyanions in polar solvents, whereas polybases form polycations. Polyampholytes possess groups of both categories. The type of the functional group as well as the solvent affects their degree of dissociation. Hence, PEL can be discriminated into weak and strong. Once dissolved in water, the latter ones dissociate independent of the pH and possess a permanent charge, while for the former ones the pH value of the solution determines their degree of dissociation and, thus, charge density and conformation. Intramolecular repulsive forces due to equally charged functional groups define the conformation of dissociated PEL. These forces lead to the expansion of random coils in the charged state in comparison to uncharged polymers in solution. The volume of a random coil of a weak PEL is larger than that of an uncharged macromolecule in solution due to intramolecular repulsion of the functional groups in the dissociation state.
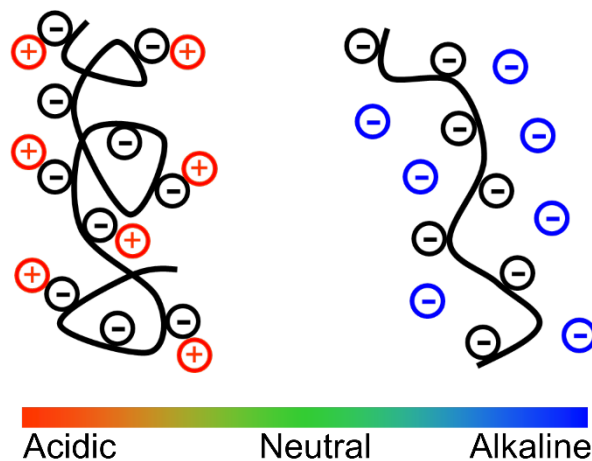

Figure 1.3 - Schematic representation of a weak polyanion's molecule structure at different pH values. A more coiled conformation is observed at acidic conditions, while alkaline pH values lead to more stretched conformations. Similar results are obtained for weak polycations at opposite pH values. Further, increased temperature or high ionic strength can also result in coiled molecule conformation.

In dependence on the pK_a value, this is the case for weak polycations at slightly acidic or neutral pH value. As a result, the smallest dimension of a weak polycation might further decrease by stretching in the highly charged state at low pH value. In contrast, if the pH value becomes basic the coil is compressed to some extent since the intramolecular repulsion forces are screened due to (negative) counter ions in solution (Figure 1.3). In addition, the presence of ions in the solvent defined by the ionic strength greatly affects PEL conformation and charge density. At high salt concentration, intramolecular repulsion forces are screened and lead to more coiled conformations of weak PEL, resulting in the deposition of thicker layers. Further,

the same effect is caused by the temperature during PEM assembly. An increase in temperature leads to overcoming of electrostatic intramolecular repulsion and, thus, to enhanced entanglement of the molecule.

The simple control of the ambient conditions (pH value, ionic strength, temperature) as well as the choice of PEL (molar mass, charge density, chain stiffness) enable for facile control of resulting PEM properties such as surface charge, wettability, thickness, and viscoelasticity, which is one big advantage of the LbL technique [209]. As mentioned above, charge and conformation of weak PEL are affected to a higher degree by a change of the pH value than that of strong PEL such as heparin (HEP). With that in mind, the control of PEL conformation as well as adsorption characteristics can lead to unique PEM structures and compositions [209]. Further, PEL from natural or synthetic sources can be applied to design systems with desired properties. Synthetic PEL are a widely used group in basic research for biomedical applications. Here, polyanions such as poly (styrene sulfonate) (PSS, strong polyanion) or poly (acrylic acid) (PAA, weak polyanion) and polycations like poly (allylamine hydrochloride) (PAH) are commonly used. Since the PEM assembly of synthetic systems can be easily controlled by pH value and ionic strength, linear growing PSS/PAH multilayers are frequently used. Their thickness can be fine-tuned from a few up to several tens of nanometers [217, 218]. Another synthetic PEM system is composed of PAA/PAH [136]. Here, not only the thickness, but also the topography can be fine-tuned by simply changing the pH value of the PEL solution [219, 220]. Its porosity can be rendered as nano- or submicroporous by post-treatment in acidic solutions [136], whereas the viscoelasticity can be adjusted from rather soft (200 kPa) to highly rigid (142 MPa) surfaces, which influences cellular interaction, too [221]. Nevertheless, initial cell interactions with synthetic PEL are primarily based on nonspecific physical interaction forces (e.g., *Coulomb* and *van der Waals* forces) if no proteins are present *in vitro* and cell adhesion is influenced by non-specific adsorption of proteins from the surrounding media [34]. This adsorption can lead to conformational changes in proteins that affect negatively the interaction with cells. Hence, the prediction of cell behavior on such kind of multilayers is limited [31, 222].

Even though many results obtained with synthetic PEM systems are useful for building a knowledge base on PEM assembly, biomedical applications of multilayer systems require natural, biocompatible or even degradable polymers. Since cells are surrounded by the ECM, a mixture of proteins, polysaccharides (i.e. mainly GAG), and other bioactive molecules that provide mechanical and chemical stimuli to the cells, it seems likely to use ECM components as or within PEM systems. Hence, bioactive PEM can be composed, for example, of chondroitin sulfate (ChS) [53, 223], COL [224], gelatin (GEL) [225], HEP [226, 227], and hyaluronic acid (HA) [51, 228], which mostly represent polyanions. Biocompatible polycations applied in natural systems can be polysaccharides like chitosan (CHI) [229, 230], or synthetic

polypeptides like poly-L-lysine (PLL) [138]. Natural polymers offer unique mechanical and biochemical signals to the cells due to cellular receptors for proteins like COL and GAG-like HA, or by specific binding of proteins to GAG-like HEP, which are important for adhesion, growth, and differentiation of cells [224, 228, 231]. Similar to synthetic systems PEM formation with polysaccharide-based molecules is highly affected by the charge of the molecules. Hence, pH value and ionic strength of the PEL solution can be used to tune multilayer composition and thickness [232, 233]. It was found that the increase in film thickness is enhanced when the pH value of the adsorbing PEL is close to its pK_a value or if the ionic strength increases only within a narrow range [233, 234]. In addition, hydration and swelling properties of natural PEM are influenced in a similar fashion [235]. Important to note is that the nature of PEL forming the outermost layers influence local interactions within the PEM during multilayer assembly, which is interesting [236]. The ionization of weak PEL within the multilayers was clearly affected by interaction with solutions of strong PEL which, in turn, resulted in variations in corresponding film characteristics such as thickness, hydration and mechanical properties upon contact with subsequent PEL [237]. As a result, later events such as adsorption of proteins, controlled release of bioactive molecules like growth factors or cell interactions can be affected by these minute variations [51]. Nevertheless, an obvious disadvantage of natural polymers is that they are derived from animal sources such as porcine intestinal mucosa or bovine lung in case of HEP. Thus, their availability in larger quantities is limited to some extent. Moreover, the molecular composition might significantly vary from batch to batch, which reduces the accuracy of predictable PEM properties [238]. As a result, synthetic modification of natural polymers such as cellulose (CS) might be an option to obtain controlled heparinoid characteristics, which are also dependent on the pH value [239, 240]. However, most PEM systems are designed in discreet form, i.e. that the layers are stacked in vertical direction. Though, it is also possible to design pH gradients of PEM in lateral direction which clearly affects cellular behavior [241].

In summary, not only the biocompatibility of materials intended to be used for biomedical applications, but also the viscoelasticity and other biomaterial surface properties can be fine-tuned using the rather simple and quite effective LbL technique. Changing the environmental conditions such as pH value, ionic strength, etc. during PEM formation leads to unique viscoelastic and other biomaterial surface properties dependent on the desired biomedical application.

2   Motivation

Cells in their natural environment live in a 3D network of soluble factors and nanoscaled macromolecular fibers that provide chemical and mechanical stimuli. Especially ligand spacing and the mechanical properties of the ECM greatly influence cellular survival and growth. Hence, it seems reasonable to modify a biomaterial's surface at the nanoscale to control cellular events such as adhesion, proliferation, or differentiation. Since different cell types respond in a different manner to nanostructures with similar dimensions, the study aims to contribute to the knowledge of topography-induced cellular response. Out of various methods to obtain structures at the nanoscale, NSL is used here to design tetrahedral nanostructures on planar silicon dioxide varying in size and distance by applying different particle diameters for lattice formation. CCM formation as self-organization process is prone for defects within the colloidal arrangement. Hence, it is crucial to optimize process parameters affecting mask assembly to minimize such defects and to obtain large-area, homogeneously distributed nanostructures. Human dermal fibroblasts (HDF) are used here as model system and it is aimed to control precisely their adhesion and growth by specific interaction with gold nanostructures of different size and distance. Since that interaction is not trivial in the two-component system, an effective passivation strategy is developed here to block the silicon dioxide background. Hence, a long-chain silane containing 43 PEG units is synthesized for backfilling purposes that shall hamper protein adsorption as well as cell interaction with silicon dioxide. Since cells also need chemical signals for adhesion and growth and bare gold does not provide such signals, the nanostructures are modified with a SAM with a terminal carboxylic acid group that is prone for further modification. Different analytical methods as well as short- (<24 h) and long-term (>24 h) culture of HDF shall help to draw a conclusion that contributes to the understanding on how nanoscaled surface features influence the response of that particular cell type.

In the second part of the study, additional chemical signals are introduced to the nanostructured system to broaden the exercise of influence of nanotopography on cellular response. Hence, the LbL technique is used to modify the tetrahedral nanostructures with a PEM system. Such a combination of NSL and LbL has not been reported in the literature so far and the developed system offers unique topographical, viscoelastic as well as chemical signals to cells. However, the conditions of the ambient phase play a crucial role during multilayer assembly influencing PEM composition and properties and it is tried to manipulate the characteristics especially of the terminal layers. Again, various analytical methods as well as short- and long-term culture of HDF shall broaden the knowledge on the interplay of topographical and chemical stimuli on adhesion and growth of cells. This unique system of topographical in combination with viscoelastic features offers great potential for mimicking the natural environment of cells by simply exchanging the PEL for PEM assembly.

3 Materials and Methods

3.1 Materials

Table 3.1 is listing all reagents, which have been used as received or have been further processed. Further, Table 3.2 itemizes the used antibodies and cell structure stains, while Table 3.3 is showing the composition of frequently used buffers and media.

Table 3.1 - Reagents used during the PhD work

Reagent	Company	Cat-No.	Lot-/Charge-No.	Specification
1-Ethyl-3-(3-dimethylaminopropyl) carbodiimide (EDC)	Merck	8.00907-0005	54632607 647	-----------------
2-[Methoxy (polyethyleneoxy) propyl] trimethoxysilane (OEG)	ABCR	111226	1091557	90% 6-9 PE units
2-(*N*-morpholino)ethane sulfonic acid (MES)	VWR	441316T	K40945490 015	-----------------
3-Isocyanatopropyl triethoxysilane (IPTS)	ABCR	111201	1042794	95%
6-Aminofluorescein	Fluka	07985-1G	BCBB3843V	≥95%
11-Mercaptoundecanoic acid (MUDA)	Sigma	450561-5G	12103BE	95%
α-Methoxy-ω-amino poly (ethylene glycol) (mPEGA)	Rapp	1211.325	12200-2	-----------------
Acetone	Roth	9372.5	171171122 / 499111216	≥99.8% p.a.
Ammonium hydroxide (NH$_4$OH)	Roth	6774.1	30680634	25% p.a.
Antibiotic-antimycotic-solution (AAS)	Promocell	C-42020	D09766P	-----------------
Bovine serum albumin (BSA)	Merck	1.12018.0025	K38642218 840	-----------------
Calcium chloride dihydrate (CaCl$_2$*2H$_2$O)	Roth	HN04.1	222187557	≥99%
Chloroform D1 with TMS	Roth	AE59.1	8591	≥99.8%
Cyclohexane	Roth	6886.1	251172169	≥99.5% p.a.
Dichloromethane	Roth	8424.1	38788606	>99.5%
Dimethyl sulfoxide (DMSO)	Merck	1.16743.1000	K33960243 504	≥99%
di-Sodium hydrogen phosphate dihydrate (Na$_2$HPO$_4$*2H$_2$O)	Merck	1.06580.500	K39626980 924	-----------------
Dulbecco's modified Eagle's medium (DMEM)	Biochrom	FG0435	1326W; 1116K	-----------------
Ethanol	Roth	K928.4	431178502 / 131169305	≥99.8%, MEK
		9065.3	041166570	≥99.8% p.a.
Ethylacetate	Roth	7338.1	18678766	>99.5%
Fetal bovine serum (FBS)	Biochrom	S0115	0608T	-----------------
Fibronectin (FN)	YoProteins	663	40520	-----------------
Fluorescein isothiocyanate (FITC)	Sigma	F3651-100MG	084K5319	≥90%

Glutaraldehyde	Sigma	G6403-100ML	MKBG2498	50%
Glycerol	Roth	7530.1	09569913	≥98%
Heparin (HEP, H)	Applichem	A3004.0005	05008469	190.8 IU mg^{-1}
Hexamethyldisilazane (HMDS)	Roth	3840.1	100198069	-----------------
Hydrogen peroxide (H$_2$O$_2$)	Roth	9683.4	270156754	35%
Magnesium chloride hexahydrate (MgCl$_2$*6H$_2$O)	Merck	1.05833.0250	A423433 517	-----------------
Methanol	Roth	4627.4	500165620	99.9%
Mowiol® 4-88	Calbiochem	475904	B73224	-----------------
N-Hydroxysuccinimide (NHS)	Sigma	130672-25G	1398297 42808165	≥98%
N,N - dimethyl formamide (DMF)	Applichem	A2359,0500	9T007222	dried
Poly (ethylene imine) (PEI, P)	Sigma	18.197-8	05119TD-087	50% w/v
Polystyrene nanoparticles (PS-NP)	Micro-particles	PS-F-0.3	PS-F-B1271	5% w/v
		PS-F-0.5	PS-F-L2311	10% w/v
		PS-F-0.8	PS-F-B1360	10% w/v
		PS-F-1.4	PS-F-L1136	10% w/v
Potassium chloride (KCl)	Merck	1.04936.0250	K32518836 348	-----------------
Potassium-di-hydrogen phosphate (KH$_2$PO$_4$)	Merck	1.04873.250	A433173 522	-----------------
Potassium permanganate (KMnO$_4$)	--------------	-----------------	--------------------	-----------------
Roti® Histofix	Roth	P087.4	231172719	4% PFA
Sodium chloride (NaCl)	Roth	3957.1	339109045	≥99.5% p.a.
Sodium-di-hydrogen phosphate dihydrate (NaH$_2$PO$_4$*2H$_2$O)	Merck	1.06345.1000	K91284445 516	-----------------
Sodium dodecyl sulfate (SDS)	Applichem	A2263,0100	8G005779	≥99.5% p.a.
Sodium hydroxide (NaOH)	Roth	9356.1	14674657	≥99%
Sulfuric acid (H$_2$SO$_4$)	Roth	0971.2	299108090	96%
Toluene	Roth	AE06.1	4737/10CR	≥99.5%
Triethylamine (TEA)	Sigma	47,128-3	S56791-388	99.50%
Tris	Applichem	A2264,1000	5J004612	≥99.9%
Triton X-100	Sigma	T8532-100ML	084K0027	-----------------
Trypsin/ EDTA	Biochrom	L2163	0963W	0.25%/ 0.02%

Table 3.2 - Antibodies and cell structures stains

Antibodies/ stains	Company	Cat.-No.	Lot-No.	Specifics	Dilution
primary antibodies					
monoclonal mouse anti-Vinculin IgG	Sigma	V9131-.2ML	129K4849	hVIN-1	1:200
monoclonal mouse anti-FN IgG	Sigma	F7387-.2ML	081M4791	FN-15	1:200
secondary antibodies					
polyclonal goat anti-mouse IgG (CY2)	Dianova	115-225-146	78409		1:200
cell structure stains					
BODIPY® 558⁄568 Phalloidin	Invitrogen	B3475	25710W		1:50
TO-PRO®-3 Iodide (642⁄661)	Invitrogen	T3605	612354		1:500

Table 3.3 - Buffers and media composition

Buffers and solutions	Chemical composition	
0.1% Triton X-100	0.1% (v/v) Triton X-100 dissolved in PBS II	
1% BSA	1% (w/v) BSA dissolved in PBS II	
Mowiol	2.4 g Mowiol® 4-88, 6.0 g glycerol, 6.0 mL H_2O, 12.0 mL 0.2 M Tris-HCl, 25 mg ml^{-1} DABCO	
Phosphate buffered saline (PBS I)	5.1 mM NaH_2PO_4, 11.7 mM Na_2HPO_4, 140 mM NaCl, pH 7.4	
Phosphate buffered saline (PBS II)	2.7 mM KCl, 137 mM NaCl, 1.4 mM KH_2PO_4, 4.3 mM Na_2HPO_4, pH 7.4	
Phosphate buffered saline (PBS III)	2.7 mM KCl, 137 mM NaCl, 1.4 mM KH_2PO_4, 4.3 mM Na_2HPO_4, 0.49 mM $MgCl_2$*$6H_2O$, 0.9 mM $CaCl_2$*$2H_2O$, pH 7.4	
RCA clean	H_2O : NH_4OH : H_2O_2 = 5:1:1 (80°C)	
Dulbecco's modified Eagle's medium (DMEM)	without FBS	4 g L^{-1} glucose, 1% AAS, without sodium pyruvate
	with FBS	additionally 10% FBS

3.2   Design of nanostructured biomaterial surfaces

3.2.1   Surface cleaning

The substrates used for the experimental procedures were standard glass cover slips ((15x15) mm², Menzel GmbH, Braunschweig, Germany), specially manufactured glass slides ((10x20) mm², 0.5 -0.6 mm in thickness, Menzel) or 150 mm silicon wafers (Si-Mat, Kaufering, Germany), which were cut to the desired size and of which specifications are listed in Table 3.4.

Table 3.4 - Specifications of the used silicon wafers based on the information of Si-Mat

Diameter:	150 mm
Type/ dopant:	P/ Boron
Orientation:	<100>
Growth method:	CZ
Resistivity:	1 - 30 Ωcm
Thickness:	675 ± 25 μm
Front surface:	polished
Back surface:	etched
Flats:	1 SEMI with 57.5 ± 2.5 mm

All samples were cleaned before use applying the standard cleaning procedure 1, first described by Werner Kern in 1965 while working for the Radio Corporation of America, which leads to the better known abbreviation 'RCA clean' [242]. Here, ultrapure water, ammonia solution, and hydrogen peroxide are used at the ratio 5:1:1 (v/v/v) to remove organic residues from the sample surfaces. First, water and ammonia solution were mixed and heated to 75 - 80°C and hydrogen peroxide was added to the solution while switching off the heating. The solid samples were placed into the solution for 10 min, excessively rinsed with ultrapure water (6 cycles for 5 min), dried with a stream of nitrogen, and used immediately for further modification.

3.2.2   Nanosphere lithography (NSL)

As described in section 1.2.3.1, different approaches can be used to obtain colloidal masks. Here, the spin coating technique as well as a modified LB method were applied to design CCM of polystyrene nanoparticles (PS-NP, Microparticles GmbH, Berlin, Germany)

with different diameter (319 nm, 476 nm, 756 nm, 1390 nm). In dependence on that diameter, either spin coating or the LB technique was used. PS-NP with a diameter <1 μm were spin coated to planar substrates to obtain monodisperse monolayers. The optimal process parameters were determined by extensive initial experiments. First, PS-NP were diluted in 0.25% triton X-100 in methanol and sonicated for 15 min to remove possible aggregates. Cleaned glass or silicon samples were mounted to a spin coater (Süss MicroTec AG, Garching, Germany) and 10 μL cm^{-2} of a PS-NP suspension were transferred to the surface and spin coated for 180 s at varying speeds (Figure 3.1). Depending on the diameter, the rotation speed was set to ~800 rpm for 756 nm PS-NP, ~1,000 rpm for 476 nm PS-NP and ~1,200 rpm for 319 nm PS-NP.
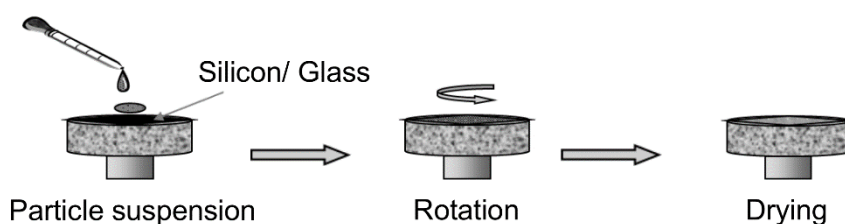
Figure 3.1 - Spin coating of PS-NP with a diameter <1μm.

Templates with PS-NP >1 μm were prepared using a modified LB technique, of which basic principle is the self-organization of colloidal particles on liquid surfaces. Thus, areas of several micrometer in lateral dimension can be obtained relatively simple, effective, and defect free. The single steps of the LB technique are displayed in Figure 3.2. First, the PS-NP were diluted 1:2 in ethanol p.a. and sonicated for 15 min to remove particle aggregates. Further, a clean petri dish was completely filled with ultrapure water and the PS-NP solution was transferred to the water surface at an angle of ~30° using a clean silicon sample (a). The disordered monolayer on the water surface was transformed to an *hcp* one adding 2% (w/v) sodium dodecyl sulfate (SDS) in water dropwise to the petri dish to reduce the surface tension of water (b). The so-formed stable monolayer was skimmed from the water surface using clean glass or silicon samples (c, d) and allowed to dry at room temperature (RT), resulting in an almost defect-free monolayer of PS-NP on planar surfaces.
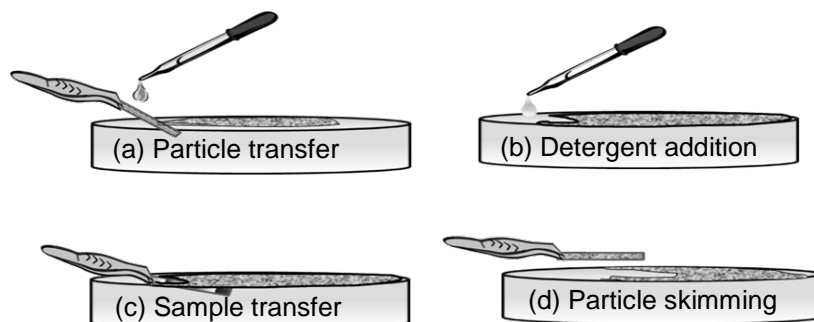
Figure 3.2 - Modified LB technique for PS-NP with a diameter >1 μm.

Once stable PS-NP monolayers were formed, tetrahedral gold nanostructures were generated using electron beam physical vapor deposition (EBPVD) (Figure 3.3). The samples were mounted in 26 cm distance centered above the rotary crucible electron beam evaporator EV M-6 (6 kW, FerroTec GmbH, Unterensingen, Germany) in the high-vacuum coating system MSBA-400 TE (Malz & Schmidt GbR, Meißen, Germany). First, 10 nm chromium were deposited at 8 kV accelerating voltage, 17.5 mA emission current, and an evaporation rate of 1.2 Å s^{-1}. Afterwards, 75 nm of gold were coated at 7 kV accelerating voltage, 66 mA emission current, and an evaporation rate of 2.7 Å s^{-1}. The base vacuum was 2x10^{-7} mbar and the chromium layer was used to manifest the binding of gold to the sample surface. Finally, a lift-off process was used to remove the PS-NP templates and to obtain discrete nanostructures. Hence, all samples were sonicated in dichloromethane for 2 min and excessively rinsed with acetone, ethanol p.a., and ultrapure water. Afterwards, the samples were dried with a stream of nitrogen and stored in a desiccator until further use.
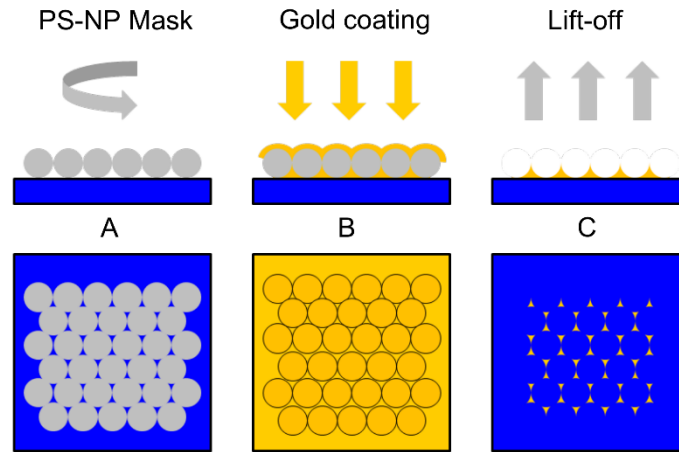
Figure 3.3 - Basic principle of NSL. After formation of a PS-NP monolayer (A), a noble metal layer (e.g. gold) is deposited via EBPVD on top of the PS-NP (B). Afterwards, a lift-off process removes the PS-NP mask to obtain tetrahedral nanostructures (C).

The dimensions of the designed nanostructures can be calculated in dependence on the colloid diameter [164]. However, since not only monolayers (ML), but also double (DL) or multilayers can be formed, the dimensions of the nanostructures also can vary in size and distance. The distance d_{ML} of structures in monolayers is calculated as follows:

$$d_{ML} = \frac{D}{\sqrt{3}}$$

Equation 3.1

D -   Particle diameter

The size a_{ML} of the tetrahedral nanostructures can be calculated with the following equation:

$$a_{ML} = \frac{3}{2}\sqrt{32}\left(\sqrt{3} - 1 - \frac{1}{\sqrt{3}}\right)D = 0.233D$$

Equation 3.2

In case of double layers the distance d_{DL} is calculated according to

$$d_{DL} = D$$

Equation 3.3

and the size a_{DL} according to

$$a_{DL} = \left(\sqrt{3} - 1 - \frac{1}{\sqrt{3}} \right) D = 0.155 D .$$

Equation 3.4
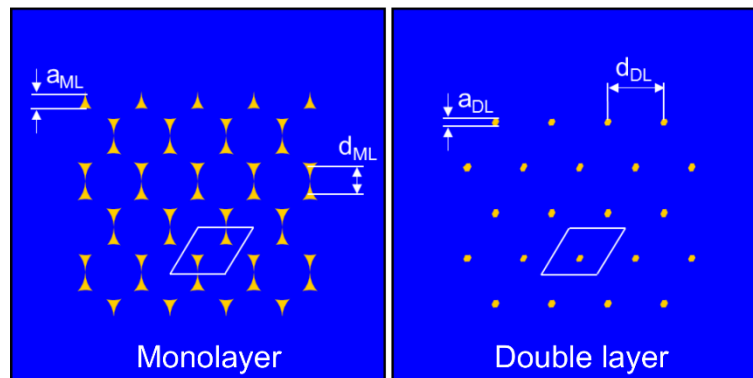
Figure 3.4 - Nanostructure arrangement after removal of PS-NP mask. The distance *d* and size *a* of the nanostructures are defined by monolayer (ML, left) or double-layer (DL, right) formation. A primitive cell is indicated in the image as well.

3.3   Modification of nanostructured biomaterial surfaces

3.3.1   Self-assembled monolayers

3.3.1.1 Silane synthesis and their characterization

Self-assembled monolayers (SAM) were used to modify nanostructured surfaces to obtain a surface chemistry of interest. However, since not all reagents could be purchased ready-to-use, specific silanes were synthesized during the course of this PhD work. A method was used which has been described previously by Spatz and coworkers [243]. Here, α-methoxy-ω-amino poly (ethylene glycol) (mPEGA) and 3-isocyanatopropyl triethoxysilane (IPTS) were used to synthesize a silane with a urea linkage (Figure 3.5). Therefore, 1 mM IPTS was added to a 1 mM solution of mPEGA in 15 mL dimethyl formamide (DMF) at RT under nitrogen atmosphere and stirred for 72 h. After removing the solvent by distillation at RT, the product was purified by recrystallization with a mixture of toluene/ cyclohexane (1:4, v/v) to obtain a faintly beige powder.
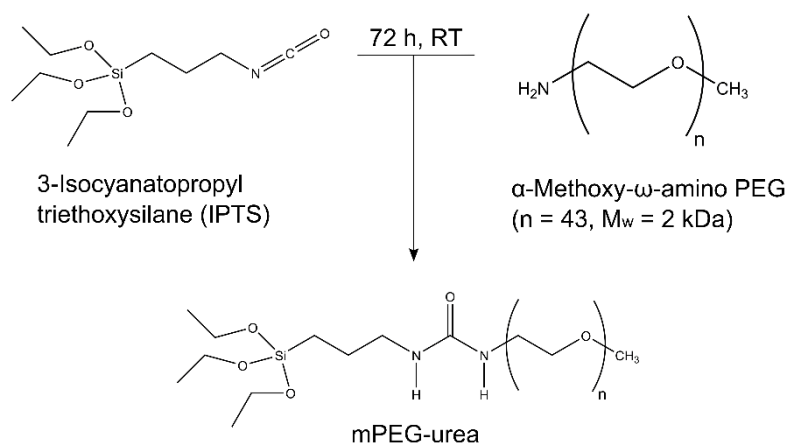
Figure 3.5 - Synthesis of mPEG-urea with 3-Isocyanatopropyl triethoxysilane (IPTS) and α-methoxy-ω-amino poly (ethylene glycol) (mPEGA).

The composition of the synthesized molecule was investigated using ^{1}H- and ^{13}C-nuclear magnetic resonance (NMR) as well as matrix-assisted laser desorption ionization (MALDI) - time of flight (TOF) mass spectrometry (MS). For NMR analysis, the powder was dissolved in deuterated chloroform and 16 repetitions for ^{1}H- and 5,000 repetitions for ^{13}C-NMR were performed, respectively, using an INOVA 500 (Agilent GmbH, Böblingen, Germany). The result of the modification is as follows:

^{1}**H-NMR** (400 MHz; CDCl$_3$): δ = 0.60 - 0.63 (m, 2H, Si-*CH$_2$*), 1.22 (t, ^{3}J = 5.2 Hz, 9H, O-CH$_2$-*CH$_3$*), 1.55 - 1.62 (m, 2H, Si-CH$_2$-*CH$_2$*), 3.13 - 3.17 (m, 2H, NH-*CH$_2$*-CH$_2$-CH$_2$), 3.38 (s, 3H, O-*CH$_3$*), 3.35 - 3.38 (m, 2H, N-*CH$_2$*-CH$_2$-O), 3.53 - 3.55 (m, 2H, N-CH$_2$-*CH$_2$*-O), 3.59 - 3.69 (m, 172H, O-*CH$_2$-CH$_2$*-O), 3.79 - 3.83 (m, 6H, Si-O-*CH$_2$*-CH$_3$), 5.02 (br s, 2H, *NH*)

^{13}C-NMR (125 MHz; CDCl$_3$): δ = 7.7 (Si-*CH$_2$*), 18.3 (Si-O-CH$_2$-*CH$_3$*), 23.7 (Si-CH$_2$-*CH$_2$*), 40.2 (CH$_2$-CH$_2$-*CH$_2$*-NH), 42.9 (NH-*CH$_2$*-CH$_2$-O), 58.4 (Si-O-*CH$_2$*-CH$_3$), 58.9 (O-*CH$_3$*), 70.4 - 70.7 (CO-NH-CH$_2$-*CH$_2$*, O-*CH$_2$*-*CH$_2$*-O), 158.6 (C=O)

The analysis with MALDI-TOF MS was carried out using a 4,800 MALDI-TOF/ TOF Analyzer (AB Sciex GmbH, Darmstadt, Germany) equipped with a neodymium-doped yttrium aluminum garnet (Nd:YAG) laser with a repetition rate of 200 Hz. Therefore, 1 mg of the sample was mixed with 9 *µ*L of a solution of 10 mg mL^{-1} α-cyano-4-hydroxycinnamic acid (CHCA) in a mixture of acetonitrile and 0.1% trifluoroacetic acid (1:1, v/v). Afterwards, 0.5 *µ*L of the resulting mixture was manually spotted onto the sample plate and allowed to dry at RT. Mass spectra within the *m/z* range 700 to 4,000 were acquired in the positive ionization and reflectron mode accumulating data from 1,200 laser shots per spot.

MALDI: M_n = 2158 Da, M_w = 2189 Da, M_w/M_n = 1.01

Further, the successful SAM formation was indirectly quantified recording an adsorption isotherm of human fibronectin (FN), which has been labeled with fluorescein isothiocyanate (FITC). Therefore, 0.5 mL of FITC-FN was added at different concentrations (5.0, 10.0, 20.0, and 40.0 *µ*g mL^{-1}) to each well of a 24-well-plate, where samples of plain silicon dioxide, SAM-modified silicon dioxide as well as Thermanox® slides, which represent tissue culture poly (styrene) (TCPS), have been placed and were incubated at 37°C for 1 h. All silicon samples had a size of (10x10) mm², while the TCPS slides had a diameter of ø14 mm. After terminating the adsorption, the samples were carefully rinsed with PBS II, transferred to a new 24-well-plate and the adsorbed protein was desorbed with a 0.2 N sodium hydroxide solution at RT for 2 h. Subsequently, fluorescence intensities of the supernatants were quantified with a fluorescence plate reader (FLUOStar Optima, BMG Labtech GmbH, Ortenberg, Germany) at 485 nm excitation/ 520 nm emission. The experiment was run in triplicate and mean and standard deviation were calculated.

3.3.1.2 Process parameters

Two different one-step approaches were used to obtain SAM on the free glass or silicon dioxide surface on nanostructured samples for back filling purposes to avoid protein adsorption, cell adhesion and multilayer formation. In the first method, the nanostructured samples were incubated in a 1% solution of 2-[methoxy (polyethyleneoxy) propyl] trimethoxysilane (OEG silane) in ethanol p.a. at RT overnight, rinsed with the solvent and ultrapure water, dried with a stream of nitrogen, and stored in a desiccator until further use. In the second method, the nanostructured samples were added to a 0.25 mM solution of mPEG-urea in dry toluene and catalytic amounts of triethylamine were added. The samples were incubated at 80°C under nitrogen atmosphere overnight and afterwards sonicated with ethyl acetate for 2 min, rinsed with ethyl acetate and methanol, dried with a stream of nitrogen, and

stored in a desiccator until further use. The one-step procedure was also performed on plane glass and silicon dioxide as control surfaces for comparative studies.

After passivation of the surrounding silicon dioxide or glass, the gold nanostructures were activated incubating the samples with 2 mM mercaptoundecanoic acid (MUDA) in ethanol p.a. at RT overnight. The obtained SAM with terminating carboxylic acid groups resulted in surface charges similar to silicon dioxide or glass and shall allow specific interaction of cells with and facilitate multilayer formation on the nanostructures. Finally, the samples were rinsed with the solvent and ultrapure water, dried with a stream of nitrogen, and stored in a desiccator until further use.

3.3.2   Polyelectrolyte multilayers (PEM)

3.3.2.1   Polyelectrolytes

The PEM were built up with two different macromolecules with ionogenic groups, namely poly (ethylene imine) (PEI, P) and heparin (HEP, H). Thereby, the former one represents a polycation and the latter one a polyanion at the conditions used for PEM formation.

Poly (ethylene imine) (PEI)

PEI is an organic, synthetic, highly branched, and strongly alkaline polymer and its large amounts of primary, secondary and tertiary amino groups could become protonated in an aqueous environment. The charge density of the resulting polycation character of PEI is pH dependent (Figure 3.6).
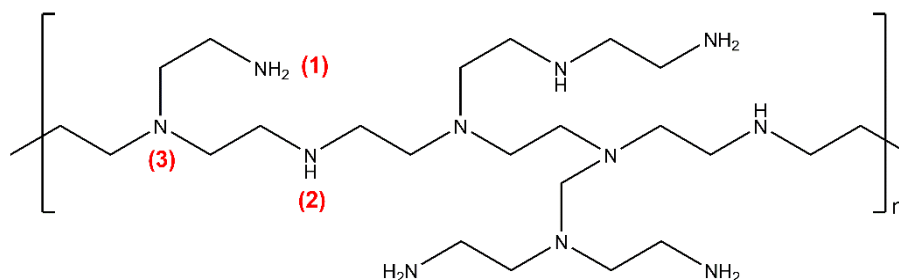
Figure 3.6 - Molecular structure of PEI with primary (1), secondary (2), and tertiary amino groups (3) based on the suppliers information (Sigma-Aldrich) [244].

However, as weak polyelectrolyte (PEL) its degree of dissociation is highly dependent on the solution pH value and its reported pK_a value is around 8.3 [245, 246]. PEI is typically used in wastewater treatment, the paper industry and as precipitating agent for the conditioning of cell extracts. Further, PEI is applied in the biomedical field as precursor base layer during PEM formation, since its positive net charge at physiological conditions allows the electrostatic interaction with negatively charged surfaces [207, 230, 245, 247]. During the last decade, the

application of PEI as non-viral transfection agent to transfer DNA inside cells gained in importance. However, its transfection efficiency as well as its cytotoxicity are dependent on the molecular weight as low molecular weight PEI tends to have a higher effectiveness and lower cytotoxicity [248, 249].

Out of the many commercially available PEIs, a high molecular weight PEI was used in this study. Its molar mass was determined as M_n ~ 60,000 Da (gel permeation chromatography) and M_w ~ 750,000 Da (light scattering) [244, 250].

Heparin (HEP)

HEPs are a group of highly sulfated GAG, which mainly consist of repeating units of iduronic acid and glycosamine residues [251]. The saccharide units are forming polymers due to α- and β-1,4-glycosidic bonds (Figure 3.7). The highly anionic character of HEP originates from the acidic functional groups, namely sulfate monoesters, sulfamido groups, and carboxylate groups [252]. The latter one is less acidic with a pK_a value of 3.13 while the former two are highly acidic with pK_a values ranging from 0.5 to 1.5 [252]. When HEP dissolves in water, the highly acidic functional groups are deprotonated immediately, making HEP a strong PEL, of which conformation is almost independent of the pH value of the ambient phase.

L-iduronate-2-sulfate   *N*-sulfo-D-glucosamine-6-sulfate
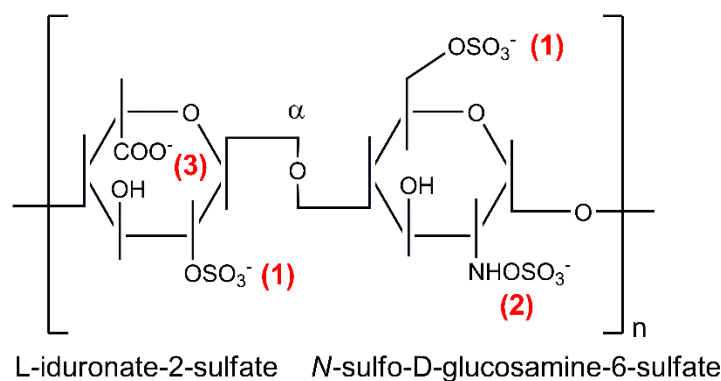
Figure 3.7 - Molecular monomer structure of HEP containing sulfate monoesters (1), a sulfamido group (2) and a carboxyl group (3).

HEP has a strong anticoagulant activity, which arises due to the antithrombin-III binding of the blood plasma, forming a complex which inactivates different coagulation enzymes, such as thrombin or factor Xa, which later inactivates the conversion of fibrinogen (FNG) to fibrin [253, 254]. HEP is produced as proteoglycan in mast cells of the connective tissue and is usually derived from mucosal tissues of animals such as porcine intestine or bovine lung [254]. Upon enzymatic cleavage fragments of varying molecular weight, ranging from 5,000 Da to 30,000 Da, can be obtained [254]. It is used to prevent and cure thrombosis, embolisms, or rethrombosis in various venous and arterial deceases, but also as anti-inflammatory molecule [255].

The biological activity and the degree of sulfation of HEP are highly dependent on the animal source [256]. The minimum activity of HEP used in this study is reported as 190.8 IU mg^{-1}, whereas the molecular weight ranges between $M_w \sim$ 8,000 - 25,000 Da (Applichem).

3.3.2.2 Labeling of heparin

The carboxylic acid group of HEP was labeled with 6-aminofluorescein crosslinking it using the 1-ethyl-3-(3-dimethylaminopropyl) carbodiimide/ *N*-hydroxysuccinimide (EDC/ NHS) chemistry. Therefore, HEP was dissolved in 100 mL of 50 mM 2-(*N*-morpholino) ethane sulfonic acid (MES) buffer at pH 4.75. After dissolution, EDC and NHS were added to the solution depending on the molarity of HEP. Here, the doubled molarity of the amount of HEP was used and the whole solution was stirred at RT for 1 h. After adjusting the pH value to pH 7.0 with 1 N sodium hydroxide solution, a solution of 2 mg mL^{-1} 6-aminofluorescein in dimethyl sulfoxide (DMSO) was added. The amount was calculated according to Equation 3.5 to achieve a conversion of the carboxyl group of 10%.

$$V = \frac{\% \text{ of intended conversion}}{100} * Y * M_w * \frac{1}{c} \qquad \text{Equation 3.5}$$

Y   - Molarity of HEP

M_w - Molecular weight of 6-amino-fluorescein

c   - Concentration of 6-amino-fluorescein

Afterwards, the solution was stirred in the dark at RT overnight and additionally dialyzed (dialysis tube with $M_{w\ cut-off} \sim$ 3,500 kDa, Roth) against water for several days until the water did not show any signs of fluorescein residues. Finally, the solution was lyophilized overnight in a freeze dryer (Christ GmbH, Osterode, Germany) to obtain a solid HEP sample, which can be used for further investigations.

3.3.2.3 Process parameters

Both PEL were dissolved in PBS I pH 7.4 to obtain a final concentration of 2 mg mL^{-1}. The intrinsic pH value of the PEI solution was pH 10.3 ± 0.1, which was not controlled during the layer formation process. However, the intrinsic pH value of the HEP solution was pH 7.4 ± 0.05 that was adjusted to either pH 5.0 or pH 7.0 for the terminal HEP layer only, which represented the 8th overall layer. Ultrapure water was used as rinsing solution and its intrinsic pH value of pH 6.5 ± 0.3 was not adjusted. All electrolyte and rinsing solutions have been filtered with a polysulfone (PSU) filter with 0.2 μm pore size.

The nanostructured samples, which have been modified with OEG silane and MUDA, were transferred to a 12-well-plate ((15x15) mm²) or a 6-well-plate ((10x20) mm²) and placed on a shaker for gentle agitation. Both PEL were allowed to adsorb alternately on the

nanostructured samples at RT for 30 min, starting with PEI as primary layer. After incubation, the PEL solutions were removed carefully with a vacuum aspiration unit and ultrapure water was added to rinse all samples for 5 min twice. The PEM formation was terminated after the 8th, which represents HEP and is abbreviated $(PH)_4$, or 9th layer, which represents PEI and is abbreviated $(PH)_4P$. As a result, four different kinds of terminal layers were obtained: two with HEP at pH 5.0 and two with HEP at pH 9.0. Finally, all samples were dried with a stream of nitrogen and stored in a desiccator until further use.

3.4 Physicochemical and morphological surface characterization

Native nanostructured and chemically modified nanostructured surfaces were characterized using various analytical methods. Since chemistry and topography of the designed surfaces are of importance, physicochemical methods such as water contact angle (WCA) measurements, zeta potential as well as ellipsometry will be discussed in more detail. Further, imaging techniques like scanning electron microscopy (SEM) or atomic force microscopy (AFM) are described.

3.4.1 Water contact angle (WCA) measurements

The wettability of nanostructured and chemically modified nanostructured surfaces was characterized using static and dynamic WCA measurements with ultrapure water as test liquid. The WCA of a sessile drop on a solid surface can be described with Young's equation (Equation 3.6), which calculates the cosine of the contact angle θ at the equilibrium state of the interfacial tensions (Figure 3.8).

$$\cos\theta = \frac{\gamma_{sv} - \gamma_{sl}}{\gamma_{lv}}$$

Equation 3.6

θ - Contact angle of the test liquid

γ - Interfacial tension at the phase boundary (sv - solid/ vapor; sl - solid/ liquid; lv - liquid/ vapor
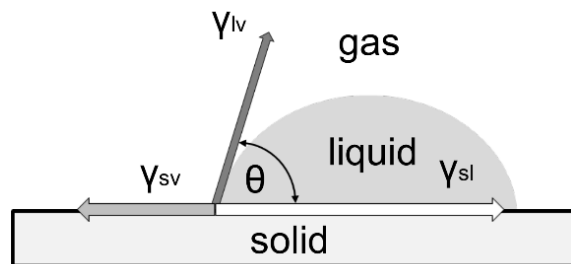
Figure 3.8 - Equilibrium of interfacial tensions of a sessile drop on a smooth surface, adapted from [257].

A reduced wettability results in a higher WCA and, thus, in a higher interfacial energy which is related to a lower surface free energy and vice versa. In general, surfaces can be divided into hydrophilic, i.e. water attracting, or hydrophobic, i.e. water repellent. However, the border between these conditions is sometimes not clear. Occasionally, surfaces with WCA values of $\theta \geq 90°$ are referred as hydrophobic [258] or they are defined with the help of the pure water adhesion tension τ^0, which can be calculated with the following equation [14]:

$$\tau^0 = \gamma_{lv}^0 \cos\theta \qquad \text{with } \gamma_{lv}^0 = 72.8 \text{ mN m}^{-1} \qquad\qquad \text{Equation 3.7}$$

If water is in contact with solid surfaces, localized perturbations occur which result in a change of the chemical potential of water, that later on has an effect on biological interactions of materials with their aqueous environment due to the self-association of water [14]. This self-association of water, per definition a *Lewis* acid or base, is affected by both the type and surface concentration of water-interactive *Lewis* acid or base functional groups on material surfaces, which correlates with the wettability [1, 14]. According to Vogler, forces during the self-association of water at the solid-liquid-interphase can only be overcome with a large number of *Lewis* pairings, which is usually the case at a water adhesion tension of $\tau^0 = 30$ mN m^{-1}. This threshold value is called '*Berg limit*' and correlates with a contact angle of $\theta = 65°$. In conclusion, surfaces with a lower WCA are termed as 'hydrophilic' and surfaces with a higher WCA are termed as 'hydrophobic', which also has been adapted to this study.

The calculation of WCA according to Equation 3.6 is only valid, if the following prerequisites are met: (i) existence of a thermodynamic equilibrium, (ii) a smooth, clean, solid, homogeneous surface and (iii) no swelling or dissolution of the material in the test liquid [259]. Even the prerequisites cannot always be met, the determination of WCA can give still useful information such as the degree of hydrophobicity [259]. Further, the measurement of dynamic WCA provides information of topography and heterogeneity of material surfaces, even though the calculation is not that simple as for static WCA measurements [19, 260-262]. Many surfaces show two stable values upon wetting with liquids, an advancing WCA θ_a as well as a receding WCA θ_r. The difference between both WCA

$$\Delta\theta = \theta_a - \theta_r \qquad\qquad\qquad\qquad \text{Equation 3.8}$$

is called the WCA hysteresis. Even though the estimation of the hysteresis is difficult for rough and heterogeneous surfaces [19, 260], still thermodynamic trends might be observed evaluating the hysteresis values (Table 3.5) [263].

Table 3.5 - Thermodynamic WCA hysteresis

Assumption	Specific Assumption	Effect on Hysteresis
Surface is smooth	Surface must be smooth at the 0.1 to 0.5 μm level	$\Delta\theta$ increases with increasing roughness (θ_a increases and θ_r decreases with increasing roughness)
Surface is homogenous	Surface must be homogeneous at the 0.1 μm level and above	θ_a dependent on low energy phase; θ_r dependent on high energy phase

The WCA of planar, nanostructured and chemically modified nanostructured surfaces were determined with the OCA 15+ system (Dataphysics GmbH, Filderstadt, Germany). Static WCA were recorded adding five droplets á 1 μL of fresh ultrapure water to each surface. Further, dynamic WCA were determined dispensing 5 μL of fresh ultrapure water with a velocity of 0.2 μL s^{-1} to the surface and aspirating the liquid with the same velocity. The number of droplets was dependent on the wettability of the surfaces, but at least two droplets per surface were recorded. The experiments were run at least in triplicate and mean and standard deviation were calculated. WCA <10° were set as zero due to the inappropriate signal-to-noise ratio.

3.4.2   Zeta potential measurements

Zeta (ζ) potential measurements are used to determine the surface charge of materials by recording the electrokinetic potential. In general, interphases lead to perturbations in charges of the bulk material. For example, polymer surfaces in contact with liquids might not only be charged, but also ions might adsorb from the surrounding liquid, provided it is a buffer solution. Due to the fact that counterions will adsorb on the charged surface, a electrochemical double layer is formed [264]. Different models have been developed or modified by *Helmholtz*, *Gouy*, *Chapman*, *Stern*, and *Grahame* and the model of the latter four researchers is the nowadays generally accepted one, the so-called GCSG model (Figure 3.9).
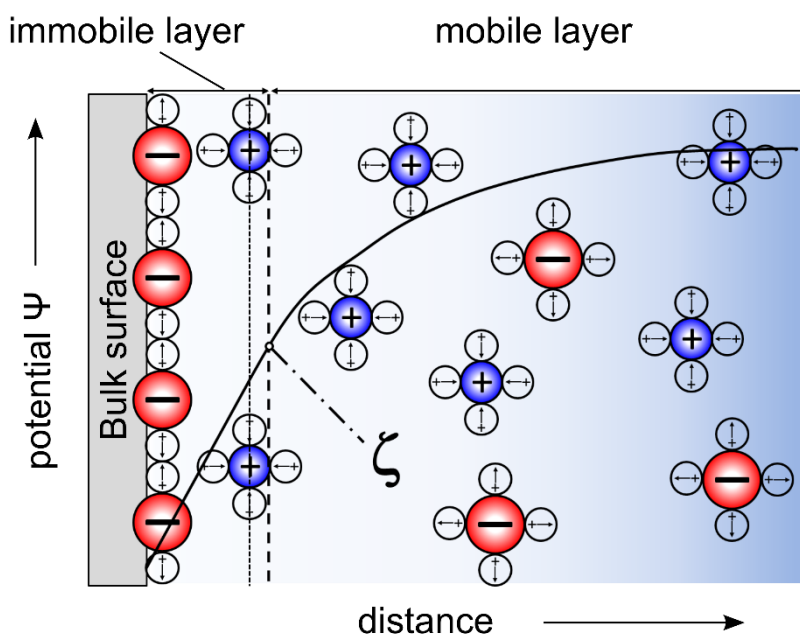
Figure 3.9 - Scheme of the electrochemical double layer, adapted from [265].

According to this model, the electrochemical double layer is divided into a hydrodynamically immobile and mobile or diffuse layer. The former one is sub-divided in an inner Helmholtz plane (IHP), where charges of adsorbed and partly dehydrated ions are

concentrated, and an outer Helmholtz plane (OHP), where the charges are accumulated due to the hydrated counterions, which are adsorbed mainly via electrostatic interactions. The area in between the IHP and OHP is the so-called Stern layer [264]. The phase boundary between both the immobile and diffuse layer is the slipping plane, where the ζ - potential can be measured due to the motion of the adjacent electrolyte solution. The electrostatic forces within the diffuse layer lead to an approximation of ions to the surface, while the thermodynamic motion tends to an equal distribution of ions within the liquid. Thus, the potential difference within the immobile layer is linear, whereas it decays exponentially within the diffuse layer according to the *Debye-Hückel*-approximation (Equation 3.9).

$$\Psi\left(x\right) = \Psi_d \cdot e^{-\kappa x}$$ Equation 3.9

$\Psi\left(x\right)$ – Potential at position x

Ψ_d – Potential at distance d from the slipping plane

κ – Conductivity of the channel

The ζ - potential can be calculated using either the streaming current or the streaming potential. Due to the electrolyte flow across the material surface within the channel, ions within the diffuse layer of the electrochemical double layer are entrained from the surface and they accumulate at one electrode, which leads to a measurable potential difference. On conducting surfaces, charge carriers might be able to migrate against the flow, which would lead to incorrect determination of the potential. However, it can be remediated by surface conductivity correction or by direct recording of the streaming current. An equilibrium between migration and remigration of ions is established due to the a back flow of charge carriers [264]. Thus, the ζ-potential can be calculated using the equations of *Helmholtz-Smoluchowski* (Equation 3.10), which uses the streaming potential, or *Fairbrother-Mastin* (Equation 3.11), which processes the streaming current.

$$\varsigma_p = \frac{dU}{dp} \cdot \frac{\eta}{\varepsilon \cdot \varepsilon_0} \cdot \frac{L}{A \cdot R}$$ Equation 3.10

$$\varsigma_c = \frac{dI}{dp} \cdot \frac{\eta}{\varepsilon \cdot \varepsilon_0} \cdot \frac{L}{A}$$ Equation 3.11

ζ - Zeta potential (index p - potential, index c - current)
dU/dp - Change in streaming potential in dependence on the pressure
dI/dp   - Change in streaming current in dependence on the pressure
η - Viscosity of the electrolyte solution
ε - Permittivity in vacuum
ε_0 - Relative dielectric constant

    L   - Length of the streaming channel

    A   - Cross section of the streaming channel

    R   - Electrical resistance of the measuring cell

Once calculated, the ζ - potential can be used to gain knowledge on the presence of functional groups and their degree of dissociation, on the adsorption of mono- or multivalent ions on solid surfaces or on the break-off of material components. Since the absolute value of the ζ - potential is dependent on the used electrolyte and the pH value, it should be recorded by changing the environmental conditions [264, 266]. Depending on the material, the dissociation of the charge carriers leads to different curve progressions (Figure 3.10).
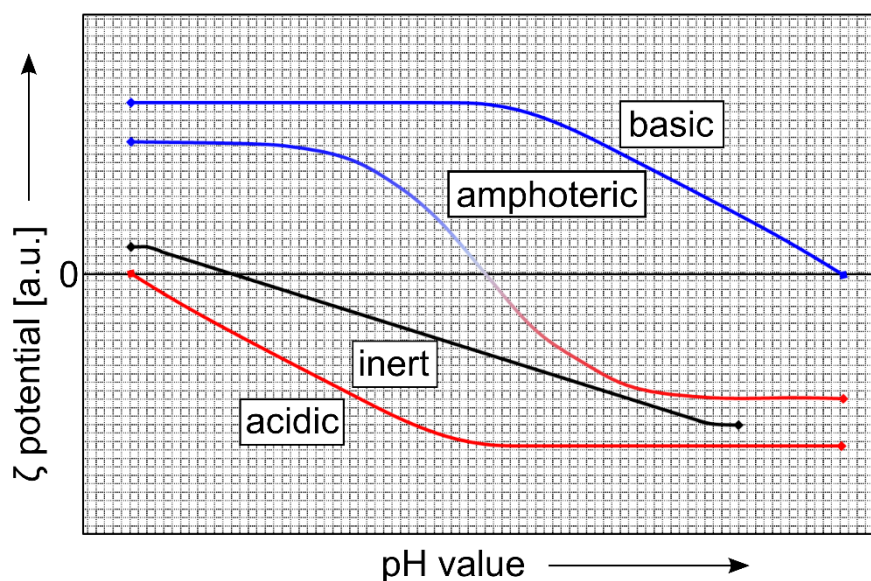
Figure 3.10 - Schematic representation of characteristic potential of surfaces with different functional groups, adapted from [264].

Inert material surfaces such as poly (tetrafluoro ethylene) possess a point of zero charge (PZC) at pH 4.0 independent of the ionic strength due to asymmetrical ion adsorption [264]. Here, cations are more hydrated than anions due to the water structure and, thus, the ζ - potential is declining with increasing pH values [264]. In case of materials with large amounts of basic or acidic charge carriers the ζ - potential is increasing in direction of the stronger ionization of those carriers. Thus, the location of the PZC or p*I* is dependent on the type and concentration of functional groups. In both cases, the asymmetrical ion adsorption also takes place at around pH 4.0. However, if basic as well as acidic groups are present on the material, the curve progression is an overlap of both single processes, indicating an amphoteric character. In this case, clear conclusions can only be drawn for excess groups at the phase boundary [264].

In this study, the ζ - potential was measured with the SurPASS Electrokinetic Analyzer (Anton Paar, Graz, Austria). Special manufactured cover slips with a size of (10x20) mm² were modified with nanostructures (section 3.2.2) and PEM (section 3.3.2.3). The cover slips were mounted with double-sided tape to the sample holders of the adjustable gap cell and the gap was adjusted manually to achieve a flow rate between 100 and 150 mL min^{-1} at a maximum pressure of 300 mbar. 1 mM potassium chloride was used as model electrolyte while 0.1 N hydrochloric acid was used for pH titration. The pH was titrated from pH 10.0 to pH 3.0 in 0.25 pH steps and, finally, the ζ - potential was determined using the streaming current and calculated according to Equation 3.11.

3.4.3   Ellipsometry

Ellipsometry is an optical method, which is used to investigate changes in thickness and refractive index (RI) of thin films at interfaces. The technique is sensitive to changes in the polarization state of elliptical polarized light, which is reflected at the phase boundary [267]. A polarizer polarizes unpolarized light from a source and linearly polarized light is transmitted with a phase shift since the incident light has passed different optical path lengths (Figure 3.11). The incident light beam can now be reflected, absorbed, or transmitted by the surface of interest. Thus, the light reflected by the layer and the light reflected by the bulk surface, which has to penetrate the upper layer again, is elliptically polarized, i.e. it is shifted in phase and amplitude. This polarization can be parallel (p) or perpendicular (s) to the plane of incidence. In this case, the optical path length of the system can be calculated with Equation 3.12 [268].

$$\beta = 2\pi \left(\frac{d}{\lambda}\right) n_2 \cos \phi_2 \qquad\qquad \text{Equation 3.12}$$

d	- Film thickness
λ	- Wavelength
n_2	- Refractive index (RI) of film
ϕ_2	- Refractive angle in film

Once the optical path length is known, the reflection coefficients R^p and R^s can be calculated using the following equations [268]:

$$R^p = \frac{r_{12}^p + r_{23}^p \exp(-i2\beta)}{1 + r_{12}^p r_{23}^p \exp(-i2\beta)} \qquad\qquad \text{Equation 3.13}$$

$$R^s = \frac{r_{12}^S + r_{23}^S \exp(-i2\beta)}{1 + r_{12}^S r_{23}^S \exp(-i2\beta)} \qquad\qquad \text{Equation 3.14}$$

r	- Reflectivities

The phase shift angle Δ between phase differences of p- ad s-components of the incident (δ_1) and reflected (δ_2) light can be determined with

$$\Delta = \delta_1 - \delta_2 \qquad\qquad \text{Equation 3.15}$$

Independent of the phase shift angle Δ, the ratio of the absolute values of the amplitudes, which is defined as tangent of an angle Ψ, stays constant.

$$\tan\Psi = \frac{|R^p|}{|R^s|} \qquad\qquad \text{Equation 3.16}$$

Combining Equation 3.15 with Equation 3.16 leads to the fundamental equation in ellipsometry [268].

$$\tan\Psi \, \exp(i\,\Delta) = \frac{|R^p|}{|R^s|} \qquad\qquad \text{Equation 3.17}$$

Plotting Δ and Ψ in a graph for a specific RI and a fixed angle leads to a so-called Δ/Ψ-trajectory as a function of film thickness. These trajectories are often elliptical in shape and close at a multiple of the film thickness [268].

$$d = \frac{\lambda}{2\sqrt{n_2^2 - sin^2\phi_1}} \qquad\qquad \text{Equation 3.18}$$

d - Film thickness

n_2 - RI of film

ϕ_1 - Angle of incident light
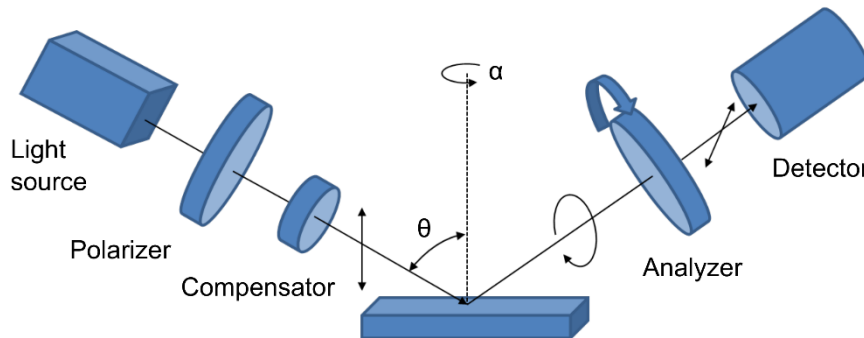
Figure 3.11 - Schematic representation of the principle of ellipsometry, adapted from [269]. The polarizer compensator sample analyzer (PCSA) ellipsometer is shown, were the polarizer changes the angle *P* until the reflected light of the sample is linearly polarized. Adjusting the angle *A* with the analyzer extinguishes the polarized light detected by the photodetector.

In this study, the thickness of SAM and adsorbed protein layers was determined with the M-2000® Ellipsometer (J.A. Woollam Co., Lincoln, USA). The samples were mounted to the

stage of the ellipsometer and fixed with a 500 μL liquid cell with a static scanning angle of 70°. The SAM thickness was calculated in air and in PBS II after equilibration. Afterwards, FN adsorption was investigated *in situ* filling the liquid cell with a FN solution of different concentration, which increased from 2 to 5 to 10 to 20 and to 40 μg mL^{-1}. Each solution was allowed to interact with the surface at RT for 30 min and the change in thickness was monitored in dynamic mode. Subsequently, the protein solution was removed and replaced by PBS II and a single scan was taken to determine the final thickness. The experiments were run at least in duplicate and mean and standard deviation were calculated. In addition, the measured samples were taken for WCA measurements to investigate the change in wettability upon FN adsorption.

3.4.4   Scanning electron microscopy (SEM)

The morphology of PS-NP masks of different size and the resulting hexagonal arranged nanostructures as well as of adherent human dermal fibroblasts (HDF, Promocell, Heidelberg, Germany) was investigated by scanning electron microscopy (SEM). Here, the Philips ESEM XL 30 FEG (Eindhoven, Netherlands) was used to investigate the samples in high vacuum (p = 10^{-6} mbar) or environmental SEM mode (ESEM, p = 1 - 10 mbar).

The PS-NP masks and corresponding nanostructures were investigated in high-vacuum SEM mode. Since gold was used for the design of the nanostructures, no additional conducting layer had to be introduced.

Adhesion of HDF was performed according to section 3.5.1. The nanostructured samples have been modified with OEG silane and MUDA to allow specific interaction of the cells with the designed nanostructures. Further, the samples were incubated with 2 μg mL^{-1} FN and 1 mL of a suspension with 25,000 cells mL^{-1} without FBS was added to each well. After 4 h incubation, the culture medium was removed and the samples were washed with PBS III twice. Adherent HDF were fixed with 2.5% (v/v) glutaraldehyde in PBS III at 4°C overnight. After removing the fixing solution and rinsing the samples with PBS III thrice, they were dehydrated with ethanol of elevating concentrations for 15 min each: 10% (twice), 30%, 50%, 70%, 90%, 96% (all once) and dried ethanol (twice). Additionally, the samples were dried with a mixture of hexamethyldisilazane (HMDS) in ethanol (dried) at the following ratios for 15 min each: 1:2, 2:1 and pure HMDS. Finally, after removing HMDS the samples were allowed to dry in air and stored in a desiccator until further use. All dehydration and drying steps were performed at RT and the samples were investigated with the ESEM mode.

3.4.5 Atomic force microscopy (AFM)

Unmodified and PEM modified nanostructures were investigated with atomic force microcopy (AFM). Here, the AFM Nano-R® (Pacific Nanotechnology Inc., Santa Clara, USA) was used in close contact mode and all scans were performed in environmental atmosphere with air as ambience. Further, cantilevers of AppNano (Applied Nanostructures Inc., Santa Clara, USA) were used for imaging, of which specifications are listed in Table 3.5. At least three images of (10x10) μm², (5x5) μm², and (2x2) μm² were recorded per sample using a scan rate of 0.2 Hz as well as a resolution of (512x512) pixel². Image analysis was conducted using an evaluation copy of a full working version of SPIP® (version 6.0.13, Image Metrology A/S, Hørsholm, Denmark).

Table 3.6 - AFM tip specifications based on the information of AppNano

Material:	Si, N-type, 0.01 - 0.025 Ω cm^{-1}
Cantilever:	L: 125 μm W: 35 μm T: 4.5 μm
Tip radius:	<10 nm H: 14 - 16 μm
Frequency:	f = 200 - 400 kHz
Spring constant:	k = 25 - 75 N m^{-1}
Coating:	none

3.4.6 Confocal laser scanning microscopy (CLSM)

First, confocal laser scanning microscopy (CLSM, LSM710, Carl Zeiss, Jena, Germany) was used to quantify the intensity of FITC-FN adsorbed on planar surfaces modified with SAM to compare the passivation effectiveness. Thus, 0.5 mL of a 50 μg mL^{-1} solution of FITC-FN was added to each well of a 24-well-plate, where samples of plain silicon, OEG-modified silicon, mPEG-urea modified silicon as well as Thermanox® slides have been placed. The adsorption of FITC-FN was terminated after 1 h incubation at 37°C and all samples were rinsed with PBS II, ultrapure water, and mounted to object holders with Mowiol. The experiment was run in duplicate and five images per sample were recorded at constant software settings. Afterwards, the data was quantified defining two regions of interest (ROI) at the same area per image and calculating mean, standard deviation and analysis of variance (ANOVA). Further, Box-Whisker-diagrams are shown where appropriate. The box indicates the 25th and 75th percentile, the median (dash) and mean value (black square), respectively, whereas the 95-5% confidence interval is represented by the whiskers.

In addition, CLSM was used to investigate the backfilling success of nanostructured surfaces with mPEG-urea and the activation of the nanostructures with MUDA to allow specific

interaction of proteins and cells preferably with the designed patterns. For this reason, nanostructured samples modified with mPEG-urea and MUDA were incubated in a 12-well-plate with 1 mL of a 50 μg mL^{-1} FITC-FN solution in PBS II at 37°C for 1 h. After rinsing the samples with PBS II and ultrapure water, they were mounted to object holders with Mowiol, dried at 4°C overnight and investigated with a 63x oil immersion objective. The experiments were run in duplicate collecting five images per sample and the software settings were kept constant for all samples for comparative reasons.

Finally, CLSM was used to monitor the PEM formation on nanostructured surfaces as previously described in section 3.3.2.3. However, unlabeled HEP was replaced by fluorescein-labeled HEP and the pH was kept at pH 7.4 without changing the other process parameters. After PEM formation was finished, the samples were dried with a stream of nitrogen, mounted with Mowiol to object holders, dried at 4°C overnight and examined with a 63x oil immersion objective. Again, five images per sample were recorded without changing the software parameters and PEM assembled on plain silicon were used as reference.

3.5 Biological studies

3.5.1 Cell culture conditions

HDF were used to study the influence of the above-mentioned biomaterial surface modifications on cellular processes, such as adhesion, proliferation or FN matrix formation. The cells were grown in Dulbecco's modified Eagle's medium (DMEM) supplemented with 10% fetal bovine serum (FBS), 1% antibiotic-antimycotic solution (AAS) 37°C in a humidified 5% CO_2/ 95% air atmosphere using a NUAIRE® DH Autoflow incubator (NuAire Corp., Plymouth, USA). Cells of sub-confluent cultures were harvested with 0.25% trypsin/ 0.02% ethylene-diaminetetraacetic acid (EDTA) at 37°C for 5 min. The trypsin was inactivated with DMEM containing 10% FBS. After centrifugation at 250xg and RT for 5 min, the cells were resuspended in DMEM and seeded on the different samples at a density of 25,000 cells mL^{-1}. Short-term culture (4 h) was performed with serum-free DMEM, whereas for long-term culture (24 h and longer) the cell culture medium was supplemented with 10% FBS.

3.5.2 Cell adhesion

The adhesion of cells was investigated on planar control surfaces, nanostructured surfaces and nanostructures modified with PEM of PEI and HEP. Since proteins have a promoting effect on cell adhesion processes, comparative studies were conducted to investigate the influence of protein-free and protein-containing surfaces on the adhesion cascade. Hence, part of the samples was pre-coated with human FN. The samples were placed in a 12-well-plate and one half of the modified samples were incubated with 1 mL of a 2 μg mL^{-1} solution of human FN in PBS II at 37°C for 1 h, while the other half was incubated with PBS II only and used as reference. After rinsing all samples with PBS II twice, 1 mL of a cell suspension with 25,000 cells mL^{-1} was added to each well and the cells were incubated at 37°C for 4 h. Afterwards, adherent cells were visualized with live cell staining or immunocytochemistry. Live cell staining was performed incubating adherent HDF with a 1 μM solution of CellTracker® Red in serum-free DMEM pre-warmed to 37°C for 30 min. Subsequent, the staining solution was replaced with fresh DMEM and the cells were incubated at 37°C for another 30 min before they were investigated with CLSM. Afterwards, the medium was removed and the cells were washed once with pre-warmed PBS II to remove non-adherent cells. The remaining cells were fixed with a 4% paraformaldehyde solution (RotiHistofix®) at RT for 15 min and washed with PBS II three times. Thereafter, fixed HDF were permeabilized with 0.1% (v/v) triton X-100 for 10 min and again rinsed with PBS II three times. Non-specific binding sites were blocked with a 1% bovine serum albumin (BSA) solution in PBS II at RT for 1 h. Filamentous actin was stained with BODIPY® phalloidin (1:50, v/v). The nucleus was stained with TO-PRO®3 (1:500, v/v) and focal adhesion complexes were visualized with a

primary mouse antibody raised against vinculin (1:100, v/v) and a CY2-conjugated secondary anti-mouse antibody (1:100, v/v). All dyes and antibodies were diluted in PBS II containing 1% BSA and labeling was performed at RT for 30 min. The samples were washed with PBS II after each staining step and with ultrapure water after the last washing to avoid salt crystal formation. Finally, all samples were mounted with Mowiol containing 25 mg mL^{-1} 1,4-diazabicyclo-(2,2,2)-octane (DABCO) to object holders. Finally, CLSM imaging was used to determine the cell count with low magnification objectives (10x) and cell morphology, such as cell area and aspect ratio, with higher magnification objectives (20x, 63x oil immersion). ZEN (2011) and ImageJ (version 1.46r) were used to quantify the data of at least duplicate experiments and five images per sample. Mean, standard deviation and ANOVA were calculated and indicated in the respective figures. Further, Box-Whisker-diagrams are shown where appropriate. The box indicates the 25th and 75th percentile, the median (dash) and mean value (black square), respectively, whereas the 95-5% confidence interval is represented by the whiskers.

3.5.3 Fibronectin matrix formation

HDF have the ability to secrete their own matrix with persistent culture time. Therefore, the formation of the FN matrix on planar and nanostructured surfaces was investigated using immunocytochemistry. First, samples of interest were placed to a 12-well-plate and 1 mL of cell suspension with a density of 25,000 cells mL^{-1} in serum-free DMEM was added to each well and the cells were allowed to adhere for 24 h. Immunocytochemistry was performed as described above. Briefly, after rinsing the cells with pre-warmed PBS II adherent cells were fixed with 4% paraformaldehyde solution (RotiHistofix®) at RT for 15 min and washed with PBS II three times. After permeabilization (0.1% (v/v) triton X-100, 10 min) and PBS II rinsing (three times), non-specific binding sites were blocked with a 1% BSA solution in PBS II at RT for 1 h. Again, filamentous actin was stained with BODIPY® phalloidin (1:50, v/v) and the nucleus was stained with TO-PRO®3 (1:500, v/v). However, the FN matrix was visualized with a primary mouse antibody raised against human FN (1:200, v/v) and a CY2-conjugated secondary anti-mouse antibody (1:200, v/v). All dyes and antibodies were diluted in PBS II containing 1% BSA and labeling was performed at RT for 30 min. The samples were washed with PBS II after each staining step and with ultrapure water after the last washing to avoid salt crystal formation. Finally, all samples were mounted with Mowiol containing 25 mg mL^{-1} DABCO to object holders and examined with CLSM using a 63x oil immersion objective. Qualitative image analysis was performed again with ZEN software.

3.5.4 Cell proliferation

In contrast to cell adhesion studies, cell proliferation was performed using serum-containing DMEM. Again, 1 mL of a cell suspension with 25,000 cells mL^{-1} was added to each sample in a 12-well-plate and the cells were allowed to proliferate for 1 d, 3 d, and 7 d. Since all used samples are non-transparent, again immunocytochemistry was used as described above to visualize the cells. In brief, the cells were rinsed with pre-warmed PBS II and fixed with 4% paraformaldehyde solution (Roti® Histofix) for 15 min at RT. After washing (PBS II, three times), permeabilization (0.1% (v/v) triton X-100, 10 min), and washing (PBS II, three times), non-specific binding sites were blocked with a 1% BSA solution in PBS II at RT for 1 h. Again, filamentous actin was stained with BODIPY® phalloidin (1:50, v/v), the nucleus was stained with TO-PRO®3 (1:500, v/v) and focal adhesion complexes were visualized with a primary mouse antibody raised against vinculin (1:100, v/v) and a CY2-conjugated secondary anti-mouse antibody (1:100, v/v). All dyes and antibodies were again diluted in PBS II containing 1% BSA and labeling was performed at RT for 30 min. The samples were washed with PBS II after each staining step and with ultrapure water after the last washing to avoid salt crystal formation. Finally, all samples were mounted with Mowiol containing 25 mg mL^{-1} DABCO to object holders. The stained cellular structures were monitored with CLSM and cell count and morphology of at least duplicate experiments and five images per sample were again quantified by image examination with ZEN and ImageJ. Statistical analysis was applied calculating mean, standard deviation and ANOVA, which are indicated in the respective figures. Further, Box-Whisker-diagrams are shown where appropriate. The box indicates the 25th and 75th percentile, the median (dash) and mean value (black square), respectively, whereas the 95-5% confidence interval is represented by the whiskers.

4   Results

This section is separated into subsections, where surface characteristics of planar, nanostructured, and nanostructured materials modified with PEM are described using various physicochemical, topographical, and microscopical analytical methods. In addition, the interaction of mammalian cells with each single system is monitored in terms of adhesion and proliferation using immunocytochemical methods. Based on existing knowledge of material-cell-interaction, a control of cellular processes using topographical and chemical stimuli is aimed and defined.

4.1   Planar surfaces

4.1.1   Assessment of antifouling properties

4.1.1.1   Protein adsorption

The efficiency to inhibit single protein adsorption of SAM containing short- (n_{PEG} = 6-9) and long-chain PEG units (n_{PEG} = 43) was investigated *in situ* by scanning ellipsometry and the change in thickness of the protein layer upon adsorption of human plasma FN is depicted in Figure 4.1. The thickness increase of the protein layer was highest on unmodified silicon dioxide. Here, FN of different concentrations led to an averaged absolute layer thickness of >1.5 nm per adsorption step. However, with increasing FN concentration the change in layer thickness became less prominent due to the saturation of the surface with protein.
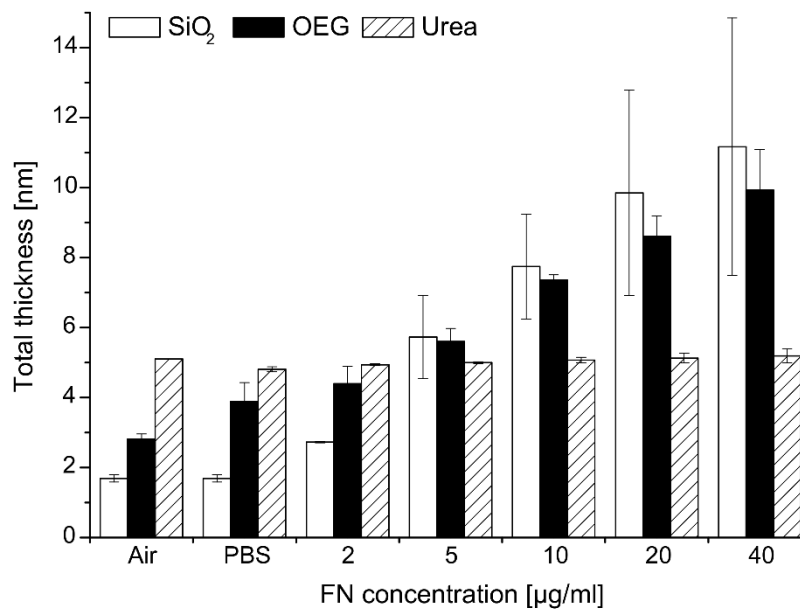
Figure 4.1 - Change in total thickness upon adsorption of different concentrations of FN on plain silicon dioxide (white) and silicon dioxide modified with either oligo (ethylene glycol) (OEG, black) or mPEG-urea (Urea, hatched).

In contrast, the slope of layer thickness increase on the short-chain SAM (OEG) was lower compared to silicon dioxide. Initially, the introduction of PBS led to an increase in layer thickness possibly due to a change in RI. In addition, the sequential exposure of the substrate to increasing FN concentrations led to an enlarged layer thickness indicating incomplete antifouling properties of the OEG-SAM. However, the averaged absolute thickness change was <1 nm per adsorption step. In comparison to silicon dioxide and OEG-SAM, the long-chain SAM (Urea) prevented the adsorption of FN very efficiently. Initially, the thickness did not change upon contact with PBS. Further, the total layer thickness was almost constant after addition of increasing FN concentrations. Here, the absolute layer thickness changed <0.1 nm per adsorption step, which clearly indicates the antifouling properties of mPEG-urea.

4.1.1.2 Protein desorption

In addition to scanning ellipsometry, adsorption to and, especially, desorption from plain and modified planar surfaces of a single protein was investigated using FITC-labeled FN (Figure 4.2). CLSM was used here to determine the fluorescence intensity of adsorbed FN and to compare the antifouling properties of the different planar surfaces. Similar to scanning ellipsometry it was found here, that protein adsorption was highly impaired on the long-chain SAM (Urea) indicated by the lowest intensity values (Figure 4.2A). In contrast, highest intensities were found on TCPS, which was chosen as an additional reference to compare a less hydrophilic surface with highly hydrophilic surfaces. Interestingly, the amount of adsorbed FN on plain silicon dioxide and silicon dioxide modified with the short-chain SAM (OEG) was statistically not significant, exhibiting equal intensity values. However, the differences in intensity values of all other surfaces were significantly different.

Additionally, the amount of desorbed FITC-labeled FN from planar surfaces in dependence on the protein concentration was determined fluorometrically (Figure 4.2B). The largest amount of FN was desorbed from the intermediate wettable TCPS that also had the highest adsorbed amounts previously detected by CLSM studies. Here, the protein amounts were always highest at different FN concentrations. Again, urea-modified surfaces showed the lowest values of desorbed protein, similar to the intensity studies. However, a complete absence of desorbed protein was not observed. Interestingly, less amounts of FN were desorbed from plain silicon dioxide in comparison to the OEG-modified surfaces at concentrations up to 20 μg mL^{-1}. However, at the highest FN concentration of 40 μg mL^{-1} the values of desorbed protein exceeded even the values of TCPS. Finally, an equilibrium adsorption was observed on most surfaces at FN concentrations of 40 μg mL^{-1}. Since these investigations revealed a strong resistance of the long-chain SAM (Urea) to single protein adsorption, subsequent studies not including PEM focused on the design of nanopatterns sandwiched by these long-chain SAM.
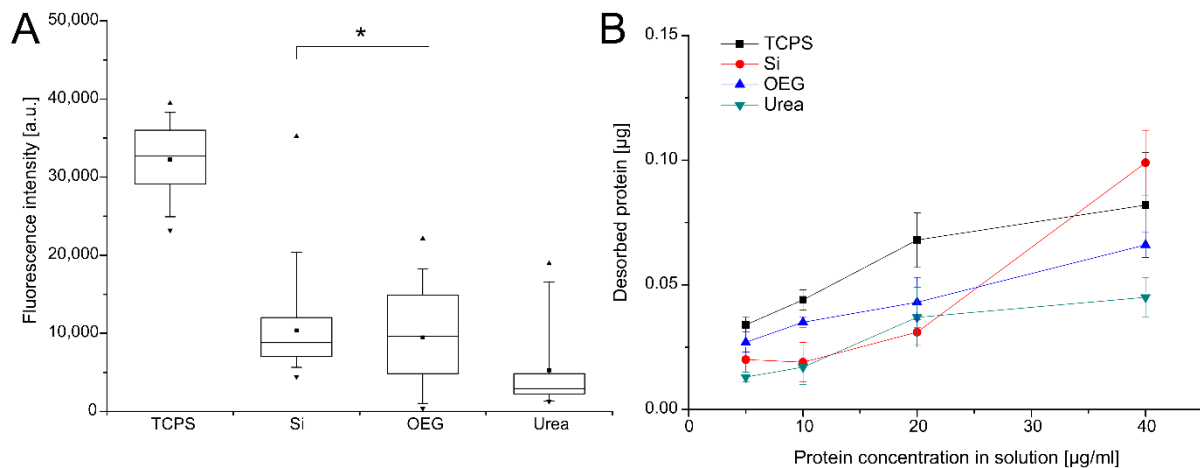
Figure 4.2 - Adsorption and desorption of FITC-FN to unmodified and modified planar surfaces. The fluorescence intensities (A) after adsorption of 50 μg mL^{-1} FITC-FN were calculated via image analysis (p < 0.05), whereas the amount of desorbed protein (B) was measured fluorometrically after adsorption of different FITC-FN concentrations. The asterisk in (A) indicates *no* significant difference, while all other values are significantly different. [TCPS - tissue culture polystyrene, Si - silicon dioxide, OEG - silicon dioxide with oligo (ethylene glycol), Urea - silicon dioxide with mPEG-urea]

4.1.2 Surface characteristics

4.1.2.1 Atomic force microscopy (AFM)

AFM was used to investigate the surface topography of plain and SAM-modified silicon dioxide. Unmodified silicon was smooth with no surface irregularities (Figure 4.3). However, the formation of short-chain SAM led to a change in surface appearance, showing clusters in the nanoscale on the surface. Nevertheless, the *z*-scale did not change significantly here, which was the case for silicon dioxide modified with long-chain SAM. There, the *z*-scale more than doubled in comparison to the other surfaces. Anyway, cluster formation was unexpectedly less prominent in comparison to the short-chain SAM.
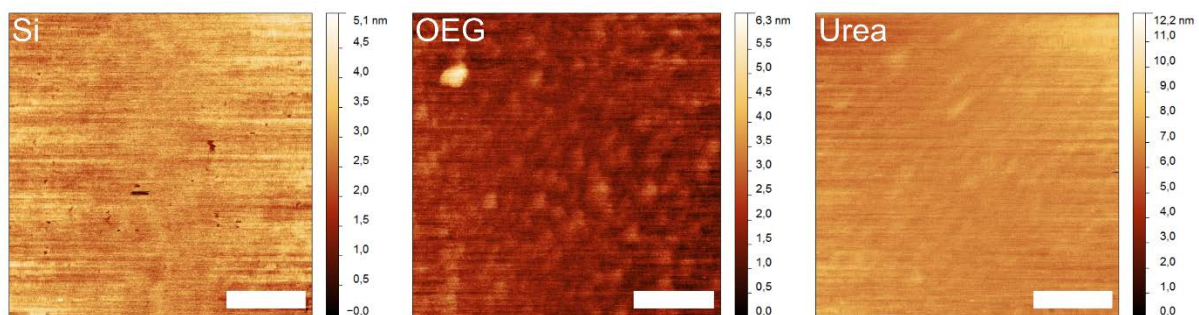
Figure 4.3 - AFM images of planar silicon (left) and silicon modified with either oligo (ethylene glycol) (OEG, middle) or mPEG-urea (Urea, right) [Scale: 200 nm, scan size: 0.77x0.77 μm²]

4.1.3 Polyelectrolyte multilayer formation

PEM formation on planar surfaces was monitored by CLSM analysis using fluorescein-labeled HEP during multilayer assembly to get insight in the evolution of the PEM thickness. Figure 4.4 displays images taken after each adsorbed PEL layer. However, the primary PEI layer is not shown since no fluorescently active molecule was present. The adsorption of fluorescein-labeled HEP, which pH value was adjusted to pH 7.0, led to an increase in fluorescence intensity (left column), while the adsorption of a successive PEI layer always led to a decrease in intensity (right column). Nevertheless, the intensity evolution was stronger than the regression, indicating a consistent PEM formation.
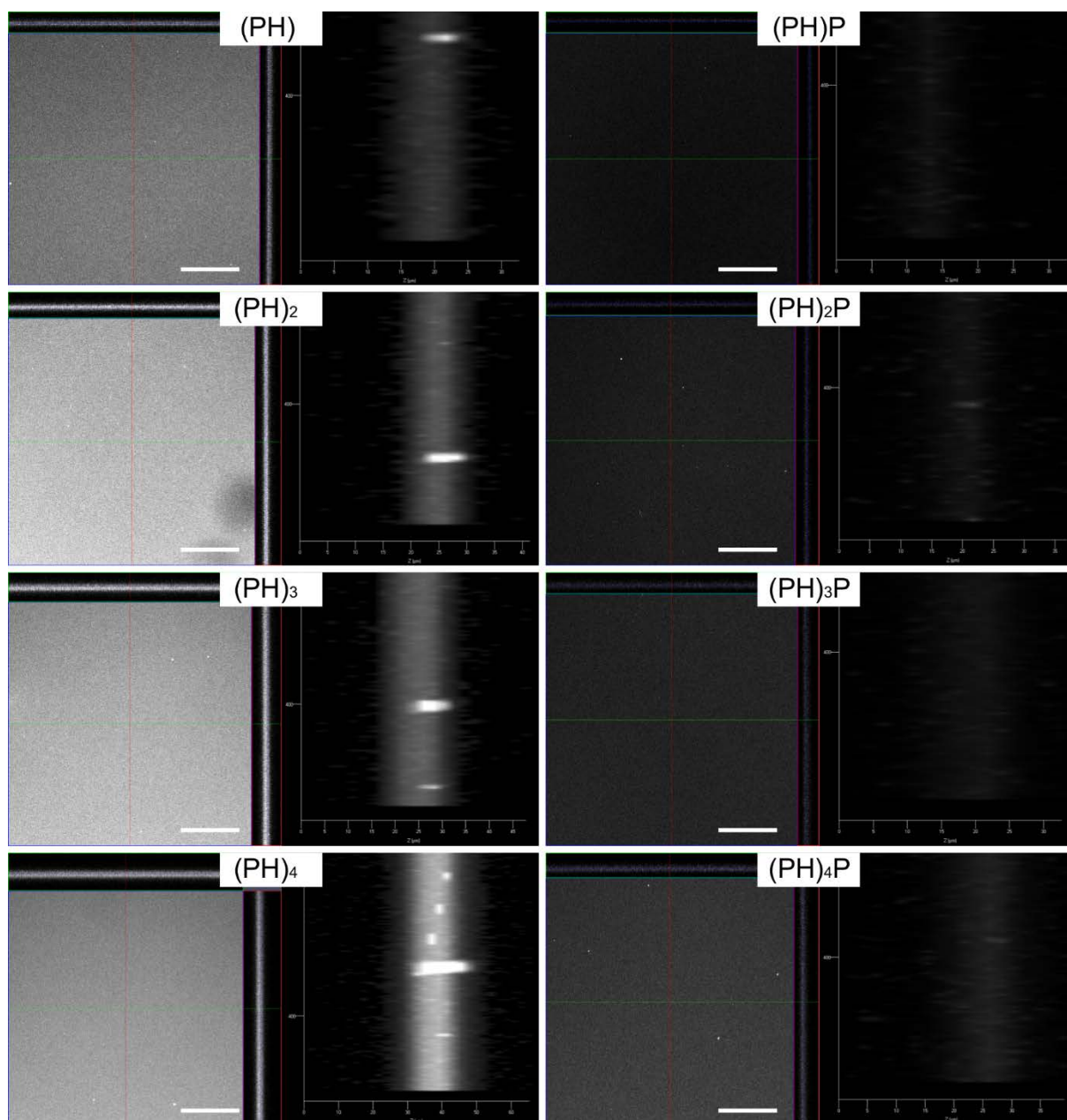
Figure 4.4 - PEM formation on planar silicon dioxide using fluorescein-labeled HEP. Fluorescence intensities of terminal HEP layers (left column pair) as well as terminal PEI layers (right column pair) are shown. [Scale: 100 μm]

The progression in apparent layer thickness halted already after the first adsorbed layer and only the intensity was increasing with every addition of HEP, indicating an accumulation of molecules within the PEM structure, leading to more intermingled layers. Further, the calculated thickness after the final layer did not reflect the apparent thickness due to emission artefacts. However, it can be concluded from Figure 4.5 that the adsorption of HEP seemed to follow an exponential growth regime, whereas the adsorption of PEI was linear, revealed by CLSM analysis of various regions of interest on several images.
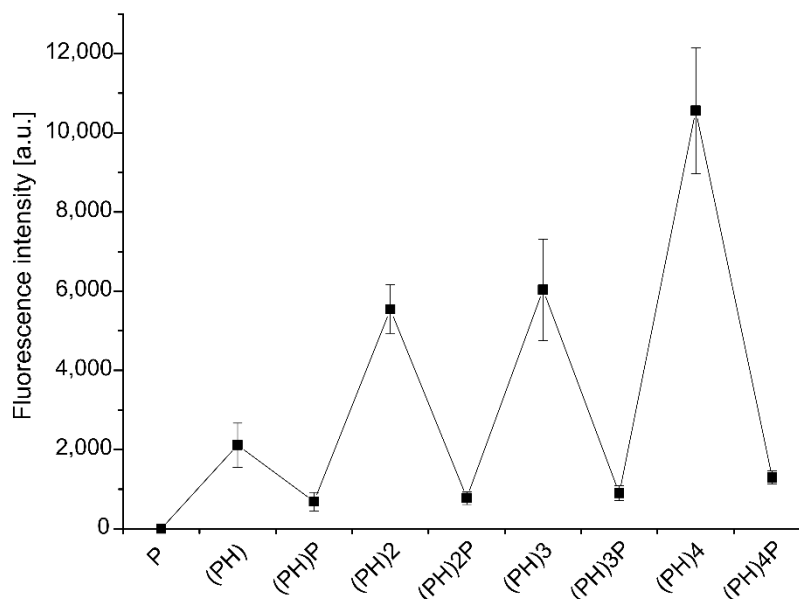
Figure 4.5 - Change in fluorescence intensity upon alternating adsorption of HEP (H) and PEI (P) on planar silicon dioxide. The pH value of the HEP solution was adjusted to pH 7.0, while the pH of the PEI solution was not controlled. The intensities were calculated by CLSM image analysis (n = 25).

4.1.4   Surface wettability

4.1.4.1   Static water contact angle (WCA)

Figure 4.6 represents the static WCA of differently modified planar surfaces. Clean silicon dioxide was highly hydrophilic, exhibiting WCA of $\theta = (24.7 \pm 1.2)°$. In contrast, plain gold had an intermediate wettability, presenting WCA of $\theta = (59.1 \pm 6.5)°$. The formation of SAM with different terminating groups influenced the wettability on all planar surfaces. The coupling of short- (OEG, black bars) or long-chain SAM (Urea, hatched bars) to planar silicon dioxide rendered the surfaces less hydrophilic. However, no significant differences were found here. In addition, the coupling of MUDA increased the hydrophilicity of plain gold, which WCA dropped to $\theta = (33.7 \pm 6.7)°$.

56
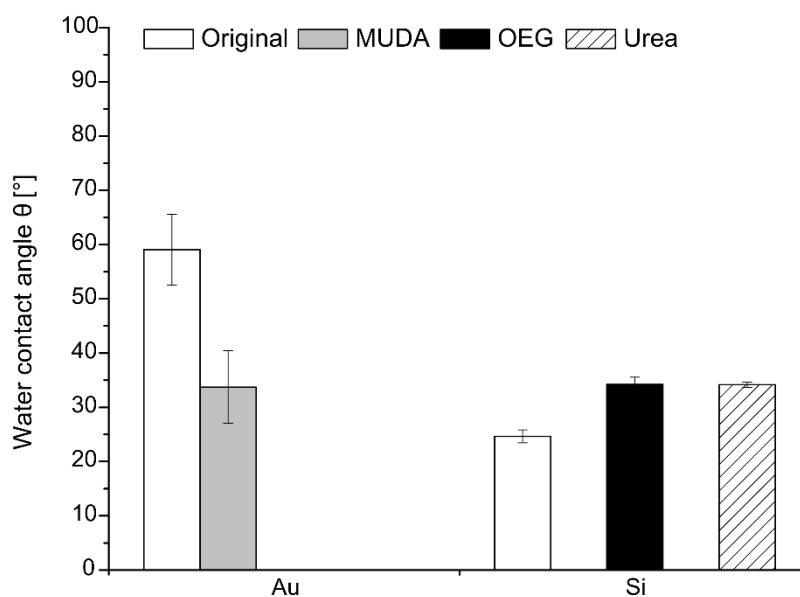
Figure 4.6 - Static WCA on planar surfaces, which have been modified either with oligo (ethylene glycol) (OEG, black) or mPEG-urea (Urea, hatched) as well as with mercaptoundecanoic acid (MUDA, gray).

4.1.4.2 Dynamic WCA

Dynamic WCA measurements were used to record the advancing (θ_a) and receding (θ_r) WCA and to determine the WCA hysteresis ($\Delta\theta$), which was calculated according to Equation 3.8. The advancing WCA on planar surfaces reflected the results obtained with static WCA measurements (Figure 4.7, white bars). However, the WCA hysteresis revealed differences in the surface composition (hatched bars). It was higher on plain gold in comparison to plain silicon dioxide. Anyway, the receding WCA (black bars) on silicon dioxide was much lower than that of plain gold. The coupling of MUDA led to a drop in advancing and receding WCA of gold, but with no significant difference in WCA hysteresis in comparison to unmodified gold since advancing and receding WCA decreased to the same extent. In contrast, an explicit difference in WCA hysteresis was found on silicon dioxide after modification with either OEG- or mPEG-urea SAM. Here, it was higher on the short-chain SAM, even though the terminal headgroup was the same ($-CH_3$).
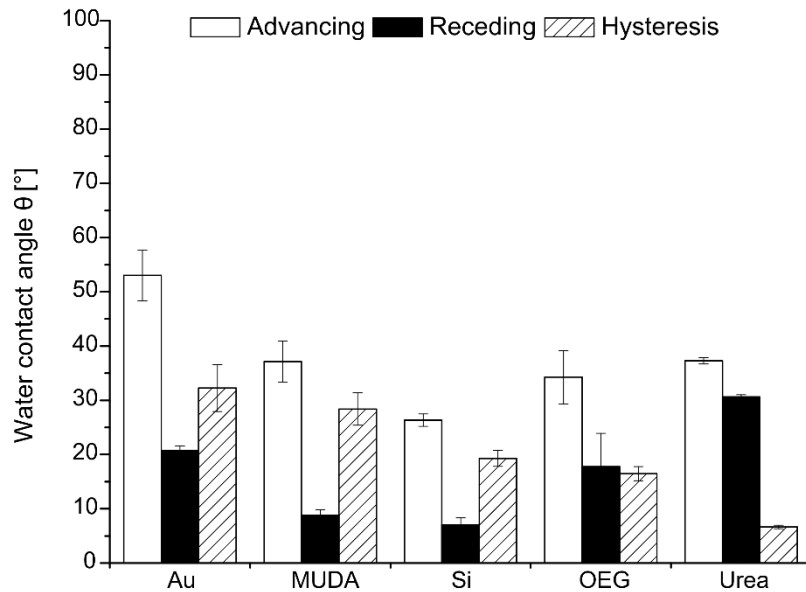
Figure 4.7 - Dynamic WCA on planar surfaces. Advancing (white bars) and receding WCA (black bars) as well as the WCA hysteresis (hatched bars) are shown for the differently modified surfaces. [Au - gold, MUDA - gold with mercaptoundecanoic acid, Si - silicon dioxide, OEG - silicon dioxide with oligo (ethylene glycol), Urea - silicon dioxide with mPEG-urea]

4.1.4.3 Static WCA after protein adsorption

As described in section 4.1.1.1, it was found that layer thickness of a single protein was influenced by the antifouling properties of the surface. In addition to that, the amount of adsorbed protein also influenced the surface wettability of the differently modified surfaces (Figure 4.8). The adsorption of FN to silicon dioxide, a naturally hydrophilic material ($\theta \sim 25°$), drastically changed its wettability, rendering the surface hydrophobic ($\theta \sim 70°$), indicating a stable adsorbed protein layer, which could also not be removed with several PBS rinsing steps. In contrast, OEG-SAM was less hydrophilic ($\theta \sim 42°$) than silicon dioxide. Furthermore, the wettability decreased after FN adsorption ($\theta \sim 65°$) as well; supporting the results of scanning ellipsometry, that protein adsorption could not be inhibited completely. Increasing the chain length ($n_{PEG} = 43$) effectively decreased the amount of adsorbed protein, indicated by a stable wettability ($\theta \sim 30°$) before and after contact to FN.
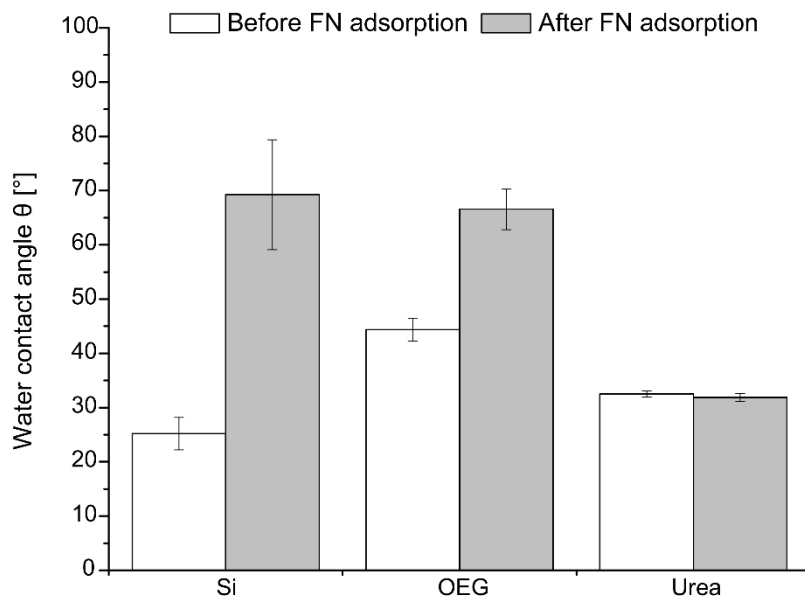
Figure 4.8 - Static WCA on plain silicon dioxide and silicon dioxide modified with either oligo (ethylene glycol) (OEG) or mPEG-urea (Urea) before and after FN adsorption of different concentrations.

4.1.4.4 Static WCA after polyelectrolyte multilayer formation

Static WCA measurements were applied to investigate the wettability of a PEM system consisting of HEP and PEI, assembled at different pH conditions.
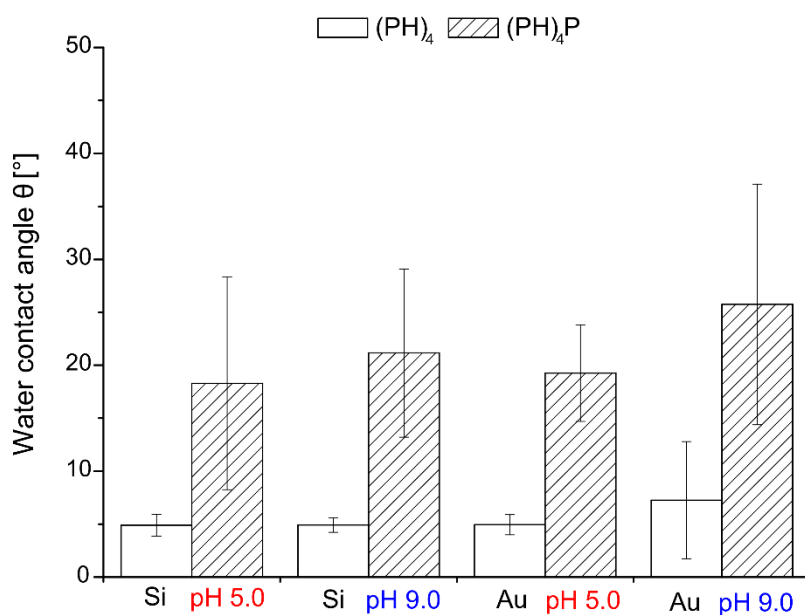
Figure 4.9 - Static WCA on planar surfaces modified with PEM of HEP (H) and PEI (P). WCA are shown for the terminal HEP (white bars) and PEI layer (hatched bars) formed at either pH 5.0 or pH 9.0.

59

Figure 4.9 shows that silicon dioxide as well as gold surfaces were hydrophilic after PEM formation, but with obvious differences dependent on the terminal layer. First, surfaces terminated with HEP assembled at pH 5.0 were highly hydrophilic, no matter if silicon or gold was used as substrate. Further, the change of the pH value of the HEP solution to pH 9.0 did not decrease the wettability on silicon, but on gold surfaces. Surfaces terminated with PEI were less hydrophilic in comparison to HEP layers. Here, a clear difference was found in dependence on the pH value. Terminal PEI layers formed at acidic conditions were slightly more hydrophilic than PEM assembled at pH 9.0, no matter which substrate was chosen.

4.1.4.5 Dynamic WCA after polyelectrolyte multilayer formation

Dynamic WCA recording was used to identify difference in the surface chemistry and heterogeneity. However, dynamic recording of PEM with HEP as terminal layer was not assessable due to their highly hydrophilic nature, no matter at which pH condition. Hence, only dynamic WCA of the terminal PEI layer are depicted in Figure 4.10. The advancing WCA (white bars) were similar to the static ones, independent of the pH value of the HEP solution. The WCA hysteresis (hatched bars) on silicon dioxide was higher at pH 5.0, whereas it was higher at pH 9.0 on gold as substrate.
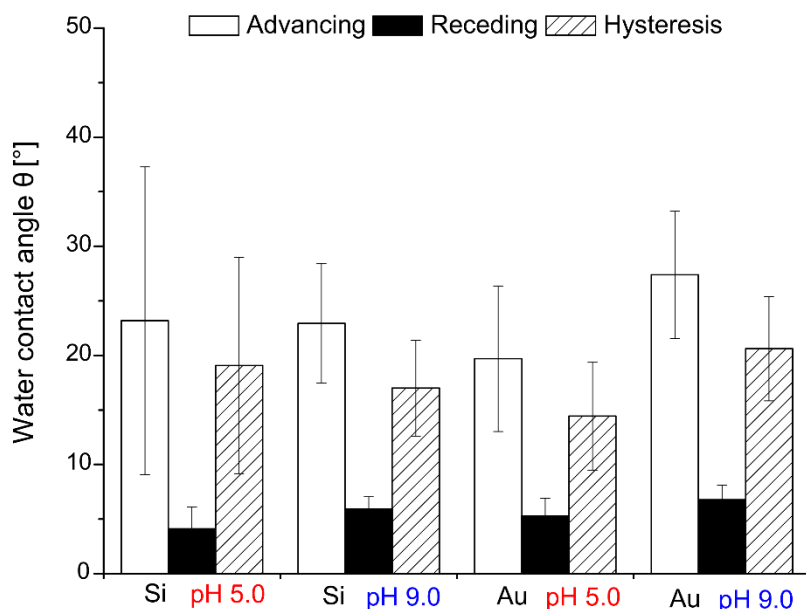
Figure 4.10 - Dynamic WCA on planar surfaces modified with PEM of HEP and PEI at either pH 5.0 or pH 9.0. Advancing (white bars) and receding WCA (black bars) as well as the WCA hysteresis (hatched bars) are shown only for the terminal PEI layer since the WCA on the terminal HEP layers was not detectable.

4.1.5　Cellular response to planar surfaces

4.1.5.1　Cell adhesion

The adhesion of HDF to planar control surfaces (Figure 4.11) was investigated after 4 h of cell culture under protein-free conditions with and without preadsorption of 2 μg mL^{-1} FN. The cells were stained for cellular structures such as nucleus, actin cytoskeleton and vinculin in focal adhesions (FA) using immunocytochemistry. Differences in cytoskeleton organization and FA formation were found in dependence on the surface chemistry as well as culture conditions. Under protein-free conditions, HDF seeded on gold or silicon dioxide expressed longitudinal actin fibers and FA in the periphery of the cell body. Further, FA formation and actin stress fibers were absent on MUDA-modified gold or short- (OEG) and long-chain SAM (Urea) on silicon dioxide. However, after preadsorption of FN a very different behavior was observed. Cells started to express FA in the periphery and the center of the cell body and actin stress fibers were organized in bundles circumferentially on gold, MUDA-modified gold and silicon dioxide. In contrast, cells seeded on the long-chain SAM (Urea) did not adhere to the same extent if compared to all other control surfaces. Moreover, most of these cells were lost during the staining and washing procedures required for immunofluorescence staining. However, in the few cells found FA formation as well as actin organization was absent, indicating the protein and cell repellent properties of the surface. In contrast, cells seeded on the short-chain SAM (OEG) expressed FA and organized the cytoskeleton in a similar fashion as on the other control surfaces.

Quantitative image analysis revealed that the cell count was not significantly different on gold or MUDA-modified gold under protein-free and FN conditions (Figure 4.12A). However, significantly more cells attached to OEG-SAM after preadsorption of FN if compared to protein-free conditions, indicating lower protein repellent properties. In contrast to all other planar surfaces, no cells were found on silicon dioxide modified with the long-chain SAM (Urea). Cells attached to planar control surfaces spread significantly more when the surfaces have been pre-coated with FN, which resulted in larger projected cell areas (Figure 4.12B) and increased aspect ratios (Figure 4.12C). Nevertheless, significant differences in cell area were only found between gold and OEG after FN adsorption. Interestingly, cells on OEG spread to the highest extent, which also was confirmed by aspect ratio analysis.
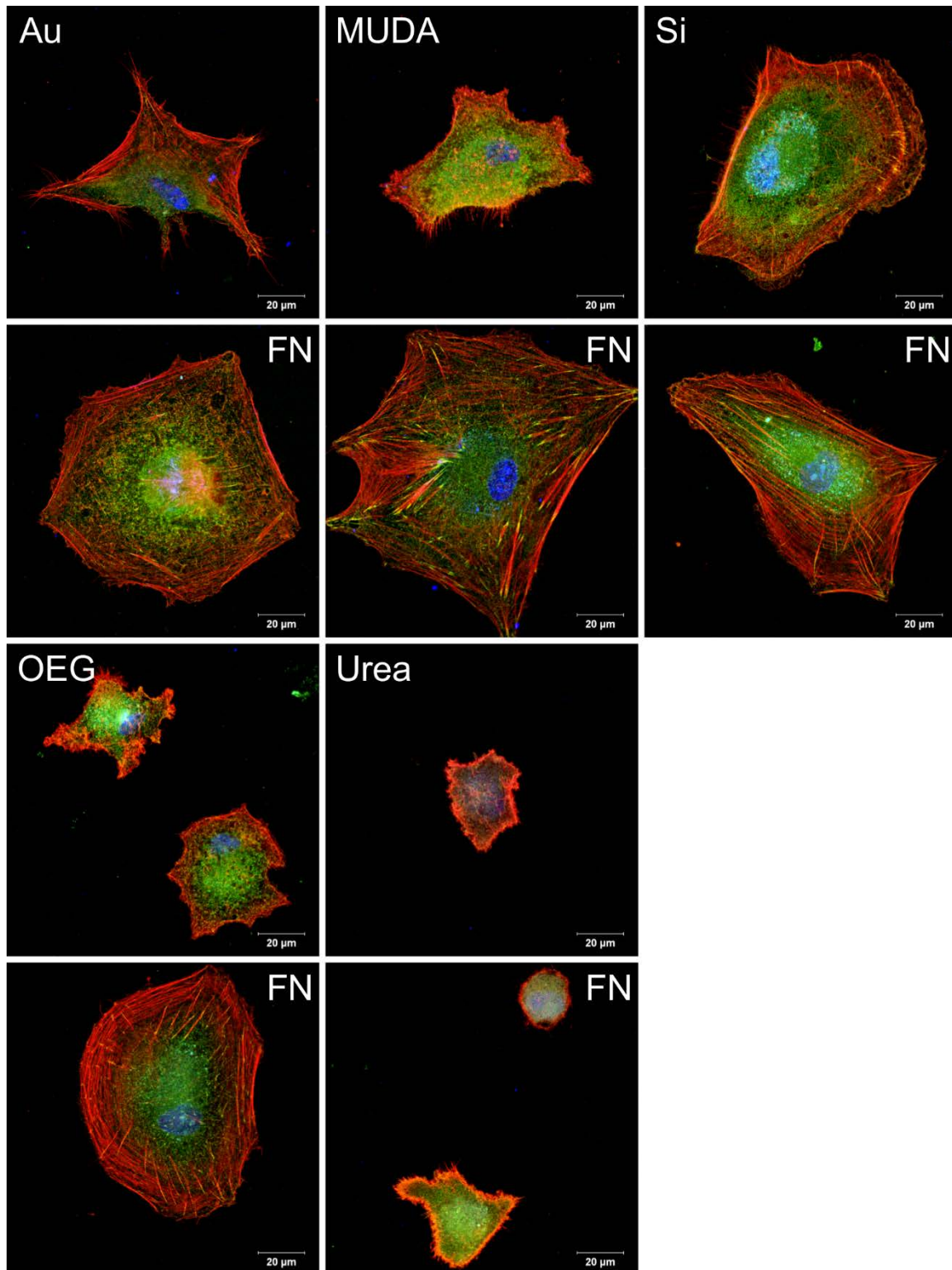
Figure 4.11 - CLSM images of HDF adherent on planar control surfaces either without (1st and 3rd row) or with preadsorption of 2 μg mL^{-1} FN (2nd and 4th row) after 4 h of incubation. The cells were stained for actin (red), vinculin (green) and nucleus (blue). [TCPS - tissue culture polystyrene, Si - silicon dioxide, OEG - silicon dioxide with oligo (ethylene glycol), Urea - silicon dioxide with mPEG-urea, Au - gold, MUDA - gold with mercaptoundecanoic acid] [Scale: 20 μm]
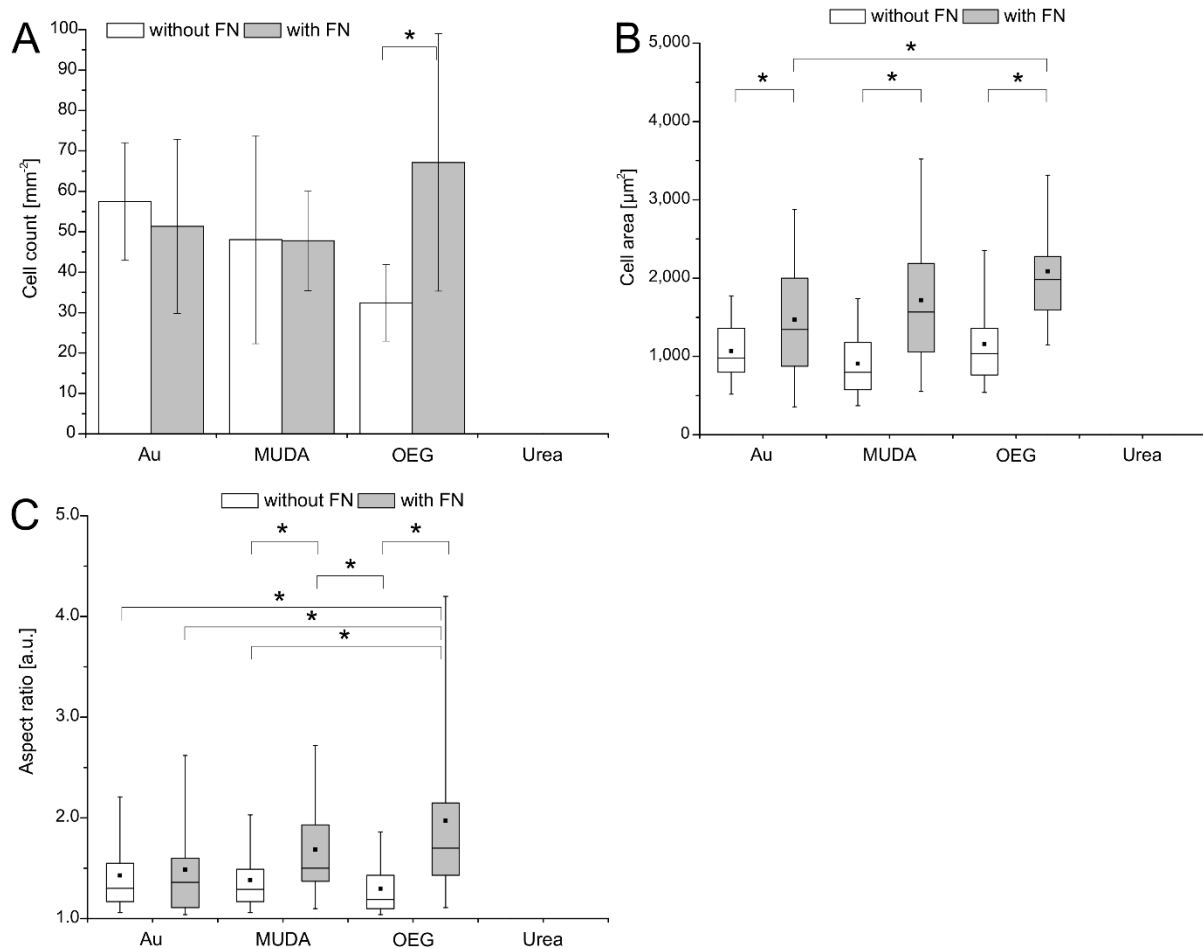
Figure 4.12 - Count (A), area (B), and aspect ratio (C) of cells seeded on planar surfaces either without (open bars) or with preadsorption of 2 μg mL^{-1} FN (gray bars) after 4 h of incubation (p < 0.05). The missing values for urea surfaces are attributed to the absence of adherent cells. Analyses of significant difference (ANOVA) are summarized in Table A.1 due to clarity reasons. [OEG - silicon dioxide with oligo (ethylene glycol) (open bars), Urea - silicon dioxide with mPEG-urea (hatched bars), Au - gold, MUDA - gold with mercaptoundecanoic acid]

4.1.5.2 Fibronectin matrix formation

Since the formation of an extracellular FN matrix is crucial for cell growth and function, it was investigated here if HDF were able to secrete their own matrix in dependence on the surface composition. After 24 h of culture, extracellular FN was visualized using a primary antibody raised against human FN and CLSM analysis. Clear differences in FN matrix formation were found on planar control surfaces (Figure 4.13). Here, cells seeded on plain gold secreted FN to a lower extent if compared to MUDA-modified gold. Additionally, cells seeded on silicon dioxide also were able to organize their own FN matrix. In contrast, HDF attached to the non-ionic hydrophilic short- (OEG) or long-chain SAM (Urea) were not able to synthesize FN in fibrils. However, cells seeded on TCPS were also able to perform FN fibrillogenesis.
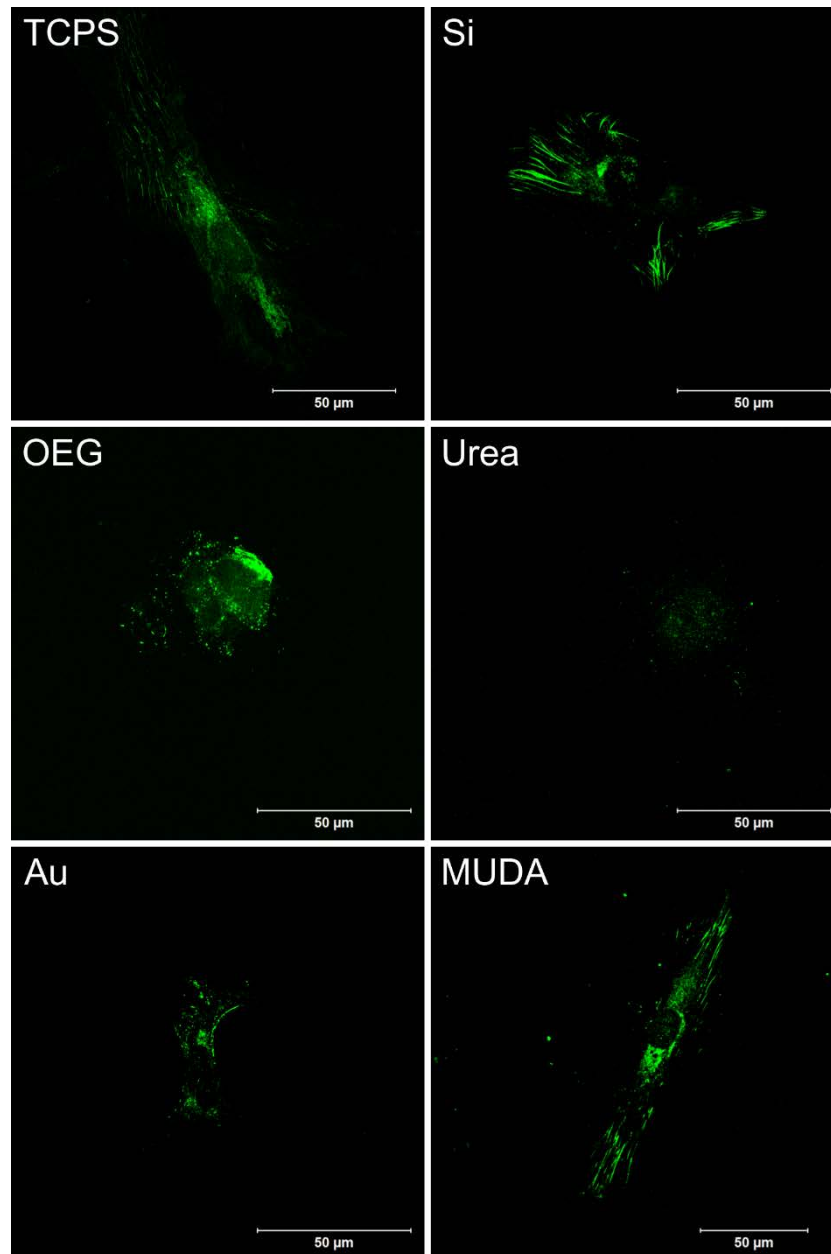
Figure 4.13 - FN matrix formation on planar control surfaces. [TCPS - tissue culture polystyrene, Si - silicon dioxide, OEG - silicon dioxide with oligo (ethylene glycol), Urea - silicon dioxide with mPEG-urea, Au - gold, MUDA - gold with mercaptoundecanoic acid]

4.1.5.3 Cell proliferation

The growth of HDF on planar surfaces was determined over a period of seven days under serum-conditions (Figure 4.14) and with (A) or without (B) preadsorption of FN. The cells maintained a long lag phase and did not proliferate to a high extent up to three days on all surfaces, no matter if FN was present or not. However, after seven days the cell count increased dramatically. Most cells were found on MUDA-modified gold and gold. However, the increase in cell number on MUDA-modified gold was less prominent since the cell count was already twice as high as on gold due to the increased hydrophilicity. Despite being a hydrophilic

material, silicon dioxide did not support cell proliferation to the same extent as gold or MUDA-modified gold. In contrast to that, even on mPEG-urea SAM more cells were present after seven days, which was not expected. Over the course of three days, these layers inhibited the growth of HDF to the highest extent. However, after seven days the cell count suddenly increased. The difference in growth regime was also found in cell morphology. Here, cells significantly spread more in the initial phase when FN was present (Figure A.2 and Figure A.3). However, after seven days of culture the difference was not detectable any longer, which is reasonable due to matrix secretion of cells.
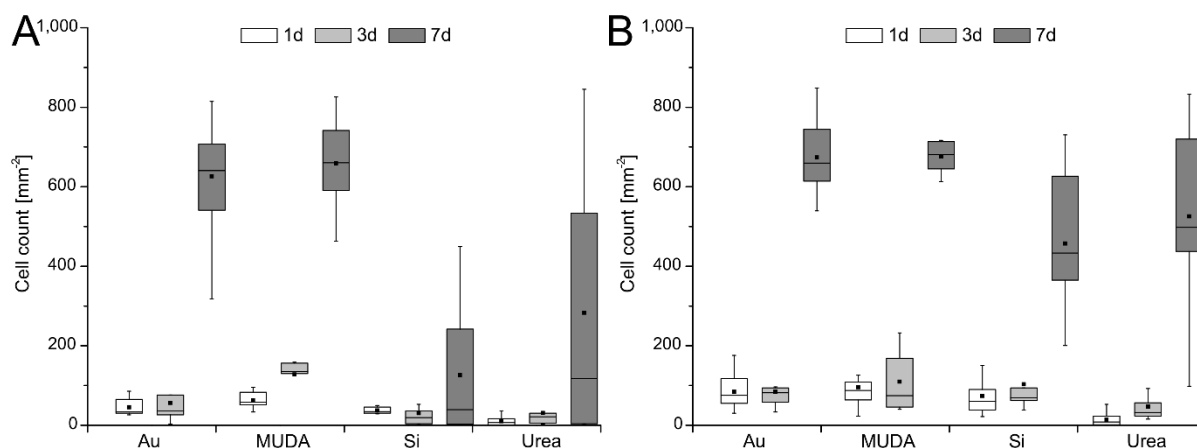
Figure 4.14 - Cell proliferation on planar surfaces either without (A) or with preadsorption of 2 μg mL^{-1} FN (B) after 1 d (open bars), 3 d (light gray bars), and 7 d (dark gray bars) of culture (p < 0.05). Analyses of significant difference (ANOVA) are summarized in Table A.6 and Table A.7 due to clarity reasons. [Au - gold, Si - silicon dioxide]

4.1.5.4   Cell proliferation after polyelectrolyte multilayer formation

Proliferation of HDF on planar surfaces modified with PEM of HEP and PEI was determined over a period of seven days under serum-conditions (Figure 4.15). Similar to the results obtained on planar surfaces without PEM, cells maintained a long lag phase and did not proliferate to a high extent up to three days of culture on all surfaces. Again, after seven days the cell count increased dramatically. Even though not significant, more cells adhered to the terminal HEP layer formed at pH 5.0 on gold than on silicon dioxide (Figure 4.15A) and the same result was found on HEP assembled at pH 9.0 (Figure 4.15C). In addition, more cells were found on the terminal PEI layer assembled at pH 5.0 on gold in comparison to silicon dioxide (Figure 4.15B). However, no significant differences were found in cell count on the terminal PEI layer at pH 9.0 (Figure 4.15D). It was low in comparison to all other chemically modified planar surfaces. The difference in cell quantity was also reflected by cell morphology studies. Cells spread more in the initial phase on HEP terminated PEM assembled on planar surfaces (Figure A.6 and Figure A.7) independent of the pH value. In contrast, spreading was

weak in PEI terminating layers, especially at pH 9.0. However, after seven days of culture the difference in cell morphology was negligible due to cell-cell contacts as well as matrix secretion of the cells. Nevertheless, cells seeded on HEP layers were growing to confluence, while cells on PEI layers clearly did not, especially at alkaline conditions (Figure A.7).
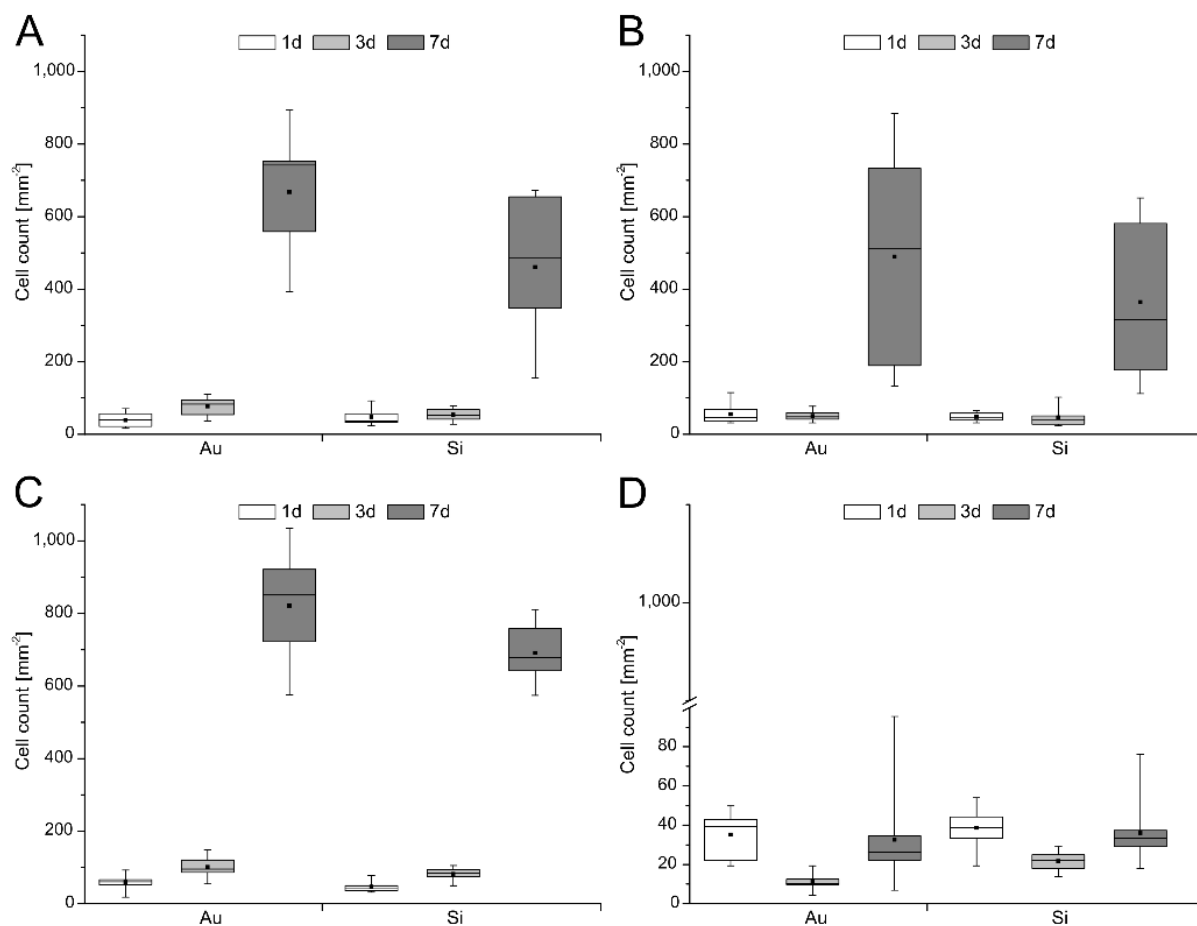
Figure 4.15 - Cell proliferation on PEM-modified planar surfaces. The evolution of cell count is shown for the terminal HEP (PH)$_4$ (A, C) as well as terminal PEI layer (PH)$_4$P (B, D) assembled at either pH 5.0 (A, B) or pH 9.0 (C, D) over a period of 1 d (open bars), 3 d (light gray bars), and 7 d (dark gray bars) of culture (p < 0.05). Analyses of significant difference (ANOVA) are summarized from Table A.14 to Table A.17 due to clarity reasons. [Au - gold, Si - silicon dioxide]

4.2 Nanostructured surfaces

4.2.1 Nanostructure formation

4.2.1.1 Scanning electron microscopy (SEM)

SEM imaging was used to investigate the formation of PS-NP monolayers as well as gold nanostructures on silicon substrates. Figure 4.16 displays the alignment of PS-NP of varying diameter within a monolayer (ML). Typically, the particles in such ML arrange in hexagonal close-packed (*hcp*) structures leading to triangular-shaped voids in between the spheres, as seen exemplarily in Figure 4.16 (top left). However, the assembly process can also lead to less close-packed masks as seen in the image with the 756 nm particles. The larger uncovered areas in between the nanoparticles would lead to gold structures, which are larger and lacking uniformity. Since the PS-NP were spin coated onto the substrates, ML formation started at different nucleation sites. Thus, the contact of homogeneously coated areas with other nucleation sites led to a shift in the overall uniformity of the ML, that later resulted in so-called grain boundaries (GB) after deposition of gold or other materials of interest. The GB formation was highly dependent on the PS-NP diameter. Further, the assembly of the PS-NP also led to double- (DL) or multilayer formation, which later resulted in smaller or missing nanostructures due to the shadow effect during gold deposition.
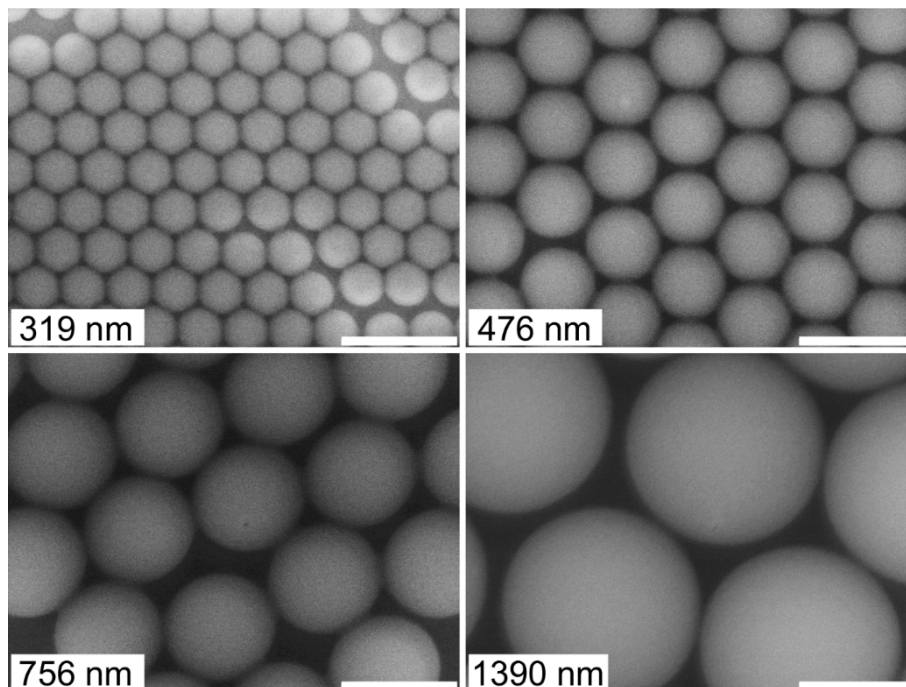
Figure 4.16 - SEM images of PS-NP of different diameter (see image) spin coated on cleaned silicon oxide. [Scale: 800 nm]

Figure 4.17 shows the distribution of tetrahedral nanostructures at low magnification after deposition of a chromium (10 nm) and gold layer (75 nm) as well as after removal of the PS-

NP mask. Further, optimally arranged nanostructures at high magnification are depicted in Figure 4.18. The lower magnification images revealed that GB formation was present on all surfaces due to the nature of the assembling process. However, the fraction of these boundaries was highest on surfaces obtained with 756 nm PS-NP followed by 319 nm and 476 nm PS-NP. The nanostructured surfaces prepared with the solvent evaporation method (1390 nm PS-NP) showed the lowest fraction of GB due to the longer time for drying and, thus, ML formation. In addition to the GB, relatively large homogeneous areas of gold in relation to the nanostructure dimension were present on surfaces obtained with the smallest PS-NP diameter, which were attributed to large void fractions during ML assembly. Overall, the fraction of undisturbed tetrahedral structures was highest on surfaces obtained with the largest PS-NP, even though the fraction of vacancies and dislocations was highest here. However, the fraction decreased from 476 nm over 756 nm to 319 nm PS-NP.
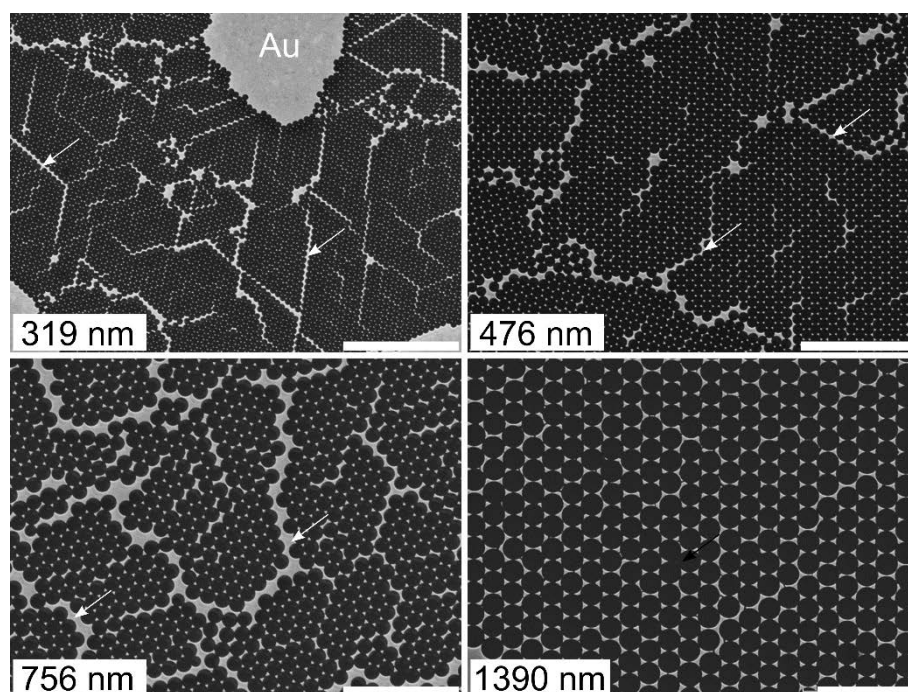
Figure 4.17 - Low magnification SEM images of nanostructures obtained with PS-NP of different diameter (see image). Grain boundaries (white arrow) and vacancies (black arrow) occur due to the fabrication process. Further, homogeneous gold areas (Au) are typically found on surfaces with the smallest nanostructure dimensions. [Scale: 6 μm]

4.2.1.2 Atomic force microscopy (AFM)

AFM analysis was performed to determine the height of the different nanostructures. Figure 4.19 displays the shape and distribution together with the height profiles of nanostructures on representative images.
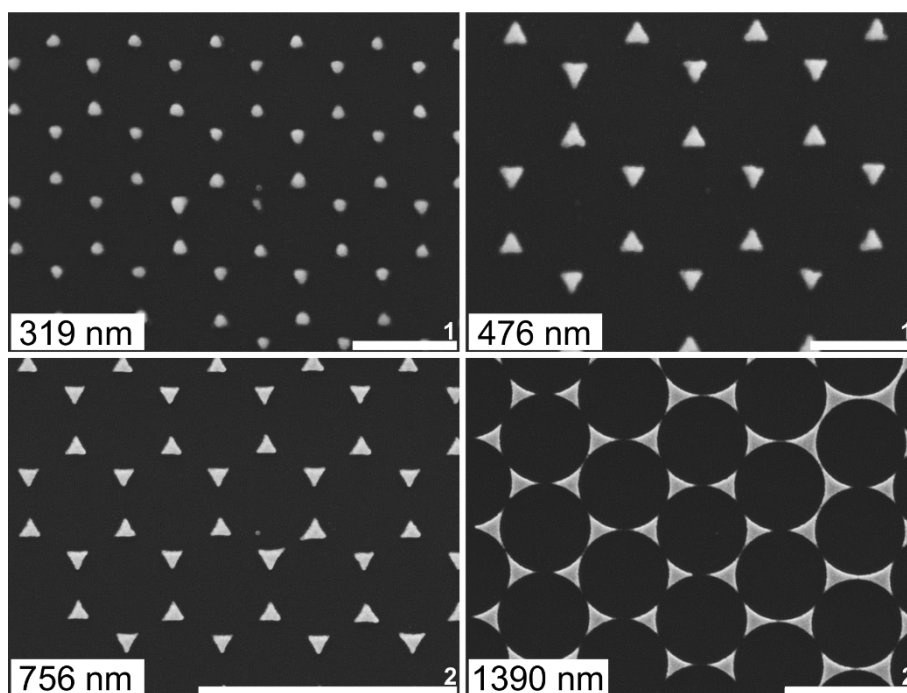
Figure 4.18 - High magnification SEM images of nanostructures obtained with PS-NP of different diameter (see image). [Scale 1, 400 nm; scale 2, 2 *μ*m]

GB formation, previously observed with SEM, was also monitored with AFM and it was found here that the fraction of these boundaries was much higher on nanostructured surfaces obtained with the smallest PS-NP diameter of 319 nm. The ideal distance and width of the nanostructures were calculated using Equation 3.1 and Equation 3.2, respectively. Further, the apparent distance and width together with the height of the nanostructures were determined by evaluating numerous height profiles as indicated in Figure 4.19. Comparison of the summarized results in Table 4.2 revealed that the measured distance of adjacent nanostructures virtually matched the calculated values. However, comparing the measured and calculated width of the structures did not lead to the same result. Here, it was observed that the measured width was always larger than the calculated one. Nevertheless, the percentage difference between both values dropped drastically the larger the nanostructures became, meaning the highest difference was found at the smallest structures and vice versa. Finally, comparing the nominal height of the nanostructures with the quantified values also led to virtually matching results. Ideally, the nanostructures should have a height of ~85 nm, consisting of ~10 nm chromium and ~75 nm gold, and it was found here, that only the height of structures obtained with the smallest PS-NP diameter of 319 nm was below 80 nm.
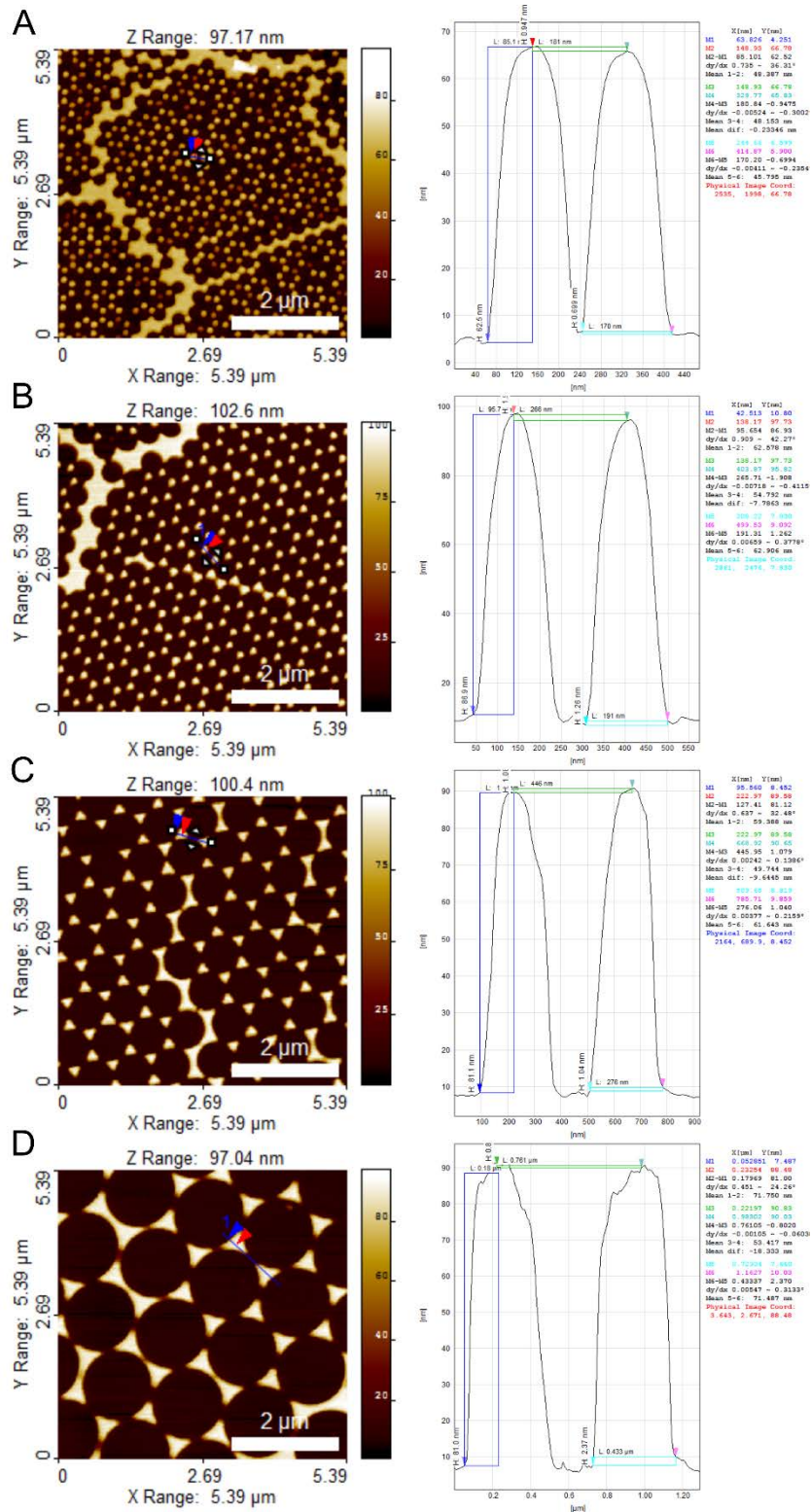
Figure 4.19 - AFM images and height profiles of nanostructures obtained with 319 nm (A), 476 nm (B), 756 nm (C) and 1390 nm (D) PS-NP. [Scan size: 5.39x5.39 μm²]

Table 4.1 - Calculated and measured nanostructure dimensions

PS-NP [nm]	Distance d_{ML} [nm]		Width a_{ML} [nm]		Height [nm]
319	184[a]	181.2 ± 1.2[b]	74[a]	118.8 ± 5.9[b]	79.7 ± 2.4
476	275[a]	263.3 ± 10.2[b]	111[a]	133.8 ± 5.3[b]	86.0 ± 1.4
756	436[a]	430.8 ± 15.9[b]	176[a]	196.3 ± 11.1[b]	84.3 ± 2.1
1390	803[a]	750.6 ± 13.7[b]	324[a]	368.9 ± 17.7[b]	81.9 ± 0.8

a - calculated; b - measured

4.2.2 Passivation of nanostructured surfaces

4.2.2.1 Confocal laser scanning microscopy (CLSM)

The passivation of the free substrate surface with long-chain SAM (Urea) and the activation of the gold structures with MUDA shall lead to a specific interaction of cells with the designed nanostructures. Again, FITC-labeled FN was used here to investigate the success of the passivation/ activation strategy. For this reason, FN was allowed to adsorb on the nanostructures at a concentration of 50 μg mL^{-1} at 37°C for 1 h and the effect was visualized using CLSM. It was found that protein adsorption only took place on the MUDA-modified nanostructures and that no protein was detectable on the long-chain SAM (Urea) in between the nanostructures (Figure 4.20), indicated by dark void fractions especially on the high magnification images (right column). In addition, the CLSM images also revealed the increased fraction of GB on samples obtained with the smallest PS-NP and that this fraction reduced with increasing PS-NP, which was previously revealed by SEM and AFM analysis. In addition to that, least GB were present on surfaces with the largest nanostructures (1390 nm). However, more dislocations were found here, which was attributed to the manufacturing method. The results confirmed that a selective modification of surface features in multi-component systems was possible and allowed the control of protein adsorption using mPEG-urea SAM.

4.2.3 Surface wettability

4.2.3.1 Static water contact angle (WCA)

The design of gold nanostructures on planar silicon dioxide surfaces obviously led to an increase in WCA, rendering the surfaces hydrophobic (Figure 4.21). Further, a clear, but not significant trend was observed in dependence on the nanostructure dimension, with highest WCA for the largest PS-NP diameter (white bars). The passivation of the free silicon dioxide surface with different SAM also led to differences in wettability.
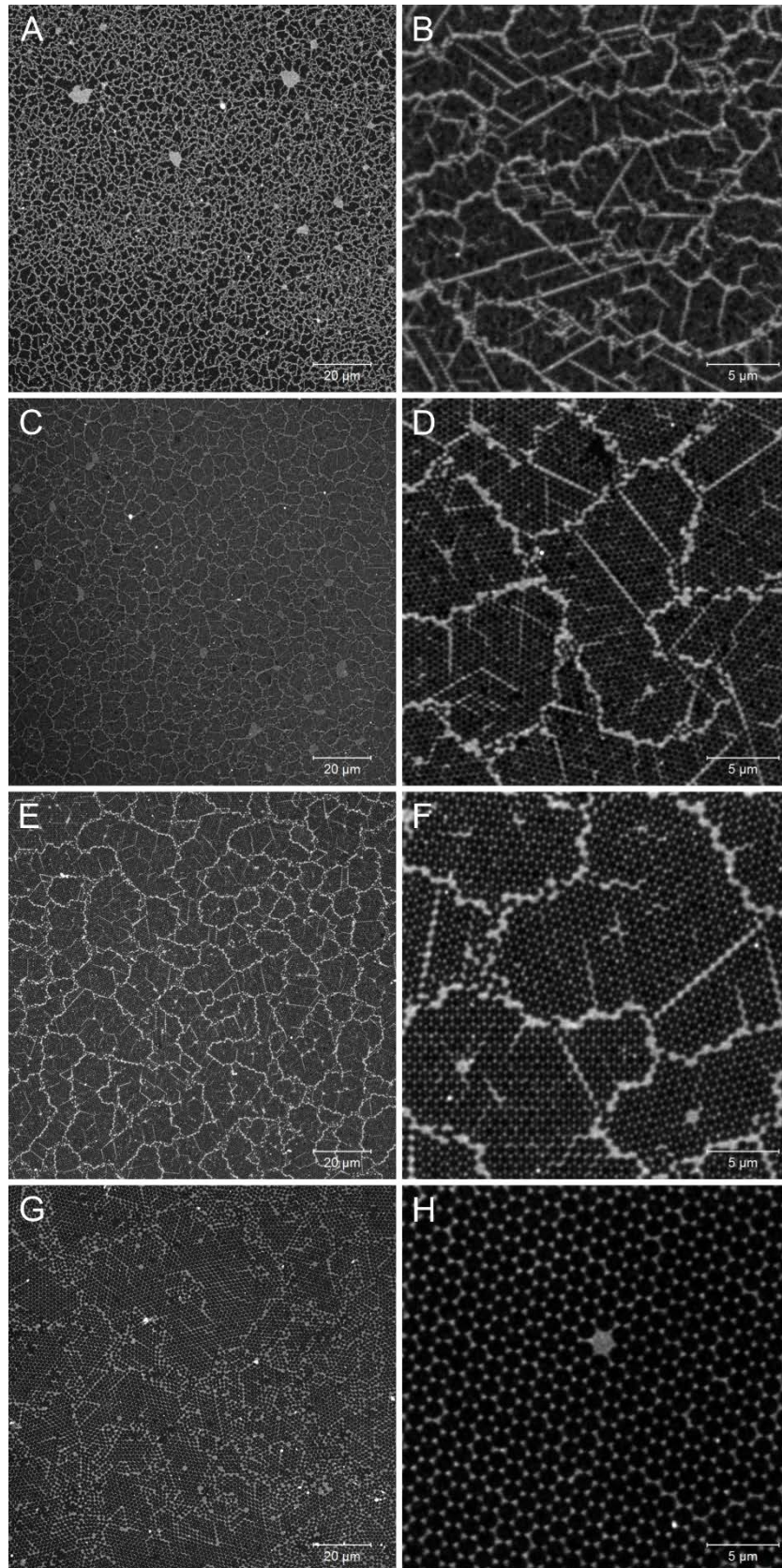
Figure 4.20 - Adsorption of FITC-labeled FN on nanostructured surfaces obtained with 319 nm (A, B), 476 nm (C, D), 756 nm (E, F) and 1390 nm (G, H) PS-NP. Bright areas indicate adsorbed protein, whereas dark areas show absence of protein. [Scale left column: 20 μm; scale right column: 5 μm]

According to the definition made in chapter 3.4.1, OEG-modified surfaces exhibited a slightly hydrophobic character, whereas urea-modified surfaces were more hydrophilic. Nevertheless, a prominent trend of WCA in dependence on the nanostructure dimension was not observed. The additional modification of gold nanostructures with MUDA, which possessed a terminating carboxyl group, improved the wettability, too. However, the WCA dropped to a higher extent on OEG-modified (gray bars) than on urea-modified (hatched bars) nanostructured surfaces. In addition, no significant differences were observed in dependence on the nanostructure dimension after MUDA-modification.
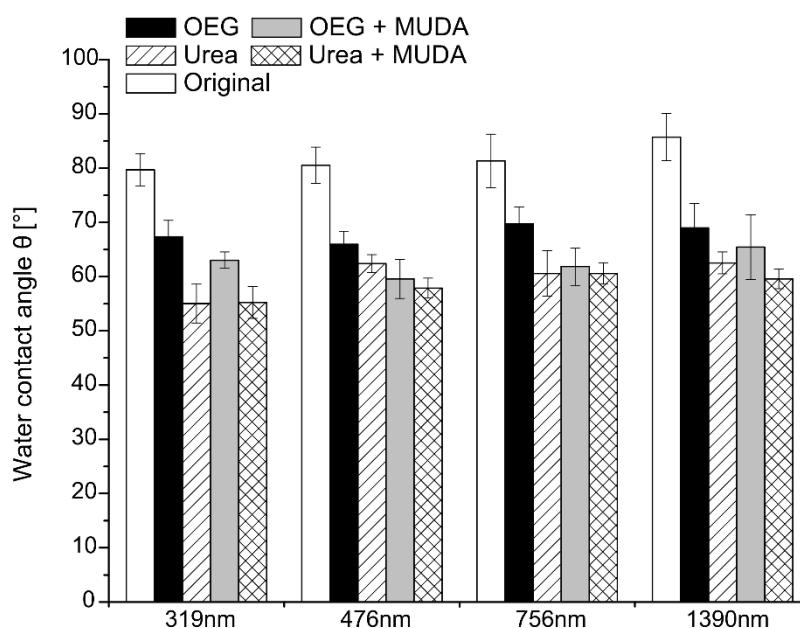
Figure 4.21 - Static WCA on nanostructured surfaces obtained with different PS-NP. The surfaces have been modified either with oligo (ethylene glycol) (OEG, filled bars) or mPEG-urea (Urea, hatched bars) as well as with mercaptoundecanoic acid (MUDA).

4.2.3.2 Dynamic water contact angle (WCA)

Dynamic WCA measurements were also used here to investigate the change in surface topography and chemistry upon different modification steps. The wetting properties of nanostructured surfaces were clearly affected by the type of chemical modification. First, unmodified nanostructures showed a hydrophobic character indicated by the high advancing contact angles (Figure 4.22A), which also reflected the results of the static WCA with a slight increasing trend from small to larger structures. However, a trend in WCA hysteresis was not observed since the receding WCA dropped with similar ratios in relation to the advancing contact angles. The modification with mPEG-urea SAM (Figure 4.22D) led to lower advancing and receding WCA in comparison to OEG-SAM (Figure 4.22B). However, the difference in hysteresis was not that prominent since both, advancing and receding, WCA dropped to the same extent.
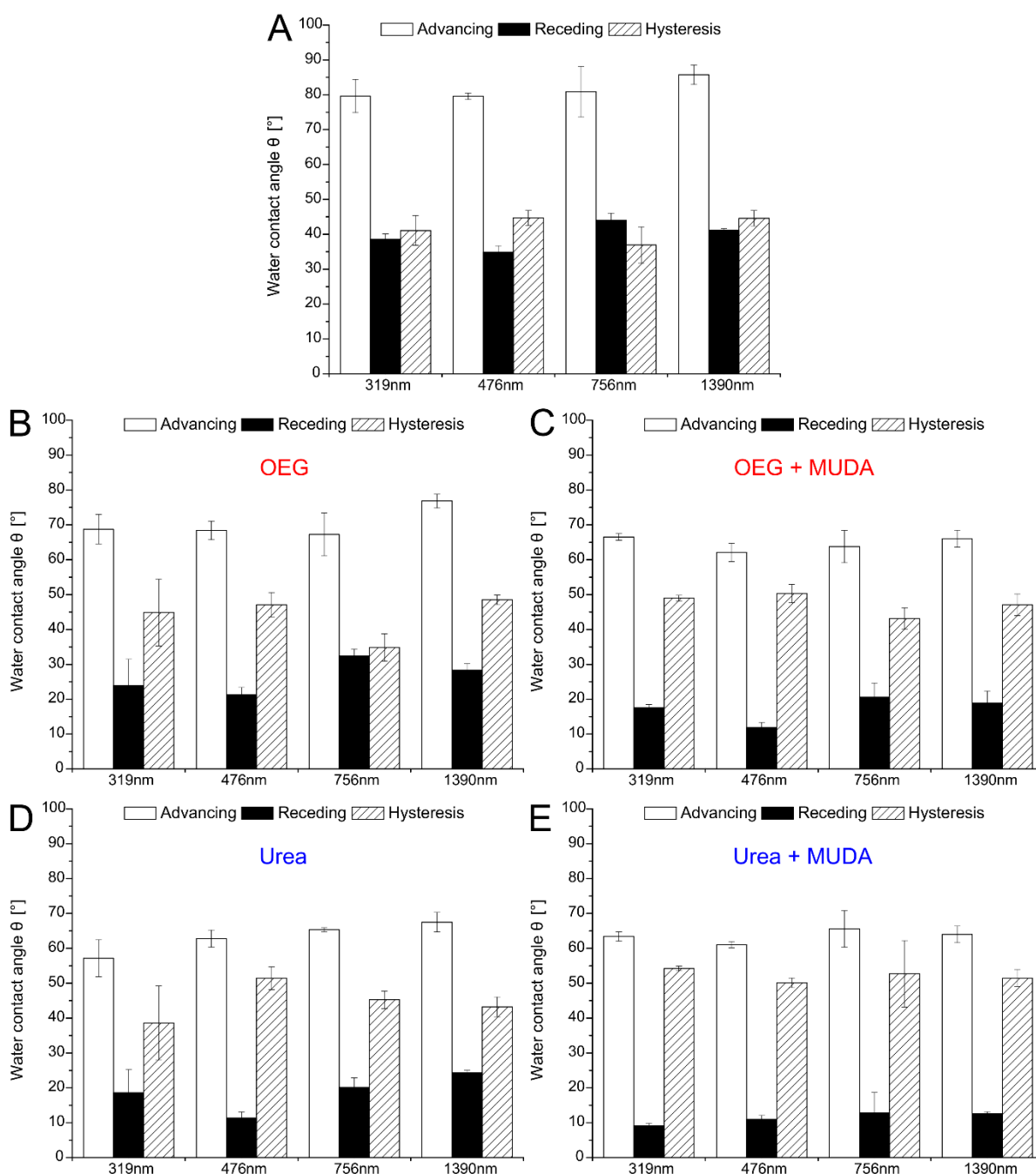
Figure 4.22 - Dynamic WCA on nanostructured surfaces obtained with different PS-NP. Advancing (white bars) and receding WCA (black bars) as well as the WCA hysteresis (hatched bars) are shown for unmodified samples (A) and after modification with either oligo (ethylene glycol) (OEG, B, C) or mPEG-urea (Urea, D, E) and additional modification with mercaptoundecanoic acid (MUDA, C, E).

Additionally, the subsequent modification of the nanostructures with MUDA did not have a strong effect on the advancing contact angle (Figure 4.22C, E). Moreover, the modification led to a noticeable decrease in the receding contact angle. The drop in receding WCA was much more pronounced on mPEG-urea-modified nanostructures, which resulted in higher WCA hysteresis (Figure 4.22E).

4.2.4   Cellular response to nanostructured surfaces

4.2.4.1   Cell adhesion

SEM was applied in environmental mode (ESEM) to monitor the interaction of cells with selected nanostructured samples to get a first idea on cell-surface-interaction. Figure 4.23 shows that the cells spread symmetrically on planar silicon oxide after adsorption of 20 μg mL^{-1} FN (top left). HDF had a large contact area with lamellipodia formation at the leading edges, which are a sign of cell migration. However, strong filopodia formation used for surface sensing purposes was not observed. Nanostructures obtained with PS-NP of 476 nm in diameter were used to investigate the interaction of HDF with non-planar surfaces. It was found that the cells also spread largely similar to cells seeded on silicon oxide. However, the strong polarization with pronounced lamellipodia formation was not developed to the same extent. Moreover, larger magnifications revealed that the cells formed significantly more filopodia to sense the environment in comparison to cells on planar silicon dioxide. Due to the unfavorable modification of the free silicon dioxide surface with OEG, these filopodia were in clear contact with the gold nanostructures and additionally followed their direction, indicating the sensing purpose. Other nanostructure dimensions were not evaluated by SEM analysis.
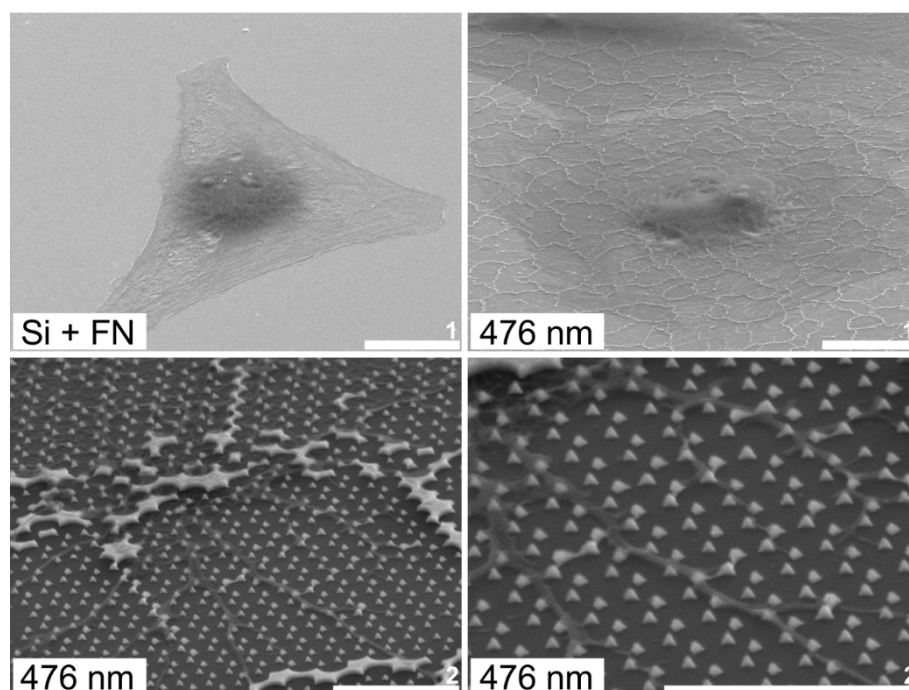
Figure 4.23 - SEM images of HDF seeded on plain silicon dioxide after adsorption of 20 μg mL^{-1} FN (top left) and on nanostructures obtained with PS-NP of 476 nm in diameter. [Scale 1: 20 μm; scale 2: 2 μm]

The adhesion of HDF to nanostructured surfaces was further investigated using immunocytochemistry and CLSM analysis. The cells were evenly distributed after 4 h of incubation (Figure 4.24, 1st and 3rd column), but showed dependence of FA formation and actin

organization on nanostructure dimension (Figure 4.24, 2nd and 4th column). It was revealed in a comparative study, that the difference in quality of cell adhesion (actin polymerization, FA formation) between short- (OEG) and long-chain SAM (Urea) was not prominent under protein-free conditions on planar surfaces (see section 4.1.5.1) and even after FN adsorption on nanostructured surfaces (Figure A.1). Hence, images of cells on nanostructured surfaces passivated with OEG were selected for further evaluation because they show that is also possible to control cell adhesion with a short-chain PEG. Cells adherent to the smallest feature size obtained with 319 nm PS-NP showed an extended filopodia formation in the absence of proteins. This formation was decreased in cells on larger nanostructures under protein-free conditions (Figure 4.24, 2nd column). In addition, actin fibers organized predominantly longitudinal and FA formation occurred mainly in the periphery of the cells adherent on the smallest feature size. The green areas in Figure 4.24 (top, 2nd column) could be allocated to non-specific secondary antibody binding on homogeneous gold areas, which originated from the manufacturing process. However, after FN adsorption FA formation and actin organization did not reveal big differences in dependence on the nanostructure dimension. Actin fibers were organized circumferentially, especially on the smallest feature dimensions (Figure 4.24, 4th column), and partly co-localized in FA in the periphery of the cells, indicated by the yellow color in the images. In addition, qualitative image analysis revealed at least on the largest feature dimensions, that FA were formed on top of the nanopatterns. Overall, the FA formation was reduced on nanostructured surfaces, which corresponds to the discrete distribution of adhesive sites compared to homogenous surfaces.

The quantification of cell count did not reveal significant differences in dependence on the protein coating (Figure 4.25A), indicating that FN coating did not lead to improved adhesion in this case, no matter if OEG or urea was used. Nevertheless, significantly fewer cells attached to nanostructured surfaces backfilled with the long-chain SAM (Urea) in comparison to OEG, especially if no FN was preadsorbed. Further, a slight decreasing trend from small to larger feature sizes was revealed in cell count, no matter which passivation strategy was used. However, such a trend was obvious when comparing the projected cell areas (Figure 4.25B). Cells on large features significantly spread to a lower extent if compared to small features, which holds for both passivation strategies as well as for protein-free or protein-containing conditions. However, cells seeded on patterned surfaces passivated with the long-chain SAM (Urea) were always smaller if compared to cells on OEG owing to the increased protein repellent properties. Finally, the determination of the aspect ratio revealed that HDF attached to OEG were always more elongated than cells on the long-chain SAM (Urea), no matter if proteins were present or not (Figure 4.25C). If FN was preadsorbed, the cells started to stretch, but to a higher extent on the short-chain SAM (OEG) due to lower protein repulsion. Further, an increased elongation from small to large structures was found on protein-containing

surfaces, indicating that the cells tried to make contact with the FN areas due to the increased distance between the nanostructures, whereas on small structures the FN areas were smaller but closer together.
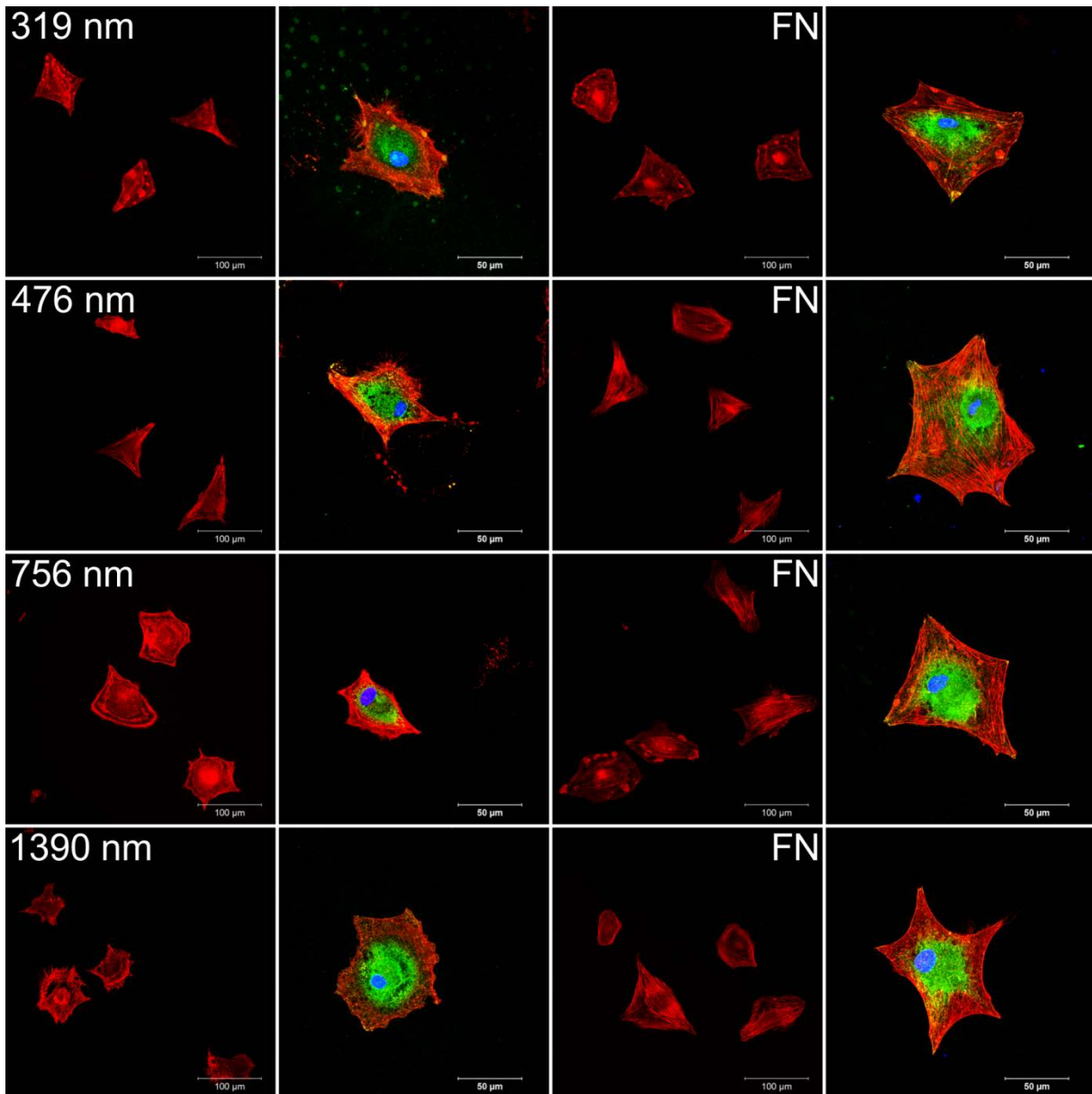

Figure 4.24 - CLSM images of HDF adherent on nanostructured surfaces backfilled with OEG-SAM and obtained with different PS-NP (see image) either without (left column pair) or with preadsorption of 2 μg mL^{-1} FN (right column pair) after 4 h of incubation. The cells were stained for actin (red), vinculin (green) and nucleus (blue) and visualized with low (1st and 3rd column, scale: 100 µm) and high magnification (2nd and 4th column, scale: 50 μm).
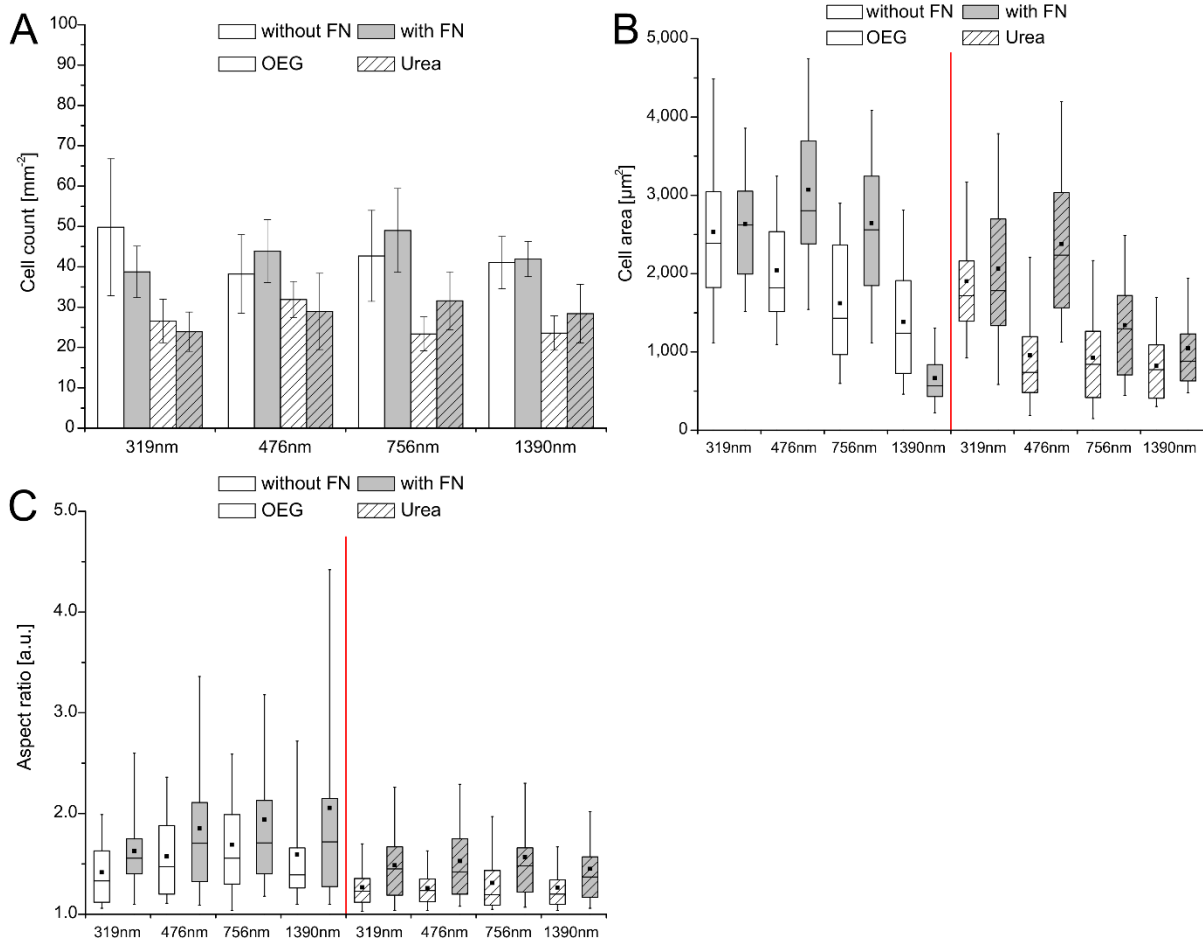
Figure 4.25 - Count (A), area (B), and aspect ratio (C) of cells seeded on nanostructured surfaces either without (open bars) or with preadsorption of 2 μg mL^{-1} FN (gray bars) after 4 h of incubation (p < 0.05). The red line in B and C separates OEG-modified (left) from urea-modified surfaces (right). Analyses of significant difference (ANOVA) are summarized in Table A.3, Table A.4, and Table A.5 due to clarity reasons.

4.2.4.2 Fibronectin matrix formation

FN matrix formation was influenced to some extent by the topography of the underlying substrate (Figure 4.26) in addition to the surface chemistry (see section 4.1.5.2). In general, FN matrix formation was more prominent on the structured surfaces if compared to the planar control surfaces (see Figure 4.13). However, FN fibrils showed typically footprints like FN fibrils formed on non-structured surfaces, but with pronounced fibrillogenesis on large feature dimensions. Image analysis revealed at least on the largest nanopatterns obtained with 1390 nm PS-NP that the FN fibrils are linked to the underlying structure and it was assumed here that the same held for smaller nanostructures (Figure 4.26, right column).
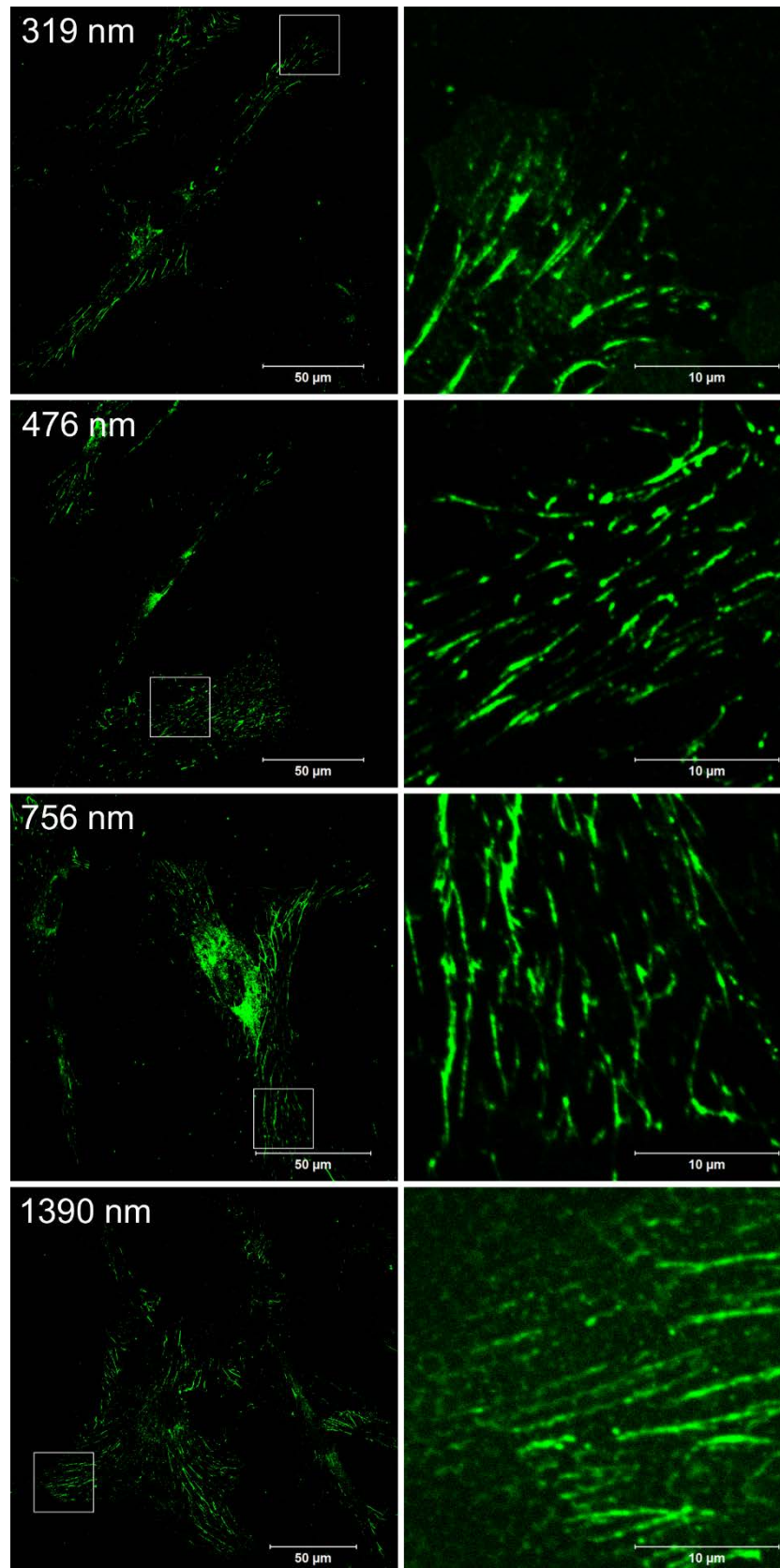
Figure 4.26 - FN matrix formation on nanostructured surfaces obtained with different PS-NP diameters. [Scale left column: 50 μm; scale right column: 10 μm]

4.2.4.3 Cell proliferation

Finally, the growth of HDF on nanostructured surfaces was determined over a period of seven days under serum-conditions (Figure 4.27). Additionally, FN was preadsorbed (B) or not (A). Similar to cells seeded on planar surfaces, HDF maintained a long lag phase and did not proliferate up to three days on all surfaces to a high extent, no matter if FN was present or not. However, after seven days the cell count increased significantly. Thereby, the cell growth followed the same trend as previously found in cell adhesion studies. Most cells were found on the smallest patterns and the cell count decreased with increasing pattern dimension, even though slightly more cells were found on the largest patterns if compared to the second largest patterns, when no FN was preadsorbed (Figure 4.27A). This trend was also preserved after FN preadsorption (Figure 4.27B). However, the effect of FN preadsorption on cell morphology was not as prominent as found on the planar surfaces. Here, cells on nanostructures spread to almost the same extent with strong actin polymerization and organization in bundles (Figure A.4 and Figure A.5). Overall, fewer cells were found on nanostructured surfaces in comparison to planar gold surfaces after seven days.
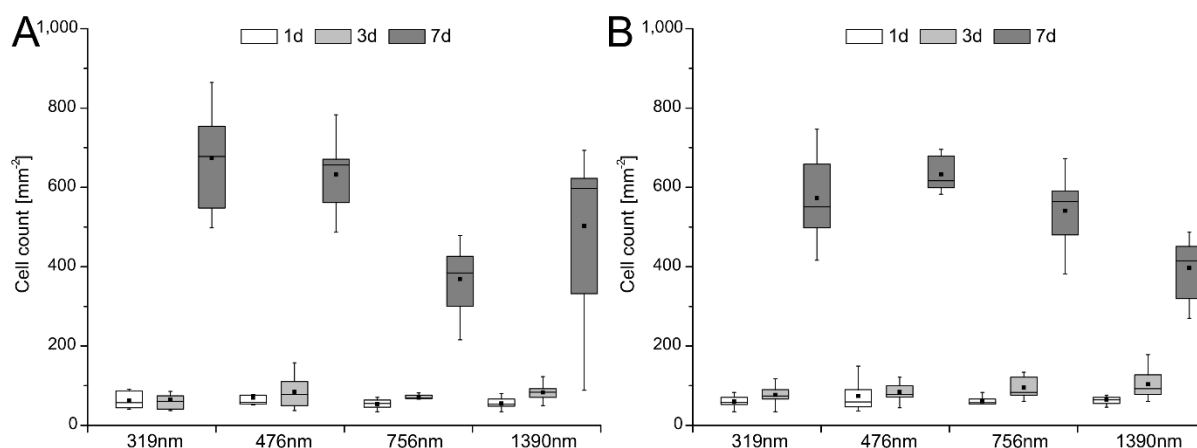
Figure 4.27 - Cell proliferation on nanostructured surfaces either without (A) or with preadsorption of 2 μg mL^{-1} FN (B) after 1 d (open bars), 3 d (light gray bars), and 7 d (dark gray bars) of culture (p < 0.05). Analyses of significant difference (ANOVA) are summarized in Table A.6 and Table A.7 due to clarity reasons.

It can be summarized here, that adhesion and growth of HDF can be controlled to some degree by varying the size and distance of surface structures in the nanoscale. Moreover, the passivation strategy using either short- or long-chain PEG increases the flexibility for directing adhesion and growth of cells. However, unexpected results such as the reduced protein repellence of short-chain OEG-SAM or increased cell growth on long-chain Urea-SAM after long-term culture give rise to further investigations.

4.3 Nanostructures and polyelectrolyte multilayers

4.3.1 Polyelectrolyte multilayer formation

4.3.1.1 Confocal laser scanning microscopy (CLSM)

Fluorescein-labeled HEP was used here to investigate the PEM formation on top of nanostructures of different size and the result can be seen in Figure 4.28, which displays the fluorescence intensities of multilayers assembled at either pH 5.0 (left double column) or pH 9.0 (right double column). All nanostructured surfaces had in common that HEP terminated layers exhibited a higher fluorescence intensity in comparison to PEI terminated layers, which was found on planar surfaces, too. However, nanostructures with terminal HEP layers did not appear as clear as structures with a terminal PEI layer. Moreover, they were hardly to recognize since the images had a more blurry character, whereas structures were clearly visible on PEI terminated layers. An obvious difference in dependence on the pH value could not be found; especially on PEI terminated layers. It seemed that HEP layers assembled at pH 9.0 (third column) had a slightly higher intensity than layers formed at pH 5.0 (first column). Since most of the structures, or at least the GB, were detectable on the images, it can be concluded that multilayer formation preferentially took place on the activated gold structures.

4.3.2 Surface characteristics

4.3.2.1 Atomic force microscopy (AFM)

AFM analysis was used here to determine if the formation of PEM on top of the nanostructured surfaces has an effect on the height of the structures and roughness of the surfaces. Since two pH values were used during multilayer formation, Figure 4.29 displays images of the terminal HEP (left column) and PEI layer (right column) assembled at pH 5.0, whereas Figure 4.30 represents images of terminal layers assembled at pH 9.0. It is recalled here, that only the pH value of the terminal HEP layer was adjusted to the respective values, while it was not controlled for all other layers during PEM assembly. All measurements were performed in dry state with air as ambience. The properties of hydrated PEM were not investigated here. First, it was found that the z-range, which indicates the maximum peak-to-valley parameter, has increased on all surfaces in comparison to the nanostructures that have not been modified with PEM (see Figure 4.19), which proved that PEL adsorbed on all surfaces. However, there were clear differences in z-range as well as surface structures when comparing terminal layers assembled at different pH value as well as with different terminal molecules. Starting with PEM assembled at pH 5.0 (Figure 4.29) it was found that the terminal HEP layer (left column) appeared more rough than the successive PEI layer (right column).
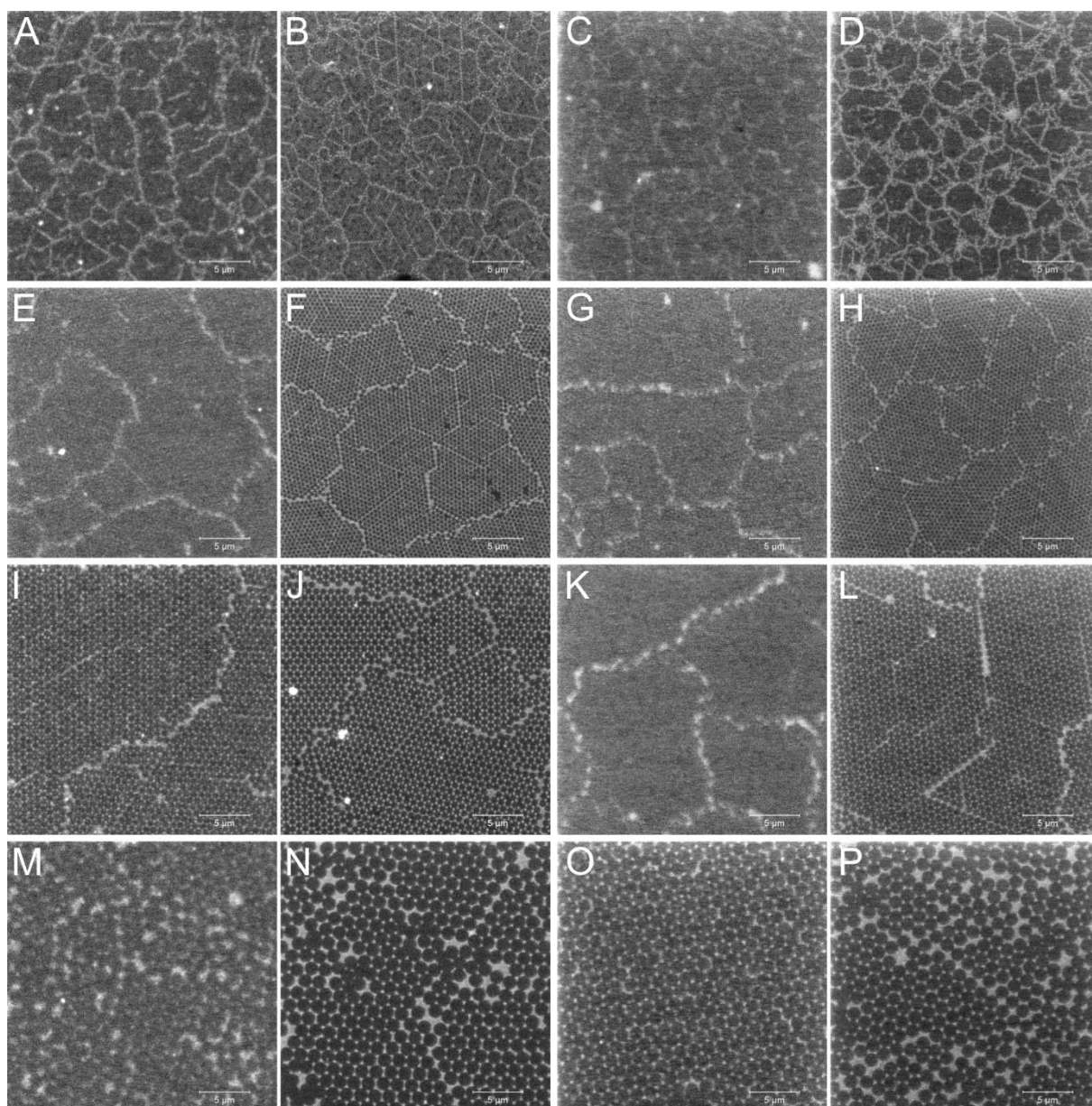
Figure 4.28 - PEM formation on nanostructured surfaces obtained with 319 nm (A - D), 476 nm (E - H), 756 nm (I - L) and 1390 nm (M - P) PS-NP using fluorescein-labeled HEP. The left double column represents PEM formation at pH 5.0 whereas the right double column represents PEM formation at pH 9.0. Each double column displays fluorescence intensities of the terminal HEP layer (PH)$_4$ (A, C, E, G, I, K, M, O) and terminal PEI layer (PH)$_4$P (B, D, F, H, J, L, N, P). [Scale: 5 µm]

Further, it seemed that multilayer formation was not restricted to the gold structures since vermiculate assemblies were also found in between the nanostructures, at least on the HEP terminated surfaces. Quantitative analysis of the areas in between the nanostructures revealed that HEP layers assembled at pH 5.0 were significantly rougher than PEI layers, indicated by an increased roughness average (R_a) and root mean square (RMS) and displayed by Figure 4.31. The same phenomenon was observed for PEM assembled at alkaline conditions.

82
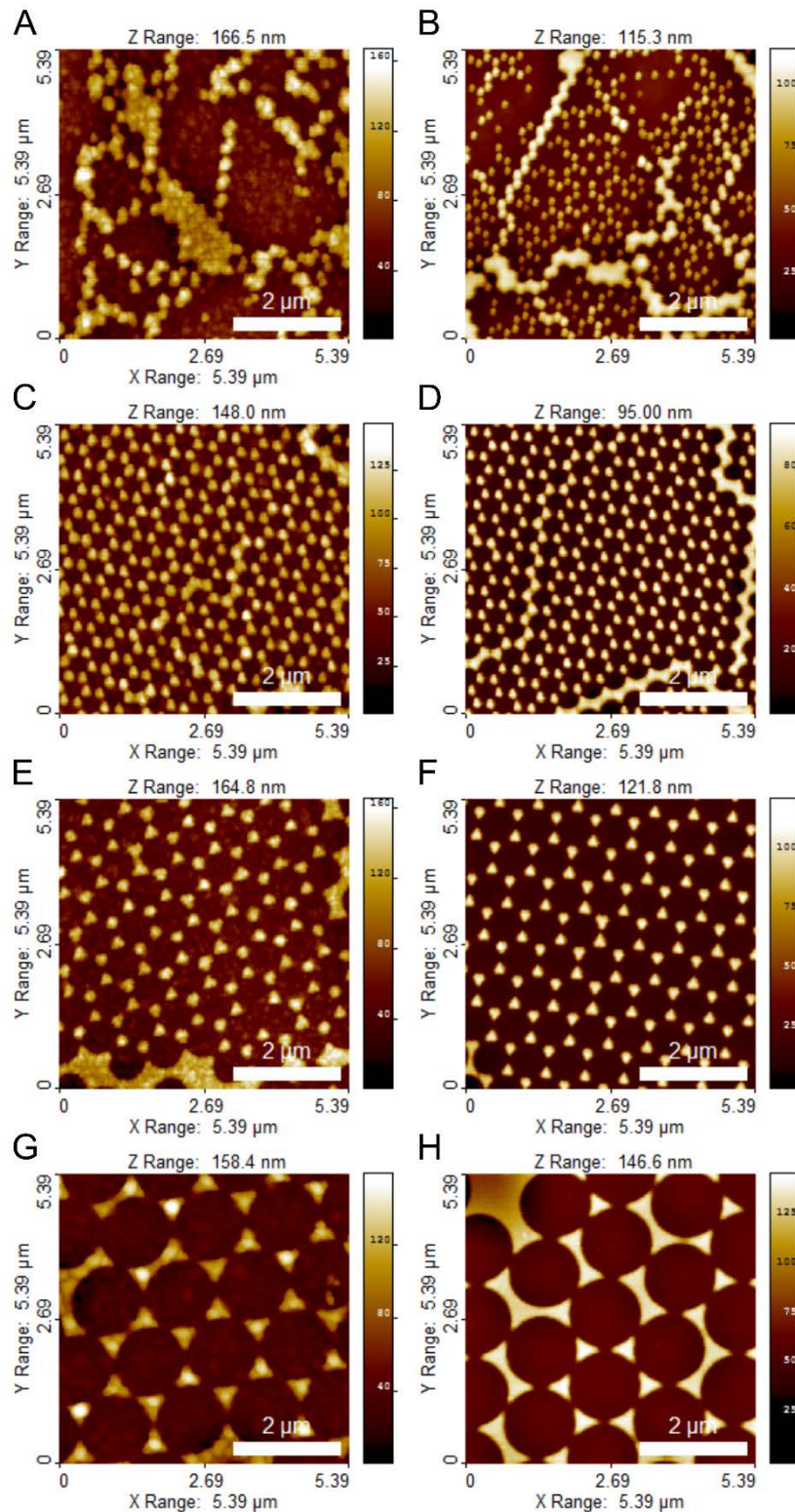
Figure 4.29 - AFM images of nanostructures obtained with 319 nm (A, B), 476 nm (C, D), 756 nm (E, F) and 1390 nm (G, H) PS-NP and modified with PEM. The left column (A, C, E, G) displays the terminal HEP layer (PH)₄ and the right column displays the terminal PEI layer (PH)₄P. The pH value of the terminal HEP layer was adjusted to pH 5.0. [Scan size: 5.39x5.39 μm²]
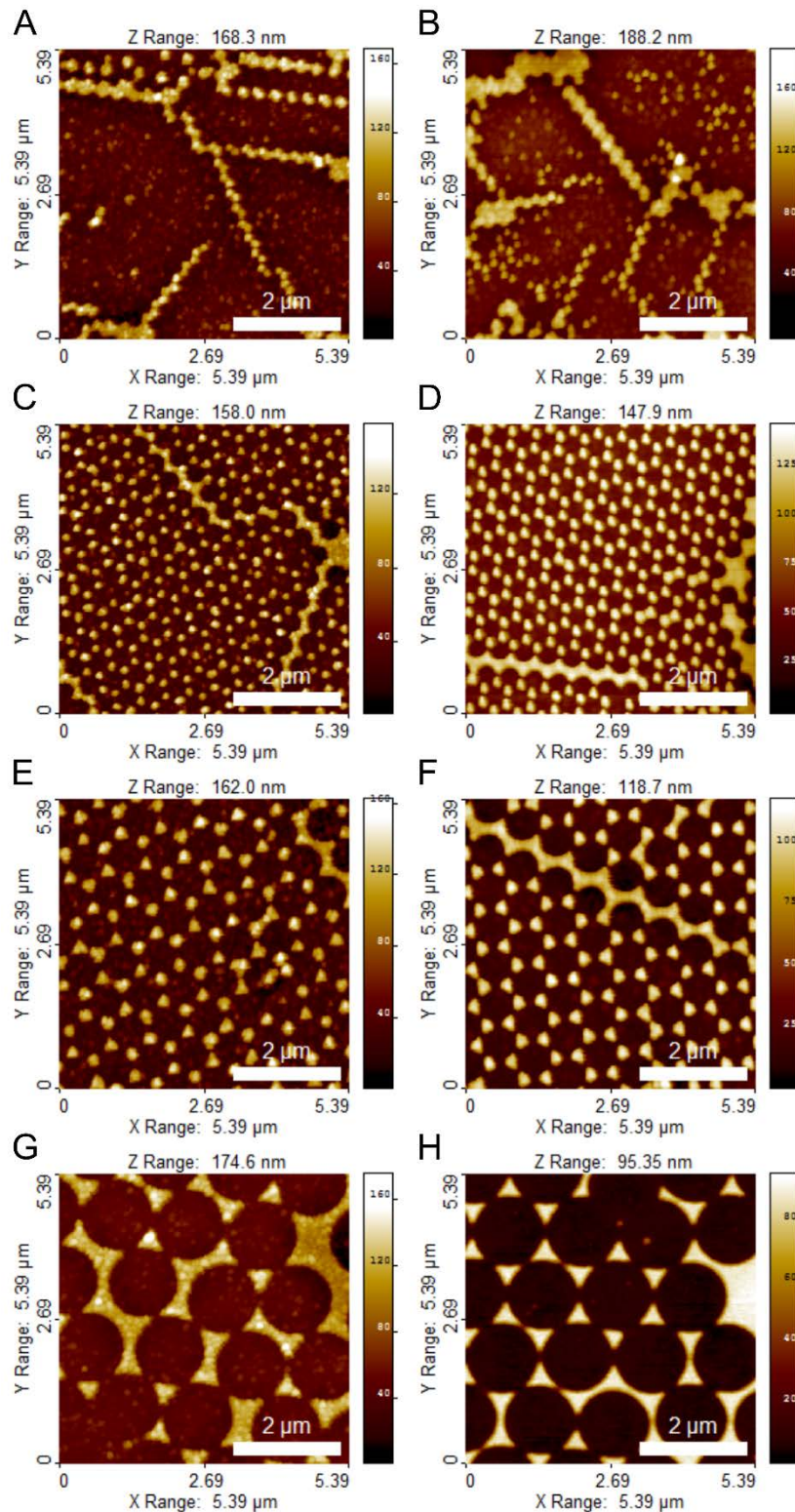
Figure 4.30 - AFM images of nanostructures obtained with 319 nm (A, B), 476 nm (C, D), 756 nm (E, F) and 1390 nm (G, H) PS-NP and modified with PEM. The left column (A, C, E, G) displays the terminal HEP layer (PH)₄ and the right column displays the terminal PEI layer (PH)₄P. The pH value of the terminal HEP layer was adjusted to pH 9.0. [Scan size: 5.39x5.39 μm²]
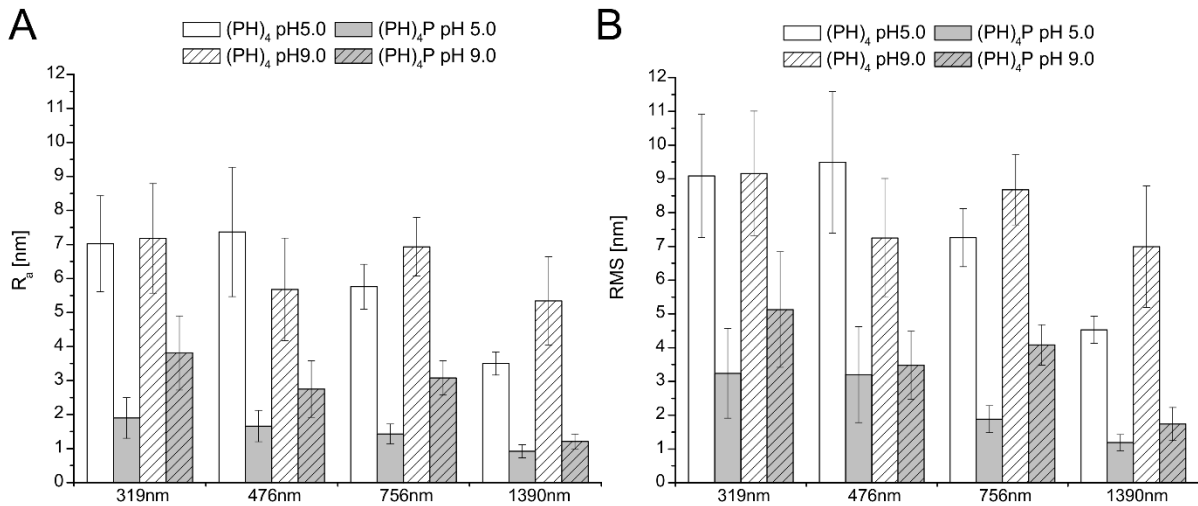
Figure 4.31 - Roughness average (R_a, A) and root mean square (RMS, B) of nano-structures modified with PEM of HEP and PEI. Analyses of significant difference (ANOVA) are summarized in Table A.2 due to clarity reasons.

However, no significant differences in surface roughness were found on HEP layers assembled at different pH values, but it was obvious that the roughness decreased with increasing nanostructure dimension. In contrast, PEI layers assembled at pH 5.0 were always less rough than PEI layers at pH 9.0. Moreover, a decreasing trend from small to larger structures was determined here. In addition to the increased roughness of HEP layers, also the z-range was higher than on PEI layers. However, it was found here, at least on surfaces obtained with 319 nm small PS-NP, that nanostructures were dislocated with additional vacancies. This phenomenon was also found on samples with PEM assembled at pH 9.0 (Figure 4.30), again only for the smallest structures.

4.3.3 Surface wettability

4.3.3.1 Static water contact angle (WCA)

Again, static WCA measurements were applied to investigate the wettability of the nanostructured surfaces after buildup of a PEM system consisting of HEP and PEI. Figure 4.32 shows that all surfaces were hydrophilic after PEM formation, but with obvious differences in dependence on the terminating layer as well as the assembling pH value. Nanostructured surfaces terminated with HEP assembled at pH 5.0 were highly hydrophilic, that means no WCA values could be recorded due to the low signal-to-noise ratio of values $\theta <10°$ and, thus, were considered as zero values. Further, water droplets with an irregular shape, which number was increased on highly wettable surfaces, were not considered for calculation and neglected. However, after changing the pH value of the HEP solution to pH 9.0 a change in wettability was observed. Nanostructures modified with such a system were less wettable, but still highly

hydrophilic. Interesting to see is that a trend was found in dependence on the nanostructure dimensions. Here, PEM assembled on the smallest structures had lower WCA than PEM on larger structures and the wettability was decreasing with increasing nanostructure dimensions. Multilayers terminated with the synthetic polymer PEI were always less wettable than PEM terminated with HEP. The WCA ranged from $\theta = 36°$ to $\theta = 43°$. Remarkable is that there was no difference in wettability dependent on the assembling conditions, meaning that the wettability of PEM assembled at pH 5.0 was not increased in comparison to layers at pH 9.0, like it was found on HEP terminated layers. Further, a drift in wettability in dependence on the nanostructure dimensions like on HEP terminated PEM was not detectable, which is noteworthy, too. Overall, the implementation of PEL with various ionogenic groups led to a reduction of the pristine hydrophobicity of the unmodified, regular ordered gold nanostructures.
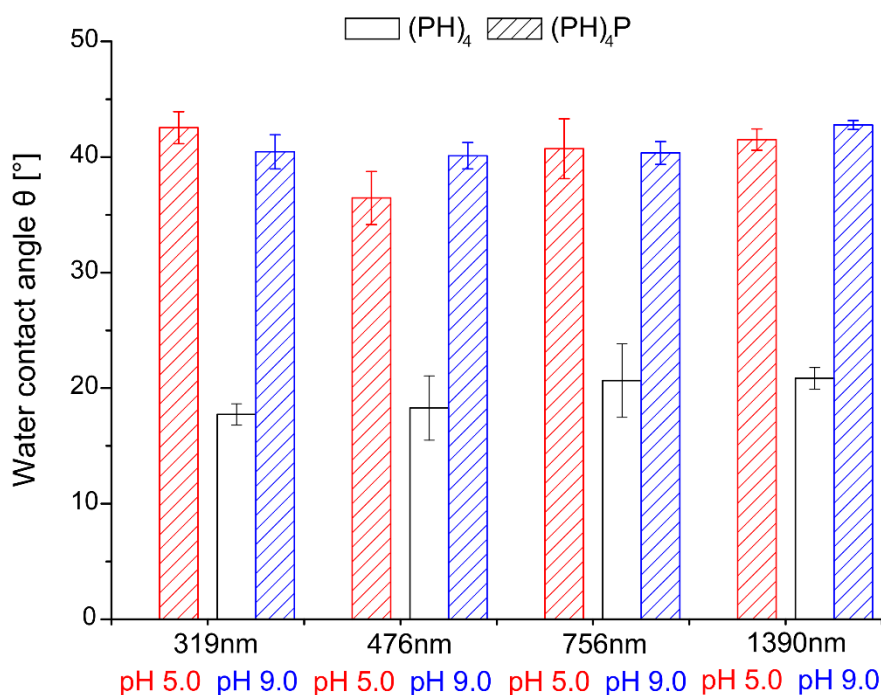
Figure 4.32 - Static WCA on nanostructured surfaces modified with PEM of HEP (H) and PEI (P). WCA are shown for the terminal HEP (white bars) and PEI layer (hatched bars) formed at either pH 5.0 or pH 9.0.

4.3.3.2 Dynamic water contact angle (WCA)

The modification of nanostructured surfaces with PEM of HEP and PEI led to differences in the dynamic recording of WCA, as represented by Figure 4.33. In consistency with static WCA measurements, it was found that HEP terminated PEM assembled at pH 5.0 were highly wettable and no WCA could be monitored, no matter on which nanostructure dimension (Figure 4.33A).
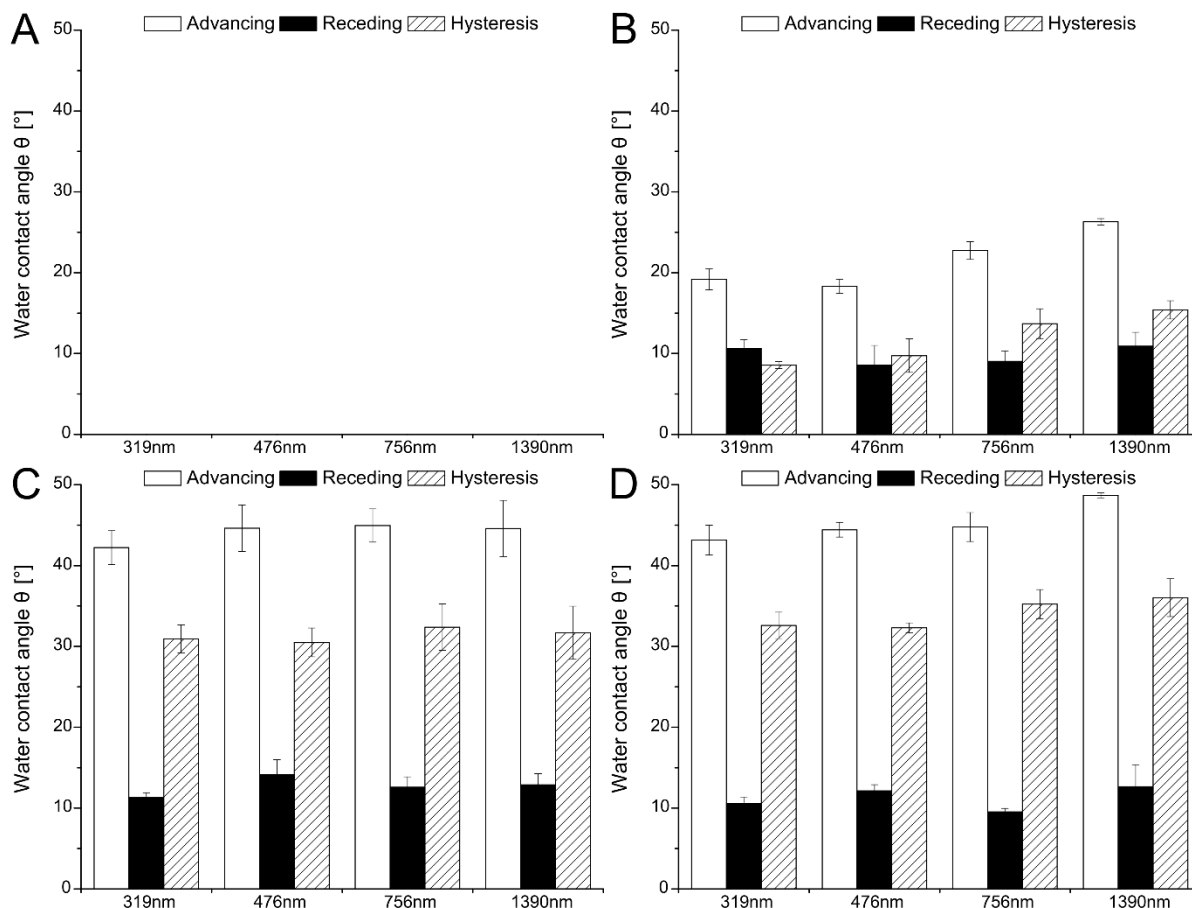
Figure 4.33 - Dynamic WCA on nanostructured surfaces modified with PEM of HEP (H) and PEI (P). Advancing (white bars) and receding WCA (black bars) as well as the WCA hysteresis (hatched bars) are shown for the terminal HEP (A, B) and PEI layer (C, D) formed at either pH 5.0 (left column) or pH 9.0 (right column) on nanostructures obtained with different PS-NP diameters.

Further, the advancing WCA increased from HEP at pH 9.0 (B) through PEI at pH 5.0 (C) to PEI at pH 9.0 (D). Again, an increase in advancing WCA from small to larger nanostructures was found on both, HEP terminating layers at pH 9.0 and all PEI terminated layers. Since the receding contact angles had similar values on all but the HEP layer at pH 5.0, clear differences in WCA hysteresis dependent on the nanostructure dimension were found as seen in Figure 4.34. In general, hysteresis values were higher on PEI terminated layers due to the lower wettability. However, a clear drift in WCA hysteresis was found in all PEM systems from small to larger nanostructures, meaning that the hysteresis was lowest on structures obtained with 319 nm PS-NP and highest on structures obtained with 1390 nm PS-NP.
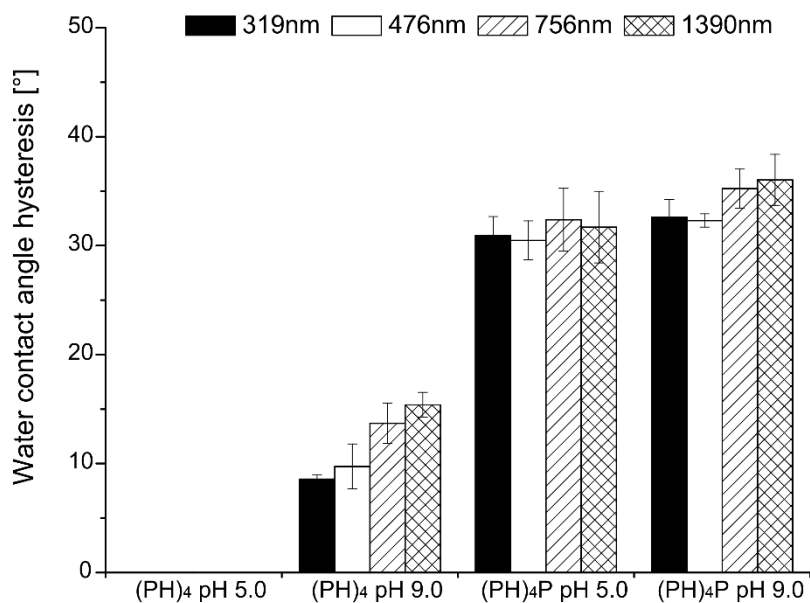
Figure 4.34 - WCA hysteresis on nanostructured surfaces modified with PEM of HEP (H) and PEI (P) assembled at pH 5.0 or pH 9.0.

4.3.4 Surface potential

The zeta potential of PEM assembled on nanostructured surfaces was determined to monitor the evolution of the surface charge after various modification steps. Particularly, the effect of surface passivation with OEG and activation of gold nanostructures with MUDA as well as the net charge of the terminal multilayers at different pH conditions were of interest. Surface conductivity correction was a non-factor in evaluation since zeta potentials were recorded using streaming current monitoring.

It was found that glass as substrate had a negative zeta potential throughout the investigated pH range from pH 10.5 to pH 3.0, which was attributed to the large amount of its silanol groups (Figure 4.35). The extrapolation of the curve for determination of the point of zero charge (PZC) resulted in pH 2.70. At physiological pH, glass was found to be highly negative, exhibiting values of -86 mV and below for higher pH values. A summary of PZC and zeta potentials at pH 7.4 of all investigated surfaces can be found in Table 4.1.

All nanostructured surfaces have been modified with a short-chain PEG (OEG), which should prevent adsorption of charged molecules on the substrate surface, as well as MUDA, which, in turn, should establish the base for interaction with charged molecules. However, the determination of the zeta potential after passivation and activation of the substrates revealed only slight differences between both modification steps. In general, the passivation of the free glass surface with OEG led to a less negative zeta potential of all nanostructured samples in comparison to glass, especially at pH values above pH 7.0, which was attributed to the

molecule structure exhibiting a terminal methyl group. Further, the extrapolation of the curves resulted in PZC close to or below that of plain glass, indicating higher amounts of deprotonated functional groups above pH 3.0. However, a clear trend in dependence on the nanostructure dimension was not found.
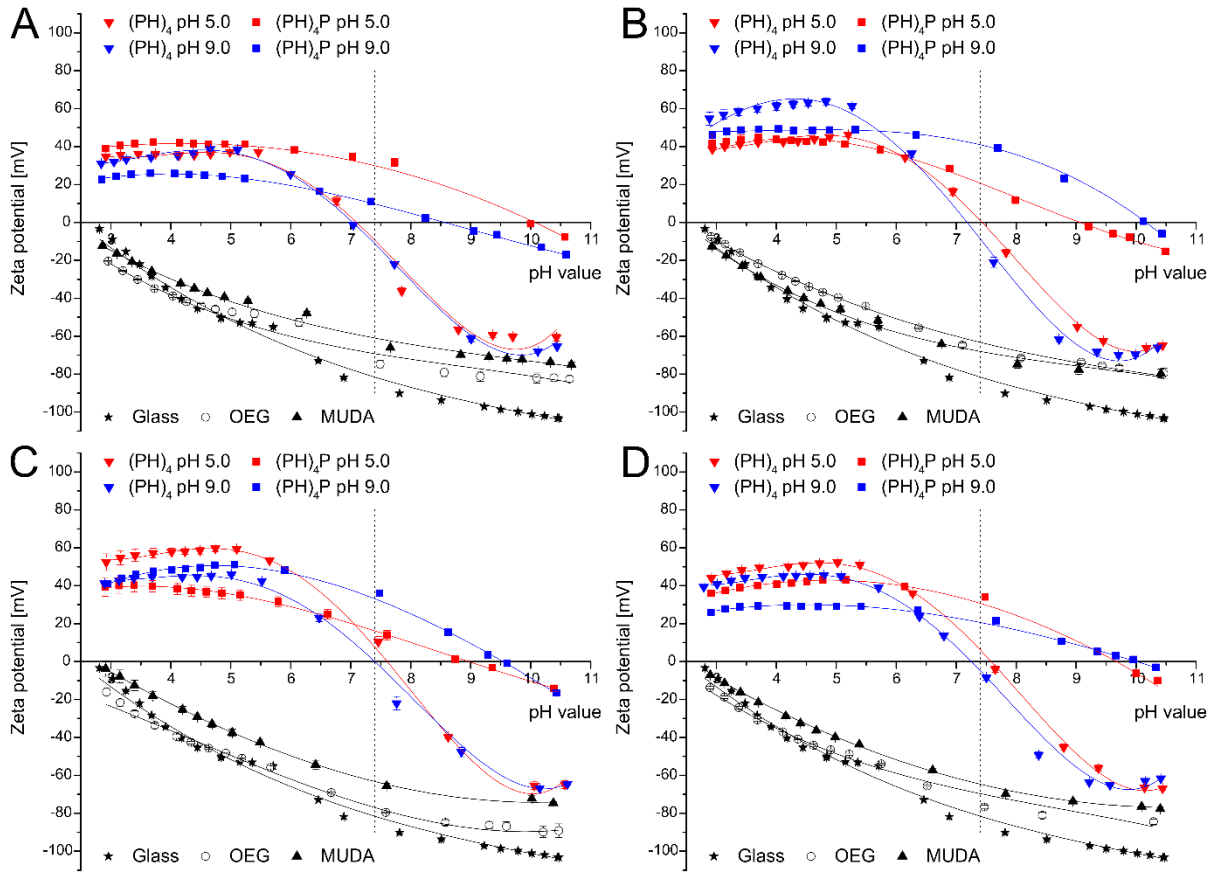

Figure 4.35 - Zeta potential of surfaces with nanostructures obtained with 319 nm (A), 476 nm (B), 756 nm (C) and 1390 nm (D) PS-NP. The nanostructured surfaces were modified with oligo (ethylene glycol) (OEG, ○), mercaptoundecanoic acid (MUDA, ▲) and with PEM of HEP ((PH)$_4$, ▼) and PEI ((PH)$_4$P, ■) formed at pH 5.0 (red) or pH 9.0 (blue). Clean glass (stars) was used as reference.

In contrast, the introduction of a terminal carboxylic acid group by modification of the nanostructures with MUDA did not cause a rise in negative zeta potential. Moreover, all zeta potentials at pH 7.4 were less negative in comparison to OEG modification, except on structures obtained with 476 nm PS-NP (Figure 4.6 B). Again, the extrapolation of the zeta potential curves resulted in PZCs between pH 2.1 and pH 2.7, which repeatedly showed the presence of larger amounts of deprotonated functional groups above pH 3.0. Overall, the negative potentials at pH 7.4 and above represented the base for successful PEM formation, since the uncontrolled pH values of the PEL solutions were either physiological (HEP, pH 7.4) or alkaline (PEI, pH 10.4), as long as not adjusted intentionally.

Table 4.2 - Summary of point of zero charge (PZC) and zeta potential (ZP) at pH 7.4 of differently modified nanostructured surfaces and clean glass

		PZC	ZP at pH 7.4 [mV]
OEG	319nm	1.84	-73.26
	476nm	2.51	-66.73
	756nm	2.27	-77.45
	1390nm	2.27	-75.86
MUDA	319nm	2.11	-62.61
	476nm	2.29	-69.61
	756nm	2.72	-63.71
	1390nm	2.51	-65.46
(PH)$_4$ pH 5.0	319nm	7.02	-16.52
	476nm	7.40	-0.06
	756nm	7.70	12.91
	1390nm	7.51	3.19
(PH)$_4$P pH 5.0	319nm	9.99	33.07
	476nm	9.06	20.77
	756nm	9.50	16.11
	1390nm	9.61	35.37
(PH)$_4$ pH 9.0	319nm	6.96	-11.42
	476nm	7.16	-9.72
	756nm	7.14	-9.21
	1390nm	7.23	-5.27
(PH)$_4$P pH 9.0	319nm	8.55	9.40
	476nm	10.14	40.73
	756nm	8.97	37.09
	1390nm	10.05	22.65
Glass		2.70	-86.48

The assembly of PEM consisting of PEI and HEP clearly changed the surface zeta potential in dependence on the terminating molecule. First, the formation of eight PEL layers with HEP as terminating molecule resulted in sigmoidal curves with maxima and minima at the investigated pH extremes. Further, differences in PZC and zeta potential at pH 7.4 were found on the different nanostructured surfaces, even though a clear trend could not be revealed. The adsorption of HEP at pH 5.0 interestingly resulted in higher zeta potentials at the pH minima on all but the 476 nm surfaces in comparison to the adsorption at pH 9.0 that resulted in less positive potentials. At the pH maxima, the difference between HEP adsorbed at acidic or alkaline conditions was not that pronounced. However, the PZC on nanostructured surfaces was between pH 7.0 (319 nm) and pH 7.70 (765 nm), while the zeta potential followed the

same trend with lowest values for the smallest and highest values for 756 nm particles. The adsorption of HEP at pH 9.0 led to lower PZCs on all surfaces if compared to pH 5.0, which is attributed to the intermingling of layers. Additionally, the zeta potential at physiological pH showed a clear trend in dependence on the nanostructure dimension, since the absolute values decreased from 319 nm to 1390 nm PS-NP. Overall, the net charge of the terminal HEP layer was negative on all modified nanostructured surfaces above pH 10.0, which was sufficient for the subsequent adsorption of the terminal PEI layer, of which the intrinsic pH value of pH 10.4 was not controlled during PEM assembly.

The adsorption of PEI led to a complete different curve progression in comparison to HEP adsorption. Here, no sigmoidal curves were observed. Moreover, the absolute value of the zeta potentials increased from pH 10.5 to pH 3.0 on all modified surfaces with plateau phases below pH 5.0. The PZC of the terminal PEI layer was permanently above pH 8.5, which is slightly higher than the reported pK_a value. However, in PEM assembled with HEP at pH 5.0 it did not differ among the different nanostructure dimensions as strong as in PEM assembled with HEP at pH 9.0. Additionally, no clear evolution of PZC and zeta potential at physiological pH in dependence on the nanostructure dimension was observed. The absolute values at pH 7.4 of PEM built at pH 5.0 were higher on nanostructures obtained with 319 nm and 1390 nm, but lower on surfaces obtained with 476 nm and 756 nm, respectively, in comparison to PEM assembled at pH 9.0 (Table 4.1). The absolute zeta potential values of the plateau phases below pH 5.0 were either similar (319 nm, 476 nm) or even lower than that of the terminal HEP layer adsorbed at acidic pH value. An analogous result was observed on PEM assembled at pH 9.0. Here, the absolute values in the plateau region were again close to (756 nm) or even below (all other surfaces) that of the terminal HEP layer. However, the strong positive potential at pH 5.0 and the still positive potential at pH 9.0 are an indicator for real charge reversal. Hence, it would enable the adsorption of an additional HEP layer with corresponding pH values on top of the terminal PEI layer.

4.3.5   Cellular response to PEM-modified nanostructures

4.3.5.1 Cell adhesion

The adhesion of HDF on nanostructured samples modified with PEM of HEP and PEI was investigated after 4 h of cell culture under protein-free conditions with and without preadsorption of 2 μg mL^{-1} FN. Again, the cells were stained for cellular structures such as nucleus, actin cytoskeleton and vinculin in FA using immunocytochemistry. It was found here, that actin organization and FA formation were strongly dependent on the terminating molecule (HEP or PEI), the pH value during PEM assembly (pH 5.0 or pH 9.0) as well as the presence of FN. Terminal HEP layers adsorbed at pH 5.0 exhibited a cytophobic character when no

protein was present (Figure 4.36, left column). The cells appeared round with no signs of well-expressed FA or actin fibers. However, after adsorption of FN the cell morphology changed drastically. HDF spread to a high extent with lamellipodia formation, a sign of cell motility (Figure 4.36, middle column). Further, actin fibers were organized in bundles and vinculin was present in FA at the periphery of the cells. However, a clear trend in dependence on the nanostructure dimension was not observed. It was interesting to see that the cells were obviously in contact with the nanostructures indicated by pronounced filopodia formation, a sign for sensing of the nanostructures (Figure 4.36, right column). In contrast, cells seeded on the terminal PEI layer in PEM assembled at pH 5.0 had a completely different morphology (Figure 4.37). Initially, the cells appeared larger than cells seeded on the preceding HEP layer. Further, they also showed signs of beginning actin polymerization as well as FA formation and a slight increasing trend in cell size from small to larger nanostructures could be detected. However, the adsorption of FN did not have the same pronounced effect as previously seen on the preceding HEP layer. Moreover, it seemed that FN preadsorption had no effect at all. The cells spread to the same extent as under protein-free conditions. Further, actin organization as well as FA formation seemed to be silenced.

The evaluation of cells seeded on PEM assembled at alkaline conditions led to similar trends. First, cells seeded on the terminal HEP layer assembled at pH 9.0 also appeared round with no signs of well-expressed actin fibers or vinculin present in FA (Figure 4.38, left column). Further, it seemed that more cells adhered here compared to HEP at pH 5.0. Again, after adsorption of FN the cells strongly spread with pronounced lamellipodia formation. Further, actin was organized in bundles and vinculin was present in FA in the periphery as well as center of the cells. In addition, the cell size seemed to increase with increasing nanostructure dimension. Again, it was found in high magnification images that cells sensed the surface with enhanced filopodia formation, which appeared to be in contact with the nanostructures. Contradictory to the cells seeded on the terminal HEP layers, cells on the succeeding PEI layer assembled at pH 9.0 did not appear this viable (Figure 4.39). Most of the cells visualized did not even have a confine cell body. It seemed they adhered well, but the cytoplasm membrane burst with ongoing culture. As a result, actin fiber formation as well as FA development were absent. The appearance of cells did also not improve if FN was preadsorbed. Cells still seemed to be non-viable with no signs of organized actin fibers not to mention FA formation.

The quantification of cell adhesion supported the results found by qualitative analysis. It was observed that more cells adhered to layers formed at alkaline conditions in comparison to acidic conditions (Figure 4.40). Further, the effect of FN was always more pronounced on terminal HEP layers than on PEI layers, meaning that significantly more cells were counted on FN coated layers.
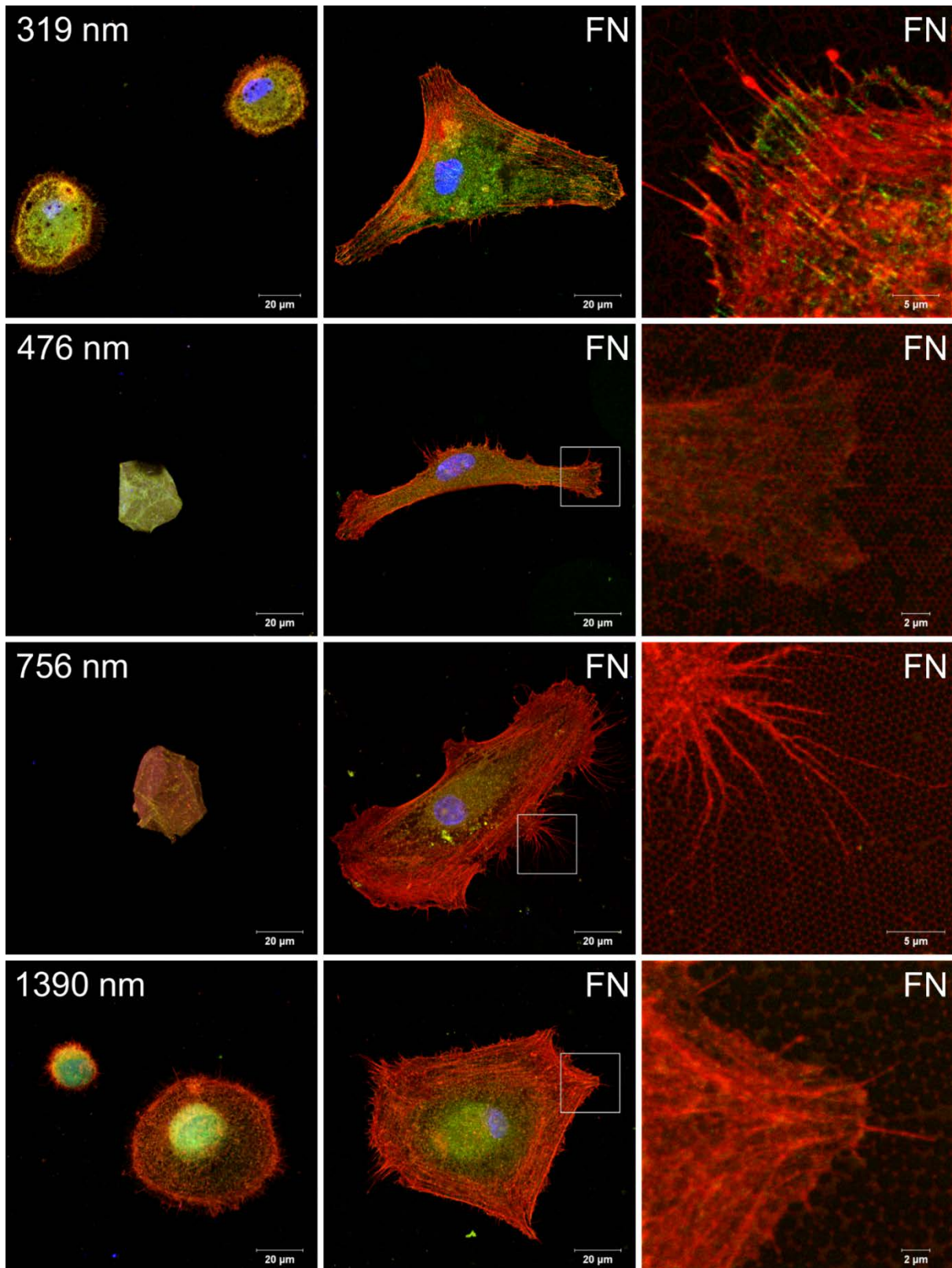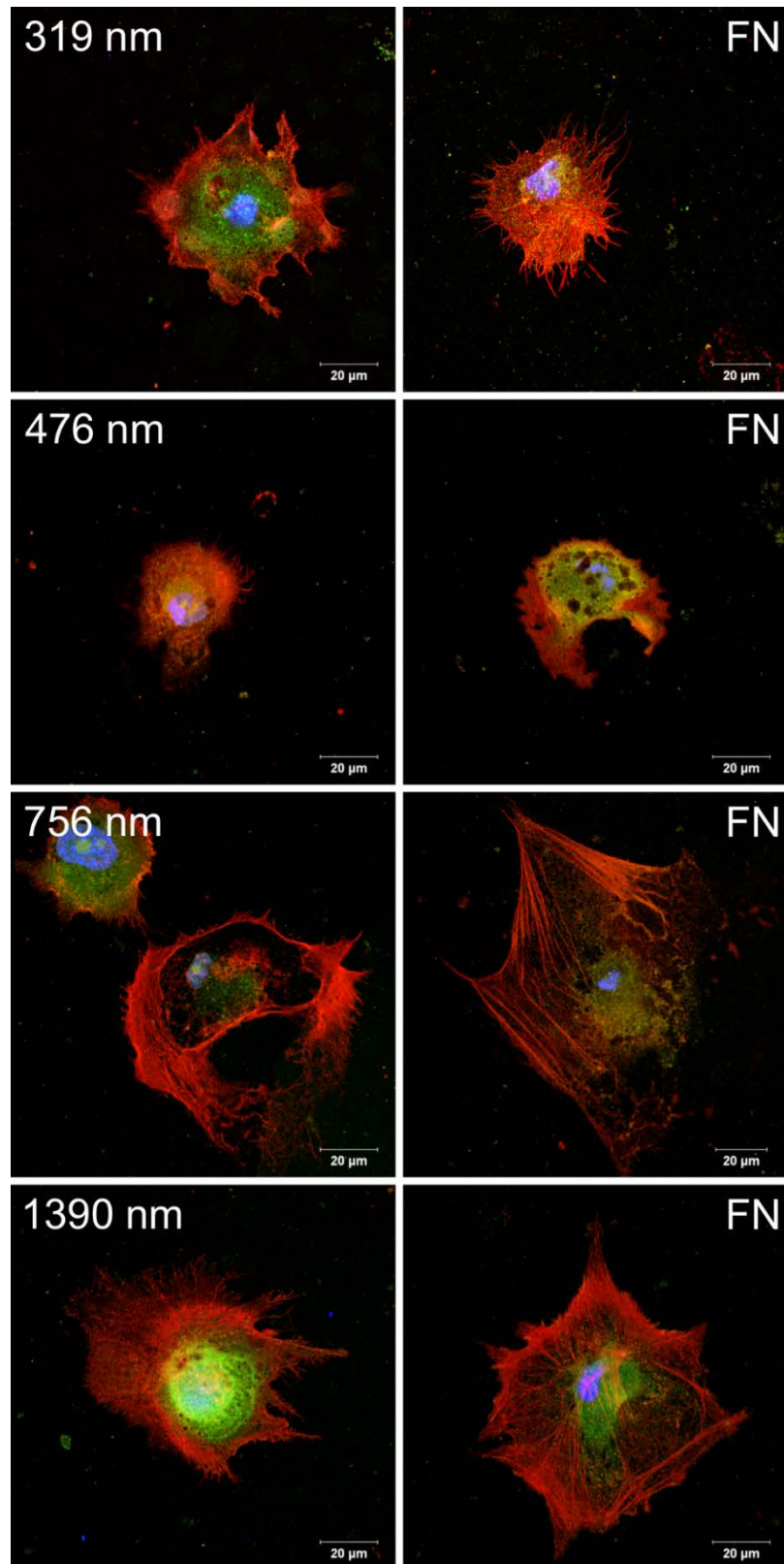
Figure 4.36 - CLSM images of HDF seeded on the terminal HEP layer *(PH)₄* prepared at pH 5.0 on different nanostructure sizes. The cells were seeded and cultured under protein-free conditions for 4 h; either without (left column) or with preadsorption of 2 *µ*g mL⁻¹ FN (middle column). Afterwards, they were stained for actin (red), vinculin (green) and nucleus (blue) [Scale: 20 *µ*m]. The right column shows magnified parts of the cells [Scale: 2 *µ*m or 5 *µ*m].

Figure 4.37 - CLSM images of HDF seeded on the terminal PEI layer *(PH)4P* **prepared at** pH 5.0 **on different nanostructure sizes. The cells were seeded and cultured under protein-free conditions for 4 h; either without (left column) or with preadsorption of 2 *μ*g mL^{-1} FN (right column). Afterwards, they were stained for actin (red), vinculin (green) and nucleus (blue). [Scale: 20 *μ*m]**

In contrast, the effect of FN adsorbed on PEI terminated layers was statistically not significant. Moreover, on most PEI surfaces less cells were detected after FN adsorption with the nanostructure dimension not mattering. Additionally, it was found that cell count was increasing on PEI layers from small to larger nanostructures, whereas it was decreasing on HEP layers, at least on structures obtained with PS-NP <1 μm. The evaluation of the projected cell areas revealed that cells seeded under protein-free conditions were always larger on PEI layers assembled at pH 5.0 in comparison to HEP, except on the smallest nanostructures (Figure 4.41A, B). However, after FN adsorption cells spread significantly more on HEP layers than on PEI layers, where the protein had no significant effect. In contrast, cells cultured under protein-free conditions on PEM assembled at pH 9.0 were always larger on HEP than on PEI (Figure 4.41C, D). Moreover, FN did not have any effect on the cell size on the terminal PEI layer. In addition, in both pH setups the cell size increased with increasing nanostructure dimensions. The results found in cell area analysis were also proved by calculation of the aspect ratio, an indicator for the polarization of cells (Figure 4.42). It was found that cells were much more polarized on HEP layers than on PEI layers, no matter which pH setup. Especially after FN adsorption, the aspect ratio increased to a high extent. Moreover, the polarization was significant on HEP of all structures. Further, polarization increased from small to larger nanostructures on HEP layers after FN adsorption. In contrast, cells seeded on the terminal PEI layer did not polarize at all after FN adsorption, fostering the results previously found in qualitative cell morphology analysis.

4.3.5.2 Cell proliferation

Proliferation of HDF on nanostructured surfaces modified with PEM of HEP and PEI was determined over a period of seven days under serum-conditions (Figure 4.43). Similar to planar and PEM-free nanostructured surfaces, the cells maintained a long lag phase and did not proliferate to a high degree up to three days of culture on all surfaces. However, after seven days the cell count increased dramatically. As previously described, PEM assembled on planar surfaces initially were less cytophobic than PEM formed on nanostructured surfaces (see section 4.1.5.4). However, cell proliferation on HEP terminated PEM assembled on nanostructured surfaces was significantly not different from that on planar surfaces, irrespective of the pH value. Here, similar values for the cell count were found (Figure 4.43A, C). The slight trend of decreasing count from small to larger structures previously found in the adhesion studies was not detected here. In contrast, proliferation of HDF on nanostructures terminated with PEI assembled at pH 5.0 was significantly lower than on planar surfaces (Figure 4.43B), especially after seven days of culture. Interestingly, the trend of increasing cell count with increasing nanostructure dimension observed in the adhesion studies was preserved here.
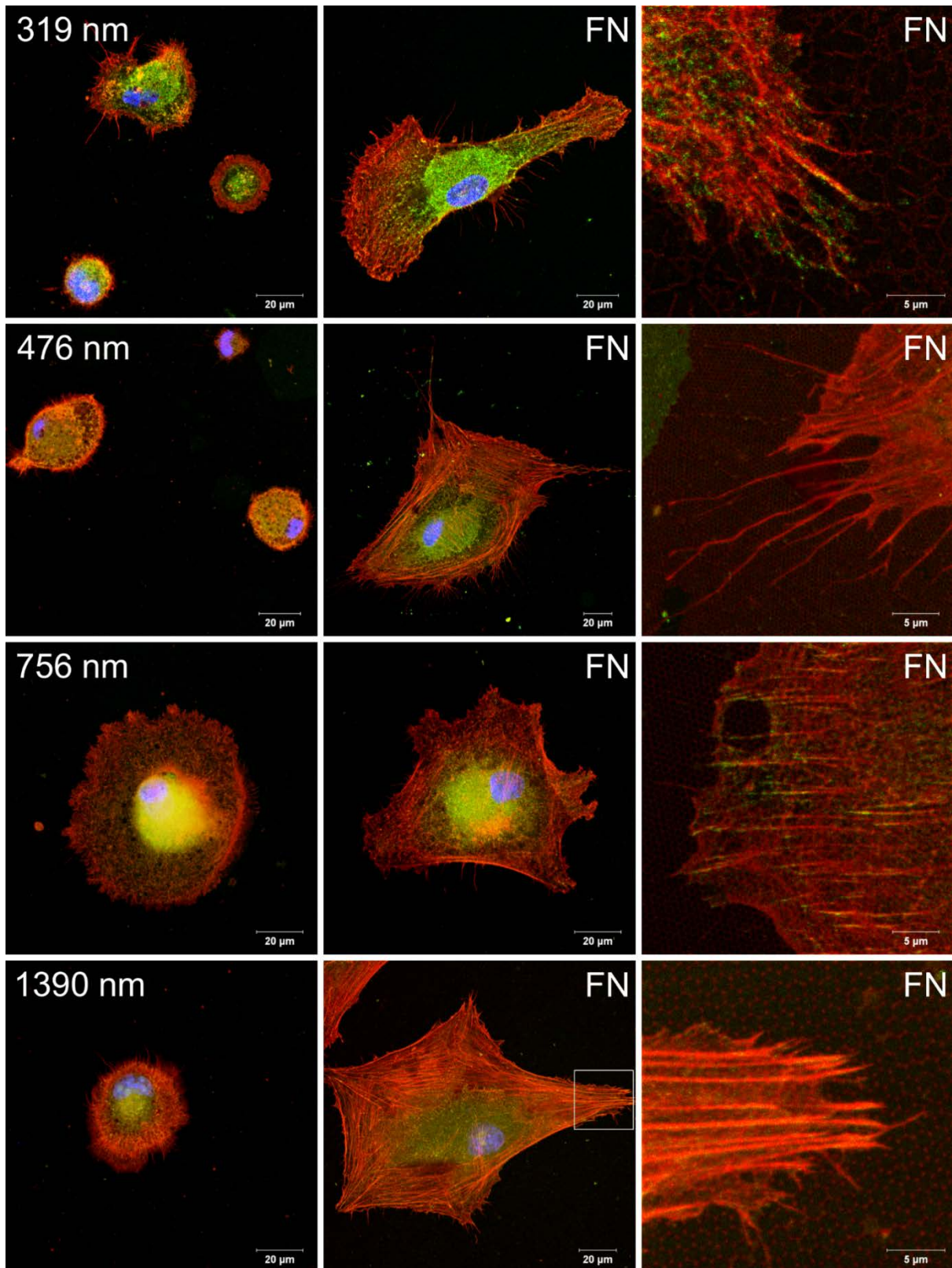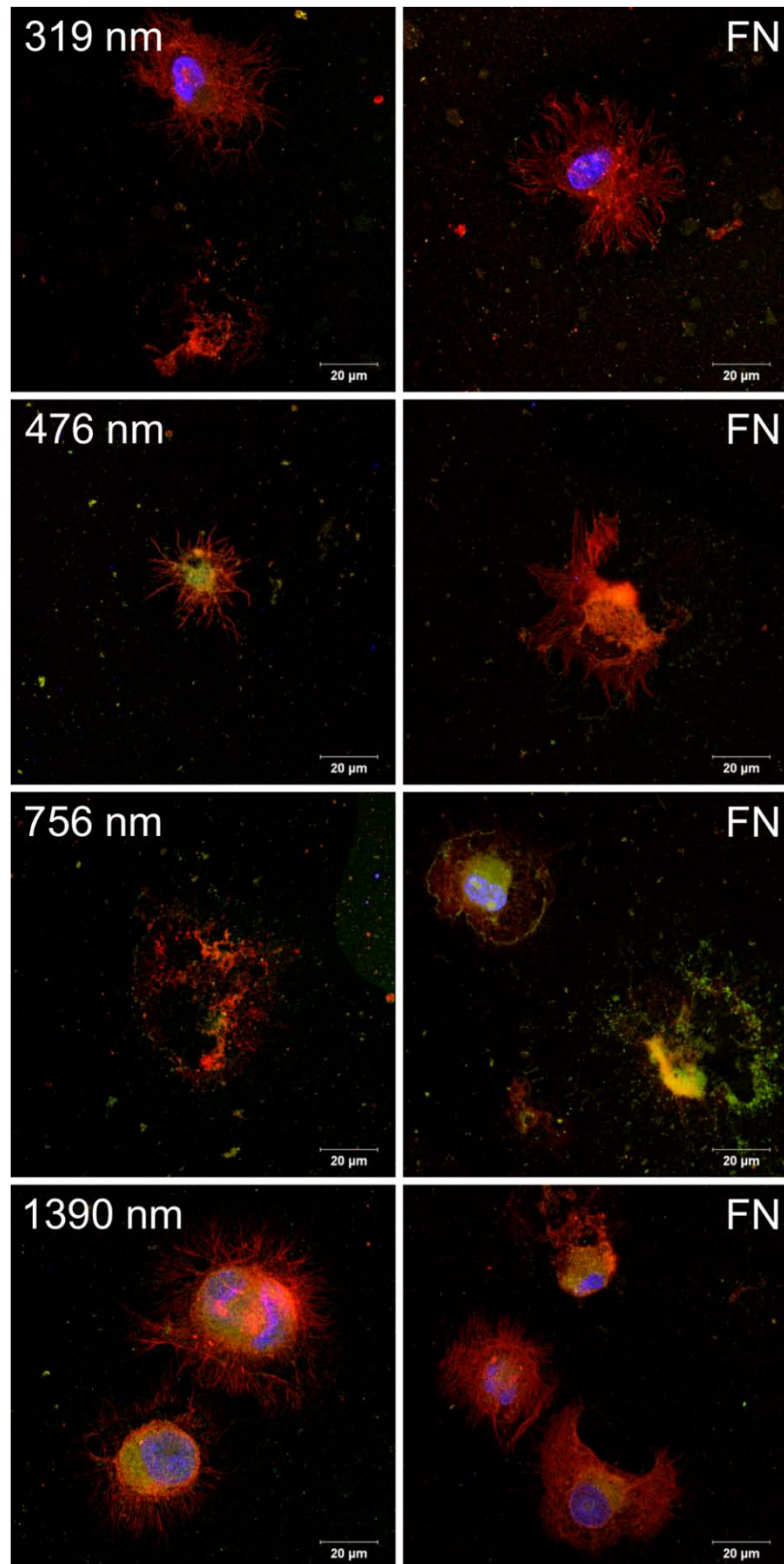
Figure 4.38 - CLSM images of HDF seeded on the terminal HEP layer *(PH)$_4$* prepared at pH 9.0 on different nanostructure sizes. The cells were seeded and cultured under protein-free conditions for 4 h; either without (left column) or with preadsorption of 2 *μ*g mL^{-1} FN (middle column). Afterwards, they were stained for actin (red), vinculin (green) and nucleus (blue) [Scale: 20 *μ*m]. The right column shows magnified parts of the cells [Scale: 5 *μ*m].

Figure 4.39 - CLSM images of HDF seeded on the terminal PEI layer *(PH)₄P* prepared at pH 9.0 on different nanostructure sizes. The cells were seeded and cultured under protein-free conditions for 4 h; either without (left column) or with preadsorption of 2 *µ*g mL⁻¹ FN (right column). Afterwards, they were stained for actin (red), vinculin (green) and nucleus (blue). [Scale: 20 *µ*m]

97
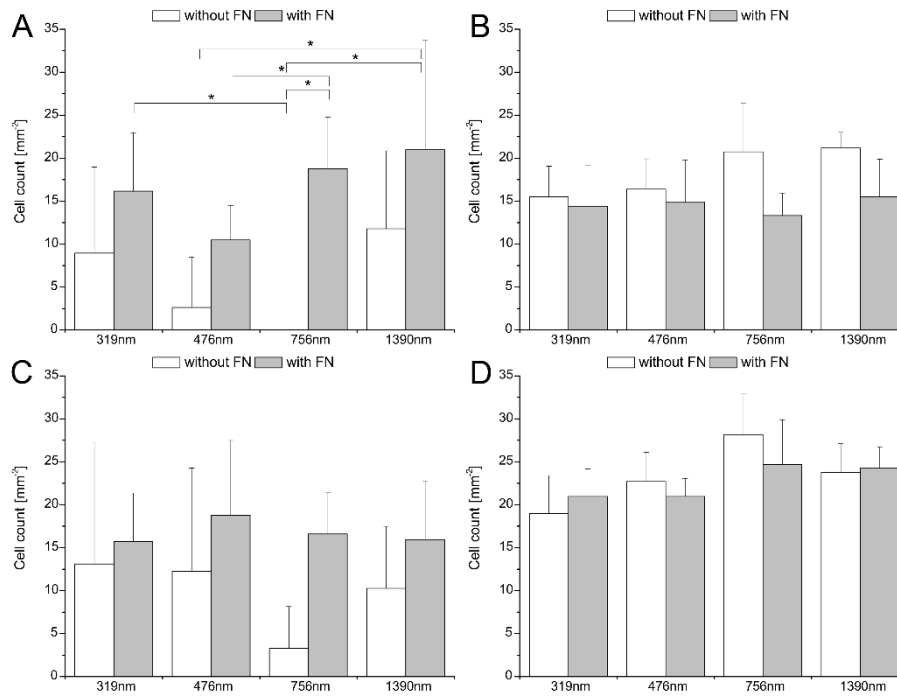
Figure 4.40 - Cell count on nanostructured surfaces with a terminal HEP (A, C) and PEI layer (B, D) prepared at pH 5.0 (A, B) or pH 9.0 (C, D) and either without (open bars) or with preadsorption of 2 μg mL^{-1} FN (gray bars) after 4 h of incubation (p < 0.05). Analyses of significant difference (ANOVA) are summarized in Table A.8 and Table A.11 due to clarity reasons.
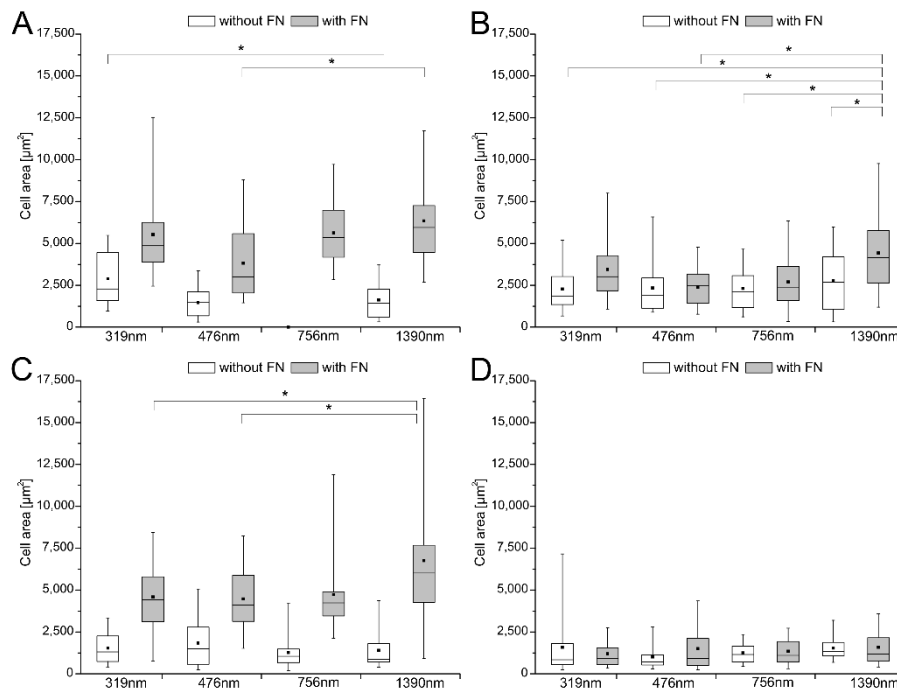
Figure 4.41 - Cell area on nanostructured surfaces with a terminal HEP (A, C) and PEI layer (B, D) prepared at pH 5.0 (A, B) or pH 9.0 (C, D) and either without (open bars) or with preadsorption of 2 μg mL^{-1} FN (gray bars) after 4 h of incubation (p < 0.05). Analyses of significant difference (ANOVA) are summarized in Table A.9 and Table A.12 due to clarity reasons.
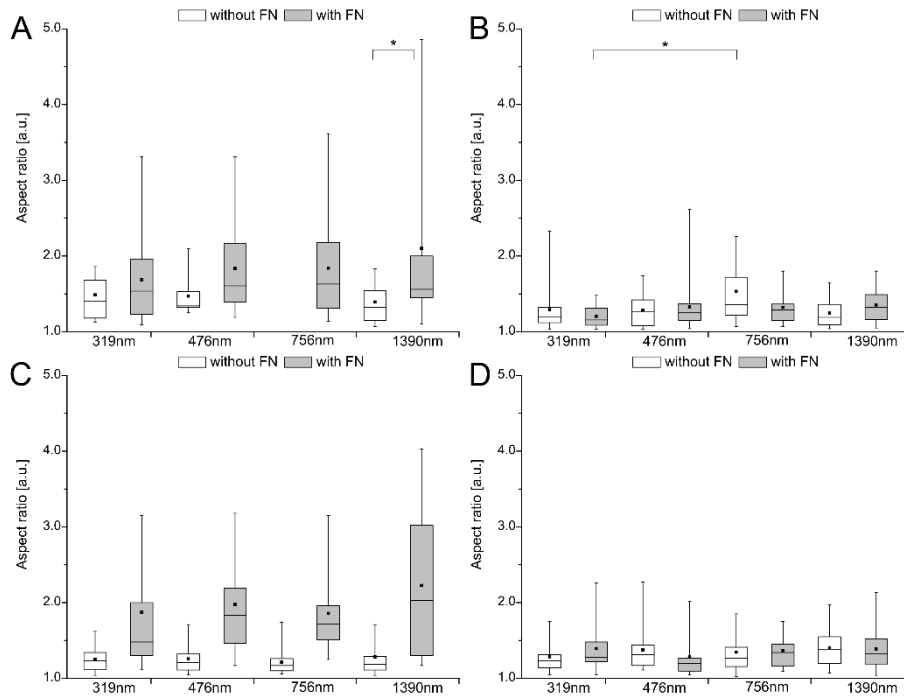
Figure 4.42 - Aspect ratio of cells on nanostructured surfaces with a terminal HEP (A, C) and PEI layer (B, D) prepared at pH 5.0 (A, B) or pH 9.0 (C, D) and either without (open bars) or with preadsorption of 2 μg mL^{-1} FN (gray bars) after 4 h of incubation (p < 0.05). Analyses of significant difference (ANOVA) are summarized in Table A.10 and Table A.13 due to clarity reasons.

However, no significant differences in cell count were found on the terminal PEI layer at pH 9.0 (Figure 4.43D). Here, cell count was low in comparison to all other chemically modified surfaces, no matter if planar or nanostructured. The difference in cell morphology on nanostructured surfaces with PEM assembled at pH 5.0 was not as strong as on planar surfaces (Figure A.8 and Figure A.9). HDF spread to the same extent and organized actin in bundles. In contrast, on PEM at pH 9.0 cells spread significantly more on HEP terminated layers, while on PEI layers HDF did not appear viable (Figure A.10 and Figure A.11). Again, cells were growing to confluence on HEP terminated PEM.

It can be summarized here, that adhesion and growth of HDF can be controlled to some degree using the novel combination of hexagonal arranged nanostructures modified with a PEM system of HEP and PEI. Since terminal PEI layers were rather cytophobic, especially at alkaline pH conditions, terminal HEP layers are more promising candidates for control of cell adhesion and growth. Still, the system of HEP and PEI layers might offer the possibility to be used for transfection purposes due to the high affinity of PEI for DNA constructs. In addition, the natural ECM environment of cells could be mimicked by using natural GAG as PEM building blocks. Further, such PEM systems might be applied as controlled release systems for localized supply of bioactive substances after multilayer loading.
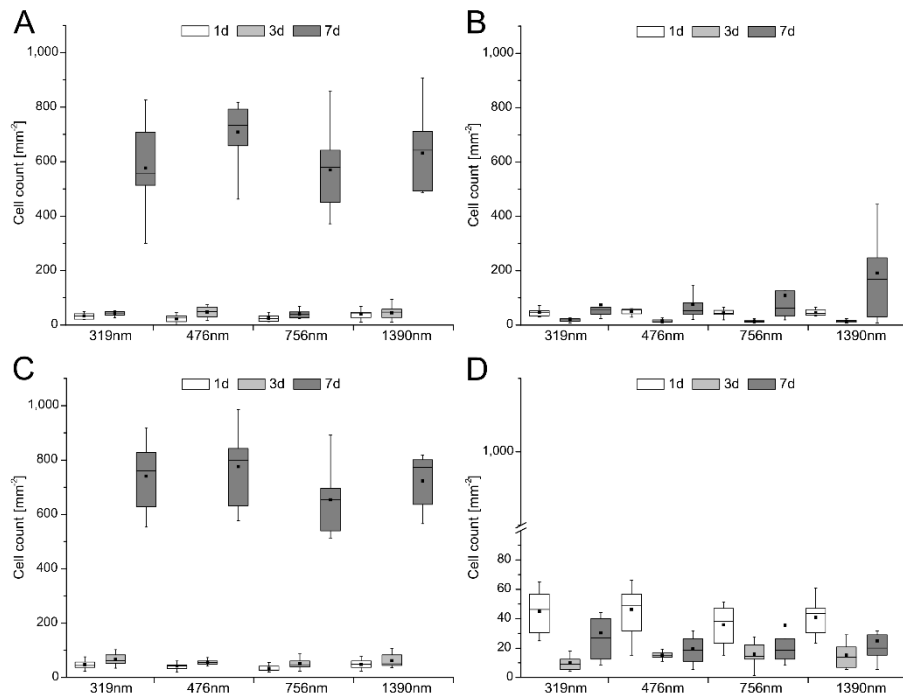
Figure 4.43 - Cell proliferation on PEM-modified nanostructured surfaces. The evolution of cell count is shown for the terminal HEP (PH)$_4$ (A, C) as well as terminal PEI layer (PH)$_4$P (B, D) assembled at either pH 5.0 (A, B) or pH 9.0 (C, D) over a period of 1 d (open bars), 3 d (light gray bars), and 7 d (dark gray bars) of culture ($p < 0.05$). Analyses of significant difference (ANOVA) are summarized from Table A.14 to Table A.17 due to clarity reasons.

5 Discussion

The highly interdisciplinary study presented here focused on design and modulation of physical and chemical properties of biomaterial surfaces to control biological interactions. One focus was the fabrication of tetrahedral nanostructures using nanosphere lithography (NSL). This technique enabled for precise control of size and distance of nanostructures by simply changing the particle diameter for preparation of colloidal masks. Moreover, the selective passivation of the biomaterial background using silane chemistry and activation of nanostructures using thiol chemistry created a unique system capable of directed control of cellular response. The particular novelty of the presented work was the combination of nanostructures designed by NSL with a polyelectrolyte multilayer (PEM) system assembled using the layer-by-layer (LbL) technique. That system, consisting of heparin (HEP) and poly (ethylene imine) (PEI), introduced unique surface characteristics upon modulation of the HEP solution pH value during multilayer assembly. Consequently, an exclusive system with topographical cues on the one hand and viscoelastic, chemical cues on the other hand enabled for control of cellular processes such as adhesion, fibronectin (FN) matrix formation, and proliferation. The first part of the discussion focuses on passivation strategies of planar surfaces and their effect on protein adsorption and, subsequently, cell adhesion and growth. The insights found are transferred to nanostructured surfaces and the effects of nanofeature size and distance are discussed in detail. Finally, the influence of the combination of NSL and LbL on cell adhesion and proliferation are highlighted in the last section and a conclusion for future investigations is drawn.

5.1 Planar surfaces

Since cells are able to sense topographical and chemical stimuli, one-component micro- or nanostructured biomaterial surfaces do not necessarily need to be passivated, at least for such applications where cell contact is desired. However, to enable specific interaction of cells with patterns of interest, an efficient passivation strategy is required in systems made of different materials. Hence, so-called PEGylation, i.e. the introduction of PEG-units on material surfaces, is often used to block proteins effectively from adsorption and, subsequently, cells from adhesion. The PEG-units can be deposited on the material surfaces by grafting [270, 271], polymerization [272], physisorption [273], hydrogel formation [274] or by simple self-assembly [275]. Additionally, the passivation efficacy can be dependent on the amount of PEG-units and, thus, the length of the immobilized molecules. Hence, a commercially available short-chain PEG (OEG) and a synthesized long-chain PEG (Urea) containing a urea linkage where compared in this study in terms of single protein adsorption and cell adhesion.

The formation of the blocking layer on silicon dioxide and glass surfaces is based on silane chemistry. The hydrolytically sensitive center of silanes reacts with hydroxyl groups of inorganic materials such as glass and silicon dioxide and forms stable covalent bonds. The simple modification procedure makes alkoxysilanes a widely used class for surface alteration. However, only methoxysilanes are capable of effectively forming a monolayer without catalysis [276], which holds for the short-chain PEG used in this study and which was dissolved in ethanol p.a. In contrast, the synthesized long-chain PEG is based on an ethoxysilane and required catalytic amounts of triethylamine to support monolayer formation. The coupling of silanes to inorganic surfaces includes four reaction steps. First, the labile methoxy or ethoxy groups are hydrolyzed by either bulk or surface-bound traces of water. After condensation to oligomers, hydrogen bonding with hydroxyl groups of the material surface occurs [276]. Finally, a covalent bond is formed upon drying or curing and simultaneous cleavage of water. In case of ethoxysilanes, ethanol is formed as byproduct, which makes them commercially interesting molecules due to the low toxicity of ethanol. Typically, only one bond is formed between the organosilane and the inorganic surface. Either the two remaining groups are condensed or free, resulting in possible formation of a dense organosilane layer, the so-called self-assembled monolayer (SAM), of which stability is dependent on intermolecular *van der Waals* interaction and length of the molecule. Thereby, the thickness of the SAM is dependent on the silane concentration and already low concentrations (0.25%) can result in multilayers [276]. The thickness of the OEG layer (~1.1 nm) in this study was in accordance with the literature [277]. Further, the covalent binding of the long-chain PEG resulted in layer thicknesses (~3.5 nm) almost meeting the expectations [243]. The different thicknesses of the silanes also resulted in slight differences in surface morphology and roughness. In comparison to plain silicon (R_a~3.3 Å), OEG exhibited cluster formation with slightly increased roughness (R_a~3.7 Å). The cluster formation was reduced on mPEG-urea-modified surfaces, but the roughness was further increased (R_a~4.5 Å). Still, all surfaces could be considered as extremely flat. The relatively low roughness values indicated that the molecules were assembled in submonolayers [277]. However, the slight differences in surface roughness did not have a significant effect on surface wettability. The static as well as the advancing contact angle characterize the general wettability of as well as low energy phases on homogeneous surfaces [263, 278, 279]. Here, both silane modified surfaces exhibited static WCA of θ~34°, which was slightly less hydrophilic than plain silicon (θ~25°), but still representing values for completely covered PEG surfaces [277]. Similar values were also obtained with a carboxyl terminated SAM on gold (θ~33°). Nevertheless, dynamic WCA measurements revealed an increased hysteresis of OEG silane in comparison to mPEG-urea-modified surfaces, that could indicate topological and/ or chemical heterogeneity [263, 278, 279]. The packing of molecules should be more compact on the OEG-SAM due to the lower steric hindrance during SAM

formation. However, the lower receding WCA, which also represents high energy phases on homogeneous surfaces, could indicate a distortion of the molecule structure, which led to water uptake and stronger polar interactions with the surrounding liquid and, thus, an increased WCA hysteresis [263, 280]. In contrast, interaction with water molecules was lower in case of mPEG-urea-modified surfaces possibly due to the stronger intermolecular interactions of the adjacent PEG chains, which resulted in higher receding WCA and, thus, in lower WCA hysteresis.

Non-specific protein binding can be reduced using polyether-based molecules such as the silanes used in this study. The polar regions in the molecules are able to form hydrogen bonds with water, which then incorporates within the silane layer and results in a repulsive barrier for proteins, the so-called hydration force [281]. Here, the chain length of surface bound molecules influenced the repulsion strength. Long-chain molecules compress during protein contact which results in entropy loss and absence of protein adsorption [30]. In contrast, short-chain molecules have less freedom for conformational changes and tight water binding is the mechanism behind such repulsive forces [30]. It was found here, that protein adsorption was not completely inhibited on OEG surfaces indicated by an increased protein layer thickness (Figure 4.1) as well as reduced wettability after protein contact (Figure 4.8). This was contradictory to other reports, where short-chain OEGs were able to prevent single protein adsorption [280, 282]. However, the inhibitory effect was improved by increasing the number of PEG-units, which resulted in stronger steric repulsion [280, 282] and which was the case for the long-chain PEG used in this study. The differences between short- and long-chain SAM were also found in adsorption/ desorption studies of FITC-labeled FN. However, the differences between silicon dioxide and OEG surfaces were not significant, and it was found elsewhere that hydrophilic surfaces bearing hydroxyl groups were also able to inhibit protein adsorption to some extent similar to OEG surfaces [10]. However, the low values of desorbed FN on mPEG-urea-modified surfaces were attributed to the reduced amounts of adsorbed FN. The high values of desorbed protein on TCPS were attributed to the increased affinity of FN to moderately wettable surfaces, where polar and hydrophobic interactions contributed to the protein adsorption to a higher extent than on highly wettable surfaces. Hence, also the binding strength was increased resulting in lower quantities of desorbed protein at high protein concentrations in comparison to plain silicon dioxide. Here, the higher protein quantities were attributed to the low binding strength of FN to the highly hydrophilic surface, which resulted in larger amounts of desorbed protein.

Protein adsorption and cell adhesion are dependent on the biomaterial properties, as described in section 1.1.2 and section 1.1.3. Except for plain gold, the WCA of the investigated surfaces was not in the reported range of moderately wettable surfaces ($\theta \sim 40°$-$70°$) [10, 14]. Moreover, all surfaces exhibited hydrophilic properties, which resulted in slightly cytophobic character under protein-free conditions indicated by differences in the cell morphology.

Nevertheless, the wettability cannot be used here as single parameter to explain cellular behavior since surface-bound molecules and functional groups influence the *Gibbs* free energy and, thus, subsequent events due to characteristic surface potentials. Here, differences in cytoskeleton organization and FA formation were found under protein-free conditions. Longitudinal actin fibers and FA in the periphery of the cell body were found in HDF on gold and silicon dioxide and were absent on MUDA-modified gold or OEG and mPEG-urea-modified surfaces. Hence, previous studies were confirmed that cell attachment was supported by moderately wettable surfaces while non-ionic hydrophilic surfaces inhibited it [10]. After preadsorption of FN, HDF started to express FA in the periphery and the center of the cell body and organized actin stress fibers in bundles circumferentially on gold, MUDA-modified gold and silicon dioxide. Hydrophilic or moderately wettable surfaces did not alter the protein conformation and the protein maintained its activity resulting in increased adhesion [35, 283]. In addition, HDF were able to adhere to the surface via their FN receptor [6]. A clear difference was found in HDF seeded on mPEG-urea-modified surfaces. First, most of these cells were lost during the staining and washing procedures required for immunofluorescence staining. The few cells found here neither did express FA nor did they organize actin in bundles. Hence, the protein and cell repellent properties of the surface already known from literature was confirmed here [243]. Since cells seeded on the OEG-SAM expressed FA and organized the cytoskeleton similar to cells on the other surfaces, the assumption was supported that OEG surfaces did not prevent protein adsorption completely, which was in accordance with previous studies [10] and which was dependent on molecule length and concentration [271]. The morphological data were supported by quantitative image analysis, which revealed that significantly more cells attached and spread on OEG-modified surfaces after preadsorption of FN while cell adhesion was completely absent on mPEG-urea-modified surfaces. Hence, the reduced protein repellent properties of OEG-modified silicon dioxide were confirmed again.

Beside cell adhesion, the ability of HDF to secrete their own extracellular FN matrix in dependence on the surface composition was investigated. ECM formation is crucial for cell growth and function and an impaired ability of matrix formation would result in apoptosis of adhesion-dependent cells [284]. After 24 h of culture, FN matrix was visualized and clear differences in dependence on the surface chemistry were found, which supported the results of cell adhesion studies. In contrast to all other planar surfaces, HDF adherent on the non-ionic hydrophilic OEG- or mPEG-urea SAM were not able to synthesize FN in fibrils, which was attributed to the weak adhesion and was also reported elsewhere [10, 285]. Further, FN fibrillogenesis depends on a substrate's hydrophobicity as it was shown that endothelial cells were able to reorganize FN fibrils to a higher extent on hydrophilic substrates due to the lower adhesion strength [286].

Finally, the results of the cell adhesion studies were also reflected by proliferation experiments over a course of seven days. Basically, an increased count of adherent cells resulted in an increased proliferation. Hence, most cells were found on gold and MUDA-modified gold. Especially on MUDA surfaces, an elevated growth was observed. Here, the dissociable carboxyl group led to a charged surface where proteins from the surrounding medium containing heat-inactivated serum could adsorb electrostatically, even exhibiting a negative net charge. However, the effect was slightly reduced when FN was preadsorbed due to competitive hindrance. Silicon dioxide and mPEG-urea-modified surfaces showed the least cytophilic character. Especially mPEG-urea initially blocked cells from adhesion up to three days if no FN was preadsorbed. However, after seven days the large confidence interval and standard deviation could indicate that the SAM lost some stability allowing the cells to adhere to exposed silicon dioxide areas. However, the reduced stability was not reported in the literature [243]. Based on the fact that protein adsorption was lowest on mPEG-urea SAM, which was also reported in the literature [243], and cell adhesion as well as FN matrix formation was effectively blocked, subsequent studies not including PEM were focused on the design of nanopatterns sandwiched by these long-chain SAM.

Another focus of the presented work was the selective formation of polyelectrolyte multilayers (PEM) on gold nanostructures. Initially, this formation was investigated on planar surfaces using fluorescein-labeled HEP. PEM formation with polysaccharide-based components was highly affected by the charge of the GAG, as it was shown recently. Thereby, thickness and PEM composition were adjusted by controlling the ionic strength and pH value of the PEL solution [232, 233]. If the ionic strength was within a narrow range or if the pH value of the adsorbing PEL was close to its pK_a value, an increase in layer thickness was observed [233, 234]. Additionally, swelling and hydration of PEM were influenced, too [235]. The PEM system used here consisted of HEP, a natural GAG, and PEI, a synthetic PEL. In a first step, the pH value of the HEP solution was adjusted to pH 7.0 and it was found that adsorption of the PEL followed different regimes [11]. Upon HEP adsorption, the fluorescence intensity always increased, while PEI led to a decrease in intensity. Evaluation of the absolute intensities after each adsorption step revealed exponential growth after HEP adsorption, while PEI adsorption resulted in more linear growth. Such exponential growth is typical for multilayers incorporating natural GAG, even though pH dependent [230]. In contrast, linear growth is typically observed in systems composed of synthetic PEL [217, 218]. Hence, a switch between exponential and linear growth seemed reasonable for the investigated system. The observed decrease in intensity after PEI adsorption could be attributed to solution complexation of previously adsorbed HEP molecules. However, since HEP adsorption always led to an increase in intensity, the large molecular weight of PEI could result in thick, water containing layers diminishing the fluorescence signal [226]. Further, the much smaller HEP molecules

could penetrate into the multilayers, resulting in more dense, intermingled PEM indicated by the increase in intensity.

The formation of the PEM system was further controlled by adjusting the pH value of the HEP solution to pH 5.0 and pH 9.0 for the adsorption of the terminal layer. Thereby, terminal layers of HEP were always more hydrophilic than terminal PEI layers, irrespective of the pH value and type of substrate. This difference was attributed to the type of functional groups since the dissociable sulfate monoesters, sulfamido groups, and carboxyl groups of HEP are more hydrophilic than the amino groups of PEI. Still, HEP at pH 9.0 was slightly less hydrophilic than HEP at pH 5.0, at least on planar gold. The pK_a value of PEI is ~8.5 and PEI should become less charged upon contact with HEP of pH 9.0, which would result in reduced HEP adsorption due to reduced ion pairing and, thus, a reduced wettability. Although different quantities of HEP could be expected in the preceding layer, no significant differences in wettability were found on the terminal PEI layer [226]. However, the slightly increased WCA at alkaline conditions might be attributed to a lower amount of HEP in the intermingled layers.

Even though the differences in wettability at the different pH conditions were marginal, clear differences were found in the bioactivity of the layers. During seven days of culture, HEP layers formed at pH 5.0 were initially less adhesive for HDF than at pH 9.0, but with slightly higher cell counts on planar gold. The increased bioactivity of HEP at pH 9.0 was also found elsewhere and could be related to its conformation [230]. The ion pairing at alkaline conditions was reduced due to the reduced charge of the preceding PEI layer, which led to lower amounts of HEP that bound with weaker interactions such as hydrogen bonding. Hence, the bioactivity was increased which was in line with other investigations [229]. In addition, the slightly reduced wettability and viscoelasticity should further support cell adhesion and growth [226]. In contrast, the difference between the pH conditions was even more pronounced on the terminal PEI layer. HDF were proliferating to a similar extent on PEI at pH 5.0 in comparison to the terminal HEP layers, even though with a stronger variation after seven days. Here, more HEP could be present in the intermingled layers, which led to an increased adsorption of proteins with HEP-binding domains such as vitronectin from the serum added to the cell culture [287]. Still, the pronounced effect of serum on cell growth found in a previous study was not seen here probably due to batch-to-batch variations of HEP [226]. Moreover, the cytotoxic effect of PEI assembled at pH 9.0, which could be shielded by serum as found in a previous study [226], was still present, impairing adhesion and growth of HDF [249]. Nevertheless, the data showed that a system of HEP and PEI could be used to regulate cell adhesion and growth by changing the pH value in the later stages of PEM assembly and that this change could have a strong effect on cellular behavior as shown in a recent paper [229].

5.2   Nanostructured surfaces

Nanosphere lithography (NSL) was used here to design tetrahedral nanostructures on planar inorganic surfaces. As mentioned in section 1.2.3.1, hexagonal close-packed (*hcp*) colloidal masks can be generated by various methods such as dip coating, self-assembly during solvent evaporation, self-assembly at the interface of two media, electrophoretic deposition or spin coating. Out of these techniques, spin coating is a fast and promising method and it was used here to assemble lattices of PS-NP, of which the diameter was <1 *μ*m. The spin coating process is defined by parameters such as ramp, rotation speed, temperature, concentration, and coating duration, which influence spreading and drying of the particle suspension [118]. Moreover, numerous defects in spin-coated layers can occur which limits the size of well-ordered areas to a few micrometers squared. Spin coating is widely used to create homogeneous films on a flat substrate. However, it is more difficult to achieve well-ordered monolayers (ML) using particle suspensions. Typically, the spin coating process follows several steps. First, a droplet of colloidal suspension is placed onto a mounted, plane substrate. Upon acceleration to a certain rotational speed, the suspension spreads and covers the whole substrate. Thereafter, an equilibrium between centrifugal force and viscous shear force thins the film. During the final stage, which is dominated by evaporation, the film thickness reduces to the order of the particle size. Here, particle aggregation is significantly affected by capillary forces. Thereby, the volatility of the solvent, typically water or alcohol, defines the transition speed between the different stages. The rapid evaporation of the solvent may result in a fast setting of the system. The packing of PS-NP into *hcp* lattices is defined by a balance between thermodynamics and the geometric arrangement of the particles in the film [288]. Thereby, the thermodynamic part tries to minimize the surface free energy by packing the particles in a lattice and maximizing the contact area between them. Here, PS-NP with different diameter were used to vary the size and distance of possible nanostructures. However, this required substantial preliminary experiments since optimal spin coating parameters to obtain large areas with well-ordered particles differed for every diameter. Nevertheless, a compromise had to be defined for every particle size since it was not possible to have an ideal ML covering the complete substrate surface [181]. Hence, a low ramp, i.e. the final speed is reached in a short time, was chosen with a relatively high rotational speed. The samples with the largest areas of well-ordered *hcp* lattices were characterized by low total surface coverage, as indicated by SEM and AFM images. This could be attributed to strong adhesive forces between the substrate surface and PS-NP, which remain trapped upon contact [289]. However, nanostructured surfaces obtained with the smallest PS-NP (319 nm) had the largest fraction of homogeneous gold due to an uncovered substrate surface, while nanostructures obtained with 756 nm PS-NP showed a large fraction of grain boundaries (GB). Nevertheless, the best results were obtained with PS-NP of 476 nm in diameter. Here, the largest, well-

107

ordered lattices were assembled, which was similar to results reported by Colson *et al.* [181]. Overall, GB are always an issue since colloidal mask formation starts at different locations of the substrate and *hcp* areas will assemble to larger masked areas without matching the borders of other masks. In contrast, the issues of GB formation and multilayer assembly were not prominent on surfaces obtained with the largest PS-NP diameter (1390 nm), since solvent evaporation was used here. Moreover, vacancies and particle dislocations appeared more often on such surfaces due to capillary forces during drying. Nevertheless, a compromise was found for each diameter resulting in a set of nanostructured surfaces with various feature dimensions applicable for protein adsorption as well as cell interaction studies. However, slight differences in calculated and measured nanostructure dimension and distance were found using AFM image analysis. Thereby, the distance between the single structures was insignificantly smaller, while the width was always larger than calculated values, which could be a result of tip correction for the used cantilevers (Table 4.1). Anyway, the height of the nanostructures was in good accordance with theoretical values that should ideally be ~85 nm (~10 nm chromium plus ~75 nm gold). Here, samples, which were randomly taken for AFM analysis, possible were not placed exactly oppositely to the gold source during the coating process, which would have resulted in lower heights due to a longer path length. Nevertheless, an overlapping of the mPEG-urea SAM, used for backfilling purposes, with the nanostructures should not occur since the nanofeature height was larger than a ML coating. In addition to that, it was reported that for single integrin binding a nanostructure distance of ~58 nm is sufficient [139, 290]. Since the distances between structures used in this study were larger, even for nanostructures obtained with the smallest PS-NP (319 nm), multiple integrin binding could occur. However, the focus of the study was on alteration of the physicochemistry of the obtained nanostructures and it still enabled for precise control of cellular response.

According to the definition made in section 3.4.1, the design of nanostructures rendered the surfaces hydrophobic with an increasing trend from small to large feature sizes. The modification with silanes (OEG or mPEG-urea) and subsequent modification with MUDA decreased the hydrophobicity on all nanostructured surfaces, resulting in hydrophilic surfaces ($\theta \leq 65°$) especially after introduction of the carboxyl group. However, the trend of decreased wettability from small to large nanopatterns was also found in advancing WCA during dynamic measurement. The modification with mPEG-urea SAM resulted in lower advancing and receding WCA if compared to OEG-SAM. Nevertheless, the difference in WCA hysteresis was not prominent since both advancing and receding WCA reduced to the same extent. The subsequent modification of the nanostructures with MUDA did not have a strong effect on the advancing, but on the receding WCA. The noticeable decrease indicated the formation of chemical heterogeneity due to the introduction of polar carboxyl groups [263]. The decrease was much more pronounced on mPEG-urea-modified nanostructures, indicating a higher

chemical heterogeneity if compared to the OEG-SAM, which also resulted in larger WCA hysteresis. The WCA is often calculated according to the model of Cassie and Baxter, assuming that air is entrapped within the nanostructures [291, 292]. These air fractions are dependent on the nanostructure dimensions as well as distances. Hence, higher WCA would exist on small feature dimensions in comparison to larger features, provided a defect-free pattern exists, which was not the case on most of the modified surfaces investigated here. It is assumed, that the decreased wettability from small to large feature dimensions was an effect of the increased fraction of GB on samples obtained with the smallest PS-NP due to impaired defect-free masking for large area fractions [293]. Hence, such surfaces appeared more homogeneous than surfaces with large feature dimensions and less GB. Overall, the trend of decreased wettability from small to large nanostructures was consistent with additional chemical modification and, hence, supported this assumption.

The specific interaction of cells with the tetrahedral nanostructures should be achieved by passivation of the free substrate surface with mPEG-urea SAM and by activation of the gold structures with MUDA. FITC-labeled FN was used to confirm not only the change in surface chemistry, but also the selective passivation/ activation of the material surfaces. After 1 h incubation at a high concentration of 50 μg mL^{-1}, it was approved by CLSM that FN adsorbed solely on MUDA-modified nanostructures and that no protein was detected on mPEG-urea SAM on the interstices. Still, large fractions of GB on samples obtained with the smallest PS-NP were found, which reduced with increasing PS-NP. Less GB were present on the largest nanostructures, but with more dislocations owing to the manufacturing method [159, 293]. In conclusion, the results confirmed that a selective modification of surface features in multicomponent systems was possible and allowed for control of protein adsorption using mPEG-urea SAM [243].

Besides protein adsorption, also cell adhesion was selectively controlled by nanostructured surfaces. Here, a clear difference was found in terms of FA formation and actin organization. Since OEG surfaces still showed a passivating effect under protein-free conditions (Figure 4.25) and the difference in comparison to mPEG-urea-modified surfaces was not distinct, images were selected for OEG conditions because they show that it was also possible to control cell adhesion with a short-chain PEG. On non-structured surfaces, more FN was present on OEG than on mPEG-urea surfaces and it was assumed here, that this was the same on nanostructured surfaces. However, the binding force of FN to OEG should be less than the binding force of FN to the gold structures [294-296]. Hence, during initial cell adhesion, the contractile forces of the cells were weak and FA formation was impaired in a similar way as on mPEG-urea. Even though the difference between OEG and mPEG-urea in terms of cell spreading was not prominent, still less cells were found on nanostructured surfaces modified with the long-chain SAM. Cell adhesion without FN preadsorption was driven only by physical

interaction forces. On one hand site, it was assumed that cell surface receptors could not make contact with the passivated silicon surface due to steric repulsion of PEG, which was also evident by the reduced adsorption of FN. On the other hand, gold-coated areas were modified with thiols that displayed a terminal carboxyl group. Here, physical interactions due to electrostatic interaction with positively charged epitopes of cell surface proteins and *van der Waals* interactions dominated at the beginning [43, 47], while cells started subsequently to secrete proteins (e.g., FN) and provided specific adhesive cues [7]. However, it could be assumed that the cell surface could only interact with the gold dots and was repelled by the surrounding passivated silicon dioxide. Hence, the effect of different size and distances of gold dots should be sensed by the cells. Another interesting finding was that cells adherent to the smallest feature size showed an extended filopodia formation in the absence of proteins, which decreased with increasing nanostructure dimensions under protein-free conditions. The extended filopodia formation, if compared to planar surfaces, was also found in other studies using nanopilars with similar dimensions as the smallest feature dimensions in the present work, even though the height was doubled [297]. An interesting finding of qualitative image analysis was that FA were formed on top of the nanopatterns, at least on the largest feature dimensions, which was an indicator for stable adhesion. It was also reported in the literature, that cells exclusively prefer patterns and avoid grooves [298]. The reduced FA formation on nanostructured surfaces in comparison to planar surfaces corresponded to the heterogeneous distribution of adhesive sites. Hence, potential ligation of integrins was confined to the adhesive surface structures and subsequent signal transduction pathways from FAK and activation of Rho events were affected [48, 62]. As a result, the less mature cytoskeleton on nanostructures in the absence of proteins applied less tension to integrins and led to smaller contacts, which were in the range of the structures. The dependence of adhesion plaque size on structure dimensions was reported elsewhere and it was proven that the plaques were increasing from small to larger structures as well [299]. Further, the binding of F-actin and its binding mechanism was found to be dependent on nanostructure size and distance [300].

Quantification of the previous observations did not reveal significant differences in cell count dependent on the protein coating on all nanostructured surfaces with both passivation strategies. However, the reduced cell count on mPEG-urea surfaces in comparison to OEG surfaces could be attributed to stronger repulsion forces. The obvious trend of decreasing cell area with increasing nanostructure dimension for both passivation strategies could be related to the surface homogeneity. The small surface patterns appeared more homogeneous to the cells since more adhesion sites were present on the same area fraction in comparison to the large surface patterns, even though they were smaller. In contrast, the distance between the large surface patterns was increased and larger areas of passivated substrate were exposed to the cells. Hence, HDF tried to avoid making contact with the passivated surface and cell

spreading was reduced [271]. Further, the cells did not need to sense additional adhesion sites since the large surface patterns allowed stable binding of more than one integrin [290]. Consequently, within the signaling cascade stable integrin binding led to stronger tension on the cytoskeleton and the cells became less motile [48, 62]. The lower repulsive forces of OEG-SAM also resulted in more elongated cells, especially if FN was preadsorbed. However, the slight trend of more elongated cells on larger structures was attributed to the distance between the FN coated areas, which were larger on larger structures. In addition, the larger feature sizes could lead to enlarged FA, which are a prerequisite for signal transduction events and subsequent actin polymerization [6, 10], leading to more stable adhesions and lower cell motility. Further, FN matrix formation was more pronounced on nanostructured surfaces in comparison to planar surfaces, but still showed typical footprints of FN fibrils observed on control surfaces. However, the FN fibrils were linked to the nanostructures and it was revealed by others that FN matrix synthesis was dependent on the pattern dimensions and increased with an elevated feature size [299]. However, because of the strong spreading and low height of cells the estimation about location of FN fibrils is not easy. It was assumed here that the FN fibrils were formed predominantly on the ventral cell surface, which was also found in other investigations [301, 302]. Despite the fact that the features were too large and too far away from each other to allow single integrin binding, it was proven that the cells were affected by the patterns as previously reported in the literature [243, 290].

Finally, cell proliferation followed the same trends as found in cell adhesion studies. Here, cell count decreased with increasing feature dimension. Even though no significant difference was found in the initial stages, the reduced amount of cells on nanostructured surfaces in comparison to planar gold surfaces after seven days of culture was attributed to the fact that potential ligation of integrins to adhesive surface structures was reduced. Hence, subsequent signal transduction pathways from FAK and other kinases were affected [48, 62]. Further, mitogen-activated protein kinases were activated through adapter proteins such as Grb2, SOS, and Ras [59]. As a result, not only initial events in cell-biomaterial-interaction could be controlled by size and dimension of adhesion sites. Moreover, subsequent cellular events such as growth were clearly affected by the system presented here. It is assumed that the steep increase in cell count after seven days was not caused by a loss in function of the surface coating. Even though the stability of the SAM was not investigated here, it was known from literature that they were stable for two weeks and longer, which would be necessary for stem cell culture [303, 304]. The change of growth behavior seemed to be attributed to the ECM synthesis by the cells. It was interesting to see that also during these longer culture periods the effect of topography was still sensed meaning that the distance of anchoring points for such a FN matrix effected cell behavior. Further, such topographic effects could also influence cell differentiation, which typically occurs after long-term culture.

5.3   Nanostructures and polyelectrolyte multilayers

The combination of NSL with LbL should lead to a unique system with specific topographical and chemical cues for control of cell adhesion and growth. The aim was to modify selectively nanostructures with a PEM system of HEP and PEI without coating the interstices, which were passivated with OEG-SAM to prevent PEL adsorption. Since LbL is based on electrostatic interaction and both short- and long-chain silanes possessed a terminal methyl group, which should not provide anchoring points for PEM assembly, the short-chain silane was selected for passivation purposes. Hence, in a first step it was investigated if it is possible to direct PEM assembly to the nanostructures only, using fluorescein-labeled HEP. The nanostructures were clearly detectable with CLSM, which was a first hint that the multilayer formation occurred mainly on the MUDA-modified nanostructures. However, differences were found in the fluorescence intensity in dependence on the terminating molecule. Thereby, HEP terminated layers appeared more blurry with a higher intensity than PEI layers. This was attributed to the fact that HEP was fluorescein-labeled and PEI not. Hence, the increased intensity seemed reasonable. However, a clear dependence on the pH value was not visible to the naked eye, but AFM investigations revealed that HEP layers assembled at pH 9.0 were slightly rougher than at pH 5.0. This phenomenon was also observed in one of the previous studies on planar surfaces [226] and it was speculated that erosion and solution complexation occurred due to lower electrostatic interaction and increased hydrogen bonding at alkaline conditions [240]. Further, ion pairing of HEP to adsorbed PEI at pH 5.0 resulted in a more complex and flat conformation of HEP than hydrogen bonding at pH 9.0, which led to more homogeneous surfaces and increased wettability [226]. In contrast, the smoother appearance of PEI terminated layers was also reported elsewhere and could be attributed to its large molecular weight which enables for straightening out of low surface irregularities [305]. The roughness was calculated from the interstices between the nanostructures, since a determination across the whole image would have led to non-reliable results due to the height of the structures themselves. However, the reduced roughness of terminal PEI layers could indicate that layer formation occurred everywhere, but reversibly on the interstices since the free substrate surface was passivated with uncharged OEG-SAM. Hence, material was removed from these interstices due to solution complexation leading to smoother appearance [240]. Another indicator for the removal of adsorbed material could be the reduced z-range on PEI layers in comparison to HEP terminated layers, which was apparent on all feature dimensions. Still, the increased z-range in contrast to pristine nanostructures, which have not been modified with PEM, was a further indicator for stable layer formation on top of the gold structures. Further, the difference in wettability, especially on the HEP terminating surfaces, indicated that layer formation was successful. First, the alteration between HEP and PEI layers was reasonable due to the different type of functional groups. The amino groups of PEI were

per se less hydrophilic than the acidic groups of HEP, which resulted in higher WCA. However, HEP layers at pH 5.0 were much more hydrophilic than HEP layers assembled at pH 9.0, meaning that the WCA were not accessible no matter which nanostructure dimension was investigated. This could indicate that more material was deposited here since the preceding PEI layer became highly charged at pH 5.0 resulting in a higher match of ion pairing, which was also shown for other systems using HEP [226, 230]. Further, a more flat conformation of HEP due to increased intramolecular repulsion, indicated by a lower surface roughness, led to increased exposure of the charged groups to the environment, resulting in stronger interaction with water molecules of the test liquid. In contrast, the adsorption of HEP at pH 9.0 was based on hydrogen bonding since PEI, of which the pK_a is ~8.5, was less charged and the electrostatic attraction was reduced [226]. However, the clear trend found in dependence on the nanostructure dimension could be explained with the gold fraction. Ideally, the amount of gold should be the same [306]. However, an increased GB formation was observed on the smallest nanostructures, which would increase the amount of homogeneous gold areas and, thus, the possibility of stable PEM assembly on top of the gold areas. Hence, more HEP was exposed to the environment resulting in an increased wettability. With increasing feature dimensions, the GB formation was slightly reduced leading to an increase of optimally arranged nanostructures and, thus, lower fractions of HEP terminated PEM, which resulted in a slightly reduced wettability with increasing feature dimension. In contrast, the adsorption of PEI did not cause a severe difference in wettability, neither in dependence on the pH value nor in dependence on the nanostructure dimension. This seemed to be attributed to its high molecular weight and, hence, its large amount of amino groups. However, the slight increasing trend in WCA hysteresis with increasing structure dimension found during dynamic WCA recording indicated an alteration not only in chemical, but also in topographical heterogeneity due to the reduction of GB.

The differences in surface wettability in dependence on the terminating molecule were also reflected by zeta potential measurements. First, passivation of the free substrate surface with OEG-SAM resulted in slightly reduced, yet still negative potential in comparison to bare glass, which indicated that the zeta potential was not only influenced by the outermost layer, but also by the bulk composition [307]. Hence, the thin OEG layer did not completely block the accessibility of the substrate. Further, one would expect a pronounced change in surface charge upon modification with MUDA due to the introduction of carboxyl groups on the gold structures. However, since the zeta potential was obtained across the whole sample surface, and not only across the nanostructures, again the bulk composition contributed to the potential including the OEG-SAM. Further, the reduced absolute values of MUDA-modified surfaces in comparison to OEG-modified surfaces were attributed to the enlarged fraction of modified background in contrast to the lower fraction of modifiable nanostructures. However, PEM

formation resulted in clear differences in zeta potential in dependence on the terminating molecule. First, HEP exhibited a sigmoidal progression of zeta potential between the selected pH extremes. Such progressions again indicated that not only the outermost layer, but also previous layers contributed to the potential [307], which was also found for other systems using HEP [230]. The point of zero charge (PZC) was an additional proof for this assumption, since it was located between that of HEP (pK_a ~ 0.5-1.5 for sulfate groups; pK_a ~ 3.0 for carboxylate groups) and PEI (pK_a ~ 8.5). However, the PZC as well as the zeta potential at physiological pH value were increasing with increasing feature dimension, which supported the previously made assumption that more HEP was present on the smallest structures due to the increased gold fraction because of the GB, which resulted in larger fractions of homogeneous PEM and, thus, lower zeta potential values. In turn, PEI layers always exhibited a positive potential throughout the investigated pH range, which indicated an effective screening of HEP molecules in the preceding layer through PEI [211] and a substantial charge reversal necessary for multilayer formation. However, clear trends in dependence on the nanostructure dimension were not found, which indicated as well that PEI also adsorbed reversibly on the OEG-modified substrate, supporting the results of WCA and AFM investigations.

The difference in zeta potential and surface wettability clearly had an influence on adhesion and growth of HDF. Since PEI layers exhibited intermediate wettability together with a positive zeta potential at physiological conditions, more cells adhered to these layers in comparison to HEP due to the innate negative potential of the cell membrane, which resulted in stronger electrostatic attraction. Further, less cells were present on layers assembled at pH 5.0 probably due to the increased amounts of HEP previously observed on planar surfaces [226]. Further, the cells did not show extended filopodia formation on HEP terminating layers due to their cytophobic character, which could be attributed to larger amounts of HEP that bound water to a high extent, which resulted in strong repulsive hydration forces. Such filopodia formation would at least indicate an active sensing of the surface. Hence, no clear trend was found here in dependence on the nanostructure dimension under protein-free condition. However, after preadsorption of FN, which should specifically bind to HEP due to the presence of HEP-binding domains [308, 309], cell adhesion was drastically improved on HEP terminating layers, which was also observed on planar surfaces before [230]. Since already more cells adhered to HEP at pH 9.0, the effect was more pronounced on HEP at pH 5.0. Further, an extended filopodia formation was observed after FN adsorption showing that the cells actively sensed the environment and tried to make contact with the nanostructures, where most of the FN should have adsorbed due to the preceding HEP layer. Even though negatively charged at physiological pH value, FN did not have a pronounced effect on cell adhesion to the positively charged PEI layers. Moreover, the cells, which showed signs of necrosis under protein-free conditions during cell adhesion studies, did not favor PEI terminated layers. Especially at

pH 9.0, the cells did not appear viable, which showed that PEI could also adsorb on the OEG-modified interstices, even though reversibly. Such cytotoxic effects were also observed on planar surfaces [226] and they were dependent on the molecular weight with lower cytotoxicity for low molecular weight PEI [249]. The cytotoxic effect was attributed to the disruption of the cell membrane (immediate) or of the mitochondrial membrane after uptake of PEI (delayed) [310]. The slightly reduced cytotoxic effect of PEI at pH 5.0 might be attributed to 'hidden' HEP in the intermingled layers, which was present in larger amounts in contrast to the terminal PEI layer at pH 9.0 [226]. The initial higher cell count on HEP layers at alkaline in contrast to acidic conditions was also observed in proliferation studies. However, since these were conducted with 10% serum, which contained additional proteins with HEP-binding domains such as vitronectin [287], the effect got lost during the culture period and similar cell counts were observed at the end of culture. Previously, it was observed that serum could lower the cytotoxicity of PEI terminated layers on planar surfaces [226]. Interestingly, such protective effect of serum on PEI layers was not observed on nanostructured surfaces. On PEI layers assembled at pH 9.0, serum had no effect at all and the cells were not growing and being necrotic right from the beginning. However, on PEI layers at pH 5.0 at least some cells survived, probably due to the intermingling with the large amounts of HEP, and proliferated. Moreover, a trend of increasing cell count was observed from small to large feature dimensions, which was contradictory to the pristine nanostructures without PEM modification, which could be attributed to layer stability. The reversible adsorption of PEI to the OEG-modified substrate might increase the favorable area for cells with time as it was shown that protein adsorption was not completely absent on OEG (see section 4.1.1.1). However, the cell supporting properties were still a multiple times lower than for HEP terminating layers.

Overall, the observations made here are promising for future investigations. PEI was used for intended application as transfection agent due to its high affinity to bind DNA constructs. However, due the observed cytotoxicity it could be exchanged with other polycations such as chitosan [229, 230] or poly-L-lysine [138], which would also result in other PEM properties. Further, ECM structures could be mimicked with such a PEM system using natural GAG such as collagen [224] or chondroitin sulfate [53]. Moreover, the viscoelasticity could be controlled precisely by cross-linking of molecules [50] or such PEM systems could be used as reservoir for bioactive molecules for localized release [311, 312]. Hence, possible applications are manifold and even stem cell self-renewal and differentiation could be controlled in the future [313, 314].

6   Summary and outlook

The aim of the presented PhD work was the modification of biomaterial surfaces at the nanoscale to manipulate surface properties and subsequent biological events such as protein adsorption, cell adhesion as well as proliferation. Hence, different strategies were applied here to achieve the ambitious targets. First, a passivation strategy was established to allow specific interaction of proteins and cells only with the material of interest in the used multicomponent system. Second, out of various methods to design nanostructures, the NSL was used here to obtain tetrahedral gold structures on planar surfaces to control adhesion and growth of HDF by changing size and distance of the nanofeatures. Finally, chemical heterogeneity and viscoelasticity were introduced to the already heterogenic, nanostructured system, which increased the degree of freedom for the researcher to control biological events. For this reason, the nanostructures have been modified with a PEM system composed of HEP and PEI using the widely applied LbL technique. It must be emphasized here that the combination of both techniques (NSL with LbL) was reported here for the first time ever. Such a unique system offers great potential and flexibility for application in regenerative medicine due to the possible control of substrate viscoelasticity or incorporation of bioactive molecules for potential localized release.

The passivation of material surfaces can be achieved with different strategies. The strategy used in this study was based on silane chemistry containing PEG units. Hence, a commercially available silane with low PEG content (n_{PEG} = 6-9) was compared in terms of protein repellent properties with a silane with high PEG content (n_{PEG} = 43). Since the latter one was not commercially available, it was synthesized during the course of the PhD work. It was shown that the increase in chain length had a promoting effect on protein repellence and it was decided to use such long-chain PEG silanes for further investigations with nanostructures. These nanostructures were obtained using the cost-effective NSL. The size and distance of the structures was controlled using colloids with varying diameter for mask formation. Since the nanostructured materials were a system composed of silicon and gold, selective chemistry was used here for modification. The silicon background was passivated with silane-based molecules, while the gold nanostructures were activated with thiols. It was shown that such selective chemistry led to control of protein adsorption and subsequent cellular events. Here, FITC-labeled FN selectively adsorbed on MUDA-modified gold nanostructures indicating an effective passivation strategy since no protein was found on the free substrate surface. Additionally, it was shown that adhesion of HDF was clearly affected by size and distance of the nanostructures, indicating a decrease in cell count and cell area from small to large feature dimensions. Further, HDF were able to secrete their own FN matrix and it was shown here that the FN fibrils followed the pattern direction. Finally, proliferation studies revealed that HDF growth was controlled by the feature size as well which pointed to

the importance of adhesive contacts, integrin ligation and signal transduction events for the long-term cell behavior, even though the cells secreted their own FN matrix during the culture period. Hence, the presented system of distinct patterns surrounded by passivating molecules offered the possibility for further modifications as well as other applications in controlling differentiation of stem cells as published by others [315].

A specific novelty of the study was the introduction of additional viscoelasticity by combining the NSL with the LbL technique, which would also allow for buildup of ECM-like structures upon usage of natural GAG. It was tried here to assemble a multilayer system composed of the natural GAG HEP and the synthetic polycation PEI selectively on top of the nanostructures. Multilayer composition and properties could be controlled by various parameters during PEM assembly and the pH value of the HEP solution was used here as tool to control resulting surface characteristics. The pH value was set to pH 5.0 and pH 9.0 during later stages of multilayer assembly and it was shown that such changes affected surface properties such as wettability, charge, or topography. It was proven with fluorescein-labeled HEP that PEM formation mainly occurred on the nanostructures, but also on the interstices which have been modified with short-chain PEG silanes to prevent such adsorption. However, it was assumed that the adsorption was reversible since surface wettability, charge, and topography changed in dependence on the nanostructure dimension and terminating molecule. Hence, solution complexation could be favored at certain conditions. However, adhesion and growth of HDF was influenced by the LbL-modified nanostructures, even though in an opposite manner than on nanostructures without such a PEM system. Here, the terminating molecule seemed to have a stronger effect on cellular events than the underlying nanostructures. Thereby, HEP layers supported adhesion of HDF to a higher extent than PEI layers with a stronger promoting effect at pH 9.0 probably due to the lower HEP content. However, PEI layers at pH 9.0 were highly cytotoxic and even serum-containing culture could not reduce the toxic effects as previously found on planar surfaces [226] probably due to the reduced adhesive areas. Provided the cytotoxic effect of PEI can be limited, such systems are attractive for *in situ* transfection studies. In contrast, the precise control of the characteristics of terminal HEP layers makes such systems interesting for applications, where cellular interaction needs to be controlled such as in implantology. Overall, pristine nanostructures or in combination with assembled multilayers might find application in fundamental studies to guide stem cell differentiation.

7   References

1.   Ratner B.D., H.A.S., Schoen F.J., Lemons J.E., *Biomaterials science: An Introduction to Materials in Medicine, 2nd edition.* Elsevier Academic press, 2004.

2.   Hench, L.L. and J.M. Polak, *Third-Generation Biomedical Materials.* Science, 2002. **295**(5557): p. 1014-1017.

3.   Groth, T., *"Biomaterialien" und Biokompatibilität.* Quintessenz Zahntech, 2005. **31**(12): p. 1309-1314.

4.   Shin, H., S. Jo, and A.G. Mikos, *Biomimetic materials for tissue engineering.* Biomaterials, 2003. **24**(24): p. 4353-4364.

5.   Groth, T., et al., *Development of Bioactive Surface Coatings for Tissue Engineering Applications.* Biomedicine & Pharmacotherapy, 2008. **62**(8): p. 488-489.

6.   Altankov, G., F. Grinnell, and T. Groth, *Studies on the biocompatibility of materials: fibroblast reorganization of substratum-bound fibronectin on surfaces varying in wettability.* J Biomed Mater Res, 1996. **30**(3): p. 385-91.

7.   Altankov, G. and T. Groth, *Fibronectin matrix formation by human fibroblasts on surfaces varying in wettability.* Journal of Biomaterials Science-Polymer Edition, 1996. **8**(4): p. 299-310.

8.   Altankov, G., K. Richau, and T. Groth, *The role of surface zeta potential and substratum chemistry for regulation of dermal fibroblasts interaction.* Materialwissenschaft Und Werkstofftechnik, 2003. **34**(12): p. 1120-1128.

9.   Keselowsky, B.G., D.M. Collard, and A.J. Garcia, *Surface chemistry modulates fibronectin conformation and directs integrin binding and specificity to control cell adhesion.* Journal of Biomedical Materials Research Part A, 2003. **66A**(2): p. 247-259.

10. Faucheux, N., et al., *Self-assembled monolayers with different terminating groups as model substrates for cell adhesion studies.* Biomaterials, 2004. **25**(14): p. 2721-2730.

11. Niepel, M.S., et al., *Nanoscaled Surface Patterns Influence Adhesion and Growth of Human Dermal Fibroblasts.* Langmuir, 2013. **29**(43): p. 13278-13290.

12. Castner, D.G. and B.D. Ratner, *Biomedical surface science: Foundations to frontiers.* Surface Science, 2002. **500**(1–3): p. 28-60.

13. Tzoneva, R., N. Faucheux, and T. Groth, *Wettability of substrata controls cell-substrate and cell-cell adhesions.* Biochimica Et Biophysica Acta-General Subjects, 2007. **1770**(11): p. 1538-1547.

14. Vogler, E.A., *Structure and reactivity of water at biomaterial surfaces.* Advances in Colloid and Interface Science, 1998. **74**(1–3): p. 69-117.

15. Wang, Y.X., et al., *Effects of the chemical structure and the surface properties of polymeric biomaterials on their biocompatibility.* Pharmaceutical Research, 2004. **21**(8): p. 1362-1373.

16. Vitte, J., et al., *Is there a predictable relationship between surface physical-chemical properties and cell behaviour at the interface?* Eur Cell Mater, 2004. **7**: p. 52-63; discussion 63.

17. Yamanlar, S., et al., *Surface functionalization of hyaluronic acid hydrogels by polyelectrolyte multilayer films.* Biomaterials, 2011. **32**(24): p. 5590-5599.

18. Gribova, V., R. Auzely-Velty, and C. Picart, *Polyelectrolyte Multilayer Assemblies on Materials Surfaces: From Cell Adhesion to Tissue Engineering.* Chemistry of Materials, 2012. **24**(5): p. 854-869.

19. Extrand, C.W., *Contact angles and hysteresis on surfaces with chemically heterogeneous islands.* Langmuir, 2003. **19**(9): p. 3793-3796.

20. Wong, S.Y., et al., *Drastically Lowered Protein Adsorption on Microbicidal Hydrophobic/Hydrophilic Polyelectrolyte Multilayers.* Biomacromolecules, 2012.

21. Iliev, D., N.C. Pesheva, and S. Iliev, *Contact Angle Hysteresis and Meniscus Corrugation on Randomly Heterogeneous Surfaces with Mesa Type Defects.* Langmuir, 2013.

22. Dee, K.C., D.A. Puleo, and R. Bizios, *Protein-Surface Interactions*, in *An Introduction To Tissue-Biomaterial Interactions*. 2003, John Wiley & Sons, Inc. p. 37-52.

23.   Nychka, J.A. and M.M. Gentleman, *Implications of Wettability in Biological Materials Science.* Jom, 2010. **62**(7): p. 39-48.

24.   Andrade, J.D. and V. Hlady, *Vroman effects, techniques, and philosophies.* J Biomater Sci Polym Ed, 1991. **2**(3): p. 161-72.

25.   Hubbell, J.A., *Biomaterials in Tissue Engineering.* Bio-Technology, 1995. **13**(6): p. 565-576.

26.   Czeslik, C., *Proteinadsorption an festen Grenzflächen.* Chemie unserer Zeit, 2006. **40**: p. 8.

27.   Norde, W. and J. Lyklema, *Why proteins prefer interfaces.* J Biomater Sci Polym Ed, 1991. **2**(3): p. 183-202.

28.   Andrade, J.D., V. Hlady, and A.P. Wei, *Adsorption of Complex Proteins at Interfaces.* Pure and Applied Chemistry, 1992. **64**(11): p. 1777-1781.

29.   Groth, T., et al., *Protein Adsorption, Lymphocyte Adhesion and Platelet-Adhesion Activation on Polyurethane Ureas Is Related to Hard Segment Content and Composition.* Journal of Biomaterials Science-Polymer Edition, 1994. **6**(6): p. 497-510.

30.   Zheng, J., et al., *Strong repulsive forces between protein and oligo (ethylene glycol) self-assembled monolayers: A molecular simulation study.* Biophysical Journal, 2005. **89**(1): p. 158-166.

31.   Salloum, D.S. and J.B. Schlenoff, *Protein adsorption modalities on polyelectrolyte multilayers.* Biomacromolecules, 2004. **5**(3): p. 1089-1096.

32.   Tsai, W.B., et al., *Platelet adhesion to polystyrene-based surfaces preadsorbed with plasmas selectively depleted in fibrinogen, fibronectin, vitronectin, or von Willebrand's factor.* Journal of Biomedical Materials Research, 2002. **60**(3): p. 348-359.

33.   Tang, L.P. and J.W. Eaton, *Fibrin(Ogen) Mediates Acute Inflammatory Responses to Biomaterials.* Journal of Experimental Medicine, 1993. **178**(6): p. 2147-2156.

34.   Ngankam, A.P., G.Z. Mao, and P.R. Van Tassel, *Fibronectin adsorption onto polyelectrolyte multilayer films.* Langmuir, 2004. **20**(8): p. 3362-3370.

35.   Grinnell, F. and M.K. Feld, *Fibronectin Adsorption on Hydrophilic and Hydrophobic Surfaces Detected by Antibody-Binding and Analyzed during Cell-Adhesion in Serum-Containing Medium.* Journal of Biological Chemistry, 1982. **257**(9): p. 4888-4893.

36.   Ishihara, K., et al., *Effects of Phospholipid Adsorption on Nonthrombogenicity of Polymer with Phospholipid Polar Group.* Journal of Biomedical Materials Research, 1993. **27**(10): p. 1309-1314.

37.   Tziampazis, E., J. Kohn, and P.V. Moghe, *PEG-variant biomaterials as selectively adhesive protein templates: model surfaces for controlled cell adhesion and migration.* Biomaterials, 2000. **21**(5): p. 511-520.

38.   Lee, J.H., J. Kopecek, and J.D. Andrade, *Protein-Resistant Surfaces Prepared by Peo-Containing Block Copolymer Surfactants.* Journal of Biomedical Materials Research, 1989. **23**(3): p. 351-368.

39.   Andrade, J.D. and V. Hlady, *Protein Adsorption and Materials Biocompatibility - a Tutorial Review and Suggested Hypotheses.* Advances in Polymer Science, 1986. **79**: p. 1-63.

40.   Bosman, F.T. and I. Stamenkovic, *Functional structure and composition of the extracellular matrix.* Journal of Pathology, 2003. **200**(4): p. 423-428.

41.   Hynes, R.O., *Integrins: Bidirectional, allosteric signaling machines.* Cell, 2002. **110**(6): p. 673-687.

42.   Giancotti, F.G. and E. Ruoslahti, *Integrin Signaling.* Science, 1999. **285**(5430): p. 1028-1033.

43.   Bongrand, P., C. Capo, and R. Depieds, *Physics of cell adhesion.* Progress in Surface Science, 1982. **12**(3): p. 217-285.

44.   Altankov, G., et al., *Modulating the biocompatibility of polymer surfaces with poly(ethylene glycol): effect of fibronectin.* J Biomed Mater Res, 2000. **52**(1): p. 219-30.

45.   Tamada, Y. and Y. Ikada, *Fibroblast Growth on Polymer Surfaces and Biosynthesis of Collagen.* Journal of Biomedical Materials Research, 1994. **28**(7): p. 783-789.

46. Schauer, R., *Sialic acids and their role as biological masks.* Trends in Biochemical Sciences, 1985. **10**(9): p. 357-360.

47. Trommler, A., D. Gingell, and H. Wolf, *Red Blood-Cells Experience Electrostatic Repulsion but Make Molecular Adhesions with Glass.* Biophysical Journal, 1985. **48**(5): p. 835-841.

48. Ladoux, B. and A. Nicolas, *Physically based principles of cell adhesion mechanosensitivity in tissues.* Reports on Progress in Physics, 2012. **75**(11): p. 116601.

49. Discher, D.E., P. Janmey, and Y.L. Wang, *Tissue cells feel and respond to the stiffness of their substrate.* Science, 2005. **310**(5751): p. 1139-1143.

50. Ren, K.F., et al., *Polyelectrolyte multilayer films of controlled stiffness modulate myoblast cell differentiation.* Advanced Functional Materials, 2008. **18**(9): p. 1378-1389.

51. Boudou, T., et al., *Polyelectrolyte multilayer nanofilms used as thin materials for cell mechano-sensitivity studies.* Macromol Biosci, 2011. **11**(1): p. 77-89.

52. Hopp, I., et al., *The influence of substrate stiffness gradients on primary human dermal fibroblasts.* Biomaterials, 2013. **34**(0): p. 5070-7.

53. Grohmann, S., et al., *Colloidal Force Spectroscopy and Cell Biological Investigations on Biomimetic Polyelectrolyte Multilayer Coatings Composed of Chondroitin Sulfate and Heparin.* Biomacromolecules, 2011. **12**(6): p. 1987-1997.

54. Diener, A., et al., *Control of focal adhesion dynamics by material surface characteristics.* Biomaterials, 2005. **26**(4): p. 383-392.

55. Gentile, F., et al., *Cells preferentially grow on rough substrates.* Biomaterials, 2010. **31**(28): p. 7205-7212.

56. Guduru, D., et al., *Nanostructured material surfaces--preparation, effect on cellular behavior, and potential biomedical applications: a review.* Int J Artif Organs, 2011. **34**(10): p. 963-85.

57. McNamara, L.E., et al., *Nanotopographical control of stem cell differentiation.* J Tissue Eng, 2010. **2010**: p. 120623.

58. Teo, B.K., et al., *Nanotopography/mechanical induction of stem-cell differentiation.* Methods Cell Biol, 2010. **98**: p. 241-94.

59. Miranti, C.K. and J.S. Brugge, *Sensing the environment: a historical perspective on integrin signal transduction.* Nature Cell Biology, 2002. **4**(4): p. E83-E90.

60. Huang, H.D., R.D. Kamm, and R.T. Lee, *Cell mechanics and mechanotransduction: pathways, probes, and physiology.* American Journal of Physiology-Cell Physiology, 2004. **287**(1): p. C1-C11.

61. Iqbal, J. and M. Zaidi, *Molecular regulation of mechanotransduction.* Biochemical and Biophysical Research Communications, 2005. **328**(3): p. 751-755.

62. Eyckmans, J., et al., *A Hitchhiker's Guide to Mechanobiology.* Developmental Cell, 2011. **21**(1): p. 35-47.

63. von der Mark, K., et al., *Nanoscale engineering of biomimetic surfaces: cues from the extracellular matrix.* Cell and Tissue Research, 2010. **339**(1): p. 131-153.

64. Schaller, M.D. and J.T. Parsons, *Pp125(Fak)-Dependent Tyrosine Phosphorylation of Paxillin Creates a High-Affinity Binding-Site for Crk.* Molecular and Cellular Biology, 1995. **15**(5): p. 2635-2645.

65. Schlaepfer, D.D., S.K. Mitra, and D. Ilic, *Control of motile and invasive cell phenotypes by focal adhesion kinase.* Biochimica et Biophysica Acta (BBA) - Molecular Cell Research, 2004. **1692**(2–3): p. 77-102.

66. Salasznyk, R.M., et al., *Activation of FAK is necessary for the osteogenic differentiation of human mesenchymal stem cells on laminin-5.* Journal of Cellular Biochemistry, 2007. **100**(2): p. 499-514.

67. Salasznyk, R.M., et al., *Focal adhesion kinase signaling pathways regulate the osteogenic differentiation of human mesenchymal stem cells.* Experimental Cell Research, 2007. **313**(1): p. 22-37.

68. Chen, Y.C., et al., *Induction and regulation of differentiation in neural stem cells on ultra-nanocrystalline diamond films.* Biomaterials, 2010. **31**(21): p. 5575-5587.

69. Ge, C.X., et al., *Critical role of the extracellular signal-regulated kinase-MAPK pathway in osteoblast differentiation and skeletal development.* Journal of Cell Biology, 2007. **176**(5): p. 709-718.

70. Harburger, D.S. and D.A. Calderwood, *Integrin signalling at a glance.* Journal of Cell Science, 2009. **122**(2): p. 159-163.

71. Biggs, M.J.P., et al., *The use of nanoscale topography to modulate the dynamics of adhesion formation in primary osteoblasts and ERK/MAPK signalling in STRO-1+enriched skeletal stem cells.* Biomaterials, 2009. **30**(28): p. 5094-5103.

72. Guilak, F., et al., *Control of Stem Cell Fate by Physical Interactions with the Extracellular Matrix.* Cell Stem Cell, 2009. **5**(1): p. 17-26.

73. Lanfer, B., et al., *The growth and differentiation of mesenchymal stem and progenitor cells cultured on aligned collagen matrices.* Biomaterials, 2009. **30**(30): p. 5950-5958.

74. Kimura, K., et al., *Regulation of myosin phosphatase by Rho and Rho-Associated kinase (Rho-kinase).* Science, 1996. **273**(5272): p. 245-248.

75. Cohen, D.M. and C.S. Chen, eds. *Mechanical control of stem cell differentiation* StemBook. 2008, ed. The Stem Cell Research Community: doi/10.3824/stembook.1.26.1.

76. Klee, D., et al., *Surface modification of poly(vinylidenefluoride) to improve the osteoblast adhesion.* Biomaterials, 2003. **24**(21): p. 3663-3670.

77. Vonarbourg, A., et al., *Parameters influencing the stealthiness of colloidal drug delivery systems.* Biomaterials, 2006. **27**(24): p. 4356-4373.

78. Bacakova, L., et al., *Adhesion and proliferation of rat vascular smooth muscle cells (VSMC) on polyethylene implanted with O+ and C+ ions.* Journal of Biomaterials Science-Polymer Edition, 2001. **12**(7): p. 817-834.

79. Albrecht, W., et al., *Amination of poly(ether imide) membranes using di- and multivalent amines.* Macromolecular Chemistry and Physics, 2003. **204**(3): p. 510-521.

80. Seifert, B., et al., *Polyetherimide: A new membrane-forming polymer for biomedical applications.* Artificial Organs, 2002. **26**(2): p. 189-199.

81. Zhao, B. and W.J. Brittain, *Polymer brushes: surface-immobilized macromolecules.* Progress in Polymer Science, 2000. **25**(5): p. 677-710.

82. Rehfeldt, F., et al., *Cell responses to the mechanochemical microenvironment - Implications for regenerative medicine and drug delivery.* Advanced Drug Delivery Reviews, 2007. **59**(13): p. 1329-1339.

83. Biggs, M.J.P., R.G. Richards, and M.J. Dalby, *Nanotopographical modification: a regulator of cellular function through focal adhesions.* Nanomedicine-Nanotechnology Biology and Medicine, 2010. **6**(5): p. 619-633.

84. Feynman, R.P., *There's plenty of room at the bottom.* Engineering and Science, 1960. **23**(5): p. 22-36.

85. Liu, H. and T.J. Webster, *Nanomedicine for implants: A review of studies and necessary experimental tools.* Biomaterials, 2007. **28**(2): p. 354-369.

86. del Campo, A. and E. Arzt, *Fabrication approaches for generating complex micro- and nanopatterns on polymeric surfaces.* Chemical Reviews, 2008. **108**(3): p. 911-945.

87. Gates, B.D., et al., *New approaches to nanofabrication: Molding, printing, and other techniques.* Chemical Reviews, 2005. **105**(4): p. 1171-1196.

88. Ito, H., *Chemical amplification resists: Inception, implementation in device manufacture, and new developments.* Journal of Polymer Science Part A: Polymer Chemistry, 2003. **41**(24): p. 3863-3870.

89. Grant Willson, C. and B.C. Trinque, *The Evolution of Materials for the Photolithographic Process.* Journal of Photopolymer Science and Technology, 2003. **16**(4): p. 621-627.

90. Stewart, M.D., et al., *Organic imaging materials: a view of the future.* Journal of Physical Organic Chemistry, 2000. **13**(12): p. 767-774.

91. Bozler, C.O., et al., *Arrays of gated field-emitter cones having 0.32 μm tip-to-tip spacing.* Journal of Vacuum Science & Technology B, 1994. **12**(2): p. 629-632.

92. Zaidi, S.H. and S.R.J. Brueck, *Multiple-exposure interferometric lithography.* Journal of Vacuum Science & Technology B, 1993. **11**(3): p. 658-666.

93. Hoffnagle, J.A., et al., *Use of Interferometric Lithography to Characterize the Spatial Resolution of a Photoresist Film.* Journal of Photopolymer Science and Technology, 2003. **16**(3): p. 373-379.

94. Stay, J.L., G.M. Burrow, and T.K. Gaylord, *Three-beam interference lithography methodology.* Review of Scientific Instruments, 2011. **82**(2): p. -.

95. de Boor, J., et al., *Three-beam interference lithography: upgrading a Lloyd's interferometer for single-exposure hexagonal patterning.* Optics Letters, 2009. **34**(12): p. 1783-1785.

96. Vieu, C., et al., *Electron beam lithography: resolution limits and applications.* Applied Surface Science, 2000. **164**: p. 111-117.

97. Xia, Y. and G.M. Whitesides, *Soft Lithography.* Angewandte Chemie International Edition, 1998. **37**(5): p. 550-575.

98. Xia, Y. and G.M. Whitesides, *SOFT LITHOGRAPHY.* Annual Review of Materials Science, 1998. **28**(1): p. 153-184.

99. Xia, Y., et al., *Replica molding using polymeric materials: A practical step toward nanomanufacturing.* Advanced Materials, 1997. **9**(2): p. 147-149.

100. Colburn, M., et al. *Step and flash imprint lithography for sub-100-nm patterning.* 2000.

101. Smith, B.J., et al. *Employing Step-and-Flash imprint lithography for gate-level patterning of a MOSFET device.* 2003.

102. Colburn, M., et al. *Step and flash imprint lithography: a new approach to high-resolution patterning.* 1999.

103. Chou, S.Y., P.R. Krauss, and P.J. Renstrom, *Imprint Lithography with 25-Nanometer Resolution.* Science, 1996. **272**(5258): p. 85-87.

104. Chou, S.Y., P.R. Krauss, and P.J. Renstrom, *Nanoimprint lithography.* Journal of Vacuum Science & Technology B, 1996. **14**(6): p. 4129-4133.

105. Roos, N., et al. *Nanoimprint lithography with a commercial 4-in. bond system for hot embossing.* 2001.

106. Zhang, W. and S.Y. Chou, *Fabrication of 60-nm transistors on 4-in. wafer using nanoimprint at all lithography levels.* Applied Physics Letters, 2003. **83**(8): p. 1632-1634.

107. Ansari, K., et al., *Fabrication of high aspect ratio 100nm metallic stamps for nanoimprint lithography using proton beam writing.* Applied Physics Letters, 2004. **85**(3): p. 476-478.

108. Rogers, J.A., et al., *Printing, molding, and near-field photolithographic methods for patterning organic lasers, smart pixels and simple circuits.* Synthetic Metals, 2000. **115**(1–3): p. 5-11.

109. Xia, Y., et al., *Unconventional Methods for Fabricating and Patterning Nanostructures.* Chemical Reviews, 1999. **99**(7): p. 1823-1848.

110. Johnson, D.M. and J.A. Maurer, *Recycling and reusing patterned self-assembled monolayers for cell culture.* Chem Commun (Camb), 2011. **47**(1): p. 520-2.

111. Kuo, C.W., et al., *Investigation of the growth of focal adhesions using protein nanoarrays fabricated by nanocontact printing using size tunable polymeric nanopillars.* Nanotechnology, 2011. **22**(26): p. 265302.

112. Kumar, A. and G.M. Whitesides, *Features of gold having micrometer to centimeter dimensions can be formed through a combination of stamping with an elastomeric stamp and an alkanethiol "ink" followed by chemical etching.* Applied Physics Letters, 1993. **63**(14): p. 2002-2004.

113. Li, S.P., et al., *Magnetic nanostructure fabrication by soft lithography and vortex-single domain transition in Co dots.* Journal of Magnetism and Magnetic Materials, 2002. **241**(2–3): p. 447-452.

114. Xia, Y., D. Qin, and G.M. Whitesides, *Microcontact printing with a cylindrical rolling stamp: A practical step toward automatic manufacturing of patterns with submicrometer-sized features.* Advanced Materials, 1996. **8**(12): p. 1015-1017.

115. Jackman, R., J. Wilbur, and G. Whitesides, *Fabrication of submicrometer features on curved substrates by microcontact printing.* Science, 1995. **269**(5224): p. 664-666.

116. Tien, J., A. Terfort, and G.M. Whitesides, *Microfabrication through Electrostatic Self-Assembly.* Langmuir, 1997. **13**(20): p. 5349-5355.

117. Wood, M.A., M. Riehle, and C.D.W. Wilkinson, *Patterning colloidal nanotopographies.* Nanotechnology, 2002. **13**(5): p. 605-609.

118. Colson, P., C. Henrist, and R. Cloots, *Nanosphere Lithography: A Powerful Method for the Controlled Manufacturing of Nanomaterials.* Journal of Nanomaterials, 2013.

119. Abrams, G.A., et al., *Nanoscale topography of the basement membrane underlying the corneal epithelium of the rhesus macaque.* Cell Tissue Res, 2000. **299**(1): p. 39-46.

120. Fan, Y.W., et al., *Culture of neural cells on silicon wafers with nano-scale surface topograph.* Journal of Neuroscience Methods, 2002. **120**(1): p. 17-23.

121. Dalby, M.J., et al., *Rapid fibroblast adhesion to 27 nm high polymer demixed nano-topography.* Biomaterials, 2004. **25**(1): p. 77-83.

122. Affrossman, S. and M. Stamm, *The effect of molecular weight an the topography of thin films of blends of poly(4-bromostyrene) and polystyrene.* Colloid and Polymer Science, 2000. **278**(9): p. 888-893.

123. Yang, F., et al., *Fabrication of nano-structured porous PLLA scaffold intended for nerve tissue engineering.* Biomaterials, 2004. **25**(10): p. 1891-1900.

124. Tu, R.S. and M. Tirrell, *Bottom-up design of biomimetic assemblies.* Advanced Drug Delivery Reviews, 2004. **56**(11): p. 1537-1563.

125. Garcia, R., R.V. Martinez, and J. Martinez, *Nano-chemistry and scanning probe nanolithographies.* Chemical Society Reviews, 2006. **35**(1): p. 29-38.

126. Ryu, K.S., et al., *Integrated microfluidic linking chip for scanning probe nanolithography.* Applied Physics Letters, 2004. **85**(1): p. 136-138.

127. Ginger, D.S., H. Zhang, and C.A. Mirkin, *The Evolution of Dip-Pen Nanolithography.* Angewandte Chemie International Edition, 2004. **43**(1): p. 30-45.

128. Krämer, S., R.R. Fuierer, and C.B. Gorman, *Scanning Probe Lithography Using Self-Assembled Monolayers.* Chemical Reviews, 2003. **103**(11): p. 4367-4418.

129. Ming, Z., et al., *A MEMS nanoplotter with high-density parallel dip-pen nanolithography probe arrays.* Nanotechnology, 2002. **13**(2): p. 212.

130. Hong, S. and C.A. Mirkin, *A Nanoplotter with Both Parallel and Serial Writing Capabilities.* Science, 2000. **288**(5472): p. 1808-1811.

131. Lehn, J.-M., *Perspectives in Supramolecular Chemistry—From Molecular Recognition towards Molecular Information Processing and Self-Organization.* Angewandte Chemie International Edition in English, 1990. **29**(11): p. 1304-1319.

132. Li, Z., et al., *Enantiopure Chiral Poly(glycerol methacrylate) Self-Assembled Monolayers Knock Down Protein Adsorption and Cell Adhesion.* Advanced Healthcare Materials, 2013: p. n/a-n/a.

133. Lazzari, M. and M.A. López-Quintela, *Block Copolymers as a Tool for Nanomaterial Fabrication.* Advanced Materials, 2003. **15**(19): p. 1583-1594.

134. Krausch, G. and R. Magerle, *Nanostructured Thin Films via Self-Assembly of Block Copolymers.* Advanced Materials, 2002. **14**(21): p. 1579-1583.

135. Martín, J.I., et al., *Ordered magnetic nanostructures: fabrication and properties.* Journal of Magnetism and Magnetic Materials, 2003. **256**(1–3): p. 449-501.

136. Mendelsohn, J.D., et al., *Fabrication of Microporous Thin Films from Polyelectrolyte Multilayers.* Langmuir, 2000. **16**(11): p. 5017-5023.

137. Shen, L.Y., et al., *pH-Amplified Multilayer Films Based on Hyaluronan: Influence of HA Molecular Weight and Concentration on Film Growth and Stability.* Biomacromolecules, 2011. **12**(4): p. 1322-1331.

138. Richert, L., et al., *pH dependent growth of poly(L-lysine)/poly(L-glutamic) acid multilayer films and their cell adhesion properties.* Surface Science, 2004. **570**(1-2): p. 13-29.

139. Arnold, M., et al., *Activation of integrin function by nanopatterned adhesive interfaces.* Chemphyschem, 2004. **5**(3): p. 383-8.

140. Wolfram, T., et al., *Site-specific presentation of single recombinant proteins in defined nanoarrays.* Biointerphases, 2007. **2**(1): p. 44-48.

141. Krishnamoorthy, S., C. Hinderling, and H. Heinzelmann, *Nanoscale patterning with block copolymers.* Materials Today, 2006. **9**(9): p. 40-47.

142. Glass, R., M. Moller, and J.P. Spatz, *Block copolymer micelle nanolithography.* Nanotechnology, 2003. **14**(10): p. 1153-1160.

143. Walheim, S., et al., *Structure formation via polymer demixing in spin-cast films.* Macromolecules, 1997. **30**(17): p. 4995-5003.

144. Andrew, P. and W.T.S. Huck, *Polymer phase separation on lattice patterned surfaces.* Soft Matter, 2007. **3**(2): p. 230-237.

145. Geldhauser, T., et al., *Generation of Surface Energy Patterns by Single Pulse Laser Interference on Self-Assembled Monolayers.* Langmuir, 2008. **24**(22): p. 13155-13160.

146. Dobry, A. and F. Boyerkawenoki, *Phase Separation in Polymer Solution.* Journal of Polymer Science, 1947. **2**(1): p. 90-100.

147. Hecht, U., C.M. Schilz, and M. Stratmann, *Influence of relative humidity during film formation processes on the structure of ultrathin polymeric films.* Langmuir, 1998. **14**(23): p. 6743-6748.

148. Sprenger, M., et al., *Hierarchic structure formation in binary and ternary polymer blends.* Interface Science, 2003. **11**(2): p. 225-235.

149. Maruyama, N., et al., *Mesoscopic patterns of molecular aggregates on solid substrates.* Thin Solid Films, 1998. **327**: p. 854-856.

150. Cui, L., et al., *Ordered porous polymer films via phase separation in humidity environment.* Polymer, 2005. **46**(14): p. 5334-5340.

151. Widawski, G., M. Rawiso, and B. Francois, *Self-Organized Honeycomb Morphology of Star-Polymer Polystyrene Films.* Nature, 1994. **369**(6479): p. 387-389.

152. Pileni, M.P., et al., *Self assemblies of nanocrystals: preparation, collective properties and uses.* Faraday Discussions, 2004. **125**(0): p. 251-264.

153. Huang, T.-W., et al., *Enhance the structural stability of the FePt nanoparticle monolayer by adding gold overlayer.* Colloids and Surfaces A: Physicochemical and Engineering Aspects, 2006. **284–285**(0): p. 603-606.

154. Whatmore, R.W., *Nanotechnology: big prospects for small engineering.* Ingenia online, 2001(9): p. 28-34.

155. Harnack, O., et al., *Rectifying Behavior of Electrically Aligned ZnO Nanorods.* Nano Letters, 2003. **3**(8): p. 1097-1101.

156. Love, J.C., et al., *Three-Dimensional Self-Assembly of Metallic Rods with Submicron Diameters Using Magnetic Interactions.* Journal of the American Chemical Society, 2003. **125**(42): p. 12696-12697.

157. Gourdon, D., et al., *Mechanical and Structural Properties of BaCrO4 Nanorod Films under Confinement and Shear.* Advanced Functional Materials, 2004. **14**(3): p. 238-242.

158. Pieranski, P., *Two-Dimensional Interfacial Colloidal Crystals.* Physical Review Letters, 1980. **45**(7): p. 569-572.

159.   Zhang, G. and D.Y. Wang, *Colloidal Lithography-The Art of Nanochemical Patterning.* Chemistry-an Asian Journal, 2009. **4**(2): p. 236-245.

160.   Yang, S.-M., et al., *Nanomachining by Colloidal Lithography.* Small, 2006. **2**(4): p. 458-475.

161.   Deckman, H.W. and J.H. Dunsmuir, *Natural lithography.* Applied Physics Letters, 1982. **41**(4): p. 377-379.

162.   Fischer, U.C. and H.P. Zingsheim, *Submicroscopic pattern replication with visible light.* Journal of Vacuum Science and Technology, 1981. **19**(4): p. 881-885.

163.   Deckman, H.W. and J.H. Dunsmuir, *Applications of surface textures produced with natural lithography.* Journal of Vacuum Science & Technology B, 1983. **1**(4): p. 1109-1112.

164.   Hulteen, J.C. and R.P. Van Duyne, *Nanosphere lithography: A materials general fabrication process for periodic particle array surfaces.* Journal of Vacuum Science & Technology A: Vacuum, Surfaces, and Films, 1995. **13**(3): p. 1553-1558.

165.   Jensen, T.R., G.C. Schatz, and R.P. Van Duyne, *Nanosphere Lithography: Surface Plasmon Resonance Spectrum of a Periodic Array of Silver Nanoparticles by Ultraviolet−Visible Extinction Spectroscopy and Electrodynamic Modeling.* The Journal of Physical Chemistry B, 1999. **103**(13): p. 2394-2401.

166.   Zhang, X., C.R. Yonzon, and R.P. Van Duyne, *Nanosphere lithography fabricated plasmonic materials and their applications.* Journal of Materials Research, 2006. **21**(05): p. 1083-1092.

167.   Li, Y., W. Cai, and G. Duan, *Ordered micro/nanostructured arrays based on the monolayer colloidal crystals.* Chemistry of Materials, 2008. **20**(3): p. 615-624.

168.   Li, Y., N. Koshizaki, and W. Cai, *Periodic one-dimensional nanostructured arrays based on colloidal templates, applications, and devices.* Coordination Chemistry Reviews, 2011. **255**(3–4): p. 357-373.

169.   Li, L., et al., *Polystyrene sphere-assisted one-dimensional nanostructure arrays: synthesis and applications.* Journal of Materials Chemistry, 2011. **21**(1): p. 40-56.

170.   Denkov, N., et al., *Mechanism of formation of two-dimensional crystals from latex particles on substrates.* Langmuir, 1992. **8**(12): p. 3183-3190.

171.   Kralchevsky, P.A. and N.D. Denkov, *Capillary forces and structuring in layers of colloid particles.* Current Opinion in Colloid & Interface Science, 2001. **6**(4): p. 383-401.

172.   Micheletto, R., H. Fukuda, and M. Ohtsu, *A Simple Method for the Production of a Two-Dimensional, Ordered Array of Small Latex Particles.* Langmuir, 1995. **11**(9): p. 3333-3336.

173.   Tsuchiya, K., et al., *Nonlinear optical properties of gold nanoparticles selectively introduced into the periodic microdomains of block copolymers.* Optics Express, 2008. **16**(8): p. 5362-5371.

174.   Zhong, Z., et al., *Fabrication of submicron magnetic oxide antidot arrays by combining nanosphere lithography with sputtering technology.* Physica E: Low-dimensional Systems and Nanostructures, 2008. **40**(3): p. 516-519.

175.   Dimitrov, A.S. and K. Nagayama, *Continuous Convective Assembling of Fine Particles into Two-Dimensional Arrays on Solid Surfaces.* Langmuir, 1996. **12**(5): p. 1303-1311.

176.   Ning, T., et al., *Nonlinear optical properties of Au/ZnO nanoparticle arrays.* Applied Surface Science, 2008. **254**(7): p. 1900-1903.

177.   Nagao, D., et al., *Multiformity of particle arrays assembled with a simple dip-coating.* Colloids and Surfaces A: Physicochemical and Engineering Aspects, 2007. **311**(1–3): p. 26-31.

178.   Brown, E.C., et al., *Polymer sphere lithography for solid oxide fuel cells: a route to functional, well-defined electrode structures.* Journal of Materials Chemistry, 2010. **20**(11): p. 2190-2196.

179.   Kuo, C.-W., J.-Y. Shiu, and P. Chen, *Size- and Shape-Controlled Fabrication of Large-Area Periodic Nanopillar Arrays.* Chemistry of Materials, 2003. **15**(15): p. 2917-2920.

180.   Zheng, Y.B., et al., *Selective growth of GaAs quantum dots on the triangle nanocavities bounded by SiO2 mask on Si substrate by MBE.* Journal of Crystal Growth, 2004. **268**(3–4): p. 369-374.

181.   Colson, P., R. Cloots, and C. Henrist, *Experimental Design Applied to Spin Coating of 2D Colloidal Crystal Masks: A Relevant Method?* Langmuir, 2011. **27**(21): p. 12800-12806.

182. Jiang, P. and M.J. McFarland, *Large-Scale Fabrication of Wafer-Size Colloidal Crystals, Macroporous Polymers and Nanocomposites by Spin-Coating.* Journal of the American Chemical Society, 2004. **126**(42): p. 13778-13786.

183. Rehg, T.J. and G. Higgins, *Spin coating of colloidal suspensions.* AIChE Journal, 1992. **38**(4): p. 489-501.

184. Dushkin, C.D., et al., *Effect of growth conditions on the structure of two-dimensional latex crystals: experiment.* Colloid and Polymer Science, 1999. **277**(10): p. 914-930.

185. Chen, J., et al., *Controllable fabrication of 2D colloidal-crystal films with polystyrene nanospheres of various diameters by spin-coating.* Applied Surface Science, 2013. **270**(0): p. 6-15.

186. Rybczynski, J., U. Ebels, and M. Giersig, *Large-scale, 2D arrays of magnetic nanoparticles.* Colloids and Surfaces A: Physicochemical and Engineering Aspects, 2003. **219**(1–3): p. 1-6.

187. Ruan, W.-d., et al., *Facile Fabrication of Large Area Polystyrene Colloidal Crystal Monolayer via Surfactant-free Langmuir-Blodgett Technique.* Chemical Research in Chinese Universities, 2007. **23**(6): p. 712-714.

188. Weekes, S.M., et al., *Macroscopic Arrays of Magnetic Nanostructures from Self-Assembled Nanosphere Templates.* Langmuir, 2006. **23**(3): p. 1057-1060.

189. Zhang, L. and Y. Xiong, *Rapid self-assembly of submicrospheres at liquid surface by controlling evaporation and its mechanism.* Journal of Colloid and Interface Science, 2007. **306**(2): p. 428-432.

190. Stavroulakis, P.I., N. Christou, and D. Bagnall, *Improved deposition of large scale ordered nanosphere monolayers via liquid surface self-assembly.* Materials Science and Engineering: B, 2009. **165**(3): p. 186-189.

191. Goldenberg, L.M., et al., *Simple Method for the Preparation of Colloidal Particle Monolayers at the Water/Alkane Interface.* Langmuir, 2002. **18**(14): p. 5627-5629.

192. Giersig, M. and P. Mulvaney, *Preparation of ordered colloid monolayers by electrophoretic deposition.* Langmuir, 1993. **9**(12): p. 3408-3413.

193. Rogach, A.L., et al., *Electrophoretic Deposition of Latex-Based 3D Colloidal Photonic Crystals: A Technique for Rapid Production of High-Quality Opals.* Chemistry of Materials, 2000. **12**(9): p. 2721-2726.

194. Hayward, R.C., D.A. Saville, and I.A. Aksay, *Electrophoretic assembly of colloidal crystals with optically tunable micropatterns.* Nature, 2000. **404**(6773): p. 56-59.

195. Solomentsev, Y., M. Böhmer, and J.L. Anderson, *Particle Clustering and Pattern Formation during Electrophoretic Deposition: A Hydrodynamic Model.* Langmuir, 1997. **13**(23): p. 6058-6068.

196. Trau, M., D.A. Saville, and I.A. Aksay, *Field-Induced Layering of Colloidal Crystals.* Science, 1996. **272**(5262): p. 706-709.

197. Lumsdon, S.O., E.W. Kaler, and O.D. Velev, *Two-Dimensional Crystallization of Microspheres by a Coplanar AC Electric Field.* Langmuir, 2004. **20**(6): p. 2108-2116.

198. Gong, T. and D.W.M. Marr, *Electrically Switchable Colloidal Ordering in Confined Geometries.* Langmuir, 2001. **17**(8): p. 2301-2304.

199. Bale, M., A.J. Turner, and R.E. Palmer, *Fabrication of ordered arrays of silicon nanopillars at selected sites.* Journal of Physics D: Applied Physics, 2002. **35**(5): p. L11.

200. Allard, M., et al., *Colloidal Crystals Grown on Patterned Surfaces.* Advanced Materials, 2004. **16**(15): p. 1360-1364.

201. Xia, Y., et al., *Template-Assisted Self-Assembly of Spherical Colloids into Complex and Controllable Structures.* Advanced Functional Materials, 2003. **13**(12): p. 907-918.

202. Himmelhaus, M. and H. Takei, *Self-assembly of polystyrene nano particles into patterns of random-close-packed monolayers via chemically induced adsorption.* Physical Chemistry Chemical Physics, 2002. **4**(3): p. 496-506.

203. Fan, F. and K.J. Stebe, *Assembly of Colloidal Particles by Evaporation on Surfaces with Patterned Hydrophobicity.* Langmuir, 2004. **20**(8): p. 3062-3067.

204. Iler, R.K., *Multilayers of colloidal particles.* Journal of Colloid and Interface Science, 1966. **21**(6): p. 569-594.

205. Decher, G., J.D. Hong, and J. Schmitt, *Buildup of Ultrathin Multilayer Films by a Self-Assembly Process .3. Consecutively Alternating Adsorption of Anionic and Cationic Polyelectrolytes on Charged Surfaces.* Thin Solid Films, 1992. **210**(1-2): p. 831-835.

206. Na, K., et al., *Heparin/poly(L-lysine) nanoparticle-coated polymeric microspheres for stem-cell therapy.* Journal of the American Chemical Society, 2007. **129**(18): p. 5788-+.

207. Zhu, H.G., J. Ji, and J.C. Shen, *Biomacromolecules electrostatic self-assembly on 3-dimensional tissue engineering scaffold.* Biomacromolecules, 2004. **5**(5): p. 1933-1939.

208. Groth, T. and A. Lendlein, *Layer-by-layer deposition of polyelectrolytes - A versatile tool for the in vivo repair of blood vessels.* Angewandte Chemie-International Edition, 2004. **43**(8): p. 926-928.

209. Decher, G. and J.B. Schlenoff, in *Multilayer Thin Films: Sequential Assembly of Nanocomposite Materials*, G. Decher and J.B. Schlenoff, Editors. 2012, Wiley-VCH.

210. Hammond, P.T., *Form and function in multilayer assembly: New applications at the nanoscale.* Advanced Materials, 2004. **16**(15): p. 1271-1293.

211. Schoenhoff, M., *Layered polyelectrolyte complexes: physics of formation and molecular properties.* Journal of Physics-Condensed Matter, 2003. **15**(49): p. R1781-R1808.

212. Quinn, J.F., et al., *Next generation, sequentially assembled ultrathin films: beyond electrostatics.* Chemical Society Reviews, 2007. **36**(5): p. 707-718.

213. Schlenoff, J.B., H. Ly, and M. Li, *Charge and Mass Balance in Polyelectrolyte Multilayers.* Journal of the American Chemical Society, 1998. **120**(30): p. 7626-7634.

214. Schlenoff, J.B. and S.T. Dubas, *Mechanism of polyelectrolyte multilayer growth: Charge overcompensation and distribution.* Macromolecules, 2001. **34**(3): p. 592-598.

215. v. Klitzing, R., *Internal structure of polyelectrolyte multilayer assemblies.* Physical Chemistry Chemical Physics, 2006. **8**(43): p. 5012-5033.

216. Lyklema, J. and L. Deschênes, *The first step in layer-by-layer deposition: Electrostatics and/or non-electrostatics?* Advances in Colloid and Interface Science, 2011. **168**(1–2): p. 135-148.

217. Mhamdi, L., et al., *Study of the polyelectrolyte multilayer thin films' properties and correlation with the behavior of the human gingival fibroblasts.* Materials Science & Engineering C-Biomimetic and Supramolecular Systems, 2006. **26**(2-3): p. 273-281.

218. Picart, C., et al., *Measurement of film thickness up to several hundreds of nanometers using optical waveguide lightmode spectroscopy.* Biosensors and Bioelectronics, 2004. **20**(3): p. 553-561.

219. Shiratori, S.S. and M.F. Rubner, *pH-Dependent Thickness Behavior of Sequentially Adsorbed Layers of Weak Polyelectrolytes.* Macromolecules, 2000. **33**(11): p. 4213-4219.

220. Yoo, D., S.S. Shiratori, and M.F. Rubner, *Controlling bilayer composition and surface wettability of sequentially adsorbed multilayers of weak polyelectrolytes.* Macromolecules, 1998. **31**(13): p. 4309-4318.

221. Thompson, M.T., et al., *Tuning compliance of nanoscale polyelectrolyte multilayers to modulate cell adhesion.* Biomaterials, 2005. **26**(34): p. 6836-6845.

222. Mendelsohn, J.D., et al., *Rational design of cytophilic and cytophobic polyelectrolyte multilayer thin films.* Biomacromolecules, 2003. **4**(1): p. 96-106.

223. Mhanna, R.F., J. Vörös, and M. Zenobi-Wong, *Layer-by-Layer Films Made from Extracellular Matrix Macromolecules on Silicone Substrates.* Biomacromolecules, 2011. **12**(3): p. 609-616.

224. Zhang, J., et al., *Natural polyelectrolyte films based on layer-by layer deposition of collagen and hyaluronic acid.* Biomaterials, 2005. **26**(16): p. 3353-3361.

127

225. Cai, K.Y., et al., *Polysaccharide-protein surface modification of titanium via a layer-by-layer technique: Characterization and cell behaviour aspects.* Biomaterials, 2005. **26**(30): p. 5960-5971.

226. Niepel, M.S., et al., *pH-dependent modulation of fibroblast adhesion on multilayers composed of poly(ethylene imine) and heparin.* Biomaterials, 2009. **30**(28): p. 4939-47.

227. Lundin, M., et al., *Layer-by-Layer Assemblies of Chitosan and Heparin: Effect of Solution Ionic Strength and pH.* Langmuir, 2011. **27**(12): p. 7537-7548.

228. Liu, Z.-M., et al., *Synergistic Effect of Polyelectrolyte Multilayers and Osteogenic Growth Medium on Differentiation of Human Mesenchymal Stem Cells.* Macromolecular Bioscience, 2010. **10**(9): p. 1043-1054.

229. Aggarwal, N., et al., *Tuning Cell Adhesion and Growth on Biomimetic Polyelectrolyte Multilayers by Variation of pH During Layer-by-Layer Assembly.* Macromol Biosci, 2013. **13**(10): p. 1327-38.

230. Kirchhof, K., et al., *Multilayer coatings on biomaterials for control of MG-63 osteoblast adhesion and growth.* Journal of Materials Science-Materials in Medicine, 2009. **20**(4): p. 897-907.

231. Koewitsch, A., et al., *Bioactivity of immobilized hyaluronic acid derivatives regarding protein adsorption and cell adhesion.* Biotechnology and Applied Biochemistry, 2011. **58**(5): p. 376-389.

232. Lavalle, P., et al., *Modeling the Buildup of Polyelectrolyte Multilayer Films Having Exponential GrowthⅩ.* The Journal of Physical Chemistry B, 2003. **108**(2): p. 635-648.

233. Boddohi, S., C.E. Killingsworth, and M.J. Kipper, *Polyelectrolyte multilayer assembly as a function of pH and ionic strength using the polysaccharides chitosan and heparin.* Biomacromolecules, 2008. **9**(7): p. 2021-2028.

234. Richert, L., et al., *Layer by layer buildup of polysaccharide films: Physical chemistry and cellular adhesion aspects.* Langmuir, 2004. **20**(2): p. 448-458.

235. Burke, S.E. and C.J. Barrett, *pH-responsive properties of multilayered poly(L-lysine)/hyaluronic acid surfaces.* Biomacromolecules, 2003. **4**(6): p. 1773-1783.

236. Xie, A.F. and S. Granick, *Weak versus strong: A weak polyacid embedded within a multilayer of strong polyelectrolytes.* Journal of the American Chemical Society, 2001. **123**(13): p. 3175-3176.

237. Crouzier, T., T. Boudou, and C. Picart, *Polysaccharide-based polyelectrolyte multilayers.* Current Opinion in Colloid & Interface Science, 2010. **15**(6): p. 417-426.

238. Capila, I. and R.J. Linhardt, *Heparin - Protein interactions.* Angewandte Chemie-International Edition, 2002. **41**(3): p. 391-412.

239. Aggarwal, N., et al., *Study on multilayer structures prepared from heparin and semi-synthetic cellulose sulfates as polyanions and their influence on cellular response.* Colloids and Surfaces B: Biointerfaces, 2014. **116**(0): p. 93-103.

240. Aggarwal, N., et al., *Effect of molecular composition of heparin and cellulose sulfate on multilayer formation and cell response.* Langmuir, 2013. **29**(45): p. 13853-64.

241. Kirchhof, K., et al., *Polyelectrolyte multilayers generated in a microfluidic device with pH gradients direct adhesion and movement of cells.* Lab Chip, 2011. **11**(19): p. 3326-35.

242. Gale, G.W., R.J. Small, and K.A. Reinhardt, *Aqueous Cleaning and Surface Conditioning Processes*, in *Handbook of Silicon Wafer Cleaning Technology (Second Edition)*, A.R. Karen and K. Werner, Editors. 2008, William Andrew Publishing: Norwich, NY.

243. Blummel, J., et al., *Protein repellent properties of covalently attached PEG coatings on nanostructured SiO2-based interfaces.* Biomaterials, 2007. **28**(32): p. 4739-4747.

244. *http://www.sigmaaldrich.com/catalog/product/aldrich/181978?lang=de&region=DE#.*

245. Castelnovo, M. and J.F. Joanny, *Formation of polyelectrolyte multilayers.* Langmuir, 2000. **16**(19): p. 7524-7532.

246. Choosakoonkriang, S., et al., *Biophysical characterization of PEI/DNA complexes.* Journal of Pharmaceutical Sciences, 2003. **92**(8): p. 1710-1722.

247. Kolasinska, M., R. Krastev, and P. Warszynski, *Characteristics of polyelectrolyte multilayers: effect of PEI anchoring layer and posttreatment after deposition.* J Colloid Interface Sci, 2007. **305**(1): p. 46-56.

248. Tang, G.P., et al., *Low molecular weight polyethylenimines linked by beta-cyclodextrin for gene transfer into the nervous system.* Journal of Gene Medicine, 2006. **8**(6): p. 736-744.

249. Brunot, C., et al., *Cytotoxicity of polyethyleneimine (PEI), precursor base layer of polyelectrolyte multilayer films.* Biomaterials, 2007. **28**(4): p. 632-640.

250. von Harpe, A., et al., *Characterization of commercially available and synthesized polyethylenimines for gene delivery.* Journal of Controlled Release, 2000. **69**(2): p. 309-322.

251. Gatti, G., et al., *Studies on the Conformation of Heparin by 1H and 13C NMR Spectroscopy.* Macromolecules, 1979. **12**(5): p. 1001-1007.

252. Wang, H.M., D. Loganathan, and R.J. Linhardt, *Determination of the Pka of Glucuronic-Acid and the Carboxy Groups of Heparin by C-13-Nuclear-Magnetic-Resonance Spectroscopy.* Biochemical Journal, 1991. **278**: p. 689-695.

253. Seyrek, E., P.L. Dubin, and J. Henriksen, *Nonspecific electrostatic binding characteristics of the heparin-antithrombin interaction.* Biopolymers, 2007. **86**(3): p. 249-259.

254. Schoen, P.J., *The Anticoagulant Activity of Heparin: Biochemical Studies in Purified Systems.* 1991: Rijksuniversiteit Limburg.

255. Young, E., *The anti-inflammatory effects of heparin and related compounds.* Thrombosis Research, 2008. **122**(6): p. 743-752.

256. Barlow, G.H., M.M. Mozen, and L.J. Coen, *Biological Chemical + Physical Comparison of Heparin from Different Mammalian Species.* Biochimica Et Biophysica Acta, 1964. **83**(3): p. 272-&.

257. Gould, P., *Smart, clean surfaces.* Materials Today, 2003: p. 5.

258. Böing, J., *Modifizierung von Glas- und Titanoberflächen zur Verbesserung der Biokompatibilität.* Dissertation, 2003: p. 197.

259. Werner, C. and H.J. Jacobasch, *Surface characterization of polymers for medical devices.* International Journal of Artificial Organs, 1999. **22**(3): p. 160-176.

260. Extrand, C.W., *Model for Contact Angles and Hysteresis on Rough and Ultraphobic Surfaces.* Langmuir, 2002. **18**(21): p. 7991-7999.

261. Extrand, C.W., *Designing for Optimum Liquid Repellency.* Langmuir, 2006. **22**(4): p. 1711-1714.

262. Gao, L. and T.J. McCarthy, *Contact Angle Hysteresis Explained.* Langmuir, 2006. **22**(14): p. 6234-6237.

263. Andrade, J.D., *Surface and Interfacial Aspects of Biomedical Polymers.* Surface and Interfacial Aspects of Biomedical Polymers. Joseph D. Andrade, Ed., Plenum, New York, 1985, 1985. **1**: p. 249-292.

264. Zimmermann, R., *Charakterisierung von Ladungsbildungsprozessen an Polymeren in wässrigen Lösungen.* Dissertation, w.e.b. Universitätsverlag, 2004.

265. Werner, C., et al., *Extended electrokinetic characterization of flat solid surfaces.* Journal of Colloid and Interface Science, 1998. **208**(1): p. 329-346.

266. Sze, A., et al., *Zeta-potential measurement using the Smoluchowski equation and the slope of the current–time relationship in electroosmotic flow.* Journal of Colloid and Interface Science, 2003. **261**(2): p. 402-410.

267. De Feijter, J.A., J. Benjamins, and F.A. Veer, *Ellipsometry as a tool to study the adsorption behavior of synthetic and biopolymers at the air–water interface.* Biopolymers, 1978. **17**(7): p. 1759-1772.

268. Springer, *Handbook of Ellipsometry*, in *Handbook of Ellipsometry*, H.G. Tompkins and E.A. Irene, Editors. 2005, William Andrew Publishing: Norwich, NY.

269. Elwing, H., *Protein absorption and ellipsometry in biomaterial research.* Biomaterials, 1998. **19**(4–5): p. 397-406.

270. Zhu, X.Y., et al., *Grafting of High-Density Poly(Ethylene Glycol) Monolayers on Si(111).* Langmuir, 2001. **17**(25): p. 7798-7803.

271. Thom, V.H., et al., *Optimizing Cell−Surface Interactions by Photografting of Poly(ethylene glycol).* Langmuir, 2000. **16**(6): p. 2756-2765.

272. Groll, J., et al., *Comparison of Coatings from Reactive Star Shaped PEG-stat-PPG Prepolymers and Grafted Linear PEG for Biological and Medical Applications.* Biomacromolecules, 2005. **6**(2): p. 956-962.

273. Huang, N.-P., et al., *Poly(l-lysine)-g-poly(ethylene glycol) Layers on Metal Oxide Surfaces: Surface-Analytical Characterization and Resistance to Serum and Fibrinogen Adsorption.* Langmuir, 2000. **17**(2): p. 489-498.

274. Schulte, V.A., et al., *Surface topography induces fibroblast adhesion on intrinsically nonadhesive poly(ethylene glycol) substrates.* Biomacromolecules, 2009. **10**(10): p. 2795-801.

275. Fick, J., et al., *Swelling Behavior of Self-Assembled Monolayers of Alkanethiol-Terminated Poly(ethylene glycol): A Neutron Reflectometry Study.* Langmuir, 2004. **20**(10): p. 3848-3853.

276. GELEST, *Hydrophobicity, Hydrophilicity and Silanes.* Datasheet, 2006.

277. Papra, A., N. Gadegaard, and N.B. Larsen, *Characterization of ultrathin poly(ethylene glycol) monolayers on silicon substrates.* Langmuir, 2001. **17**(5): p. 1457-1460.

278. Bain, C.D., J. Evall, and G.M. Whitesides, *Formation of Monolayers by the Coadsorption of Thiols on Gold - Variation in the Head Group, Tail Group, and Solvent.* Journal of the American Chemical Society, 1989. **111**(18): p. 7155-7164.

279. Atre, S.V., B. Liedberg, and D.L. Allara, *Chain-Length Dependence of the Structure and Wetting Properties in Binary Composition Monolayers of Oh-Terminated and Ch3-Terminated Alkanethiolates on Gold.* Langmuir, 1995. **11**(10): p. 3882-3893.

280. Prime, K.L. and G.M. Whitesides, *Self-Assembled Organic Monolayers - Model Systems for Studying Adsorption of Proteins at Surfaces.* Science, 1991. **252**(5009): p. 1164-1167.

281. Israelachvili, J.N. and R.M. Pashley, *Molecular layering of water at surfaces and origin of repulsive hydration forces.* Nature, 1983. **306**(5940): p. 249-250.

282. Prime, K.L. and G.M. Whitesides, *Adsorption of proteins onto surfaces containing end-attached oligo(ethylene oxide): a model system using self-assembled monolayers.* Journal of the American Chemical Society, 1993. **115**(23): p. 10714-10721.

283. Altankov, G., et al., *Morphological evidence for a different fibronectin receptor organization and function during fibroblast adhesion on hydrophilic and hydrophobic glass substrata.* J Biomater Sci Polym Ed, 1997. **8**(9): p. 721-40.

284. Sottile, J., D.C. Hocking, and P.J. Swiatek, *Fibronectin matrix assembly enhances adhesion-dependent cell growth.* Journal of Cell Science, 1998. **111**: p. 2933-2943.

285. Altankov, G. and T. Groth, *Fibronectin matrix formation and the biocompatibility of materials.* Journal of Materials Science-Materials in Medicine, 1996. **7**(7): p. 425-429.

286. Werner, C., T. Pompe, and K. Salchert, *Modulating extracellular matrix at interfaces of polymeric materials.* Polymers for Regenerative Medicine, 2006: p. 63-93.

287. Dalton, B.A., et al., *Role of the heparin binding domain of fibronectin in attachment and spreading of human bone-derived cells.* Journal of Cell Science, 1995. **108**(5): p. 2083-2092.

288. Prevo, B.G. and O.D. Velev, *Controlled, Rapid Deposition of Structured Coatings from Micro-and Nanoparticle Suspensions.* Langmuir, 2004. **20**(6): p. 2099-2107.

289. Zhao, Y. and J.S. Marshall, *Spin coating of a colloidal suspension.* Physics of Fluids (1994-present), 2008. **20**(4): p. -.

290. Cavalcanti-Adam, E.A., et al., *Lateral spacing of integrin ligands influences cell spreading and focal adhesion assembly.* European Journal of Cell Biology, 2006. **85**(3-4): p. 219-224.

291. Cassie, A.B.D. and S. Baxter, *Wettability of porous surfaces.* Transactions of the Faraday Society, 1944. **40**: p. 546-551.

292. Martines, E., et al., *Air-trapping on biocompatible nanopatterns.* Langmuir, 2006. **22**(26): p. 11230-3.

293. Taylor, Z.R., et al., *Fabrication of Protein Dot Arrays via Particle Lithography.* Langmuir, 2009. **25**(18): p. 10932-10938.

294. van Oss, C.J., *Long-range and short-range mechanisms of hydrophobic attraction and hydrophilic repulsion in specific and aspecific interactions.* Journal of Molecular Recognition, 2003. **16**(4): p. 177-190.

295. Sheth, S.R. and D. Leckband, *Measurements of attractive forces between proteins and end-grafted poly(ethylene glycol) chains.* Proceedings of the National Academy of Sciences, 1997. **94**(16): p. 8399-8404.

296. Denis, F.A., et al., *Protein Adsorption on Model Surfaces with Controlled Nanotopography and Chemistry.* Langmuir, 2002. **18**(3): p. 819-828.

297. Dalby, M.J., et al., *Fibroblast response to a controlled nanoenvironment produced by colloidal lithography.* J Biomed Mater Res A, 2004. **69**(2): p. 314-22.

298. Seo, C.H., et al., *The effect of substrate microtopography on focal adhesion maturation and actin organization via the RhoA/ROCK pathway.* Biomaterials, 2011. **32**(36): p. 9568-9575.

299. Gonzalez-Garcia, C., et al., *Effect of nanoscale topography on fibronectin adsorption, focal adhesion size and matrix organisation.* Colloids and Surfaces B-Biointerfaces, 2010. **77**(2): p. 181-190.

300. Caporizzo, M.A., et al., *Nanoscale topography mediates the adhesion of F-actin.* Langmuir, 2012. **28**(33): p. 12216-24.

301. Gonzalez-Garcia, C., et al., *Vitronectin alters fibronectin organization at the cell-material interface.* Colloids Surf B Biointerfaces, 2013. **111C**: p. 618-625.

302. Salmeron-Sanchez, M., et al., *Role of material-driven fibronectin fibrillogenesis in cell differentiation.* Biomaterials, 2011. **32**(8): p. 2099-105.

303. Phillips, J.E., et al., *Human mesenchymal stem cell differentiation on self-assembled monolayers presenting different surface chemistries.* Acta Biomaterialia, 2010. **6**(1): p. 12-20.

304. Curran, J.M., R. Chen, and J.A. Hunt, *The guidance of human mesenchymal stem cell differentiation in vitro by controlled modifications to the cell substrate.* Biomaterials, 2006. **27**(27): p. 4783-4793.

305. Trimpert, C., et al., *Poly(ether imide) membranes modified with poly(ethylene imine) as potential carriers for epidermal substitutes.* Macromol Biosci, 2006. **6**(4): p. 274-84.

306. Niepel, M.S., et al., *Cell adhesion on nanostructured surfaces designed by nanosphere lithography.* CORD Conference Proceedings, 2011: p. 1-4.

307. Dukhin, S.S., R. Zimmermann, and C. Werner, *Charge density distribution at interfaces between polyelectrolyte layers and aqueous solutions--experimental access and limitations of traditional electrokinetics.* J Colloid Interface Sci, 2008. **328**(2): p. 217-26.

308. Casu, B., *Protein-binding domains of heparin and other sulfated glycosaminoglycans.* Carbohydrates in Europe, 1994. **11**: p. 18-21.

309. Pankov, R. and K.M. Yamada, *Fibronectin at a glance.* Journal of Cell Science, 2002. **115**(20): p. 3861-3863.

310. Moghimi, S.M., et al., *A two-stage poly(ethylenimine)-mediated cytotoxicity: implications for gene transfer/therapy.* Mol Ther, 2005. **11**(6): p. 990-995.

311. Crouzier, T., et al., *Layer-By-Layer Films as a Biomimetic Reservoir for rhBMP-2 Delivery: Controlled Differentiation of Myoblasts to Osteoblasts.* Small, 2009. **5**(5): p. 598-608.

312. Boudou, T., et al., *Multiple functionalities of polyelectrolyte multilayer films: new biomedical applications.* Adv Mater, 2010. **22**(4): p. 441-67.

313. Schneider, A., et al., *Polyelectrolyte multilayers with a tunable Young's modulus: influence of film stiffness on cell adhesion.* Langmuir, 2006. **22**(3): p. 1193-200.

314. Blin, G., et al., *Nano-scale control of cellular environment to drive embryonic stem cells selfrenewal and fate.* Biomaterials, 2010. **31**(7): p. 1742-1750.

315. Wang, X., et al., *Effect of RGD nanospacing on differentiation of stem cells.* Biomaterials, 2013. **34**(12): p. 2865-2874.

List of tables and figures

Tables

Figures

Appendix

Table A.1 - ANOVA of area, count and aspect ratio of cells adherent on planar control surfaces (p < 0.05; 1 = significant; 0 = NOT significant)

AREA		wo FN				FN			
		Au	MUDA	OEG	Urea	Au	MUDA	OEG	Urea
wo FN	Au		0	0	1	1	1	1	1
	MUDA	0		0	0	1	1	1	0
	OEG	0	0		1	0	1	1	1
	Urea	1	0	1		1	1	1	0
FN	Au	1	1	0	1		0	1	1
	MUDA	1	1	1	1	0		0	1
	OEG	1	1	1	1	1	0		1
	Urea	1	0	1	0	1	1	1	

COUNT		wo FN				FN			
		Au	MUDA	OEG	Urea	Au	MUDA	OEG	Urea
wo FN	Au		0	0	1	0	0	0	1
	MUDA	0		0	1	0	0	0	1
	OEG	0	0		1	0	0	1	1
	Urea	1	1	1		1	1	1	0
FN	Au	0	0	0	1		0	0	1
	MUDA	0	0	0	1	0		0	1
	OEG	0	0	1	1	0	0		1
	Urea	1	1	1	0	1	1	1	

ASPECT RATIO		wo FN				FN			
		Au	MUDA	OEG	Urea	Au	MUDA	OEG	Urea
wo FN	Au		0	0	1	0	0	1	1
	MUDA	0		0	1	0	1	1	1
	OEG	0	0		1	0	1	1	1
	Urea	1	1	1		1	1	1	0
FN	Au	0	0	0	1		0	1	1
	MUDA	0	1	1	1	0		0	1
	OEG	1	1	1	1	1	0		1
	Urea	1	1	1	0	1	1	1	

Table A.2 - ANOVA of R_a (top) and RMS (bottom) of PEM formed at pH 5.0 (left) or pH 9.0 (right) on nanostructured surfaces. (p < 0.05; 1 = significant; 0 = NOT significant)

R_a pH 5.0		(PH)4				(PH4)P			
		319	476	756	1390	319	476	756	1390
(PH)4	319		0	0	1	1	1	1	1
	476	0		1	1	1	1	1	1
	756	0	1		1	1	1	1	1
	1390	1	1	1		0	1	1	1
(PH)4P	319	1	1	1	0		0	0	0
	476	1	1	1	1	0		0	0
	756	1	1	1	1	0	0		0
	1390	1	1	1	1	0	0	0	

R_a pH 9.0		(PH)4				(PH4)P			
		319	476	756	1390	319	476	756	1390
(PH)4	319		0	0	1	1	1	1	1
	476	0		0	0	0	1	1	1
	756	0	0		1	1	1	1	1
	1390	1	0	1		0	1	1	1
(PH)4P	319	1	0	1	0		0	0	1
	476	1	1	1	1	0		0	0
	756	1	1	1	1	0	0		1
	1390	1	1	1	1	1	0	1	

RMS pH 5.0		(PH)4				(PH4)P			
		319	476	756	1390	319	476	756	1390
(PH)4	319		0	0	1	1	1	1	1
	476	0		1	1	1	1	1	1
	756	0	1		1	1	1	1	1
	1390	1	1	1		0	0	1	1
(PH)4P	319	1	1	1	0		0	0	0
	476	1	1	1	0	0		0	0
	756	1	1	1	1	0	0		0
	1390	1	1	1	1	0	0	0	

RMS pH 9.0		(PH)4				(PH4)P			
		319	476	756	1390	319	476	756	1390
(PH)4	319		0	0	1	1	1	1	1
	476	0		0	0	0	1	1	1
	756	0	0		1	1	1	1	1
	1390	1	0	0		0	1	1	1
(PH)4P	319	1	0	1	0		0	0	1
	476	1	1	1	1	0		0	0
	756	1	1	1	1	0	0		1
	1390	1	1	1	1	1	0	1	
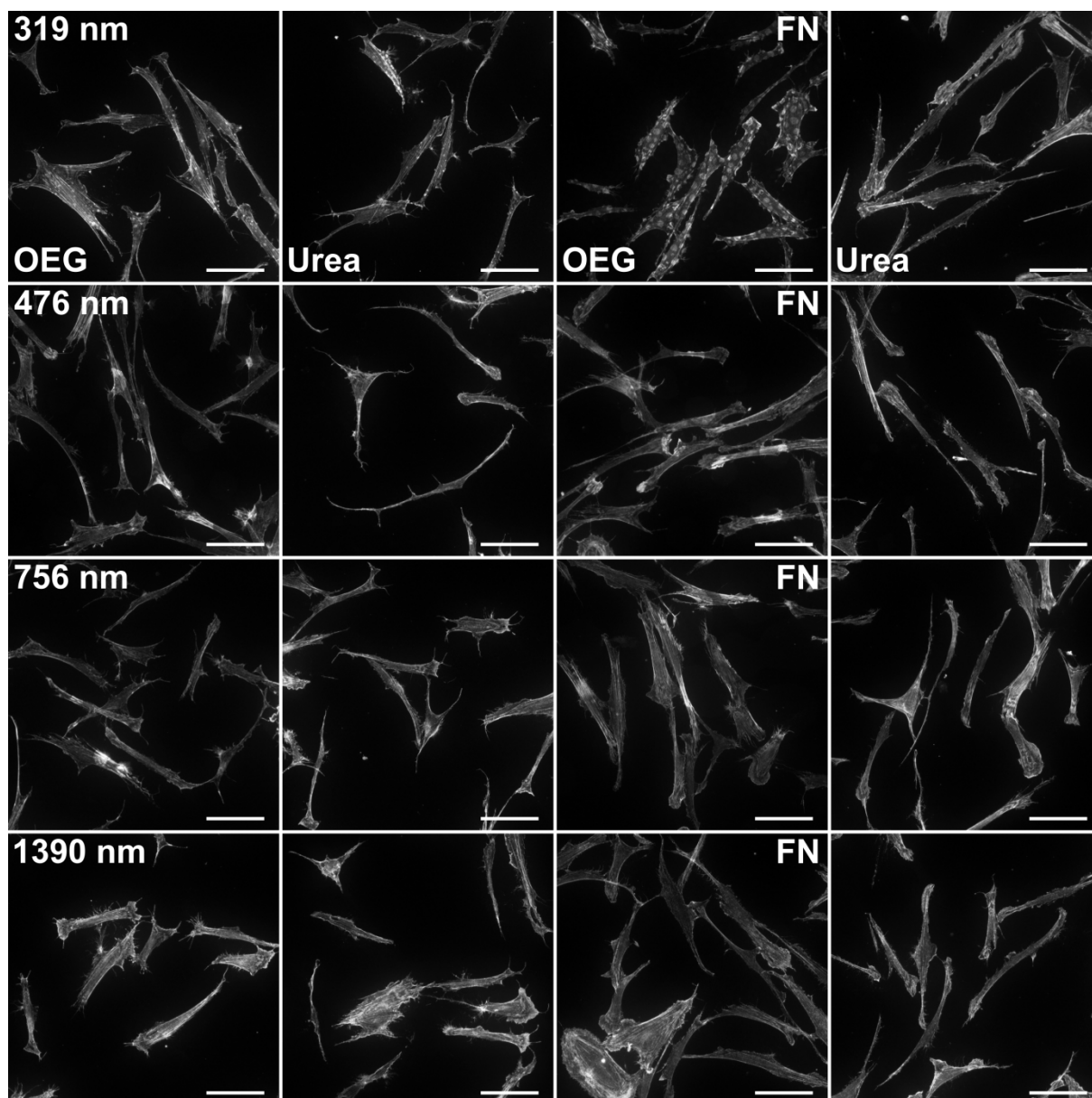
Figure A.1 - Fluorescence images of HDF adherent on nanostructures obtained with different PS-NP diameters and modified with OEG (1st and 3rd column) or mPEG-urea (2nd and 4th column). Further, the gold structures either were without (left column pair) or with 2 μg mL^{-1} FN (right column pair). The cells were cultured for 24 h and stained for actin. [Scale: 100 μm]

Table A.3 - ANOVA of cell count on nanostructured surfaces passivated with either oligo (ethylene glycol) (OEG) or mPEG-urea (Urea) after 4 h of incubation (p < 0.05; 1 = significant; 0 = NOT significant)

COUNT		OEG wo FN				OEG w FN				Urea wo FN				Urea w FN			
		319	476	756	1390	319	476	756	1390	319	476	756	1390	319	476	756	1390
OEG wo FN	319		0	0	0	0	0	0	0	1	1	1	1	1	1	1	1
	476	0		0	0	0	0	0	0	0	0	1	1	1	0	0	0
	756	0	0		0	0	0	0	0	1	0	1	1	1	1	0	1
	1390	0	0	0		0	0	0	0	1	0	1	1	1	0	0	0
OEG w FN	319	0	0	0	0		0	0	0	1	0	1	1	1	0	0	0
	476	0	0	0	0	0		0	0	1	1	1	1	1	1	1	1
	756	0	0	0	0	0	0		0	1	1	1	1	1	1	1	1
	1390	0	0	0	0	0	0	0		1	1	1	1	1	1	0	1
Urea wo FN	319	1	0	1	1	1	1	1	1		0	0	0	0	0	0	0
	476	1	0	0	0	0	1	1	1	0		0	0	0	0	0	0
	756	1	1	1	1	1	1	1	1	0	0		0	0	0	0	0
	1390	1	1	1	1	1	1	1	1	0	0	0		0	0	0	0
Urea w FN	319	1	1	1	1	1	1	1	1	0	0	0	0		0	0	0
	476	1	0	1	0	0	1	1	1	0	0	0	0	0		0	0
	756	1	0	0	0	0	1	1	0	0	0	0	0	0	0		0
	1390	1	0	1	0	0	1	1	1	0	0	0	0	0	0	0	

Table A.4 - ANOVA of cell area on nanostructured surfaces passivated with either oligo (ethylene glycol) (OEG) or mPEG-urea (Urea) after 4 h of incubation (p < 0.05; 1 = significant; 0 = NOT significant)

AREA		OEG wo FN				OEG w FN				Urea wo FN				Urea w FN			
		319	476	756	1390	319	476	756	1390	319	476	756	1390	319	476	756	1390
OEG wo FN	319		1	1	1	0	1	0	1	0	1	1	1	0	1	0	1
	476	1		0	1	1	1	1	1	1	0	0	1	1	1	1	1
	756	1	0		0	1	1	1	1	1	0	0	0	1	1	1	1
	1390	1	1	0		1	1	1	1	1	1	0	0	1	1	1	1
OEG w FN	319	0	1	1	1		0	0	1	0	1	1	1	0	0	0	1
	476	1	1	1	1	0		0	1	1	1	1	1	0	0	0	1
	756	0	1	1	1	0	0		1	0	1	1	1	0	0	0	1
	1390	1	1	1	1	1	1	1		1	1	1	1	1	1	1	0
Urea wo FN	319	0	1	1	1	0	1	0	1		1	1	1	0	1	0	1
	476	1	0	0	1	1	1	1	1	1		0	1	1	1	1	1
	756	1	0	0	0	1	1	1	1	1	0		0	1	1	1	1
	1390	1	1	0	0	1	1	1	1	1	1	0		1	1	1	1
Urea w FN	319	0	1	1	1	0	0	0	1	0	1	1	1		0	0	1
	476	1	1	1	1	0	0	0	1	1	1	1	1	0		0	1
	756	0	1	1	1	0	0	0	1	0	1	1	1	0	0		1
	1390	1	1	1	1	1	1	1	0	1	1	1	1	1	1	1	

Table A.5 - ANOVA of aspect ratio of cells adherent on nanostructured surfaces passivated with either oligo (ethylene glycol) (OEG) or mPEG-urea (Urea) after 4 h of incubation (p < 0.05; 1 = significant; 0 = NOT significant)

ASPECT RATIO		OEG wo FN				OEG w FN				Urea wo FN				Urea w FN			
		319	476	756	1390	319	476	756	1390	319	476	756	1390	319	476	756	1390
OEG wo FN	319		0	0	0	0	0	1	1	0	0	0	0	0	0	1	1
	476	0		0	0	0	0	0	1	0	0	0	0	0	0	0	1
	756	0	0		0	0	0	0	0	0	0	0	0	0	0	0	0
	1390	0	0	0		0	0	0	1	0	0	0	0	0	0	0	1
OEG w FN	319	0	0	0	0		0	0	0	0	0	0	0	0	0	0	0
	476	0	0	0	0	0		0	0	0	0	0	0	0	0	0	0
	756	1	0	0	0	0	0		0	1	0	0	0	0	0	0	0
	1390	1	1	0	1	0	0	0		1	1	0	1	0	0	0	0
Urea wo FN	319	0	0	0	0	0	0	1	1		0	0	0	0	0	1	1
	476	0	0	0	0	0	0	0	1	0		0	0	0	0	0	1
	756	0	0	0	0	0	0	0	0	0	0		0	0	0	0	0
	1390	0	0	0	0	0	0	0	1	0	0	0		0	0	0	1
Urea w FN	319	0	0	0	0	0	0	0	0	0	0	0	0		0	0	0
	476	0	0	0	0	0	0	0	0	0	0	0	0	0		0	0
	756	1	0	0	0	0	0	0	0	1	0	0	0	0	0		0
	1390	1	1	0	1	0	0	0	0	1	1	0	1	0	0	0	
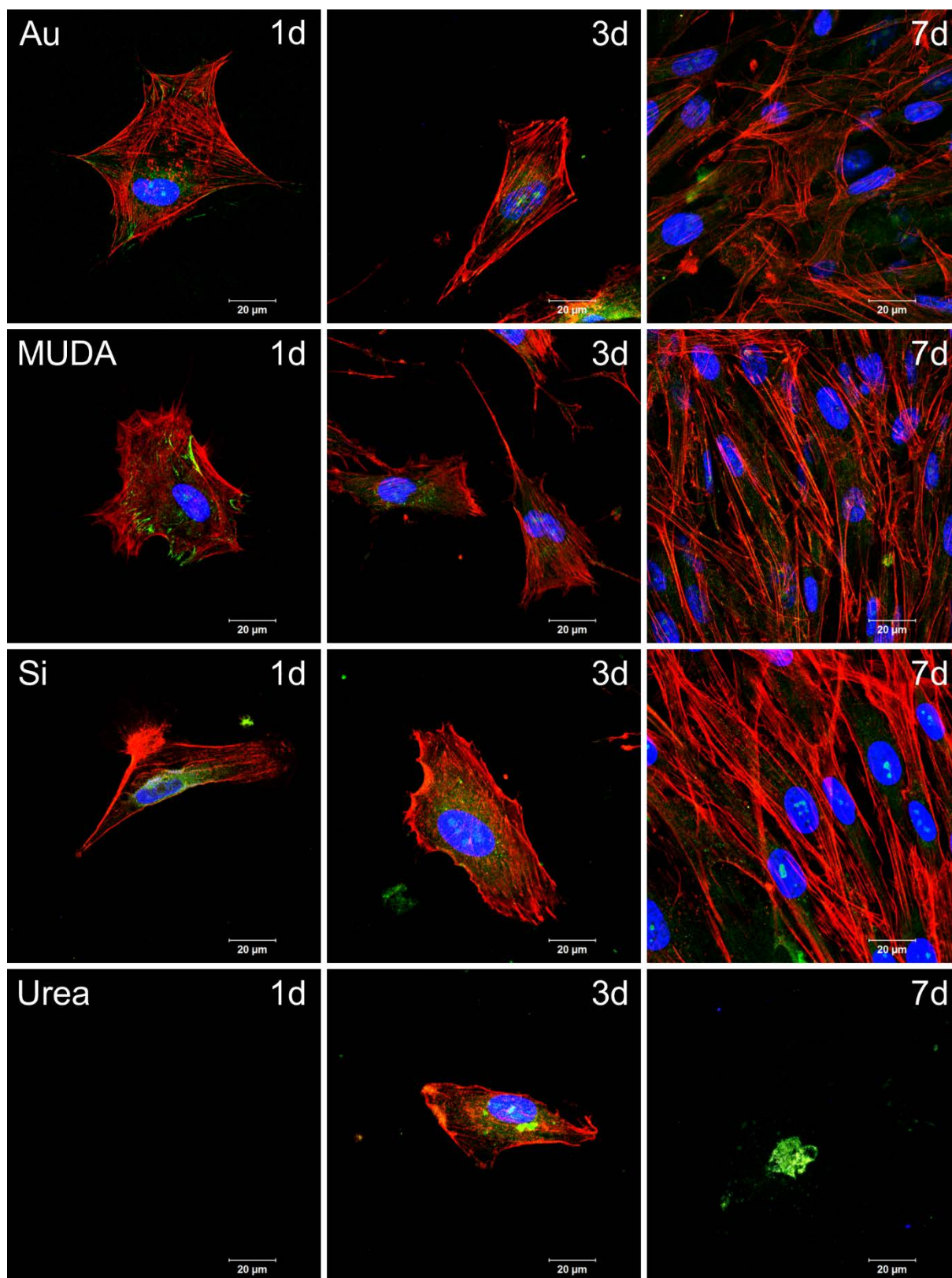
Figure A.2 - CLSM images of HDF adherent on planar control surfaces without preadsorption of FN after 1 d (left), 3 d (middle), and 7 d (right) of culture. The cells were stained for actin (red), vinculin (green) and nucleus (blue). [Au - gold, MUDA - gold with mercaptoundecanoic acid, Si - silicon dioxide, Urea - silicon dioxide with mPEG-urea] [Scale: 20 μm]
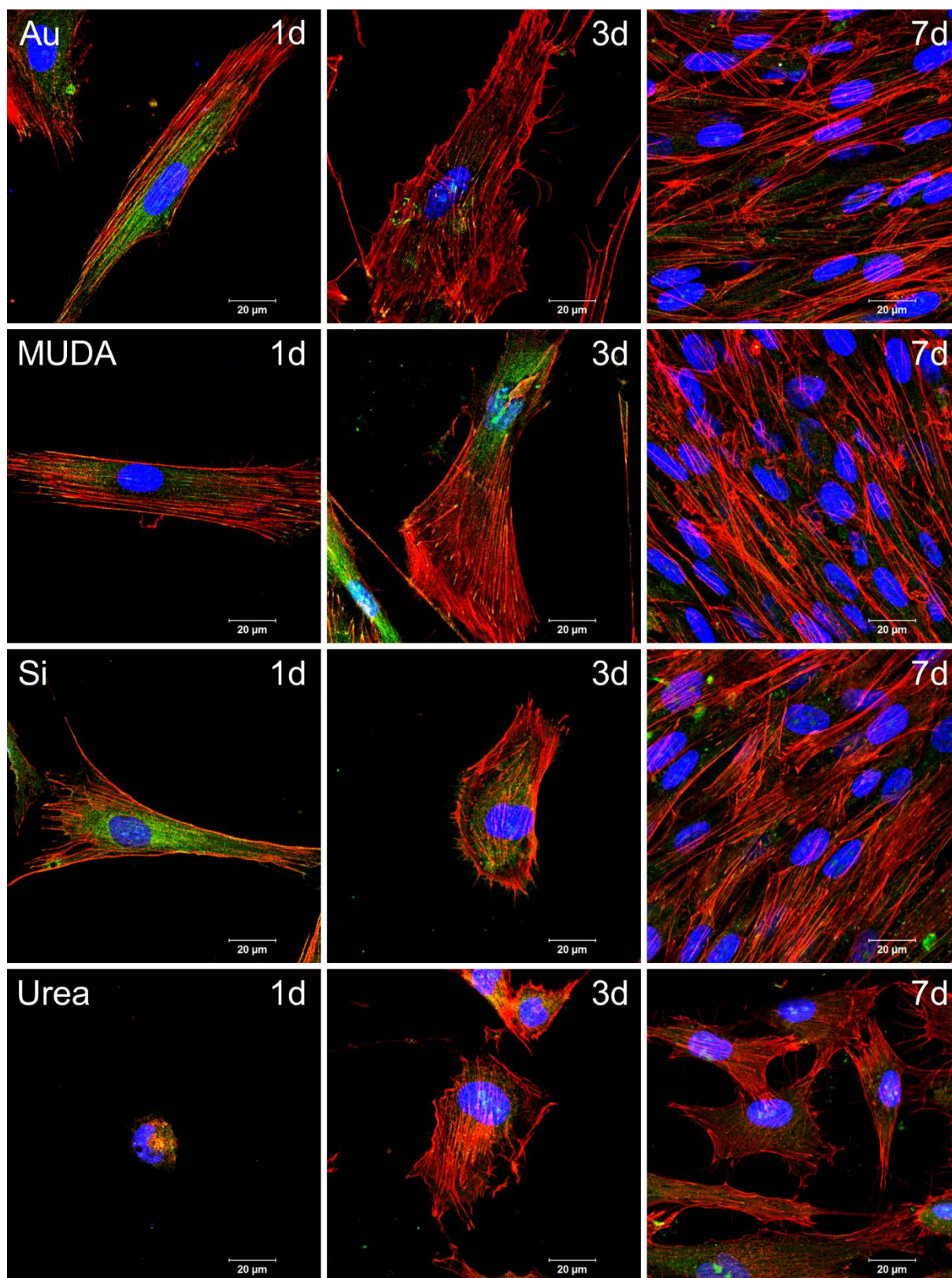
Figure A.3 - CLSM images of HDF adherent on planar control surfaces with preadsorption of 2 μg mL^{-1} FN after 1 d (left), 3 d (middle), and 7 d (right) of culture. The cells were stained for actin (red), vinculin (green) and nucleus (blue). [Au - gold, MUDA - gold with mercaptoundecanoic acid, Si - silicon dioxide, Urea - silicon dioxide with mPEG-urea] [Scale: 20 μm]
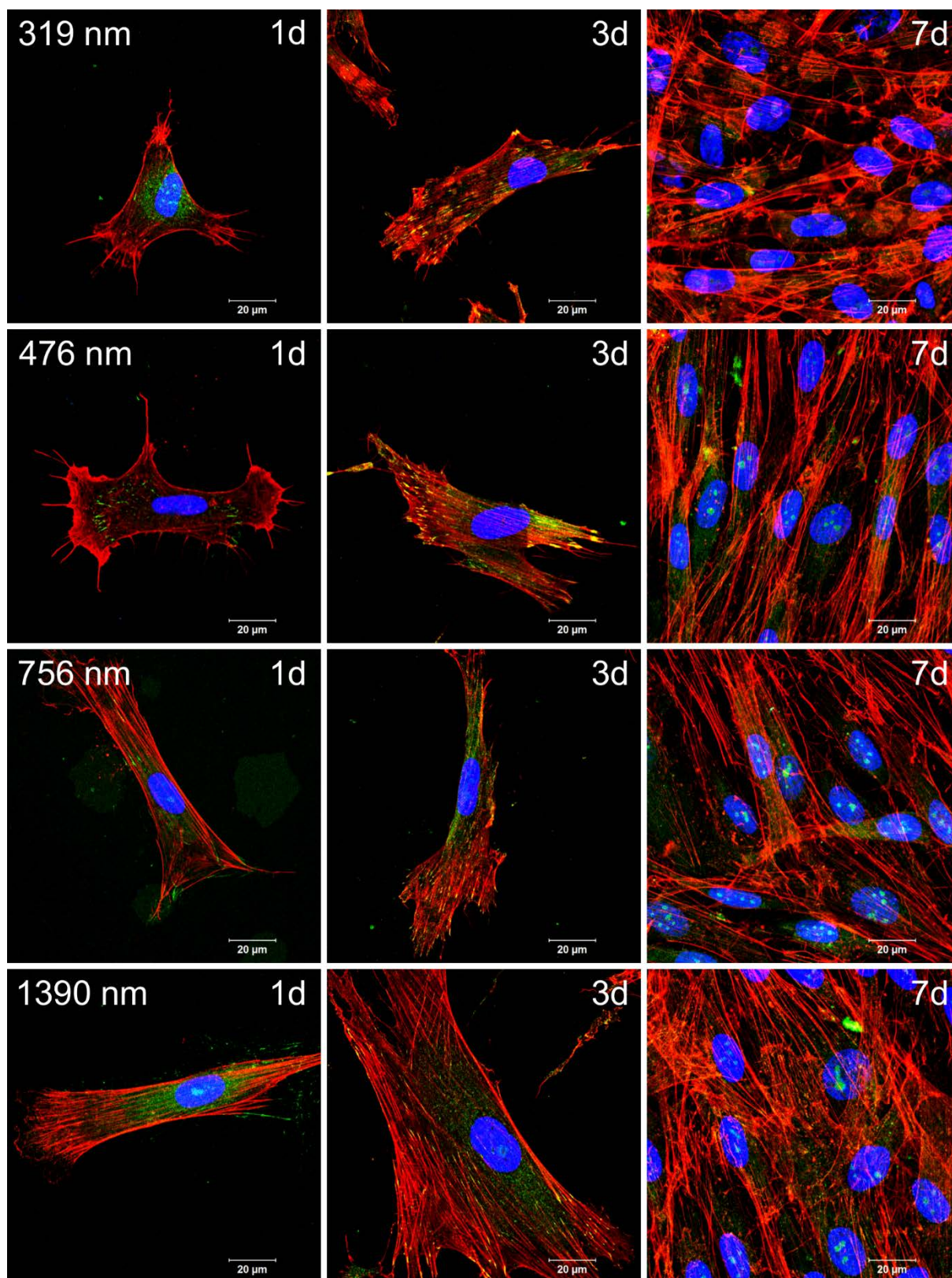
Figure A.4 - CLSM images of HDF adherent on nanostructured surfaces without preadsorption of FN after 1 d (left), 3 d (middle), and 7 d (right) of culture. The cells were stained for actin (red), vinculin (green) and nucleus (blue). [Scale: 20 μm]
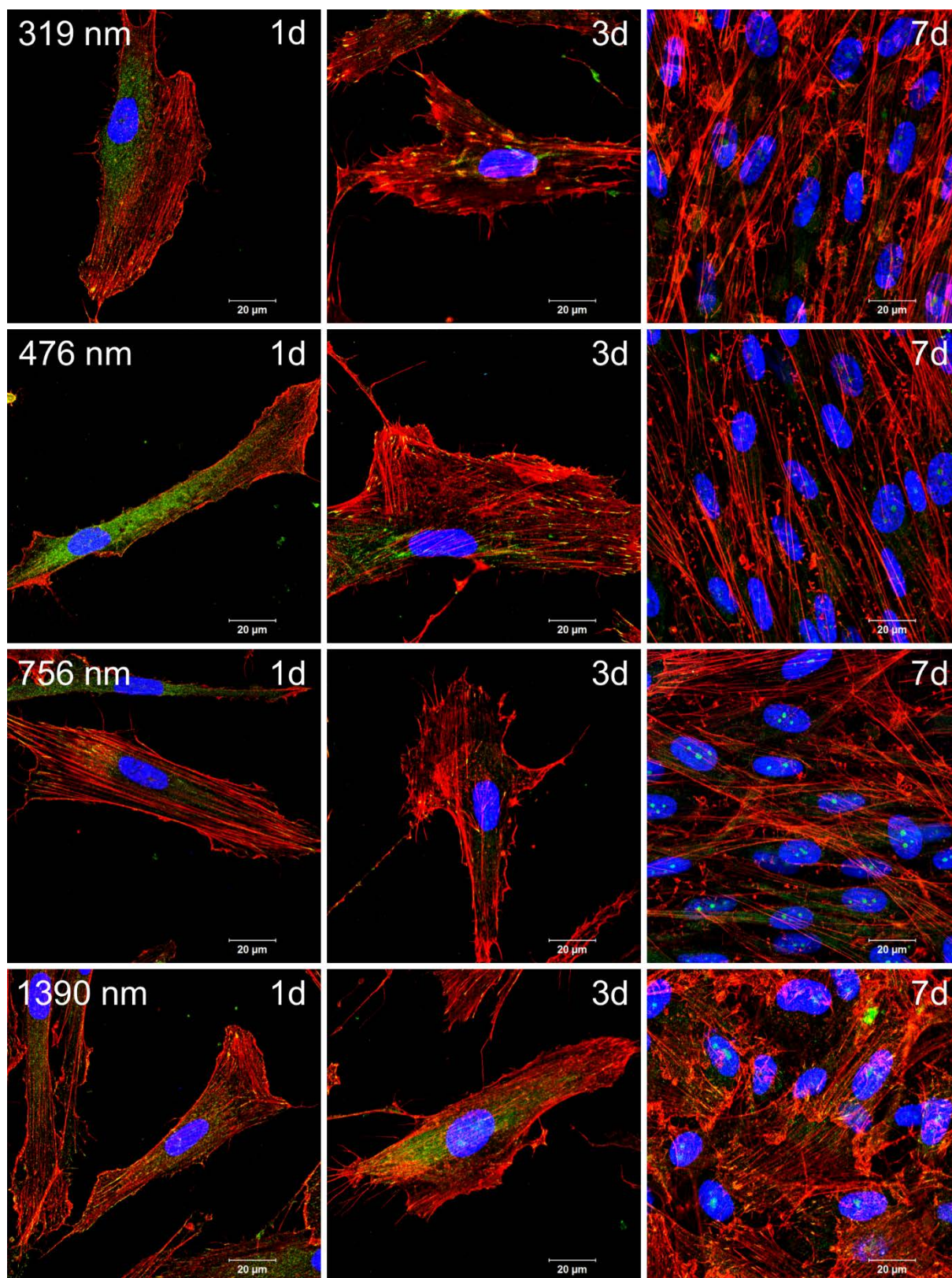
Figure A.5 - CLSM images of HDF adherent on nanostructured surfaces with preadsorption of 2 μg mL^{-1} FN after 1 d (left), 3 d (middle), and 7 d (right) of culture. The cells were stained for actin (red), vinculin (green) and nucleus (blue). [Scale: 20 μm]

Table A.6 - ANOVA of cell count on nanostructured surfaces without preadsorption of FN (p < 0.05; 1 = significant; 0 = NOT significant)

		1d								3d								7d							
		Au	MUDA	Si	Urea	319	476	756	1390	Au	MUDA	Si	Urea	319	476	756	1390	Au	MUDA	Si	Urea	319	476	756	1390
1d	Au		0	0	1	0	0	0	0	0	1	0	0	0	1	0	1	1	1	0	1	1	1	1	1
	MUDA	0		0	1	0	0	0	0	0	1	0	0	0	0	0	0	1	1	0	1	1	1	1	1
	Si	0	0		1	0	1	0	0	0	1	0	0	0	1	1	1	1	1	0	1	1	1	1	1
	Urea	1	1	1		1	1	1	1	0	1	0	0	1	1	1	1	1	1	0	1	1	1	1	1
	319	0	0	0	1		0	0	0	0	1	0	0	0	0	0	0	1	1	0	1	1	1	1	1
	476	0	0	1	1	0		0	0	0	1	0	0	0	0	0	0	1	1	0	1	1	1	1	1
	756	0	0	0	1	0	0		0	0	1	0	0	0	0	0	0	1	1	0	1	1	1	1	1
	1390	0	0	0	1	0	0	0		0	1	0	0	0	0	0	0	1	1	0	1	1	1	1	1
3d	Au	0	0	0	0	0	0	0	0		1	0	0	0	0	1	0	1	1	0	1	1	1	1	1
	MUDA	1	1	1	1	1	1	1	1	1		1	1	1	0	0	0	1	1	0	0	1	1	1	1
	Si	0	0	0	0	0	0	0	0	0	1		0	0	1	0	0	1	1	0	1	1	1	1	1
	Urea	0	0	0	0	0	0	0	0	0	1	0		0	1	0	0	1	1	0	1	1	1	1	1
	319	0	0	0	1	0	0	0	0	0	1	0	0		0	0	0	1	1	0	1	1	1	1	1
	476	1	0	1	1	0	0	0	0	0	0	1	1	0		0	0	1	1	0	0	1	1	1	1
	756	0	0	1	1	0	0	0	0	1	0	0	0	0	0		0	1	1	0	1	1	1	1	1
	1390	1	0	1	1	0	0	0	0	0	0	0	0	0	0	0		1	1	0	0	1	1	1	1
7d	Au	1	1	1	1	1	1	1	1	1	1	1	1	1	1	1	1		0	1	1	0	0	1	0
	MUDA	1	1	1	1	1	1	1	1	1	1	1	1	1	1	1	1	0		1	1	0	0	1	0
	Si	0	0	0	0	0	0	0	0	0	0	0	0	0	0	0	0	1	1		0	1	1	0	1
	Urea	1	1	1	1	1	1	1	1	1	0	1	1	1	0	1	0	1	1	0		1	1	0	0
	319	1	1	1	1	1	1	1	1	1	1	1	1	1	1	1	1	0	0	1	1		0	1	0
	476	1	1	1	1	1	1	1	1	1	1	1	1	1	1	1	1	0	0	1	1	0		1	0
	756	1	1	1	1	1	1	1	1	1	1	1	1	1	1	1	1	1	1	0	0	1	1		0
	1390	1	1	1	1	1	1	1	1	1	1	1	1	1	1	1	1	0	0	1	0	0	0	0	

Table A.7 - ANOVA of cell count on nanostructured surfaces with preadsorption of 2 μg mL^{-1} FN (p < 0.05; 1 = significant; 0 = NOT significant)

		1d								3d								7d							
		Au	MUDA	Si	Urea	319	476	756	1390	Au	MUDA	Si	Urea	319	476	756	1390	Au	MUDA	Si	Urea	319	476	756	1390
1d	Au		0	0	1	0	0	0	0	0	0	0	0	0	0	0	0	1	1	1	1	1	1	1	1
	MUDA	0		0	1	0	0	0	0	0	0	0	0	0	0	0	0	1	1	1	1	1	1	1	1
	Si	0	0		1	0	0	0	0	0	0	0	0	0	0	0	0	1	1	1	1	1	1	1	1
	Urea	1	1	1		0	1	0	0	0	1	1	0	1	1	1	1	1	1	1	1	1	1	1	1
	319	0	0	0	0		0	0	0	0	0	0	0	0	0	1	1	1	1	1	1	1	1	1	1
	476	0	0	0	1	0		0	0	0	0	0	0	0	0	0	0	1	1	1	1	1	1	1	1
	756	0	0	0	0	0	0		0	0	0	0	0	0	0	0	1	1	1	1	1	1	1	1	1
	1390	0	0	0	0	0	0	0		0	0	0	0	0	0	0	1	1	1	1	1	1	1	1	1
3d	Au	0	0	0	0	0	0	0	0		0	0	0	0	0	0	0	1	1	1	1	1	1	1	1
	MUDA	0	0	0	1	0	0	0	0	0		0	0	0	0	0	0	1	1	1	1	1	1	1	1
	Si	0	0	0	1	0	0	0	0	0	0		0	0	0	0	0	1	1	1	1	1	1	1	1
	Urea	0	0	0	0	0	0	0	0	0	0	0		0	0	0	0	1	1	1	1	1	1	1	1
	319	0	0	0	1	0	0	0	0	0	0	0	0		0	0	0	1	1	1	1	1	1	1	1
	476	0	0	0	1	0	0	0	0	0	0	0	0	0		0	0	1	1	1	1	1	1	1	1
	756	0	0	0	1	1	0	0	0	0	0	0	0	0	0		0	1	1	1	1	1	1	1	1
	1390	0	0	0	1	1	0	1	1	0	0	0	0	0	0	0		1	1	1	1	1	1	1	1
7d	Au	1	1	1	1	1	1	1	1	1	1	1	1	1	1	1	1		0	1	0	0	0	0	1
	MUDA	1	1	1	1	1	1	1	1	1	1	1	1	1	1	1	1	0		1	0	0	0	0	1
	Si	1	1	1	1	1	1	1	1	1	1	1	1	1	1	1	1	1	1		0	0	1	0	0
	Urea	1	1	1	1	1	1	1	1	1	1	1	1	1	1	1	1	0	0	0		0	0	0	0
	319	1	1	1	1	1	1	1	1	1	1	1	1	1	1	1	1	0	0	0	0		0	0	1
	476	1	1	1	1	1	1	1	1	1	1	1	1	1	1	1	1	0	0	1	0	0		0	1
	756	1	1	1	1	1	1	1	1	1	1	1	1	1	1	1	1	0	0	0	0	0	0		0
	1390	1	1	1	1	1	1	1	1	1	1	1	1	1	1	1	1	1	1	0	0	1	1	0	

Table A.8 - ANOVA of cell count on nanostructured surfaces modified with PEM at pH 5.0 after 4 h of incubation (p < 0.05; 1 = significant; 0 = NOT significant)

COUNT		(PH)4				(PH)4P				(PH)4 FN				(PH)4P FN			
		319	476	756	1390	319	476	756	1390	319	476	756	1390	319	476	756	1390
(PH)4	319		0	0	0	0	0	0	1	0	0	0	0	0	0	0	0
	476	0		0	0	1	1	1	1	0	0	1	1	0	0	0	1
	756	0	0		0	1	1	1	1	1	0	1	1	1	1	1	1
	1390	0	0	0		0	0	0	0	0	0	0	0	0	0	0	0
(PH)4P	319	0	1	1	0		0	0	0	0	0	0	0	0	0	0	0
	476	0	1	1	0	0		0	0	0	0	0	0	0	0	0	0
	756	0	1	1	0	0	0		0	0	0	0	0	0	0	0	0
	1390	1	1	1	0	0	0	0		0	0	0	0	0	0	0	0
(PH)4 FN	319	0	0	1	0	0	0	0	0		0	0	0	0	0	0	0
	476	0	0	0	0	0	0	0	0	0		0	0	0	0	0	0
	756	0	1	1	0	0	0	0	0	0	0		0	0	0	0	0
	1390	0	1	1	0	0	0	0	0	0	0	0		0	0	0	0
(PH)4P FN	319	0	0	1	0	0	0	0	0	0	0	0	0		0	0	0
	476	0	0	1	0	0	0	0	0	0	0	0	0	0		0	0
	756	0	0	1	0	0	0	0	0	0	0	0	0	0	0		0
	1390	0	1	1	0	0	0	0	0	0	0	0	0	0	0	0	

Table A.9 - ANOVA of cell area on nanostructured surfaces modified with PEM at pH 5.0 after 4 h of incubation (p < 0.05; 1 = significant; 0 = NOT significant)

AREA		(PH)4				(PH)4P				(PH)4 FN				(PH)4P FN			
		319	476	756	1390	319	476	756	1390	319	476	756	1390	319	476	756	1390
(PH)4	319		0	0	1	0	0	0	0	1	0	1	1	0	0	0	1
	476	0		0	0	0	0	0	0	1	1	1	1	0	0	0	1
	756	0	0		0	0	0	0	0	0	0	0	1	0	0	0	0
	1390	1	0	0		0	0	0	1	1	1	1	1	1	0	0	1
(PH)4P	319	0	0	0	0		0	0	0	1	0	1	1	0	0	0	1
	476	0	0	0	0	0		0	0	1	0	1	1	0	0	0	1
	756	0	0	0	0	0	0		0	1	0	1	1	0	0	0	1
	1390	0	0	0	1	0	0	0		1	0	1	1	0	0	0	1
(PH)4 FN	319	1	1	0	1	1	1	1	1		0	0	0	1	0	1	0
	476	0	1	0	1	0	0	0	0	0		0	1	0	0	0	0
	756	1	1	0	1	1	1	1	1	0	0		0	1	1	1	0
	1390	1	1	1	1	1	1	1	1	0	1	0		1	1	1	1
(PH)4P FN	319	0	0	0	1	0	0	0	0	1	0	1	1		0	0	0
	476	0	0	0	0	0	0	0	0	0	0	1	1	0		0	1
	756	0	0	0	0	0	0	0	0	1	0	1	1	0	0		0
	1390	1	1	0	1	1	1	1	1	0	0	0	1	0	1	0	

Table A.10 - ANOVA of aspect ratio of cells on nanostructured surfaces modified with PEM at pH 5.0 after 4 h of incubation (p < 0.05; 1 = significant; 0 = NOT significant)

ASPECT RATIO		(PH)4				(PH)4P				(PH)4 FN				(PH)4P FN			
		319	476	756	1390	319	476	756	1390	319	476	756	1390	319	476	756	1390
(PH)4	319		0	0	0	0	0	0	0	0	0	0	0	0	0	0	0
	476	0		0	0	0	0	0	0	0	0	0	0	0	0	0	0
	756	0	0		0	0	0	0	0	0	0	0	0	1	1	1	1
	1390	0	0	0		0	0	0	0	0	0	0	1	0	0	0	0
(PH)4P	319	0	0	0	0		0	0	0	0	0	0	1	0	0	0	0
	476	0	0	0	0	0		0	0	0	0	0	1	0	0	0	0
	756	0	0	0	0	0	0		0	0	0	0	0	1	0	0	0
	1390	0	0	0	0	0	0	0		0	1	0	1	0	0	0	0
(PH)4 FN	319	0	0	0	0	0	0	0	0		0	0	0	0	1	0	0
	476	0	0	0	0	0	0	0	1	0		0	0	1	1	1	1
	756	0	0	0	0	0	0	0	0	0	0		0	0	1	0	0
	1390	0	0	0	1	1	1	0	1	0	0	0		1	1	1	1
(PH)4P FN	319	0	0	1	0	0	0	1	0	0	1	0	1		0	0	0
	476	0	0	1	0	0	0	0	0	1	1	1	1	0		0	0
	756	0	0	1	0	0	0	0	0	0	1	0	1	0	0		0
	1390	0	0	1	0	0	0	0	0	0	1	0	1	0	0	0	

Table A.11 - ANOVA of cell count on nanostructured surfaces modified with PEM at pH 9.0 after 4 h of incubation (p < 0.05; 1 = significant; 0 = NOT significant)

COUNT		(PH)4				(PH)4P				(PH)4 FN				(PH)4P FN			
		319	476	756	1390	319	476	756	1390	319	476	756	1390	319	476	756	1390
(PH)4	319		0	0	0	0	0	0	0	0	0	0	0	0	0	0	0
	476	0		0	0	0	0	1	0	0	0	0	0	0	0	0	0
	756	0	0		0	0	1	1	1	0	0	0	0	1	1	1	1
	1390	0	0	0		0	0	1	0	0	0	0	0	0	0	0	0
(PH)4P	319	0	0	0	0		0	0	0	0	0	0	0	0	0	0	0
	476	0	0	1	0	0		0	0	0	0	0	0	0	0	0	0
	756	0	1	1	1	0	0		0	1	0	1	1	0	0	0	0
	1390	0	0	1	0	0	0	0		0	0	0	0	0	0	0	0
(PH)4 FN	319	0	0	0	0	0	0	1	0		0	0	0	0	0	0	0
	476	0	0	0	0	0	0	0	0	0		0	0	0	0	0	0
	756	0	0	0	0	0	0	1	0	0	0		0	0	0	0	0
	1390	0	0	0	0	0	0	1	0	0	0	0		0	0	0	0
(PH)4P FN	319	0	0	1	0	0	0	0	0	0	0	0	0		0	0	0
	476	0	0	1	0	0	0	0	0	0	0	0	0	0		0	0
	756	0	0	1	0	0	0	0	0	0	0	0	0	0	0		0
	1390	0	0	1	0	0	0	0	0	0	0	0	0	0	0	0	

Table A.12 - ANOVA of cell area on nanostructured surfaces modified with PEM at pH 9.0 after 4 h of incubation (p < 0.05; 1 = significant; 0 = NOT significant)

AREA		(PH)4				(PH)4P				(PH)4 FN				(PH)4P FN			
		319	476	756	1390	319	476	756	1390	319	476	756	1390	319	476	756	1390
(PH)4	319		0	0	0	0	0	0	0	1	1	1	1	0	0	0	0
	476	0		0	0	0	0	0	0	1	1	1	1	0	0	0	0
	756	0	0		0	0	0	0	0	1	1	1	1	0	0	0	0
	1390	0	0	0		0	0	0	0	1	1	1	1	0	0	0	0
(PH)4P	319	0	0	0	0		0	0	0	1	1	1	1	0	0	0	0
	476	0	0	0	0	0		0	0	1	1	1	1	0	0	0	0
	756	0	0	0	0	0	0		0	1	1	1	1	0	0	0	0
	1390	0	0	0	0	0	0	0		1	1	1	1	0	0	0	0
(PH)4 FN	319	1	1	1	1	1	1	1	1		0	0	1	1	1	1	1
	476	1	1	1	1	1	1	1	1	0		0	1	1	1	1	1
	756	1	1	1	1	1	1	1	1	0	0		0	1	1	1	1
	1390	1	1	1	1	1	1	1	1	1	1	0		1	1	1	1
(PH)4P FN	319	0	0	0	0	0	0	0	0	1	1	1	1		0	0	0
	476	0	0	0	0	0	0	0	0	1	1	1	1	0		0	0
	756	0	0	0	0	0	0	0	0	1	1	1	1	0	0		0
	1390	0	0	0	0	0	0	0	0	1	1	1	1	0	0	0	

Table A.13 - ANOVA of aspect ratio of cells on nanostructured surfaces modified with PEM at pH 9.0 after 4 h of incubation (p < 0.05; 1 = significant; 0 = NOT significant)

ASPECT RATIO		(PH)4				(PH)4P				(PH)4 FN				(PH)4P FN			
		319	476	756	1390	319	476	756	1390	319	476	756	1390	319	476	756	1390
(PH)4	319		0	0	0	0	0	0	0	1	0	1	1	0	0	0	0
	476	0		0	0	0	0	0	0	1	0	1	1	0	0	0	0
	756	0	0		0	0	0	0	0	1	0	1	1	0	0	0	0
	1390	0	0	0		0	0	0	0	1	0	1	1	0	0	0	0
(PH)4P	319	0	0	0	0		0	0	0	1	1	1	1	0	0	0	0
	476	0	0	0	0	0		0	0	0	1	0	1	0	0	0	0
	756	0	0	0	0	0	0		0	1	1	0	1	0	0	0	0
	1390	0	0	0	0	0	0	0		0	1	0	1	0	0	0	0
(PH)4 FN	319	1	1	1	1	1	0	1	0		0	0	0	0	1	0	0
	476	0	0	0	0	1	1	1	1	0		0	0	1	1	1	1
	756	1	1	1	1	1	0	0	0	0	0		0	0	1	0	0
	1390	1	1	1	1	1	1	1	1	0	0	0		1	1	1	1
(PH)4P FN	319	0	0	0	0	0	0	0	0	0	1	0	1		0	0	0
	476	0	0	0	0	0	0	0	0	1	1	1	1	0		0	0
	756	0	0	0	0	0	0	0	0	0	1	0	1	0	0		0
	1390	0	0	0	0	0	0	0	0	0	1	0	1	0	0	0	
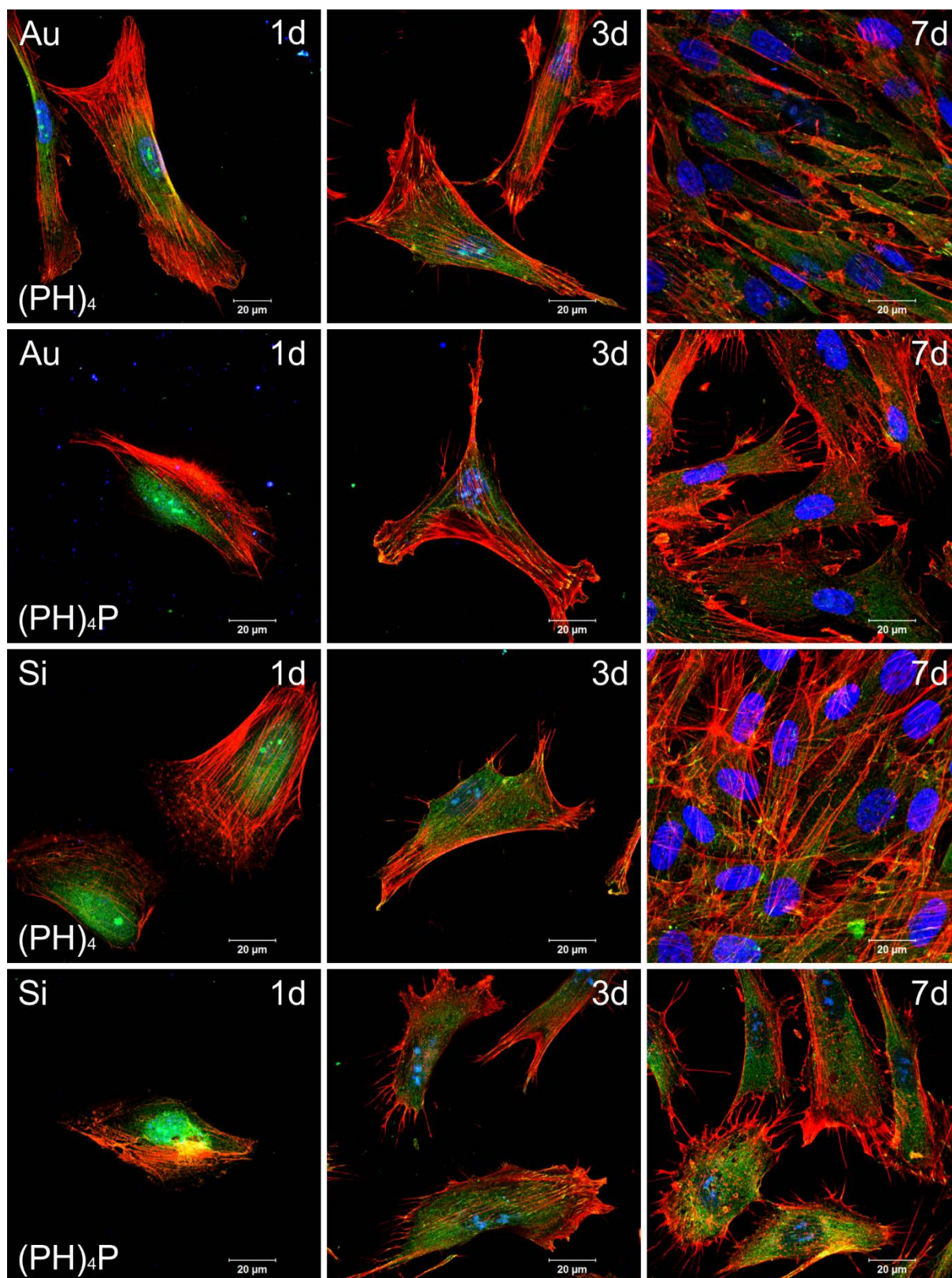
Figure A.6 - CLSM images of HDF adherent on planar control surfaces modified with PEM at pH 5.0 after 1 d (left), 3 d (middle), and 7 d (right) of culture. The cells were stained for actin (red), vinculin (green) and nucleus (blue). [Au - gold, Si - silicon dioxide] [Scale: 20 μm]

Figure A.7 - CLSM images of HDF adherent on planar control surfaces modified with PEM at pH 9.0 after 1 d (left), 3 d (middle), and 7 d (right) of culture. The cells were stained for actin (red), vinculin (green) and nucleus (blue). [Au - gold, Si - silicon dioxide] [Scale: 20 μm]

Figure A.8 - CLSM images of HDF adherent on the terminal HEP layer *(PH)₄* prepared at pH 5.0 on nanostructured surfaces after 1 d (left), 3 d (middle), and 7 d (right) of culture. The cells were stained for actin (red), vinculin (green) and nucleus (blue). [Scale: 20 μm]

Figure A.9 - CLSM images of HDF adherent on the terminal PEI layer *(PH)₄P* **prepared at pH 5.0 on nanostructured surfaces after 1 d (left), 3 d (middle), and 7 d (right) of culture. The cells were stained for actin (red), vinculin (green) and nucleus (blue). [Scale: 20 μm]**

Table A.14 - ANOVA of cell count on the terminal HEP layer *(PH)₄* prepared at pH 5.0 on nanostructured surfaces (p < 0.05; 1 = significant; 0 = NOT significant)

		1d						3d						7d					
		Au	Si	319	476	756	1390	Au	Si	319	476	756	1390	Au	Si	319	476	756	1390
1d	Au		0	0	0	0	0	1	0	0	0	0	0	1	1	1	1	1	1
	Si	0		0	1	1	0	1	0	0	0	0	0	1	1	1	1	1	1
	319	0	0		0	0	0	1	0	0	0	0	0	1	1	1	1	1	1
	476	0	1	0		0	0	1	1	0	0	0	0	1	1	1	1	1	1
	756	0	1	0	0		0	1	1	0	0	0	0	1	1	1	1	1	1
	1390	0	0	0	0	0		1	0	0	0	0	0	1	1	1	1	1	1
3d	Au	1	1	1	1	1	1		0	1	1	1	0	1	1	1	1	1	1
	Si	0	0	0	1	1	0	0		0	0	0	0	1	1	1	1	1	1
	319	0	0	0	0	0	0	1	0		0	0	0	1	1	1	1	1	1
	476	0	0	0	0	0	0	1	0	0		0	0	1	1	1	1	1	1
	756	0	0	0	0	0	0	1	0	0	0		0	1	1	1	1	1	1
	1390	0	0	0	0	0	0	0	0	0	0	0		1	1	1	1	1	1
7d	Au	1	1	1	1	1	1	1	1	1	1	1	1		0	0	0	0	0
	Si	1	1	1	1	1	1	1	1	1	1	1	1	0		0	1	0	0
	319	1	1	1	1	1	1	1	1	1	1	1	1	0	0		0	0	0
	476	1	1	1	1	1	1	1	1	1	1	1	1	0	1	0		0	0
	756	1	1	1	1	1	1	1	1	1	1	1	1	0	0	0	0		0
	1390	1	1	1	1	1	1	1	1	1	1	1	1	0	0	0	0	0	

Table A.15 - ANOVA of cell count on the terminal PEI layer *(PH)₄P* prepared at pH 5.0 on nanostructured surfaces (p < 0.05; 1 = significant; 0 = NOT significant)

		1d						3d						7d					
		Au	Si	319	476	756	1390	Au	Si	319	476	756	1390	Au	Si	319	476	756	1390
1d	Au		0	0	0	0	0	0	0	1	1	1	1	1	1	0	0	0	1
	Si	0		0	0	0	0	0	0	1	1	1	1	1	1	0	0	0	1
	319	0	0		0	0	0	0	0	1	1	1	1	1	1	0	0	0	1
	476	0	0	0		0	0	0	0	1	1	1	1	1	1	0	0	0	1
	756	0	0	0	0		0	0	0	1	1	1	1	1	1	0	0	0	1
	1390	0	0	0	0	0		0	0	1	1	1	1	1	1	0	0	0	0
3d	Au	0	0	0	0	0	0		0	1	1	1	1	1	1	0	0	0	1
	Si	0	0	0	0	0	0	0		1	1	1	1	1	1	0	0	0	1
	319	1	1	1	1	1	1	1	1		0	0	0	1	1	0	0	0	1
	476	1	1	1	1	1	1	1	1	0		0	0	1	1	0	0	0	1
	756	1	1	1	1	1	1	1	1	0	0		0	1	1	0	0	0	1
	1390	1	1	1	1	1	1	1	1	0	0	0		1	1	0	0	0	1
7d	Au	1	1	1	1	1	1	1	1	1	1	1	1		0	1	1	1	1
	Si	1	1	1	1	1	1	1	1	1	1	1	1	0		1	1	1	0
	319	0	0	0	0	0	0	0	0	0	0	0	0	1	1		0	0	0
	476	0	0	0	0	0	0	0	0	0	0	0	0	1	1	0		0	0
	756	0	0	0	0	0	0	0	0	0	0	0	0	1	1	0	0		0
	1390	1	1	1	1	1	0	1	1	1	1	1	1	1	0	0	0	0	

Figure A.10 - CLSM images of HDF adherent on the terminal HEP layer *(PH)₄* **prepared at pH 9.0 on nanostructured surfaces after 1 d (left), 3 d (middle), and 7 d (right) of culture. The cells were stained for actin (red), vinculin (green) and nucleus (blue). [Scale: 20 *µ*m]**
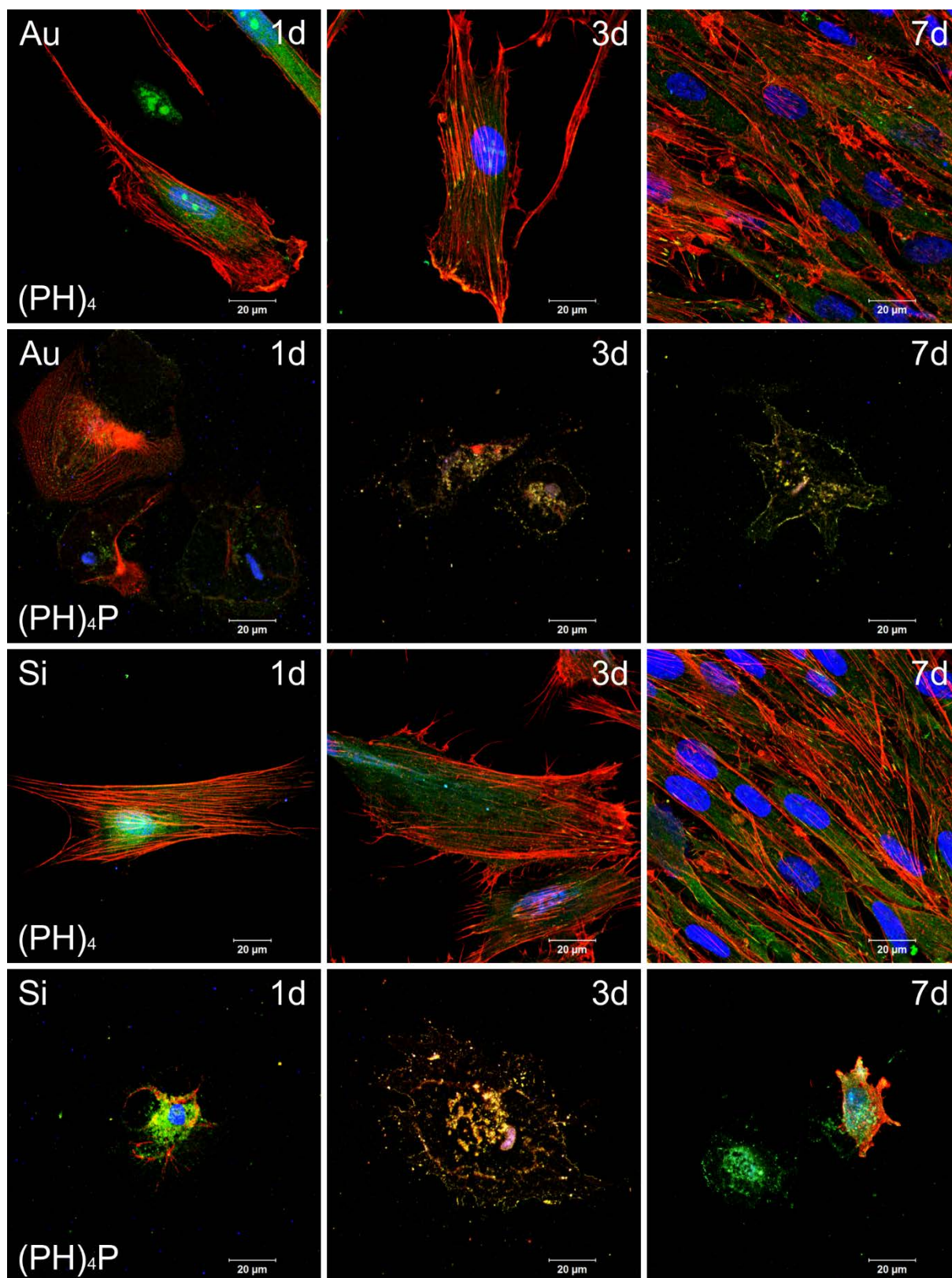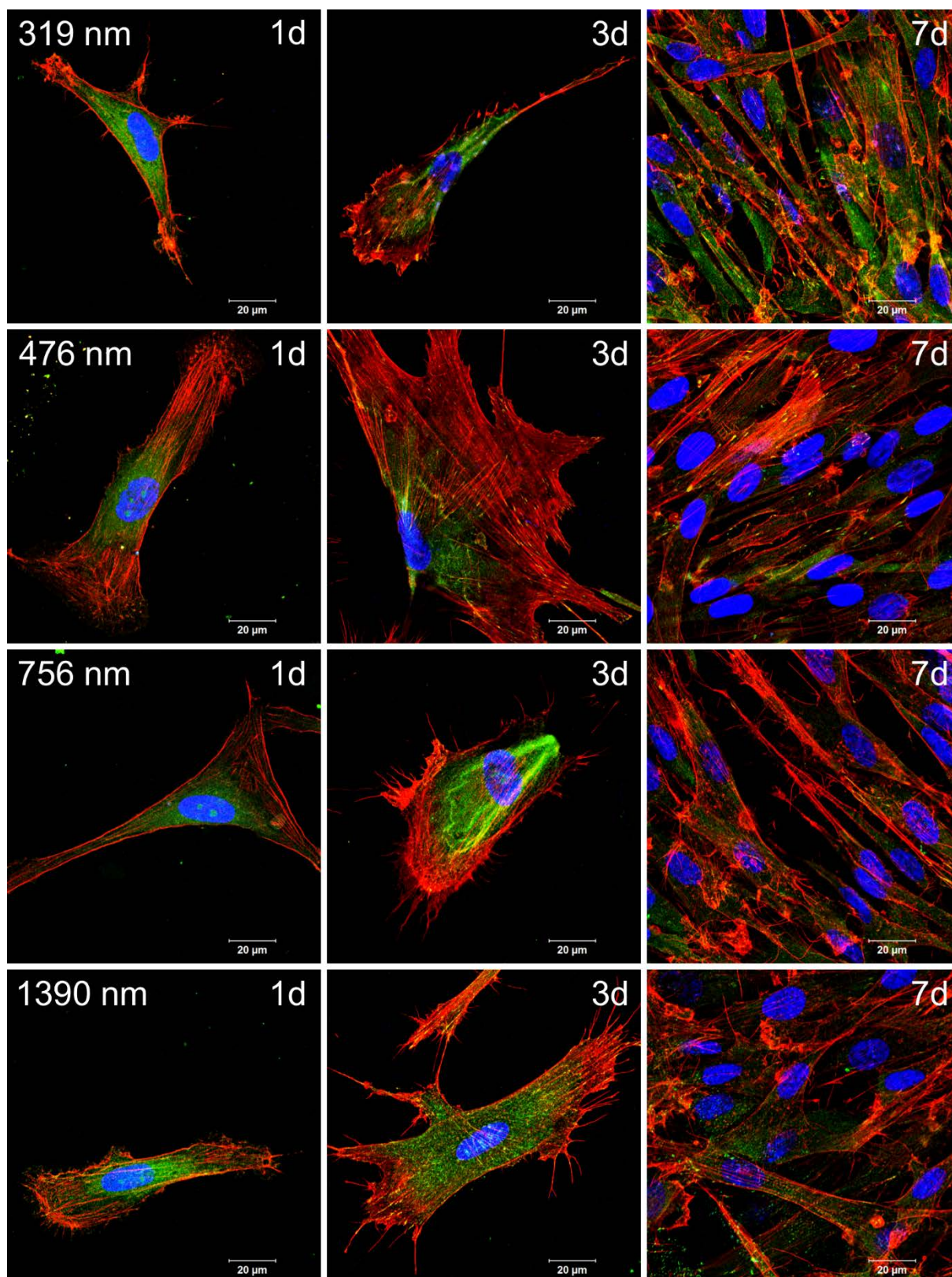
Figure A.11 - CLSM images of HDF adherent on the terminal PEI layer *(PH)₄P* **prepared at pH 9.0 on nanostructured surfaces after 1 d (left), 3 d (middle), and 7 d (right) of culture. The cells were stained for actin (red), vinculin (green) and nucleus (blue). [Scale: 20 *μ*m]**
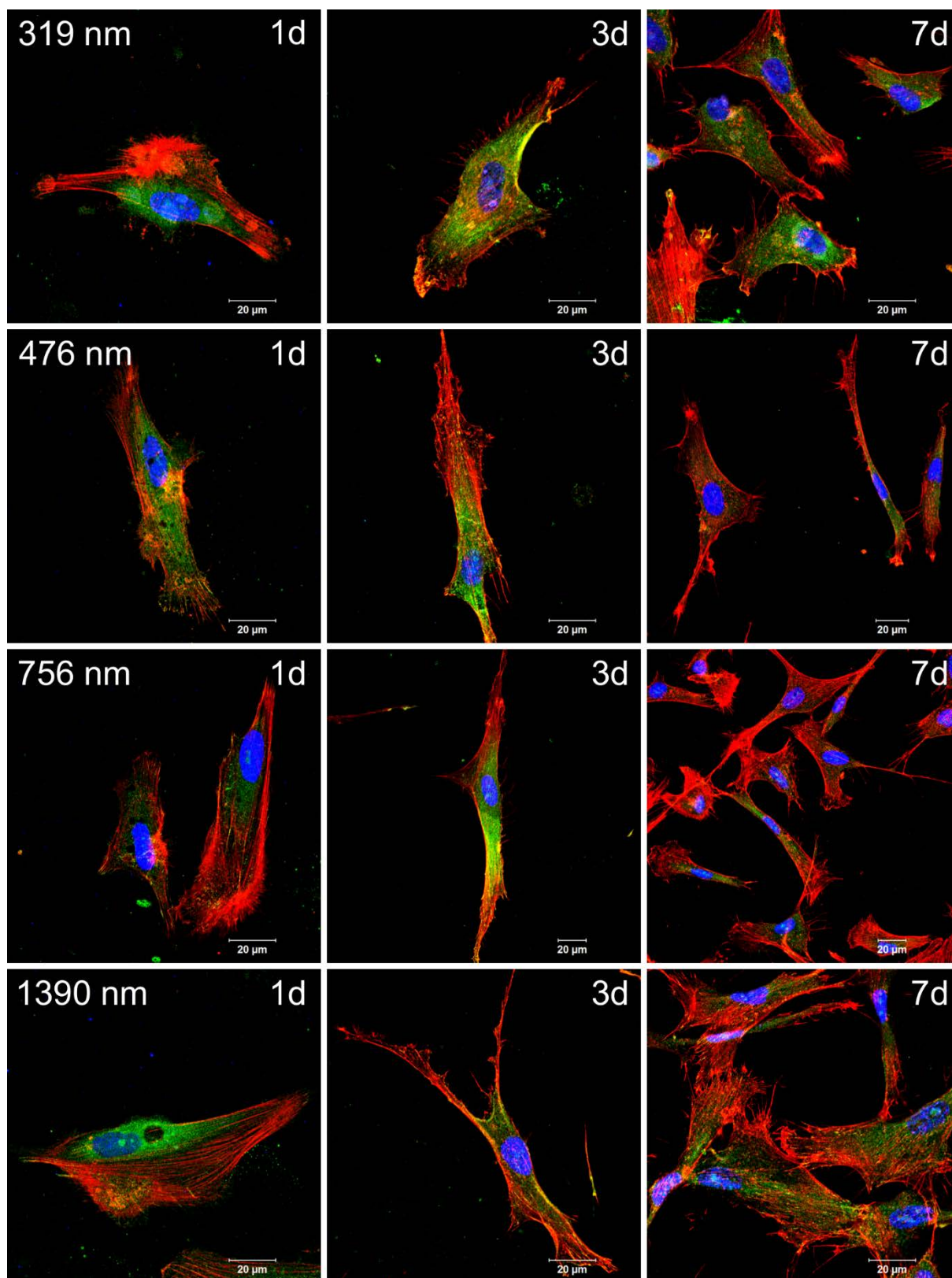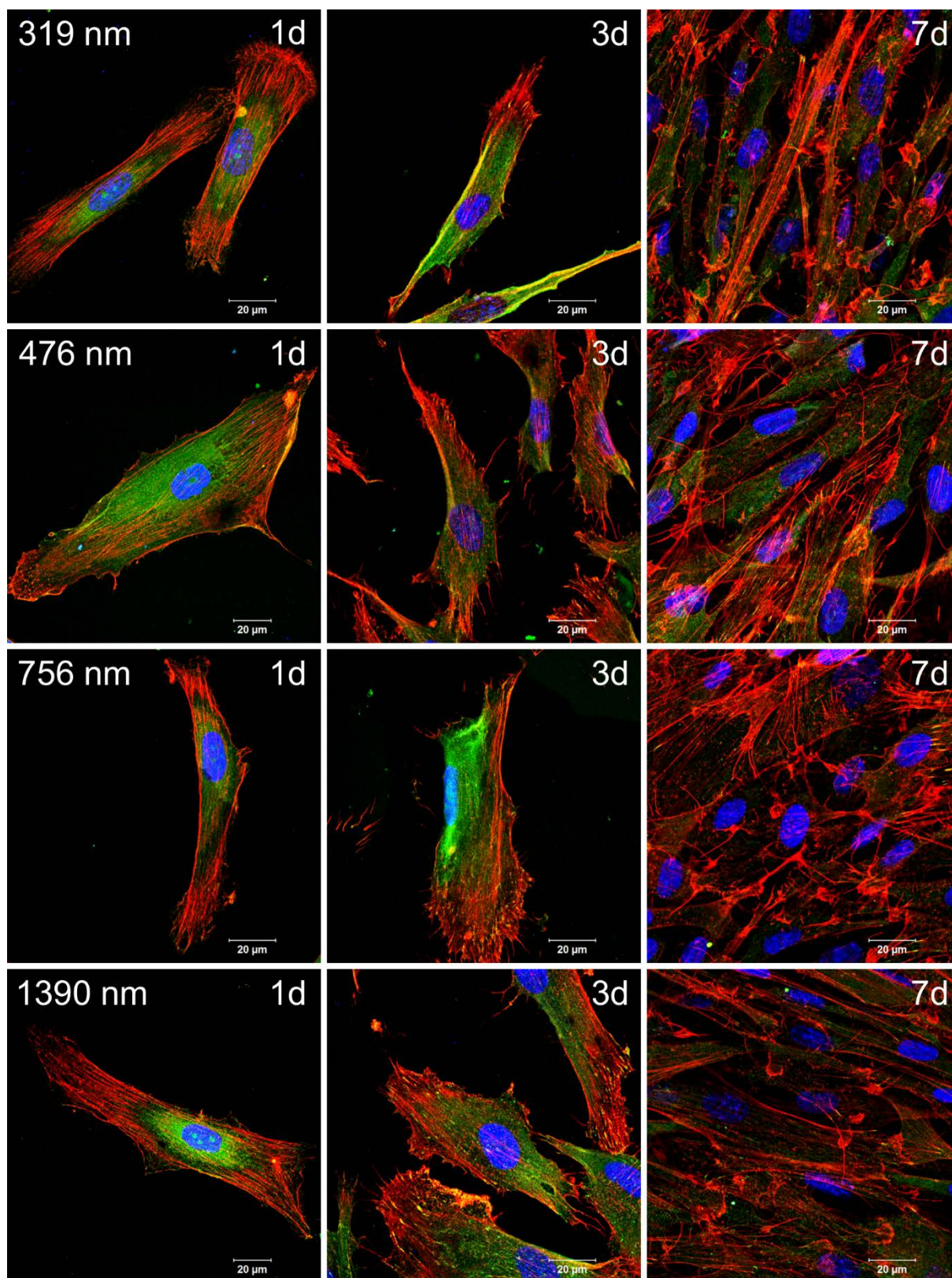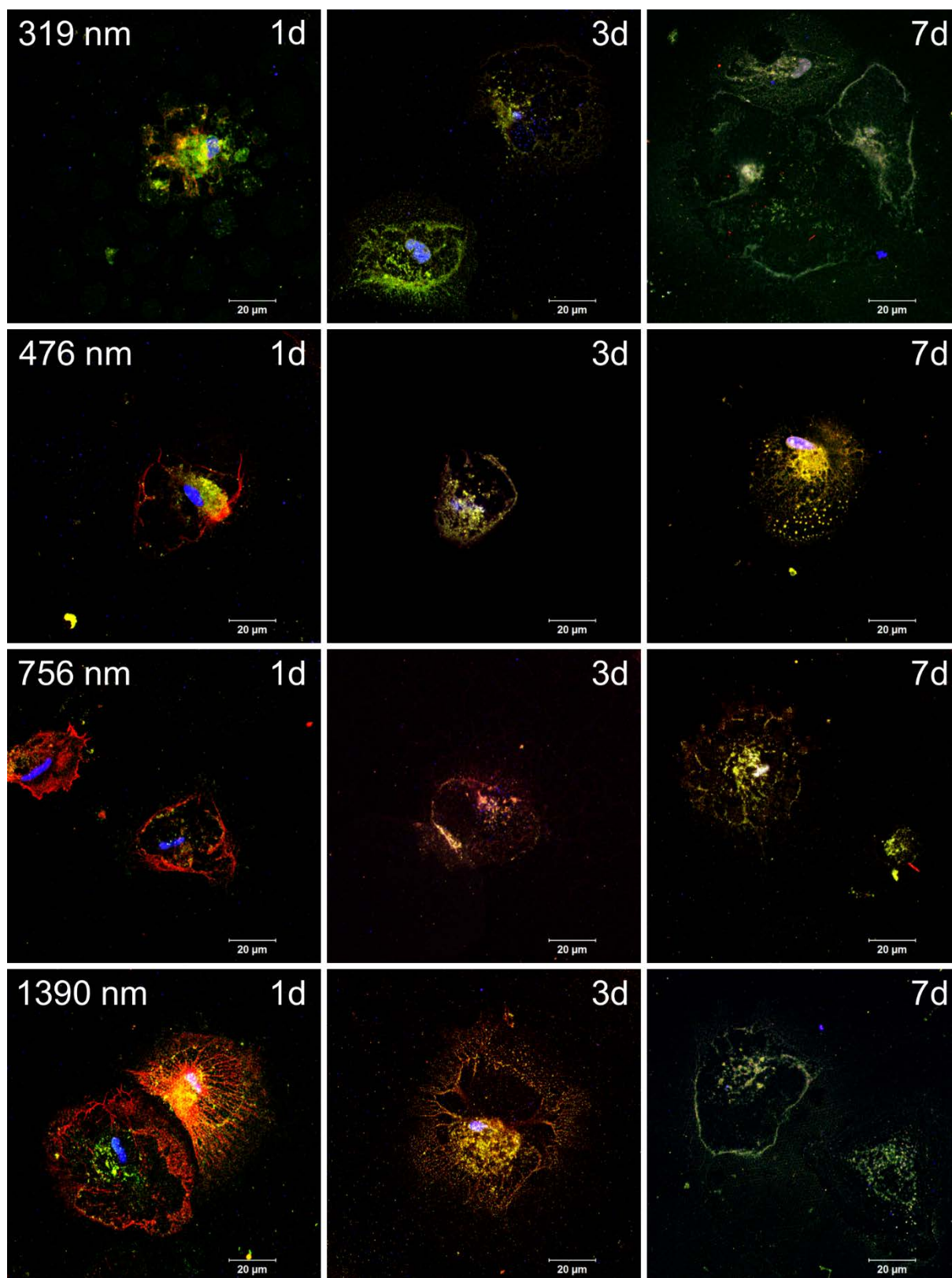
Table A.16 - ANOVA of cell count on the terminal HEP layer *(PH)$_4$* prepared at pH 9.0 on nanostructured surfaces (p < 0.05; 1 = significant; 0 = NOT significant)

		1d						3d						7d					
		Au	Si	319	476	756	1390	Au	Si	319	476	756	1390	Au	Si	319	476	756	1390
1d	Au		0	0	0	1	0	1	0	0	0	0	0	1	1	1	1	1	1
	Si	0		0	0	0	0	1	1	0	0	0	0	1	1	1	1	1	1
	319	0	0		0	0	0	1	1	0	0	0	0	1	1	1	1	1	1
	476	0	0	0		0	0	1	1	0	0	0	0	1	1	1	1	1	1
	756	1	0	0	0		0	1	1	1	0	0	1	1	1	1	1	1	1
	1390	0	0	0	0	0		1	1	0	0	0	0	1	1	1	1	1	1
3d	Au	1	1	1	1	1	1		0	1	1	1	1	1	1	1	1	1	1
	Si	0	1	1	1	1	1	0		0	0	1	0	1	1	1	1	1	1
	319	0	0	0	0	1	0	1	0		0	0	0	1	1	1	1	1	1
	476	0	0	0	0	0	0	1	0	0		0	0	1	1	1	1	1	1
	756	0	0	0	0	0	0	1	1	0	0		0	1	1	1	1	1	1
	1390	0	0	0	0	1	0	1	0	0	0	0		1	1	1	1	1	1
7d	Au	1	1	1	1	1	1	1	1	1	1	1	1		0	0	0	0	0
	Si	1	1	1	1	1	1	1	1	1	1	1	1	0		0	0	0	0
	319	1	1	1	1	1	1	1	1	1	1	1	1	0	0		0	0	0
	476	1	1	1	1	1	1	1	1	1	1	1	1	0	0	0		0	0
	756	1	1	1	1	1	1	1	1	1	1	1	1	0	0	0	0		0
	1390	1	1	1	1	1	1	1	1	1	1	1	1	0	0	0	0	0	

Table A.17 - ANOVA of cell count on the terminal PEI layer *(PH)$_4$P* prepared at pH 9.0 on nanostructured surfaces (p < 0.05; 1 = significant; 0 = NOT significant)

		1d						3d						7d					
		Au	Si	319	476	756	1390	Au	Si	319	476	756	1390	Au	Si	319	476	756	1390
1d	Au		0	0	0	0	0	1	0	1	1	1	1	0	0	0	0	0	0
	Si	0		0	0	0	0	1	1	1	1	1	1	0	0	0	0	0	0
	319	0	0		0	0	0	1	1	1	1	1	1	0	0	0	0	0	1
	476	0	0	0		0	0	1	1	1	1	1	1	0	0	0	0	0	1
	756	0	0	0	0		0	1	0	1	1	1	1	0	0	0	0	0	0
	1390	0	0	0	0	0		1	1	1	1	1	1	0	0	0	0	0	0
3d	Au	1	1	1	1	1	1		1	0	0	0	0	0	0	0	0	0	1
	Si	0	1	1	1	0	1	1		1	0	0	0	0	0	0	0	0	0
	319	1	1	1	1	1	1	0	1		0	0	0	0	0	0	0	0	1
	476	1	1	1	1	1	1	0	0	0		0	0	0	0	0	0	0	0
	756	1	1	1	1	1	1	0	0	0	0		0	0	0	0	0	0	0
	1390	1	1	1	1	1	1	0	0	0	0	0		0	0	0	0	0	0
7d	Au	0	0	0	0	0	0	0	0	0	0	0	0		0	0	0	0	0
	Si	0	0	0	0	0	0	0	0	0	0	0	0	0		0	0	0	0
	319	0	0	0	0	0	0	0	0	0	0	0	0	0	0		0	0	0
	476	0	0	0	0	0	0	0	0	0	0	0	0	0	0	0		0	0
	756	0	0	0	0	0	0	0	0	0	0	0	0	0	0	0	0		0
	1390	0	0	1	1	0	0	1	0	1	0	0	0	0	0	0	0	0	

Acknowledgment

The thesis was written during my work as a research assistant in the biomedical materials group of the Institute of Pharmacy at the Martin Luther University Halle-Wittenberg. Many people have supported me during this time and helped me feeling well, academically and interpersonally. Those people I would like to thank the following.

At first, I want to thank my advisor and first reviewer Prof. Dr. Thomas Groth who gave me the opportunity to work in the biomedical materials group and to compose this thesis. He was always encouraging me to go on and was giving generative hints what can be done better. Further, I want to thank him for giving me many chances to present my work at several distinguished conferences as well as including me in several small bilateral projects to strengthen intercultural relations.

I want to thank Prof. Dr. Regine Willumeit of the Helmholtz Center Geesthacht and Prof. Dr.-Ing. Dr. h.c. Joachim Ulrich of the Martin Luther University Halle-Wittenberg for spending time on reviewing the thesis.

I want to thank all previous and current members of the biomedical materials group for the good cooperation and the always open and friendly atmosphere. Special thanks go to Dr. Jürgen Vogel for his consistently competent advice and valuable comments. I want to thank my previous and current fellow PhD and master students Kristin Kirchhof, Neha Aggarwal, Deepak Guduru, Aminatu Barry, Tobias Schmidt, Kashayar Rhazgandi, Alexander Köwitsch, Parul Singh, Stefan Müller, Guoying Zhou, Jingxian Zheng, Husnia Kindi, Anne-Kathrin Löffler, Elisa Gedan, Haihao Tang, Mauricio Jurado Abreu, Bhargav Tulabandula, Ankur Chhalotre, Pegah Esmaeilzadeh, Mingyan Zhao, Kantida Juncheed, Oliver Rhiel, and Alida Jehring for their troubleshooting, technical discussions and the joint ventures that I will always remember of. A warm thank you goes to Marlis Porobin for performing some of the zeta potential measurements and buffer preparation. Further, I want to acknowledge the work of my project students Julia Michaelis, Katharina Kluge, Patricia Pagenkopf, and Melanie Rolle.

Special thanks go to my parents for their moral support, encouragement, patience and confidence during the entire PhD period.

Finally yet importantly, I want to give lovely thanks and sweet kisses to my wife Monique who always stood behind my goals and me. She always had trust in me and made me believe that I will successfully pass the studies. Further, she always endorsed and encouraged me to go on while stepping back her own needs and goals. Moreover, she took care of our sweet little daughters Maria Aniella and Mia Amalia during the writing period and I know it was not easy at times. I am looking forward to a stellar family life in the future with less psychological pressure.

List of publications

Journal Articles

01. Niepel M.S., Fuhrmann B., Leipner H.S., Groth T., Polyelectrolyte multilayers formed on regular ordered nanostructures influence mammalian cell adhesion and growth, **under preparation**

02. Niepel M.S., Singh P., Fuhrmann B., Leipner H.S., Groth T., Nanoscaled Surface Patterns Influence Adhesion and Growth of Human Dermal Fibroblasts, *Langmuir*, **2013**, 29 (43): 13278-90

03. Li Z., Köwitsch A., Zhou G., Groth T., Fuhrmann B., Niepel M., Amado E., Kressler J., Enantiopure Chiral Poly(glycerol methacrylate) Self-Assembled Monolayers Knock Down Protein Adsorption and Cell Adhesion, *Advanced Healthcare Materials*, **2013**, 2 (10): 1377-87

04. Niepel M., Singh P., Fuhrmann B., Leipner H.S., Groth T., Cell adhesion on nanostructured surfaces designed by nanosphere lithography, *Proceedings of 10th International Workshop on Biomedical Engineering*, **2011**, doi: 10.1109/IWBE.2011.6079045, ISBN 978-1-4577-0553-3

05. Guduru D.[§], Niepel M.[§], Vogel J., Groth T., Nanostructured material surfaces - preparation, effect on cellular behavior and potential biomedical applications - a review, *The International Journal of Artificial Organs*, **2011**, 34 (10): 963-85

06. Niepel M., Peschel D., Groth T., Controlling fibroblast adhesion with pH modified polyelectrolyte multilayers, *The International Journal of Artificial Organs*, **2011**, 34 (2): 185-91

07. Niepel M., Peschel D., Sisquella X., Planell J.A., Groth T., pH-dependent modulation of fibroblast adhesion on multilayers composed of poly (ethylene imine) and heparin, *Biomaterials*, **2009**, 30 (28): 4939-47

[§] Both authors have contributed equally

Book Chapters

01. Niepel M.S., Kirchhof K., Heilmann A., Groth T., Controlling cell adhesion using pH-modified PEM films, in: *Layer-by-Layer Films for Biomedical Applications* (Picart C., eds.), Wiley-VCH, Weinheim, **2014**, **in print**

02. Niepel M.S., Köwitsch A., Yang Y., Ma N., Aggarwal N., Guduru D., Groth T., Generic methods of surface modification to control adhesion of cells and beyond, in: *Biomaterial Surface Science* (Taubert A., Mano J.F., and Rodriguez-Cabello J.C., eds.), Wiley-VCH, Weinheim, **2013**, ISBN 978-3527330317

03. Groth T., Liu Z.-M., Niepel M., Peschel D., Kirchhof K., Altankov G., Faucheux N., Chemical and physical modifications of biomaterial surfaces to control adhesion of cells, in: *Nanoengineered Systems for Regenerative Medicine*, NATO Science Series (Shastry V. and Altankov G., eds.), Springer, New York, **2009**, ISBN 978-9048187881

04. Niepel M., Kirchhof K., Hünerbein A., Neubert R., Groth T., Adhäsion und Vitalität von Fibroblasten auf Multischichten aus Polyethylenimin und Heparin, Proceedings of the „Deutschen Gesellschaft für klinische Mikrozirkulation und Hämorheologie", in: *Aktuelles aus der Klinischen Hämorheologie und Mikrozirkulation*, Pabst Science Publishers, Lengerich, **2008**, 42 - 55, ISBN 978-89967-505-4

Published Abstracts

01. <u>Niepel M.</u>, Fuhrmann B., Leipner H.S., Groth T., The combination of topographical and chemical stimuli controls adhesion and growth of human fibroblasts, *The International Journal of Artificial Organs*, 36 (8), **2013**, p. 551

02. <u>Niepel M.</u>, Fuhrmann B., Leipner H.S., Groth T., Chemically modified nanostructures influencing mammalian cell adhesion, *The International Journal of Artificial Organs*, 35 (8), **2012**, p. 565

03. <u>Niepel M.</u>, Fuhrmann B., Leipner H.S., Groth T., Influence of topographical and chemical stimuli of biomaterial surfaces on mammalian cell adhesion, *Interface Biology of Implants*, Proccedings, **2012**, p. 55, ISBN 978-3-00-038220-8

04. <u>Niepel M.</u>, Fuhrmann B., Leipner H.S., Groth T., Multischichten aus synthetischen und Biopolymeren steuern die Zelladhäsion auf nanostrukturierten Oberflächen, *Biomaterialien*, 12 (1-4), **2011**, p. 143

05. <u>Niepel M.</u>, Peschel D., Fuhrmann B., Leipner H.S., Groth T., Controlling cell adhesion with layer-by-layer technique and nanosphere lithography, *The International Journal of Artificial Organs*, 33 (7), **2010**, p. 455

06. <u>Niepel M.</u>, Peschel D., Sisquella X., Planell J.A., Groth T., Cell response on LbL modified biomaterial surfaces, *Biomaterialien*, 10 (S1), **2009**, p. 94

07. <u>Niepel M.</u>, Peschel D., Kirchhof K., Groth T., Kontrolle der Zelladhäsion durch nanostrukturierte Polyelektrolytmultischichten, *Biomaterialien*, 8 (3), **2007**, p. 198

08. <u>Niepel M.</u>, Kirchhof K., Groth T., Modification of Biomaterials with Layer-by-Layer technique, *Regenerative Medicine*, 2 (5), **2007**, p. 662

Oral Presentations

01. <u>Niepel M.</u>, Fuhrmann B., Leipner H.S., Groth T., The combination of topographical and chemical stimuli controls adhesion and growth of human fibroblasts, 40th Congress of European Society for Artificial Organs, 11th - 14th September, **2013**, Glasgow, Scotland

02. <u>Niepel M.</u>, Fuhrmann B., Leipner H.S., Groth T., A novel system of polyelectrolyte multilayers and discrete nanostructures controls cellular processes, 539th Wilhelm und Else Heraeus Seminar on *Micro-and Nanostructured Interfaces for Biological and Medical Research*, 30th June - 03rd July, **2013**, Bad Honnef, Germany

03. <u>Niepel M.</u>, Fuhrmann B., Leipner H.S., Groth T., Nanostructured biomaterial surfaces and their influence on adhesion and growth of human fibroblasts, 4th International Congress *BioNanoMed*, 13th - 15th March, **2013**, Krems (Danube), Austria

04. <u>Niepel M.</u>, Fuhrmann B., Leipner H.S., Groth T., Chemically modified nanostructures influencing mammalian cell adhesion, 39th Congress of European Society for Artificial Organs, 26th - 29th September, **2012**, Rostock, Germany

05. Niepel M., Singh P., Michaelis J., Kluge K., Fuhrmann B., Leipner H.S., <u>Groth T.</u>, Controlled cell adhesion on layer-by-layer modified, tetrahedral nanostructures, 4th Joint ESAO-IFAO Congress, 09th - 12th October, **2011**, Porto, Portugal

06. <u>Niepel M.</u>, Singh P., Fuhrmann B., Leipner H.S., Groth T., Cell adhesion on nanostructured surfaces designed by nanosphere lithography, 10th International Workshop on Biomedical Engineering, 05th - 07th October, **2011**, Kos, Greece

07. Groth T., <u>Niepel M.</u>, Aggarwal N., Peschel D., Kirchhof K., Liu Z.-M., Glycan-coated surfaces for control of cell behavior, European Materials Research Society Spring Meeting, 07th - 11th June, **2010**, Strasbourg, France

08. <u>Niepel M.</u>, LbL designed surfaces to control cell adhesion, Award ceremony at annual meeting of the *German Society for Biomaterials (DGBM e.V.),* 20th - 22nd November, **2008**, Hamburg, Germany

09. <u>Niepel M.</u>, Peschel D., Vogel J., Groth T., Nano-structured coatings on biomaterials for control of cell adhesion, 8th World Biomaterials Congress, 28th May - 01st June, **2008**, Amsterdam, Netherlands

Posters

01. <u>Niepel M.</u>, Fuhrmann B., Leipner H.S., Groth T., Discrete nanostructures modified with polyelectrolyte multilayers guide human fibroblasts, Dresden School on *Functional Nanomaterials*, 30th September - 04th Oktober, **2013**, Dresden, Germany

02. <u>Niepel M.</u>, Fuhrmann B., Leipner H.S., Groth T., A novel system of polyelectrolyte multilayers and discrete nanostructures controls cellular processes, 539th Wilhelm und Else Heraeus Seminar on *Micro-and Nanostructured Interfaces for Biological and Medical Research*, 30th June - 03rd July, **2013**, Bad Honnef, Germany

03. <u>Niepel M.</u>, Fuhrmann B., Leipner H.S., Groth T., Mammalian cell adhesion on ordered, chemically modified nanostructures, Advanced Summer School "*Interrogations at the biointerface*", 25th - 29th June, **2012**, Barcelona, Spain

04. <u>Niepel M.</u>, Fuhrmann B., Leipner H.S., Groth T., Influence of topographical and chemical stimuli of biomaterial surfaces on mammalian cell adhesion, 4th International Symposium *Interface Biology of Implants*, 09th - 11th May, **2012**, Rostock, Germany

05. <u>Niepel M.</u>, Fuhrmann B., Leipner H.S., Groth T., Multischichten aus synthetischen und Biopolymeren steuern die Zelladhäsion auf nanostrukturierten Oberflächen, Annual meeting of the „*Deutschen Gesellschaft für Biomaterialien e.V.*", 10th - 12th November, **2011**, Gießen, Germany

06. <u>Niepel M.</u>, Fuhrmann B., Leipner H.S., Groth T., Polyelectrolyte multilayers on gold nanostructures control cell adhesion, *20 Years Layer-by-Layer Assembly: New Frontiers for Fundamental Science and for Applications*, 10th - 12th March, **2011**, Strasbourg, France

07. <u>Niepel M.</u>, Fuhrmann B., Leipner H.S., Groth T., Layer-by-layer modified nanostructures and their influence on cell adhesion, *ESAO Winter School*, 26th - 29th January, **2011**, Semmering, Austria

08. <u>Niepel M.</u>, Fuhrmann B., Leipner H.S., Groth T., Combination of nanosphere lithography (NSL) and atom transfer radical polymerization (ATRP) to direct cell adhesion on biomaterials surfaces, 14th International Conference *Polymeric Materials*, 15th - 17th September, **2010**, Halle (Saale), Germany

09. <u>Niepel M.</u>, Peschel D., Fuhrmann B., Leipner H.S., Groth T., Controlling cell adhesion with layer-by-layer technique and nanosphere lithography, *37th Congress of European Society for Artificial Organs*, 08th - 11th September, **2010**, Skopje, Macedonia

10. <u>Niepel M.</u>, Peschel D., Sisquella X., Fuhrmann B., Leipner H.S., Planell J.A., Groth T., Combination of layer-by-layer technique and nanosphere lithography to control adhesion of cells, 459th Wilhelm and Else Heraeus Seminar on *Degradable Polymers as Biomaterials*, 30th May - 02nd June, **2010**, Bad Honnef, Germany

11. <u>Niepel M.,</u> Peschel D., Sisquella X., Planell J.A., Groth T., Self-assembled nano-structures on biomaterials to control cell adhesion, 14th Symposium on *Nanostructured Polymers/ Nanocomposites*, 18th - 19th May, **2010**, Halle (Saale), Germany

12. <u>Niepel M.,</u> Peschel D., Sisquella X., Fuhrmann B., Leipner H.S., Planell J.A., Groth T., Polyelectrolyte multilayers and nanosphere lithography control the adhesion of cells, International Symposium *Bio meets Nano and IT*, 24th November, **2009**, Halle (Saale), Germany

13. <u>Niepel M.,</u> Peschel D., Sisquella X., Planell J.A., Groth T., Self-assembled nano-structures on biomaterials to control the adhesion of cells, *22nd European Conference on Biomaterials*, 07th - 11th September, **2009**, Lausanne, Switzerland

14. <u>Niepel M.,</u> Peschel D., Sisquella X., Planell J.A., Groth T., Cell response on LbL modified biomaterial surfaces, 3rd International Symposium *Interface Biology of Implants*, 13th - 15th May, **2009**, Rostock, Germany

15. <u>Niepel M.,</u> Peschel D., Groth T., Multilayered surface coatings as tool for the control of cell adhesion and growth, *Controlled Release Society 2009*, 19th - 20th March, **2009**, Halle (Saale), Germany

16. <u>Niepel M.,</u> Peschel D., Groth T., Self-assembled multilayers as nano-structuring tool to regulate cell adhesion, *BioNanoMed 2009*, 26th - 27th January, **2009**, Krems (Danube), Austria

17. <u>Niepel M.,</u> Peschel D., Vogel J., Groth T., Nano-structured multilayer coatings on biomaterials for control of cell adhesion, 13th International Conference *Polymeric Materials*, 24th - 26th September, **2008**, Halle (Saale), Germany

18. <u>Niepel M.,</u> Peschel D., Groth T., Nano-structured multilayer coatings for regulation of cell adhesion, IMPRS Workshop on *Advances in Science and Technology of Nanostructures*, 03th - 04th June, **2008**, Halle (Saale), Germany

19. <u>Niepel M.,</u> Kirchhof K., Groth T., Nano-structured coatings on biomaterials using the layer-by-layer technique, International Symposium *Bio meets Nano and IT*, 04th December, **2007**, Halle (Saale), Germany

20. <u>Niepel M.,</u> Peschel D., Kirchhof K., Groth T., Kontrolle der Zelladhäsion durch nanostrukturierte Polyelektrolytmultischichten, Annual meeting of the *German Society for Biomaterials (DGBM e.V.)*, 22nd - 24th November, **2007**, Hannover, Germany

21. <u>Niepel M.,</u> Kirchhof K., Groth T., Modification of Biomaterials with Layer-by-Layer technique, *3rd World Congress on Regenerative Medicine*, 18th -20th October, **2007**, Leipzig, Germany

Curriculum vitae

Personal data

Name:	Marcus S. Niepel
Address:	Rosenstr. 44
	D - 08468 Reichenbach
Day of birth:	18. November 1980 in Reichenbach
Family status:	married, two daughters
Nationality:	German

Experience

05/2013 - present	Postdoctoral Fellow within DFG-Project "Nanomaterials and Stem Cell Differentiation" at biomedical materials group Martin Luther University Halle-Wittenberg
02/2009 - 04/2013	Research assistant at biomedical materials group Martin Luther University Halle-Wittenberg
05/2008 - 09/2008	Graduate assistant at biomedical materials group Martin Luther University Halle-Wittenberg

Education

10/2008 - 01/2013	Martin Luther University Halle-Wittenberg Centre for Engineering, Institute of Pharmacy Ph.D. student Title: Discrete nanostructures and their physicochemical modification as tool to control cell function
10/2003 - 04/2008	Martin Luther University Halle-Wittenberg Centre for Engineering, Institute of Pharmacy Diploma in Bioengineering Emphasis on Biomedical Materials Topic: ‚LbL designed surfaces to control cell adhesion'
09/2000 - 06/2003	Interdruck Graphischer Großbetrieb GmbH, Zwenkau (New: Offizin Andersen Nexö Leipzig GmbH) Apprenticeship as industrial clerk
08/1992 - 08/1999	Secondary school Reichenbach, university-entrance diploma

Fellowships

09/2011 - 10/2011	DAAD research fellowship for Greece Institute of Biomechanics and Biomedical Engineering, University of Patras, Greece
09/2009 - 10/2009	DAAD research fellowship for China College of Materials Science and Chemical Engineering, Zhejiang University, Hangzhou, China
12/2008	Research fellowship of the Institute for Bioengineering of Catalonia (IBEC), Barcelona, Spain

10/2008 - 11/2008	DAAD research fellowship for Spain Institute for Bioengineering of Catalonia (IBEC), Barcelona, Spain
09/2008	DAAD research fellowship for Bulgaria Bulgarian Academy of Science, Sofia, Bulgaria
10/2007	DAAD research fellowship for Bulgaria Bulgarian Academy of Science, Sofia, Bulgaria

Awards

06/2012	**Best Poster Award** received from the Institute for Bio-engineering of Catalonia (IBEC) at the symposium 'Interrogations at the Biointerface', 25th - 29th June 2012, Barcelona, Spain
09/2010	**Best Poster Award** received from the Martin Luther University at 14th International Scientific Conference on Polymeric Materials, 15th - 17th September 2010, Halle (Saale), Germany
09/2010	**Best Poster Award** received from the European Society for Artificial Organs (ESAO) at 37th Congress of ESAO, 08th - 11th September 2010, Skopje, Macedonia
09/2010	**Student Travel Award** received from the German Academic Exchange Service (DAAD) for the 37th Congress of ESAO, 08th - 11th September 2010, Skopje, Macedonia
09/2009	**Best Poster Award** received from the European Society for Biomaterials (ESB) at 22nd European Conference on Biomaterials, 07th - 11th September 2009, Lausanne, Switzerland
11/2008	**Best Diploma Thesis 2008** received from the German Society for Biomaterials (DGBM e.V.)
05/2008	**Student Travel Award** received from the German Society for Biomaterials (DGBM e.V.) for the 8th World Biomaterials Congress, 28th May - 1st June 2008, Amsterdam, Netherlands

Halle (Saale), 29. April 2014

Marcus S. Niepel

Statutory declaration

I herewith declare that I have authored this thesis independently, that I have not used other than the declared sources/ resources, and that I have explicitly marked all material, which has been quoted either literally or by content from the used sources.

Hiermit erkläre ich an Eides statt, dass ich die vorliegende Arbeit selbstständig verfasst, andere als die angegebenen Quellen/ Hilfsmittel nicht benutzt, und die von den benutzten Quellen wörtlich und inhaltlich entnommenen Stellen als solche kenntlich gemacht habe.

Halle (Saale), 29. April 2014

Marcus S. Niepel